Large Eddy and Direct Numerical Simulation of Single and Multiphase Flows Relying on Lagrangian Particle Methods

Von der Fakultät für Ingenieurwissenschaften, Abteilung Maschinenbau und Verfahrenstechnik

der

Universität Duisburg-Essen

zur Erlangung des akademischen Grades

eines

Doktors der Ingenieurwissenschaften

Dr.-Ing.

genehmigte Dissertation

von

Martin Rieth
aus
München

Gutachter: Univ.-Prof. Dr.-Ing. Andreas Kempf
Univ.-Prof. Dr.-Ing. Johannes Janicka
Tag der mündlichen Prüfung: 08.02.2018

Abstract

In this work, tools are developed for different applications of Lagrangian particle methods in large eddy simulation (LES) and direct numerical simulation (DNS), to represent solid fuel particles, and notional gas phase particles in the Lagrangian transported filtered density function (FDF) method.

In the first part of this work, the computational framework for pulverized coal combustion LES relying on Lagrangian particles is extended by the incorporation of a multi-dimensional flamelet model for gas phase combustion and different devolatilization models. The multidimensional flamelet model is parameterized by two mixture fractions for volatiles and char off-gases, enthalpy and scalar dissipation rate. The framework and modeling is adapted to a semi-industrial scale coal furnace and a laboratory coal jet flame to validate the simulation approach in a realistic case and to study devolatilization models in detail. The data is analyzed and extensively compared to experimental measurements, with emphasis on species and temperature predictions, burnout statistics, radiation, and devolatilization and ignition behavior. To be able to better understand the ignition process and provide a database for flamelet modeling, the code is extended for pulverized coal combustion simulation DNS. This includes the incorporation of species transport, chemical kinetics and appropriate solvers. The DNS data is analyzed in detail, focusing on the ignition behavior, burning modes, heat losses and pseudo-flamelet structures, providing valuable implications for flamelet modeling in the LES.

For the second part of this work, a transported filtered density function (FDF) method is implemented into the LES code. This transported FDF method is then modified to combine cost-effective flamelet-based presumed FDF models with accurate transported FDF finite rate chemistry strategies in a hybrid manner. The hybrid method relies on seeding Lagrangian particles representing the transported FDF only at those locations of the flame where the flamelet model is insufficient, aiming to improve accuracy at an affordable cost. This hybrid method is tested on the Sydney/Sandia piloted jet flame with inhomogeneous inlets. It is shown that the method can accurately predict the flame with a greatly reduced number of computational particles.

Zusammenfassung

In dieser Arbeit wurden Werkzeuge für verschiedene Anwendungen von Lagrange-Partikel-Methoden in Grobstruktursimulationen (LES) und ‚Direkten Numerischen Simulationen' (DNS) entwickelt, zum einen um Partikel aus Festbrennstoff, und zum anderen um ‚fiktive' Gasphasenpartikel in der Methode der Lagrange-transportierten gefilterten Wahrscheinlichkeitsdichtefunktion zu beschreiben.

In dem ersten Teil der Arbeit wurde das numerische Grundgerüst für die Grobstruktursimulation von Kohlenstaubverbrennung, welches auf der Lagrange'schen Beschreibung der Kohlepartikel beruht, durch die Implementierung eines mehrdimensionalen Flamelet-Modells zur Beschreibung der Gasphasenverbrennung und von verschiedenen Pyrolyse-Modellen erweitert. Das mehrdimensionale Flamelet-Modell ist durch zwei Mischungsbrüche für die Volatilen und die Koksabbrandgase, sowie Enthalie und skalare Dissipationsrate parametrisiert. Die numerische Methode und Modellierung wurde für die Simulation einer semi-industriellen Brennkammer und einer Kohlestrahlflamme angepasst, um die Simulationsmethode anhand eines realistischen Falls zu validieren und Pyrolyse-modelle im Detail zu untersuchen. Die Ergebnisse wurden analysiert und umfassend mit den Experimenten verglichen, wobei der Fokus auf Spezies- und Temperaturvorhersagen, Ausbrandstatistiken, Strahlung, sowie Pyrolyse- und Zündverhalten lag. Um ein besseres Verständnis des Zündprozesses zu erlangen, sowie eine Datenbank für zukünftige Flamelet-Modellierung zu liefern, wurde der Code um die Möglichkeit der DNS von Kohlestaubfeuerung erweitert. Dies beinhaltet den Transport von chemischen Spezies, die Beschreibung chemischer Reaktionen sowie entsprechende Löser. Die DNS wurde im Detail untersucht, wobei der Fokus auf dem Zündverhalten, den Brennmodi, Wärmeverlusten und Pseudo-Flameletstrukturen lag, um so eine wertvolle Basis für detailliertere LES Flamelet-Modellierung zu liefern.

Für den zweiten Teil der Arbeit wurde die Methode der Lagrange-transportierten gefilterten Wahrscheinlichkeitsdichtefunktion (FDF) in den LES Code implementiert. Diese transportierte FDF Methode wurde im Anschluss modifiziert, um kosteneffektive Flamelet-basierte und angenommene FDF Strategien mit den auf der genauen transportierten FDF mit zeitaufgelöster detaillierter Chemie beruhenden Strategien, in einer hybriden Methode zu kombinieren. Diese hybride Methode beruht auf dem Einsatz von Partikeln nur dort, wo das Flamelet-Modell unzureichend ist, mit dem Ziel die Genauigkeit bei erschwinglichem Aufwand zu verbessern. Die hybride Methode wurde anhand der Simulation der pilotierten Sydney/Sandia Flamme mit inhomogenem Einlass getestet. Dabei zeigte sich, dass die Methode diese Flamme mit einer deutlich verkleinerten Anzahl an Partikeln genau vorhersagen kann.

Preface

The work presented here is mainly a compilation of the published works on pulverized coal combustion and the hybrid large eddy simulation with a transported filtered density function method (currently in preparation for submission). The work in Chapter 5 on the semi-industrial scale coal furnace focusing on the application of the flamelet model for pulverized coal combustion in a realistic test case has been published in *Combustion & Flame* (Rieth, Proch, Rabaçal, Franchetti, Cavallo Marincola & Kempf, 2016). The work on the refinement of the simulation on this furnace in Chapter 6 has been published in the *Proceedings of the Combustion Institute* (Rieth, Proch, Clements, Rabaçal & Kempf, 2017). The study on the coal jet flame focusing on devolatilization modeling and volatile combustion in Chapter 7 has been published in the *Proceedings of the Combustion Institute* (Rieth, Clements, Rabaçal, Proch, Stein & Kempf, 2017) as well. The direct numerical simulation study on coal particle ignition and volatile combustion in Chapter 8 has been published in *Fuel* (Rieth, Kempf, Kronenburg & Stein, 2018). Finally, the hybrid assumed and transported filtered density function study on the Sydney/Sandia jet flame with inhomogeneous inlets in Chapter 9 is currently under preparation for submission in *Combustion & Flame* (Rieth, Chen, Menon & Kempf). To give a more complete and coherent overview, most of the underlying theory has been compiled in the first four chapters at the expense of introducing a certain amount of redundancy.

Not all of the work that the author of this thesis has been involved in during his PhD studies are reported here. A study of subgrid models for the large eddy simulation tested on isothermal flows has been published in *Computers & Fluids* (Rieth, Proch, Stein, Pettit & Kempf, 2014). The implemented transported filtered density function method with a different hybrid approach has been applied to premixed and non-premixed turbulent opposed jet flames, presented at conferences and will be prepared for publication. In addition, direct numerical simulation work on the comparison of flamelet and finite-rate chemistry strategies in premixed flames has been presented at a conference and is in preparation for publication.

Contents

viii

List of Figures

List of Tables

Nomenclature

Abbreviations

AASB	Aerodynamically Air Staged Burner
ADF	Assumed filtered density function
CCSS	Center for Computational Sciences and Simulation
CDF	Cumulative density function, cumulative size distribution
CDS	Central differencing scheme
CP-DNS	Carrier-phase direct numerical simulation
CPD	Chemical Percolation model for Devolatilization
CRIEPI	Central Research Institute of Electric Power Industry
CRM	Competing rates model (Kobayashi model)
DC	Direct chemistry
DDF	Droplet distribution function
DFG	Deutsche Forschungsgemeinschaft (German Research Foundation)
DNS	Direct numerical simulation
DOM	Discrete ordinates method
DQMOM	Direct quadrature method of moments
EBU	Eddy break-up model
EDC	Eddy dissipation concept
ERZ	External recirculation zone
FC	Fixed carbon
FC	Flamelet chemistry
FDF	Filtered density function
FG-DVC	Functional-Group, Depolymerization, Vaporization, Cross-linking
FGM	Flamelet generated manifold
FI	Flame index
FPV	Flamelet/progress variable
GRI	Gas Research Institute
GWSGG	Grey weighted sum of grey gases
HDF	Hybrid filtered density function
HRR	Heat release rate
IEM	Interaction-by-exchange-with-the-mean
IFRF	International Flame Research Foundation
IRZ	Internal recirculation zone
LDV	Laser Doppler velocimetry
LEM	Linear eddy modeling

LES	Large eddy simulation
LHV	Lower heating value
LIF	Laser-induced fluorescence
LMC	Lagrangian Monte Carlo
LRZ	Leibniz Supercomputing Centre
MILD	Moderate and intense low oxygen dilution
MMC	Multiple mapping conditioning
MPI	Message passing interface
ODE	Ordinary differential equation
PCC	Pulverized coal combustion
PDF	Probability density function
PND	Particle number density
RANS	Reynolds-averaged Navier-Stokes
RHS	Right-hand side
RLS	Resolved laminar flow simulations
RTE	Radiative transfer equation
SDE	Stochastic differential equation
SFMDF	Scalar filtered mass weighted density function
SFOR	Single first order reaction
SGS	Subgrid scale
TDF	Transported filtered density function
TVD	Total variation diminishing
UDS	Upwind differencing scheme
VM	Volatile matter
WALE	Wall-adapting local eddy viscosity

Dimensionless numbers

Re	Reynolds number
Re_0	Reynolds number of the largest eddies
Le	Lewis number
Nu	Nusselt number
Pr	Prandtl number
Sc	Schmidt number
Sc_t	Turbulent Schmidt number

Greek Symbols

α	Constant in subgrid turbulence particle interaction model
α, β	Weights in Runge-Kutta procedure
$\alpha_1, \alpha_2, \alpha_3$	Invariant angles
α_{ij}	Part of the subgrid stress tensor
$\bar{\phi}$	Reynolds-filtered quantity
β_{ij}	Part of the subgrid stress tensor based on test-filtered velocities
χ	Scalar dissipation rate
χ_α	Chemical symbol of species α
Δ	Cell/filter size
δ	Dirac delta function
Δ_t	Time step width

δ_{ij}	Kronecker delta
$\dot{\omega}_\alpha^m$	Molar net production rate of species α
$\dot{\omega}_\alpha$	Chemical source term of species α
$\dot{\psi}_i$	Temporal derivative of sample space quantity
ϵ	Dissipation rate
ϵ_p	Particle emissivity
η	Effectiveness factor
η	Kolmogorov length scale
Γ	Gamma function
κ	Heat conductivity
μ	Dynamic viscosity
$\nabla \cdot q_{\mathrm{rad}}$	Radiative enthalpy source term
ν	Kinematic viscosity
ν_t	Turbulent (subgrid) viscosity
$\nu'_{\alpha\gamma}$	Forward molar stoichiometric coefficients for species α within reaction γ
$\nu''_{\alpha\gamma}$	Backward molar stoichiometric coefficients for species α within reaction γ
ν_{sgs}	Subgrid kinematic viscosity
Ω	Mixing frequency
ϕ	Arbitrary quantity
ϕ	Equivalence ratio
ϕ	Thiele modulus
ϕ'	Reynolds sub-filter fluctuation
ϕ''	Favre sub-filter fluctuation
ϕ_i^n	Arbitrary quantity component of n-th realization
$\boldsymbol{\Phi}$	Vector of arbitrary quantity
$\boldsymbol{\psi}$	Sample space vector
ψ_i	Sample space vector component
ρ	Density
ρ_p	Particle density
$\sigma_1,\ \sigma_2,\ \sigma_3$	Singular values of the filtered velocity gradient tensor
τ	Kolmogorov time scale
τ	Tortuosity of the pores
τ_{con}	Convective time scale
τ_{mix}	Mixing time scale
τ_p	Particle relaxation time
τ_t	Subgrid velocity fluctuation particle interaction time scale
τ_{ij}	Stress tensor
τ_{ij}^{SGS}	Subgrid stress tensor
$\tau_{p,\mathrm{St}}$	Particle relaxation time for Stokes flow
θ	Porosity of the coal
Θ_r	Gas radiation temperature
$\tilde{\phi}$	Favre-filtered arbitrary quantity
υ	Kolmogorov velocity scale
ξ_i	Component of vector of Gaussian-distributed random variables
$S_{\chi_{\tilde{Z}}}$	Unresolved scalar dissipation rate

Roman Symbols

$\bar{P}$	Filtered probability density function of particle phase variables
$\bar{r}_{\text{pore}}$	Mean pore radius
$\dot{m}_{\text{char}}$	Mass flow rate of char combustion
$\dot{m}_{\text{devol}}$	Mass flow rate of devolatilization
$\dot{m}_{\text{f}}$	Fuel mass flow
$\dot{m}_{\text{ox}}$	Oxidizer mass flow
$\dot{Q}$	Enthalpy source term
$\dot{q}_{\text{char}}$	Heat flux due to char combustion
$\dot{q}_{\text{devol}}$	Heat flux due to devolatilization
$\dot{S}_{\phi}$	Source term of arbitrary quantity ϕ
$\dot{S}_{\tilde{Z}_{\alpha}}$	Source term for mixutre fraction α
$\dot{W}^{+}$	Subgrid variance source term from particles
$\tilde{\mathbf{u}}$	Filtered velocity vector
$\mathbf{F}_{D,n}$	Drag force vector on n-th particle
$\mathbf{g}$	Vector of gravitational acceleration
$\mathbf{u}_p$	Particle velocity vector
$\mathbf{x_p}$	Particle position vector
$\mathcal{D}$	Domain $\mathcal{D}$
$\mathcal{F}$	Particle source term
$\mathcal{I}_1, \mathcal{I}_2, \mathcal{I}_3$	Invariants of the square of filtered velocity gradient tensor
$\mathcal{P}$	Projection from Lagrangian to Eulerian description
$\mathcal{S}$	Filtered characteristic rate of strain
$\overline{R}$	Universal gas constant
$\tilde{g}_{ij}$	Filtered velocity gradient tensor
$\tilde{\tilde{P}}$	Favre subgrid PDF
$\tilde{\tilde{S}}_{ij}$	Strain rate tensor
$\widetilde{Z''^2}$	Subgrid variance of mixture fraction Z
a	Acceleration vector
a, b, c, d, e, f	Lumped quantities for beta-PDF
A_{γ}	Pre-exponential factor of reaction γ
A_f	Cell face area
A_p	Particle projected area
B	Blowing correction
$B(r)$	Flux limiter function
C	Modeling constant in the dynamic procedure
C	Normalized progress variable
C^*	Estimated model constant in the dynamic procedure
C_0	Particle subgrid term model constant
C_{dev}	Devolatilization progress
C_{diff}	Mass diffusion limited rate constant for diffusion of oxygen
C_{v}	Model constant for subgrid variance model
C_{ϕ}	Mixing model constant, scalar-to-mechanical time scale ratio
C_{σ}	Sigma model constant

c_p	Isobaric heat capacity
C_s	Subgrid (Smagorinsky) model constant
$C_{\chi_{\tilde{Z}}}$	Subgrid scale dissipation rate model constant
C_χ	Scalar dissipation rate model constant
C_{Kn}	Constant for Knudsen diffusion
$c_{p,p}$	Particle heat capacity
C_S	Smagorinsky model constant
D	Diameter
D	Diffusion coefficient
$d\mathbf{W}$	Wiener term vector
D_0	Diffusion coefficient at reference temperature
D_α	Destruction of mass fraction of species α
D_α	Diffusion coefficient of species α
D_{eff}	Effective diffusivity
D_ϕ	Diffusion coefficient of arbitrary quantity ϕ
D_e	Effective pore diffusion coefficient
D_{Kn}	Knudsen diffusion coefficient
$D_{j,\alpha}$	Binary diffusion coefficient of species j and α
D_t	Turbulent diffusion coefficient
dW_i	Component of Wiener vector
E_γ	Activation energy of reaction γ
f	Factor to account for immersed boundaries in interpolation scheme
f	Fine-grained density function
F_{SGS}	Subgrid scalar flux
F_t	Scalar filtered mass density function
f_t	Fine-grained probability density function in transported FDF context
$f_{\alpha,i}$	Body force components acting on species α
G	Filter function
g_1	Function for evaluating volatile matter and fixed carbon heat capacity
G_{ij}	Square of filtered velocity gradient tensor
h	Specific enthalpy
h^*_{char}	Enthalpy of char off-gas
h_α	Specific enthalpy of species α
h_{char}	Enthalpy of char
h_{vol}	Enthalpy of volatiles
I_{IB}	Immersed boundary indicator
J_i^α	Diffusive flux of state vector component α in direction i
K_γ	Equilibrium constant of reaction γ
k_{devol}	Devolatilization rate
k_{SGS}	Subgrid kinetic energy
k_i	Intrinsic reactivity
$k_{f,\gamma}$	Forward rate constants of reaction γ
$k_{f,\gamma}$	Reverse rate constants of reaction γ
L	(Characteristic) length
l^*	Subgrid model length scale

l_0	Length scale of the largest eddies
L_{ij}	Leonard stresses
m_{VM}	Mass of volatile matter
m_p	Mass of a particle
M_{ij}	Tensor for contraction in the dynamic procedure
N_{DNS}	Number of cells required for direct numerical simulation
N_s	Number of species
p	Pressure
P_α	Production of mass fraction of species α
p_{mod}	Modified pressure
q_γ	Progress of reaction γ
q_i	Enthalpy flux
$q_{R,i}$	Radiative heat flux
R	Universal gas constant
r	Input of flux limiter function
R_{uni}	Universal gas constant
R_{char}	Chemical reaction rate coefficient for char conversion
R_{ox}	Bulk molecular mass diffusion coefficient of oxygen
S_α	Source term of state vector component α
S_{N_2}	Nitrogen mass going along with stoichiometric oxygen requirement
S_a	Specific internal surface area
S_{O_2}	Stoichiometric oxygen mass requirement
S_{ij}^d	Deviatoric part of the strain rate tensor
T	Temperature
t	Time
t^*	Subgrid model time scale
t_0	Width of top-hat
T_m	Mean temperature between particle and gas
T_{ij}	Subfilter stress tensor with respect to test filtering
u	(Characteristic) velocity
U^*	Subgrid model velocity scale
u_0	Velocity scale of the largest eddies
u_j	Velocity vector components
V	Volume
v	Specific volume
V_i^c	Diffusion correction velocity component
$V_{\alpha,j}$	Diffusion velocity components of species α
W	Mean molecular weight of the mixture
w	Interpolation weight
W_α	Molecular weight of species α
X_α	Molar fraction of species α
x_j	Components of the Cartesian coordinate vector
Y_α	Mass fraction of species α
Y_{f}	Fuel mass fraction
Y_{ox}	Oxidizer mass fraction

Y_C	Progress variable
Y_p	Progress variable
Z	Mixture fraction
Z_a, Z_b	Lower and upper mixture fractions for top-hat PDF
Z_y, Z_z	Flamelet tangential coordinates

Superscripts

n	N-th realization, n-th particle
n	N-th time-/iteration step
SGS	Subgrid scale

Subscripts

char	Char off-gas, char combustion
f	fuel
ox	oxidizer
st	Stoichiometric
u	Unburned
vol	Volatiles

Mathematical operators

$\bar{}$	Filtering operation
$\breve{}$	Favre test filtering operation
$\hat{}$	Test filtering operation
$\nabla_{\boldsymbol{v}}$	Gradient operator with respect to velocity vector
$\tilde{}$	Favre filtering operation
E	Expectation

Acknowledgments

The work presented in this thesis has been done during my time as a PhD student at the Chair of Fluid Dynamics at the University of Duisburg-Essen. First, I would like to thank Prof. Dr.-Ing. Andreas Kempf very much for giving me the opportunity to conduct my doctoral studies in his group. I am very thankful for his guidance, trust and support, and for opening opportunities such as research visits at the University of California at Berkeley and the Georgia Institute of Technology, and for giving me the chance to present my work at international conferences.

I would also like to thank Prof. J.-Y. Chen and Prof. Suresh Menon for their hospitality, and the fruitful and pleasant time I spent in their labs. Furthermore, I would like to thank Prof. Johannes Janicka for co-examining my work.

I thank my research group at the University of Duisburg-Essen. They all made the work much more enjoyable. Special thanks go to Fabian Proch with whom I shared an office during most of my PhD time and from whom I could learn a lot. I am also thankful for the great work of my predecessors, collaborators, colleagues and co-authors. Without them my work wouldn't have had the outcome it had.

Finally, I would like to thank my family for their constant support and belief and Richelle for her love and making the past few years so much nicer.

Chapter 1

Introduction

1.1 Motivation

Today, mankind's energy consumption is mainly (by around 81%) covered by burning fossil fuels such as natural gas, oil and coal, as evaluated by the International Energy Agency [14][1]. In addition, approximately 10% in primary energy demand is covered by combustion of biomass. Therefore, combustion by far constitutes the most important mechanism to convert primary energy into usable energy. However, fossil fuels are limited and their conversion releases so-called greenhouse gases, mostly CO_2, which are recognized as drivers of global warming [210], as well as pollutants such as NO_x, SO_x or mercury-containing species, which are health threatening to humans. Hence, international and local governmental efforts are directed towards policies that aim at reducing pollutants and greenhouse gases to limit negative impacts on earth and society [206]. Depending on the policy scenario, the International Energy Agency projects the share of combustion on the primary energy conversion (including biomass) to drop to between 75 and 88% by 2040, with the former based on the ambitious '2 degree' goal and the latter based on current policies. However, even though the total amount of primary energy converted by combustion is projected to decrease by approximately 7% by 2040, the CO_2 emissions are predicted to be reduced by roughly 41% to achieve the '2 degree' goal, which illustrates the importance of energy efficiency gains and other measures to mitigate CO_2 emissions such as the carbon capture and storage, aside from implementing renewable energy technology. This highlights that research towards cleaner combustion processes is crucial for mitigating global warming.

The goal of this work is to contribute to cleaner and more efficient combustion processes by means of developing and improving computational tools for combustion research and engineering. While there has been significant progress in turbulent combustion research, there are still many open questions that need to be answered to achieve predictive capabilities of computational models [11]. Experiments provide crucial information for the understanding of turbulent combustion, but harsh environments often do not permit access to diagnostics. However, numerical simulations can complement experimental data to obtain improved insight into the turbulent combustion process. Ultimately, the goal

---

[1]The latest figures in the World Energy Outlook 2015 correspond to the year 2013.

is to achieve predictive capabilities of numerical simulations such that combustors with increased efficiency and reduced pollutant formation can be designed on computers.

This work focuses on different aspects of the simulation of turbulent combustion. As the main part of this work, methods for large eddy simulations (LES) of pulverized coal combustion are developed, which focus on the improvement of the description of gaseous combustion by means of a flamelet model and the incorporation of detailed pyrolysis modeling in solid fuel applications. As a more fundamental study, a direct numerical simulation (DNS) of an igniting coal particle laden shear layer is performed, which provides insight into the ignition mechanism of solid fuel combustion and a dataset that will be used for further, more detailed modeling. The work presented constitutes necessary steps towards simulating and designing cleaner solid fuel combustion technology, such as biomass combustion and pulverized coal combustion with carbon capture and storage.

As a different application of LES combined with Lagrangian particle methods, the final part of this thesis focuses on a hybrid LES and transported density function modeling applied to a laboratory partially premixed flame experiment representative of conditions in modern gas turbine combustors. This aims at improving the overall accuracy of LES by combining cheap, less accurate with more expensive detailed methods that are only used where it is necessary to obtain the desired accuracy. This method can potentially be applied to a variety of problems in the future, for example, the large solid fuel combustors studied in this work.

1.2   Thesis Outline

As this work deals with LES and DNS of turbulent reacting single- and multiphase flows, Chapter 2 first describes the underlying theory, encompassing the governing equations of reacting flows, chemical kinetics, turbulence, DNS, LES, multiphase flow as well as coal combustion. Subsequently, Chapter 3 presents approaches for turbulent combustion modeling in the context of LES, which is followed by the description of how the equations are solved numerically in Chapter 4. The following chapters show applications of the methods and models outlined in the first four chapters, and are published work [199, 200, 201, 202]. Hence, some of the descriptions in the first four chapters may be redundant, but are given for a more complete and coherent overview of the theory. Chapter 5 presents simulations of a semi-industrial scale coal furnace using a multidimensional flamelet model coupled with a beta-PDF (probability density function). This chapter also describes the coal modeling in detail. As a follow-up study, Chapter 6 shows a refined simulation of the same furnace but using the top-hat instead of beta-PDF assumption for subgrid turbulence chemistry interaction. Further analyses of the numerical results are also presented. Chapter 7 aims at investigating volatile combustion and pyrolysis in more detail by studying a smaller coal jet flame which is dominated by these effects. This chapter includes a detailed investigation of the influence of devolatilization models differing in the detailedness of their description, ranging from a simple single-rate model to the complex Chemical Percolation for Devolatilization (CPD) model directly coupled to the LES. To further investigate the ignition behavior of coal streams and to provide a basis for further combustion modeling, Chapter 8 shows a DNS study of volatile ig-

nition and burning in a developing coal particle-laden mixing layer. The hybrid LES study combining assumed and transported density function methods tested on pure gas flames is presented in Chapter 9. Finally, the last chapter provides a compilation of the achievements and findings, as well as directions for further studies.

Chapter 2

Theory

2.1 Reacting Fluid Flow

2.1.1 Governing Equations

In this section, the governing equations of reacting fluid flow are introduced. Classical assumptions to describe multicomponent reacting gas mixtures in combustion applications are employed. The fluid is assumed to be a *continuum* (*continuum hypothesis*) on all scales, such that it can be described by means of partial differential equations. The fluid is assumed to be *ideal*, i.e., the ideal gas law can be used to relate (partial) pressure, (partial) density and temperature to each other, and to be in *thermodynamic equilibrium*. The set of equations fully describing reacting gas mixtures comprises equations for conservation of mass, momentum, energy and species, which are summarized in the following and can be found in classical text books (for example in the book by Williams [258] or Poinsot & Veynante [176], on which this chapter is based; there is no implied summation over α).

Conservation of mass:
$$\frac{\partial \rho}{\partial t} + \frac{\partial \rho u_j}{\partial x_j} = 0 \tag{2.1}$$

Conservation of momentum:
$$\frac{\partial \rho u_i}{\partial t} + \frac{\partial \rho u_i u_j}{\partial x_j} = -\frac{\partial p}{\partial x_i} + \frac{\partial \tau_{ij}}{\partial x_j} + \rho \sum_{\alpha=1}^{N_s} Y_\alpha f_{\alpha,i} \tag{2.2}$$

Conservation of species:
$$\frac{\partial \rho Y_\alpha}{\partial t} + \frac{\partial \rho Y_\alpha u_j}{\partial x_j} = -\frac{\partial \rho V_{\alpha,j} Y_\alpha}{\partial x_j} + \dot{\omega}_\alpha \tag{2.3}$$

Conservation of enthalpy:
$$\frac{\partial \rho h}{\partial t} + \frac{\partial \rho h u_j}{\partial x_j} = \frac{Dp}{Dt} - \frac{\partial q_i}{\partial x_i} + \tau_{ij} \frac{\partial u_i}{\partial x_j} + \dot{Q} + \rho \sum_{\alpha=1}^{N_s} Y_\alpha f_{\alpha,j} V_{\alpha,j} \tag{2.4}$$

The above equations depend on the fluid density ρ, the velocity components u_j, the pressure p, the stress tensor τ_{ij}, the mass fractions Y_α, body force components $f_{\alpha,i}$ acting on species α, diffusion velocity components $V_{\alpha,j}$ of species α, chemical source term $\dot{\omega}_\alpha$ of species α, the enthalpy h, the enthalpy flux q_i and the additional enthalpy source term $\dot{Q}$.

The conservation of mass expresses that mass is neither destroyed nor created, which holds true in the absence of nuclear reactions. The conservation of momentum, Eq. 2.2, which is based on *Newton's second law*, includes the viscous stress τ_{ij}, which is expressed by Eq. 2.5, neglecting bulk diffusion and assuming a *Newtonian fluid*. Equations 2.2 with τ_{ij} substituted by the expression for the *Newtonian fluid* are commonly referred to as the *Navier-Stokes equations* [7].

$$\tau_{ij} = \mu \left(\frac{\partial u_j}{\partial x_i} + \frac{\partial u_i}{\partial x_j} - \frac{2}{3} \frac{\partial u_k}{\partial x_k} \delta_{ij} \right) \tag{2.5}$$

The conservation of enthalpy includes a term for enthalpy flux, q_i, which is given by Eq. 2.6 using *Fourier's law* (conductive heat flux density equals $\lambda \partial T / \partial x_i$), including species enthalpy diffusion and radiation, but excluding the *Dufour effect* (heat flux due to chemical potential gradient).

$$q_i = -\lambda \frac{\partial T}{\partial x_i} + \rho \sum_{\alpha=1}^{N_s} h_\alpha Y_\alpha V_{\alpha,i} + q_{R,i} \tag{2.6}$$

In this work, the viscous heating term ($\tau_{ij} \partial u_i / \partial x_j$) in the enthalpy transport equation is neglected, due to the turbulent reacting flows studied here falling into the *low-Mach regime*. Equations 2.2, 2.3, 2.4 and 2.6 include the species diffusion velocities $V_{\alpha,i}$. A complete evaluation of $V_{\alpha,i}$, which includes *Stefan–Maxwell diffusion*, diffusion due to pressure gradient, diffusion due to body force and the *Soret effect* requires the solution of a linear system of size N_s^2 [176, 258], with N_s being the number of species involved. Employing the *Hirschfelder-Curtiss approximation* [75] greatly decreases the complexity of the description of the diffusion velocity. Using this assumption, $V_{\alpha,i}$ can be computed by Eq. 2.7 and Eq. 2.8.

$$V_{\alpha,i} = -\frac{D_\alpha}{X_\alpha} \frac{\partial X_\alpha}{\partial x_i} \tag{2.7}$$

$$D_\alpha = \frac{1 - Y_\alpha}{\sum_{\beta \neq \alpha} X_\beta D_{\beta,\alpha}} \tag{2.8}$$

Equation 2.8 expresses the diffusion coefficient of species α into the rest of the mixture. Since Eq. 2.7 does not yield the exact diffusion velocities, mass conservation is not satisfied, i.e., the diffusive fluxes of all species do not sum up to zero. A correction velocity that can be applied to enforce mass conservation can be derived from the requirement of species diffusive fluxes to sum up to zero, yielding Eq. 2.9 [176], and is added to Eq. 2.7, resulting in Eq. 2.10.

$$V_i^c = \sum_{\alpha=1}^{N_s} D_\alpha \frac{W_\alpha}{W} \frac{\partial X_\alpha}{\partial x_i} \tag{2.9}$$

$$V_{\alpha,i} = -\frac{D_\alpha}{X_\alpha}\frac{\partial X_\alpha}{\partial x_i} + V_i^c \tag{2.10}$$

A further simplification can be made to the calculation of diffusion velocities by assuming equal diffusivities. This corresponds to *Fick's law* and can, for example, be derived from the *Hirschfelder-Curtiss approximation*. This approach is often used in the context of the *unity Lewis number assumption* ($\mathrm{Le} = \kappa/(\rho c_p) = 1$, with the heat conductivity κ and the isobaric heat capacity c_p). In this case, the diffusivity is equal for species and enthalpy and is calculated by Eq. 2.11.

$$D = \frac{\kappa}{\rho c_p} \tag{2.11}$$

This diffusivity is then used to calculate diffusion velocities, Eq. 2.12.

$$V_{\alpha,i} = -\frac{D}{Y_\alpha}\frac{\partial Y_\alpha}{\partial x_i} \tag{2.12}$$

The ideal gas law is used to relate thermodynamic variables to each other. This is expressed by Eq. 2.13.

$$\frac{p}{\rho} = T\frac{R}{W} \tag{2.13}$$

The mean molecular weight W is calculated by Eq. 2.14.

$$W = \left(\sum_{\alpha=1}^{N_s} \frac{Y_\alpha}{W_\alpha}\right)^{-1} \tag{2.14}$$

2.1.2 Chemical kinetics

The source terms appearing in the transport equations of species are described by chemical kinetics. In general, the source term of a single species is a function of the concentrations of any of the other species and the thermodynamic state of the system, e.g., pressure and temperature. All source terms can be described by a system of ordinary differential equations. Starting from a system with N_s species and N_r reactions, the chemical system can be described as:

$$\sum_{\alpha=1}^{N_s} \nu'_{\alpha\gamma}\chi_\alpha \rightleftharpoons \sum_{\alpha=1}^{N_s} \nu''_{\alpha\gamma}\chi_\alpha, \quad \gamma = 1...N_r. \tag{2.15}$$
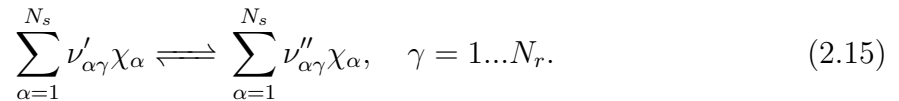
In Eq. 2.15, $\nu'_{\alpha\gamma}$ and $\nu''_{\alpha\gamma}$ are the forward and backward molar stoichiometric coefficients for species α within reaction γ, respectively, and χ_α denotes the chemical symbol of species α. Equation 2.15 is simply a mathematical representation of the reactions involved in a chemical mechanism, e.g., reactions such as $O + CH \rightleftharpoons H + CO$, where four different species are involved and where all backward and forward coefficients are either 0 or 1. The rate at which species are produced/destroyed can be described by summation over all reactions:

$$\dot{\omega}_\alpha^m = \sum_{\gamma=1}^{N_r} (\nu''_{\alpha\gamma} - \nu'_{\alpha\gamma})q_\gamma, \tag{2.16}$$

where q_γ describes the progress of reaction γ and $\dot{\omega}_\alpha^m$ the molar net production rate of species α. The progress of reaction γ is described by (with brackets indicating molar concentrations):

$$q_\gamma = k_{f,\gamma} \prod_{\alpha=1}^{N_s} [\chi_\alpha]^{\nu'_{\alpha\gamma}} - k_{r,\gamma} \prod_{\alpha=1}^{N_s} [\chi_\alpha]^{\nu''_{\alpha\gamma}}. \tag{2.17}$$

In Eq. 2.17, $k_{f,\gamma}$ and $k_{r,\gamma}$ are the forward and reverse rate constants of reaction γ, respectively. The forward rate constant is computed as an Arrhenius reaction:

$$k_{f,\gamma} = A_{f,\gamma} T^{\beta_\gamma} \exp\left(-E_\gamma/(RT)\right). \tag{2.18}$$

Equation 2.18 depends on the pre-exponential factor $A_{f,\gamma}$, the activation energy E_γ and the temperature exponent β_γ. The reverse rate constant is computed from the equilibrium constant $K_\gamma = k_{f,\gamma}/k_{r,\gamma}$, which can be computed from thermodynamic data. The above relations allow the computation of each of the molar species production rates $\dot{\omega}_\alpha^m$. The production rates required by the species transport equation can then simply be computed as:

$$\dot{\omega}_\alpha = \dot{\omega}_\alpha^m W_\alpha. \tag{2.19}$$

2.2   Turbulence

The equations presented in Section 2.1 inherently describe reacting flows under laminar as well as turbulent conditions. In engineering practice, most of the flows are turbulent [181]. As pointed out in the text book by Tennekes & Lumley [226], it is difficult to give a precise definition of turbulence. However, some characteristics can be associated with turbulent flows, which include: *irregularity* and apparent *randomness* or *disorder* (i.e., the underlying equations are deterministic, but the non-linearity leads to an apparent chaotic behavior), *unsteadiness* and *increased mixing*. These phenomena stem from the non-linear term in the *Navier-Stokes* equations and the occurrence of turbulence is linked to the ratio of inertial (non-linear) forces to stabilizing viscous forces, a relationship that has been discovered by Reynolds [195] and is expressed by the Reynolds number, Eq. 2.20.

$$\text{Re} = \frac{\rho u L}{\mu} \tag{2.20}$$

Equation 2.20 uses a characteristic length of the problem, L, e.g., the diameter of a pipe or the length of a plate in a flow.

A relationship between the largest scales of turbulent motion and the smallest scales can be established by the concept of the *energy cascade*, first introduced by Richardson in 1922 [197]. The concept of the *energy cascade* is based on the observation that a range of scales exists in a turbulent flow, i.e., there are eddies of different size with smaller eddies embedded in larger eddies. The largest scales (eddies) break up and feed kinetic energy to smaller scales, which in turn transfer energy to even smaller scales. This process continues to the point where the effect of viscosity is too strong for the eddies to survive and they are dissipated. These smallest eddies or scales, are the scales at which kinetic energy is dissipated by the action of viscosity. If viscosity only affects the smallest scales,

and large scales feed their energy down to the smallest scales, the rate of dissipation ϵ at which the smallest scales dissipate energy, must equal the rate at which the largest scales are supplied with kinetic energy. This concept, as established by Kolmogorov, leads to the derivation of the description of the smallest scales of a turbulent flow. Now known as the Kolmogorov microscales [109, 110], these are:

$$\eta \equiv \left(\frac{\nu^3}{\epsilon}\right)^{1/4}, \qquad \tau \equiv \left(\frac{\nu}{\epsilon}\right)^{1/2}, \qquad \upsilon \equiv (\nu\epsilon)^{1/4}. \tag{2.21}$$

The concept of the *energy cascade* was further refined by Kolmogorov [109, 110]. Kolmogorov's theories are based on hypotheses of local isotropy and similarity of small scales. *Kolmogorov's hypothesis of local isotropy* states that only large eddies are anisotropic and affected by the specific conditions of the flow, whereas small scales are isotropic, i.e., they have lost all information of the large scale features of the flow and can hence be characterized as being (statistically) universal. This hypothesis is linked to the mechanism of *return to isotropy*. Large eddies are most anisotropic, i.e., affected by the flow geometry, because their strain rate is of the order of the strain rate of the mean flow [226]. Small eddies, however, show strain rates that are much larger than that of the mean flow. Even though the small eddies are not constantly isotropic (because alignment with the strain imposed by larger eddies is necessary to transfer energy), they are isotropic in the mean. This is due to smaller and smaller scales being subjected to increasingly isotropic strain rate fields, such that any persisting directional information is lost at the smallest scales. Strain rates of the smallest eddies being large compared to the strain rate of the mean flow also results in eddy time scales being low and the eddies being able to adapt to the local flow conditions rapidly, i.e., being in equilibrium with the local conditions imposed by the mean flow. However, the concept of *local isotropy* is only valid if the Reynolds number of the flow is sufficiently large. Otherwise, if the strain rate of the smallest eddies is comparable to the mean strain rate of the flow, the smallest eddies cannot be statistically isotropic.

Based on the influence of strain and viscous dissipation on different scales of turbulent motion, and on the idea of an *energy cascade*, Kolmogorov derived a theoretical shape of the energy spectrum of the different scales present in a turbulent flow. A sketch of such a spectrum is shown in Fig. 2.1.

The scaling of energy of the large scales is dictated by strain and dissipation, i.e., the rates at which the large scales receive energy from the mean strain and at which they feed it to the smaller scales. Viscous effects are not expected to be important. On the other hand, the scaling of energy in the *equilibrium range* is dictated by the energy that the smallest scales receive from larger scales (i.e., equal to the dissipation) and by viscosity. These scaling laws are also referred to as *inertial* and *viscous scaling*. The scaling behavior of the inertial subrange is obtained by matching both scaling laws in the limit of infinite Reynolds numbers [226]. This results in the famous $-5/3$ scaling, as indicated in Fig. 2.1. Because the dissipation is dictated by the energy transferred by the large scales, the dissipation can be related to the length l_0 and velocity scale u_0 of the largest eddies by the proportionality:

$$\epsilon \sim \frac{u_0^3}{l_0}. \tag{2.22}$$
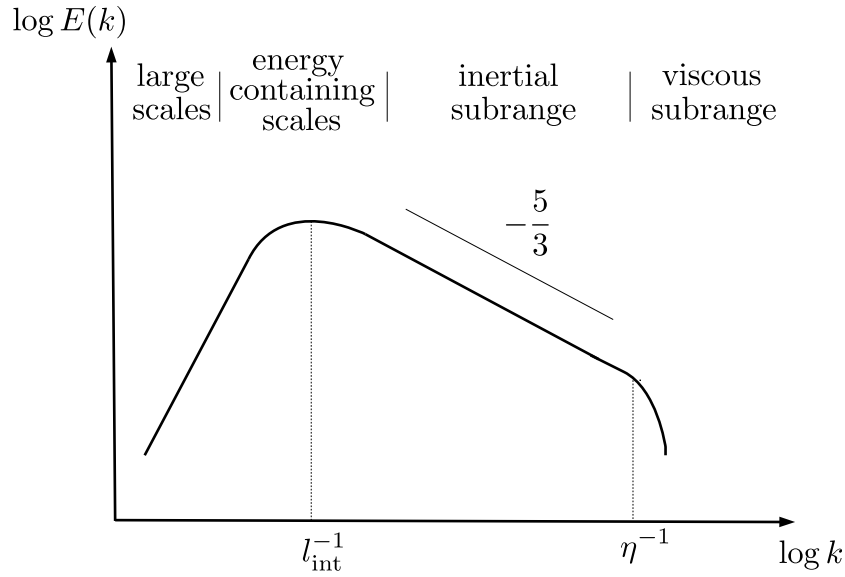
Figure 2.1: Sketch of the turbulent kinetic energy spectrum (as presented by Peters [166]).

Using the definition of the Kolmogorv length scale, the proportionality can be equated to:

$$\eta/l_0 \sim Re_0^{-3/4}. \tag{2.23}$$

It should be noted that Re_0 (the Reynolds number based on the largest turbulent scales) can be expected to be close to Re (based on characteristic scales of the flow). The proportionality in Eq. 2.23 illustrates how the scale separation increases with Reynolds number.

2.3   Large Eddy Simulation

The concept of large eddy simulation (LES) is to solve only the larger scales of turbulent motion while modeling the small scales, assuming that the large scales contain most of the energy and that the small scales show universal character. The separation of the turbulent flow into small and large scales is accomplished by spatially filtering the Navier-Stokes equations. The filtering operation applied to an arbitrary quantity ϕ can be expressed as:

$$\bar{\phi}(\boldsymbol{x}) = \int_{\mathcal{D}} \phi(\boldsymbol{x'})G(\boldsymbol{x},\boldsymbol{x'};\Delta)d\boldsymbol{x'}. \tag{2.24}$$

The integration is performed over the domain $\mathcal{D}$, and G and Δ are filter function and its filter width, respectively. The filter width corresponds to the smallest scales of $\bar{\phi}(\boldsymbol{x})$. Different filter functions G exist, and the choice largely depends on the type of code and problem studied. Typical filter functions are the *sharp Fourier cutoff filter*, the *Gaussian filter* or the *top-hat filter*. The *sharp Fourier cutoff filter* is typically used in conjunction with a spectral numerical solution method, and the *Gaussian filter* may be applied to explicitly filter the governing equations [181]. However, most LES codes (including the

code in this work) imply the *top-hat filter* as a model for the numerical discretization employing finite volume cells or finite difference grids. In this case, the filtering operation is not performed explicitly. The top-hat filter can be expressed as (in one dimension for simplicity):

$$G(x' - x) = \begin{cases} 1/\Delta & \text{if } |x' - x| \leq \Delta/2 \\ 0 & \text{otherwise.} \end{cases} \tag{2.25}$$

The filter corresponds to a spatial average over the filter volume, also referred to as *Reynolds filtering*. A useful definition is the *Favre filter*, because it reduces the number of unclosed terms in the filtered (variable density) governing equations. The *Favre filter* corresponds to a density-weighted filtering:

$$\tilde{\phi} = \overline{\rho\phi}/\bar{\rho}. \tag{2.26}$$

The decomposition accomplished by filtering can be expressed as (similar to the *Reynolds decomposition* [181]):

$$\phi = \bar{\phi} + \phi', \tag{2.27}$$

for *Reynolds averaging* and

$$\phi = \tilde{\phi} + \phi'', \tag{2.28}$$

for *Favre averaging*.

The filtering operation is applied to the governing equations and filtered terms including the density, ρ, are replaced by *Favre averages*, e.g., $\overline{\rho u_i} = \bar{\rho}\tilde{u}_i$. Additionally, commutativity of derivatives and filtering is assumed (only strictly valid for uniform filters [171]). In the case of the continuity equation, this yields:

$$\frac{\partial \bar{\rho}}{\partial t} + \frac{\partial \overline{\rho u_j}}{\partial x_j} = 0 \qquad \Leftrightarrow \qquad \frac{\partial \bar{\rho}}{\partial t} + \frac{\partial \bar{\rho}\tilde{u}_j}{\partial x_j} = 0. \tag{2.29}$$

In the case of the momentum equations, the following equation is obtained:

$$\underbrace{\frac{\partial \overline{\rho u_i}}{\partial t}}_{\text{I}} + \underbrace{\frac{\partial \overline{\rho u_i u_j}}{\partial x_j}}_{\text{II}} = \underbrace{-\frac{\partial \bar{p}}{\partial x_i}}_{\text{III}} + \frac{\partial}{\partial x_j} \underbrace{\left[\overline{\mu \left(\frac{\partial u_j}{\partial x_i} + \frac{\partial u_i}{\partial x_j} - \frac{2}{3}\frac{\partial u_k}{\partial x_k}\delta_{ij} \right)} \right]}_{\text{IV}} + \underbrace{\overline{\rho \sum_{\alpha=1}^{N_s} Y_\alpha f_{\alpha,i}}}_{\text{V}}. \tag{2.30}$$

Using Favre filtering, the first term (I) of Eq. 2.30 becomes $\partial(\bar{\rho}\tilde{u}_i)/\partial t$. The second term (II) becomes $\partial(\bar{\rho}\widetilde{u_i u_j})/\partial x_j$, which includes the term $\widetilde{u_i u_j}$ that cannot be obtained from the filtered fields and hence requires modeling. This is usually expressed in the form of a *subgrid stress (SGS) tensor* τ_{ij}^{SGS} (in analogy to the *Reynolds stress tensor*):

$$\frac{\bar{\rho}\widetilde{u_i u_j}}{\partial x_j} \qquad \Leftrightarrow \qquad \frac{\bar{\rho}\tilde{u}_i\tilde{u}_j + \tau_{ij}^{\text{SGS}}}{\partial x_j}. \tag{2.31}$$

Term IV is modeled based on the following approximation (e.g., $\overline{\mu \partial u_j/\partial x_i} \approx \bar{\mu}\partial\tilde{u}_j/\partial x_i$):

$$\overline{\mu \left(\frac{\partial u_j}{\partial x_i} + \frac{\partial u_i}{\partial x_j} - \frac{2}{3}\frac{\partial u_k}{\partial x_k}\delta_{ij} \right)} \approx \bar{\mu} \left(\frac{\partial \tilde{u}_j}{\partial x_i} + \frac{\partial \tilde{u}_i}{\partial x_j} - \frac{2}{3}\frac{\partial \tilde{u}_k}{\partial x_k}\delta_{ij} \right). \tag{2.32}$$

Term V is not of relevance for the present work, as no volume forces are applied to the filtered governing equations. Hence, it is not further detailed here. Putting all terms together and rearranging yields the final filtered form of the momentum equation:

$$\frac{\partial \bar{\rho}\tilde{u}_i}{\partial t} + \frac{\partial \bar{\rho}\tilde{u}_i\tilde{u}_j}{\partial x_j} = -\frac{\partial \bar{p}}{\partial x_i} + \frac{\partial}{\partial x_j}\left[\bar{\mu}\left(\frac{\partial \tilde{u}_j}{\partial x_i} + \frac{\partial \tilde{u}_i}{\partial x_j} - \frac{2}{3}\frac{\partial \tilde{u}_k}{\partial x_k}\delta_{ij}\right) - \tau_{ij}^{\mathrm{SGS}}\right]. \tag{2.33}$$

The modeling of τ_{ij}^{SGS} is one of the central parts of LES modeling. Often, a *Boussinesq approximation* or *eddy diffusivity approach* is employed [175], where the effect of unresolved eddies is treated as an additional viscosity, which implies that energy is only transferred from the resolved to unresolved scales and not the opposite way. In analogy to the stress tensor for the Newtonian fluid, the deviatoric part of the subgrid stress tensor is modeled as:

$$\tau_{ij}^{\mathrm{SGS}} - \frac{1}{3}\tau_{kk}^{\mathrm{SGS}} = -\bar{\rho}\nu_t\left(\frac{\partial \tilde{u}_i}{\partial x_j} + \frac{\partial \tilde{u}_j}{\partial x_i} - \frac{2}{3}\delta_{ij}\frac{\partial \tilde{u}_k}{\partial x_k}\right). \tag{2.34}$$

Usually, the isotropic part of the subgrid stress tensor does not appear explicitly in the equations, but is simply added to the filtered pressure. This is adequate in low-Mach problems, where the pressure Poisson equation (described in Chapter 4) solves for the pressure field required to satisfy continuity. In the case of above described modeling, the pressure equation simply computes a pressure parameter that incorporates the isotropic part of the subgrid stress, i.e., pressure and twice the subgrid kinetic energy (it needs to be explicitly modeled and included in a fully compressible description for high-speed flows [176]):

$$\bar{p}_{\mathrm{mod}} = \bar{p} + \frac{1}{3}\tau_{kk}^{\mathrm{SGS}} = \bar{p} + \frac{1}{3}\bar{\rho}(\widetilde{u_k^2} - \tilde{u}_k^2). \tag{2.35}$$

The calculation of the *eddy viscosity*, appearing in 2.34 is possible *via* different SGS models. The first model reported, and still widely used, is the Smagorinsky model [213], which shares similarities with Prandtl's mixing length hypothesis [181]. The Smagorinsky model relates the eddy viscosity to the resolved characteristic rate of strain. From a dimensional analysis viewpoint the turbulent viscosity can be thought of as a length scale l^* multiplied by a velocity scale U^*, which in turn is the length scale divided by a time scale t^*. The length scale of the Smagorinsky model is approximated to be proportional to the filter size Δ and the proportionality factor is expressed by a model constant C_s. The time scale used is the inverse filtered characteristic rate of strain, where the filtered characteristic rate of strain is $\mathcal{S} = \sqrt{2\tilde{S}_{ij}\tilde{S}_{ij}}$, with $\tilde{S}_{ij} = 1/2(\partial \tilde{u}_i/x_j + \partial \tilde{u}_j/x_i)$. The expression for the turbulent viscosity is then:

$$\nu_t = l^*U^* = l^{*2}t^{*-1} = (C_s\Delta)^2\mathcal{S}. \tag{2.36}$$

Due to its robustness and simplicity, and consistent modeling with terms concerning the Lagrangian particle phase described later, this model has been selected for the work in Chapters 5, 6 and 7. However, other, more recent models for the eddy viscosity exist. These are, for example, the WALE model [144] and the Sigma model [145]. These models partially overcome some of the weaknesses of the Smagorinsky model, such as the overprediction of eddy viscosity in situations with pure shear or near solid boundaries.

To this end, the Sigma model by Nicoud et al. [145] bases the time scale for ν_t on the singular values of the resolved velocity gradient tensor ($\tilde{g}_{ij} = \partial \tilde{u}_i / \partial x_j$) and is constructed in such a way that the inverse of the time scale can go to zero, e.g., in pure shear flows. The singular values of the resolved velocity gradient tensor can be computed from first calculating the invariants of the matrix $G_{ij} = \tilde{g}_{ki}\tilde{g}_{kj}$ (tr denoting the trace and det the determinant):

$$
\begin{aligned}
\mathcal{I}_1 &= tr(G_{ij}), \\
\mathcal{I}_2 &= \frac{1}{2}(tr(G_{ij})^2 - tr(G_{ik}G_{kj})), \\
\mathcal{I}_3 &= det(G_{ij}).
\end{aligned}
\tag{2.37}
$$

From the invariants, angles can be computed:

$$
\begin{aligned}
\alpha_1 &= \frac{\mathcal{I}_1^2}{9} - \frac{\mathcal{I}_2}{3}, \\
\alpha_2 &= \frac{\mathcal{I}_1^3}{27} - \frac{\mathcal{I}_1\mathcal{I}_2}{6} + \frac{\mathcal{I}_3}{2}, \\
\alpha_3 &= \frac{1}{3}\arccos\left(\alpha_2\alpha_1^{-3/2}\right).
\end{aligned}
\tag{2.38}
$$

This then allows for the computation of the singular values of $\tilde{g}_{ij}$:

$$
\begin{aligned}
\sigma_1 &= \left(\frac{\mathcal{I}_1}{3} + 2\sqrt{\alpha_1}\cos\alpha_3\right)^{1/2}, \\
\sigma_2 &= \left(\frac{\mathcal{I}_1}{3} - 2\sqrt{\alpha_1}\cos(\pi/3 + \alpha_3)\right)^{1/2}, \\
\sigma_3 &= \left(\frac{\mathcal{I}_1}{3} - 2\sqrt{\alpha_1}\cos(\pi/3 - \alpha_3)\right)^{1/2}.
\end{aligned}
\tag{2.39}
$$

The operator (or equivalently the inverse time scale) is constructed from the singular values such that the desired behavior is obtained (with $\sigma_1 \geq \sigma_2 \geq \sigma_3 \geq 0$):

$$
\nu_t = (C_\sigma \Delta)^2 \frac{\sigma_3(\sigma_1 - \sigma_2)(\sigma_2 - \sigma_3)}{\sigma_1^2}.
\tag{2.40}
$$

The Sigma model has been implemented in the LES code and tested on different non-reacting flow configurations by the author of this thesis earlier on [203] and used in parts of the work presented here.

A different way to overcome the weaknesses of the Smagorinsky model is the *dynamic procedure* or *Germano* model, which has been developed to obtain the mixing model constant C_s dynamically. Originally, this model was proposed by Germano et al. [56] and subsequently improved by Lilly [118] and Meneveau et al. [131] and extended to variable density flows by Moin et al. [136]. The model is based on a so-called test filtering operation on top of the regular filtering, here denoted with a hat symbol. The subfilter stresses with respect to the test-filtered equations are (i.e., the stresses from the scales removed by explicit filtering):

$$
T_{ij} = \widehat{\rho u_i u_j} - \frac{\widehat{\rho u_i}\,\widehat{\rho u_j}}{\widehat{\rho}}.
\tag{2.41}
$$

A central quantity for the dynamic model are the Leonard stresses:

$$L_{ij} = \frac{\overline{\widehat{\rho u_i}\,\widehat{\rho u_j}}}{\overline{\rho}} - \frac{\widehat{\overline{\rho u_i}}\,\widehat{\overline{\rho u_j}}}{\widehat{\overline{\rho}}} = \frac{\overline{\rho \tilde{u}_i}\,\widehat{\overline{\rho \tilde{u}_j}}}{\overline{\rho}} - \frac{\widehat{\overline{\rho}\tilde{u}_i}\,\widehat{\overline{\rho}\tilde{u}_j}}{\widehat{\overline{\rho}}}. \tag{2.42}$$

Correspondingly to the Favre filtering on the grid filter level, a Favre filter on the test filter level is introduced, such that: $\hat{\bar{\rho}}\check{\tilde{\phi}} = \widehat{\bar{\rho}\tilde{\phi}}$. Equation 2.42 can be computed from the resolved fields available in the LES. As demonstrated by Germano, Eq. 2.42 can also be expressed by taking Eq. 2.41 and subtracting the test-filtered SGS stresses, which is commonly known as the *Germano identity*:

$$L_{ij} = T_{ij} - \widehat{\tau}_{ij}^{\mathrm{SGS}}. \tag{2.43}$$

The deviatoric parts of both tensors on the RHS of Eq. 2.43 can be expressed by the same subfilter model, e.g., the Smagorinsky model. The only difference is that the model coefficient appears to the power of 1 instead of 2 and is named C for differentiation:

$$\tau_{ij}^{\mathrm{SGS}} - \frac{1}{3}\delta_{ij}\tau_{kk}^{\mathrm{SGS}} = -\bar{\rho}C\Delta^2 \mathcal{S}\left(\frac{\partial \tilde{u}_i}{\partial x_j} + \frac{\partial \tilde{u}_j}{\partial x_i} - \frac{2}{3}\delta_{ij}\frac{\partial \tilde{u}_k}{\partial x_k}\right) = -2C\beta_{ij}, \tag{2.44}$$

$$T_{ij} - \frac{1}{3}\delta_{ij}T_{kk} = -\widehat{\bar{\rho}}C\widehat{\Delta}^2 \check{\mathcal{S}}\left(\frac{\partial \check{\tilde{u}}_i}{\partial x_j} + \frac{\partial \check{\tilde{u}}_j}{\partial x_i} - \frac{2}{3}\delta_{ij}\frac{\partial \check{\tilde{u}}_k}{\partial x_k}\right) = -2C\alpha_{ij}. \tag{2.45}$$

In Eq. 2.44, $\check{\mathcal{S}}$ is the characteristic strain obtained from the (Favre-) test-filtered velocity field $\check{\tilde{u}}$. With the deviatoric part of the filtered strain rate tensor ($\tilde{S}_{ij}^d = 1/2(\partial \tilde{u}_i/\partial x_j + \partial \tilde{u}_j/\partial x_i) - 1/3\delta_{ij}\partial \tilde{u}_k/\partial x_k$), test filtering the stress tensor τ_{ij}^{SGS} yields:

$$\widehat{\tau}_{ij}^{\mathrm{SGS}} - \frac{1}{3}\delta_{ij}\widehat{\tau}_{kk}^{\mathrm{SGS}} = -2C\Delta^2 \widehat{\bar{\rho}\mathcal{S}\tilde{S}_{ij}^d}. \tag{2.46}$$

From the deviatoric part of the Germano identity the following equation is obtained:

$$L_{ij} - \frac{1}{3}\delta_{ij}L_{kk} = -2\widehat{\bar{\rho}}C\widehat{\Delta}^2 \check{\mathcal{S}}\check{\tilde{S}}_{ij}^d + 2C\Delta^2 \widehat{\bar{\rho}\mathcal{S}\tilde{S}_{ij}^d}. \tag{2.47}$$

Equation 2.47 can be solved for C. However, this tensorial equation produces six independent equations to obtain C (in variable density Newtonian flows, where the stress tensor is symmetric but its trace does not add up to zero). Germano et al. [56] and Moin et al. [136] proposed to contract this equation with $\tilde{S}_{ij}$ or other tensors (e.g., Eq. 2.42) to obtain a scalar equation. Lilly [118] proposed to use a least-squares approach to minimize the overall error in Eq. 2.47, which shows that M_{ij} is the optimal tensor for contraction (with $M_{ij} = -2\widehat{\bar{\rho}}C\widehat{\Delta}^2 \check{\mathcal{S}}\check{\tilde{S}}_{ij}^d + 2C\Delta^2 \widehat{\bar{\rho}\mathcal{S}\tilde{S}_{ij}^d}$) and produces:

$$C = \frac{M_{ij}(L_{ij} - \frac{1}{3}\delta_{ij}L_{kk})}{M_{kl}M_{kl}}. \tag{2.48}$$

Common to the approaches by Lilly, Germano et al. and Moin et al. is the assumption that C does not change within the test-filtered volume or is unaffected by the test filtering operation (hence it does not appear under the hat in Eq. 2.46). Additionally, the

denominator in both approaches can become zero and can generally show highly fluctuating behavior leading to unstable simulations. Therefore, numerator and denominator of Eq. 2.48 are usually volume averaged, e.g., over homogeneous directions [56]. A different approach has been proposed by Piomelli and Liu [172], where the computation of C involves the value at the last time step and averaging is not necessary any more. This approach is referred to as the *localized dynamic model*. It is based on the assumption that the model constant appearing in the expression for the test-filtered SGS stresses is known and obtained from an extrapolation of C in time (from past times). This allows for a local least-squares error minimalization without involving a denominator that can go to zero, except for situations where the numerator also vanishes. Following Piomelli and Liu, rearrangement of Eq. 2.47 first yields (without taking C out of the test filtering operation):

$$-2C\alpha_{ij} = L_{ij} - \frac{1}{3}\delta_{ij}L_{kk} - 2\widehat{C^*\beta_{ij}}, \qquad (2.49)$$

where C^* is the estimate of C and assumed to be known for the purpose of finding C. The least-squares method yields α_{ij} as the optimal tensor for contraction, such that C can be evaluated as:

$$C = -\frac{1}{2}\frac{(L_{ij} - \frac{1}{3}\delta_{ij}L_{kk} - 2\widehat{C^*\beta_{ij}})\alpha_{ij}}{\alpha_{lm}\alpha_{lm}}. \qquad (2.50)$$

Although the dynamic model greatly improves the predictability of LES due to eliminating the model constant for the subgrid stresses, some important characteristics have to be kept in mind. Because the same model form is used for τ_{ij} and T_{ij}, the model requires grid filter as well as test filter to be in the inertial subrange such that the same assumptions about the filtered scales can be made. Hence, in theory, the grid needs to be fine enough such that a 'proper' LES would be possible at the test filter level (although it has been reported that good results could be obtained if this is not the case [181]). If the dynamic procedure relies on the Smagorinsky model, it should be kept in mind that some of the deficiencies of the Smagorinsky model have implications on the dynamic procedure. In particular, the Smagorinsky model is unable to yield correct values of subgrid stresses and energy transfer to the small scales at the same time, as demonstrated by only a weak correlation of SGS stresses to strain rate tensor observed in *a-priori* tests of turbulent flows. This could also explain the highly fluctuating nature of the dynamically obtained modeling constant [181].

Overall, the LES method promises to accurately predict unsteady turbulent flows. This especially holds for high Reynolds number flows with a broad inertial subrange, where the universality of the smallest eddies can be exploited well. Closely related to this is the advantage of the cost of LES being independent of the Reynolds number (with the exception of wall-bounded flows). An increase of the Reynolds number simply extends the spectrum towards larger wave-numbers, i.e., into the range that is expected to be modeled well by the SGS model. However, in reacting flows the situation is different. In reacting flows, rate controlling processes (i.e., molecular mixing and reaction) occur on small scales, which are unresolved by the typical LES grid, posing challenges to the modeling of the interaction of turbulence and chemistry, as detailed in the next chapter.

2.4   Direct Numerical Simulation

The numerical solution method to resolve all scales of turbulent flow is called direct numerical simulation (DNS). Since all scales are resolved, no dedicated turbulence modeling is required, and the equations outlined in Section 2.1 are solved directly. Hence, the only modeling effort required in DNS is that of chemistry, molecular transport, constitutive relationships and thermodynamic state relations and properties.

Different to the LES, whose computational effort does not scale with the Reynolds-number, the cost of a DNS is directly linked to the separation of scales, since they all need to be resolved. Assuming that the cell size needs to be close to η and taking the ratio of largest scale and smallest scale (Kolmogorov scale) in a turbulent flow from Eq. 2.23 to be close to the number of cells necessary in one dimension (i.e., employing a grid that can fit the largest scale), leads to the number of cells necessary in 3D to be:

$$N_{\text{DNS}} \approx (l_0/\eta)^3 \sim Re_0^{9/4}. \tag{2.51}$$

This illustrates how the simulation effort scales super-linearly with Reynolds-number.

2.5   Extension to Multiphase Flows

Some of the flows under investigation in this work are multiphase flows. The dispersed phase in such flows can principally be solved in both Eulerian and Lagrangian frameworks. In this work, the dispersed phase is solved in a Lagrangian framework, due to some advantages that the Lagrangian framework offers compared to Eulerian methods [224]: (a) it captures particle/droplet processes such as drag or devolatilization in a closed form and captures their dependence on size due to evolving the full size distribution (i.e., kinetic non-equilibrium between gas and particles of different size is accounted for), (b) it allows for non-equilibrium non-Maxwellian velocity distributions, (c) it shows low numerical diffusion. As a disadvantage, it should be noted that the Lagrangian method is computationally more expensive than standard Eulerian methods. However, given that particles in pulverized coal furnaces show broad size distributions including large particles that are expected to have significant slip velocities, the Lagrangian framework promises to be worth the additional cost. A good alternative that has not been explored in this work is the direct quadrature method of moments (DQMOM) framework developed by Fox [51] and applied by Pedel [156, 157] in the pulverized coal combustion context.

There are different ways to describe the equations for the Lagrangian particle evolution. On the one hand, from a mechanical point of view (i.e., Newton's second law), the motion of a particle can be described by balancing the forces acting on the particle with its acceleration. On the other hand, the evolution of the dispersed phase can be defined in terms of a 'droplet distribution function' (DDF), such as the well known spray equation by Williams [259]. This equation can then be solved by utilizing the stochastic point process representation. In this case, so-called *surrogate* particles are solved [224]. These *surrogate* particles are only equivalent to their physical counterparts in a statistical sense. An advantage of viewing the Lagrangian particle equations as a solution method of the DDF is that not every physical particle needs to be represented in the simulation, but

so-called 'parcels' can be used. This is especially important for the work in Chapters 5 and 6, since a total number of coal particles of the order of several billions would have to be solved for. Instead, physical particles are combined in parcels such that all particles within a parcel have the same properties. Clearly, the instantaneous realizations of a parcel cannot be expected to correspond to the correct physical realizations of the individual particles within the parcel. However, the expectation of the realizations of all parcels corresponds to the expectation of the realizations of all physical particles. Even if particles are not combined in parcels, such as in Chapter 7, but evolve in the LES framework, they should be viewed as *surrogate* particles, since the influence of subgrid quantities on the particles is modeled by means of a stochastic process. Only in the situation of the carrier-phase DNS in Chapter 8, computational particles can be viewed as corresponding to the physical particles (it should be noted that *surrogate* particles could be used in a CP-DNS as well, for example if the total number of particles is computationally intractable). Interestingly, the Lagrangian solution of the DDF shows similarities to the Lagrangian solution of the transport of the (gas) composition PDF outlined in Chapter 3 and 9. However, the modeling of the *surrogate* particles may seem more intuitive since the natural choice of solution method for particles is Lagrangian and the modeling for the *surrogate* particles is mostly equivalent to that of the physical particles.

One of the main assumptions regarding the multiphase flow in this work is that it is dilute. It should be noted that this assumption is not necessary to obtain Eq. 2.52 (neither in the physical nor DDF framework) [224]. However, it is invoked in this work and allows for (a) neglecting the displaced volume of the particles in the transport equations of the gas phase, (b) the use of correlations for drag and heat transfer to be based on isolated particles, (c) neglecting particle collisions and inter-particle effects. A typical rule of thumb for a volume fraction for which neighbor interactions can be neglected is 0.1 [224]. Additionally, a point particle assumption is invoked (not to be confused with point process), assuming that particles are smaller than the smallest turbulence, i.e., Kolmogorov scales. This simplifies the description of interphase exchange terms, since they can be computed assuming that the particles have an infinitesimal size.

The motion of particles, either for a physical particle or modeled surrogate particle or parcel, is described by the balance of particle acceleration and the forces acting on the particle, following Newton's second law, Eq. 2.52. In the case of the surrogate particles used in the LES, an additional term that represents the influence of the subgrid fluctuations on the particles needs to be considered (last term of Eq. 2.52).

$$d\mathbf{u}_p = \frac{\tilde{\mathbf{u}} - \mathbf{u}_p}{\tau_p}dt + \left(1 - \frac{\bar{\rho}}{\rho_p}\right)\mathbf{g}dt + \underbrace{\sqrt{C_0\frac{k_{SGS}}{\tau_t}}d\mathbf{W}}_{=0 \text{ for CP-DNS}} \qquad (2.52)$$

The three terms on the RHS of Eq. 2.52 stand for drag, gravity/buoyancy and forces due to SGS velocity fluctuations. Details on the evaluation of drag and the particle relaxation time are given in Chapter 5 and the last term is detailed in the following.

The last term in Eq. 2.52 describes the influence of the subgrid velocity fluctuations on the particle motion. Its treatment mainly follows the methodology proposed by Bini & Jones [12] for the simulation of spray LES, which is based on filtering William's

spray equation [259]. The model is based on the assumption that the instantaneous state of a particle can be described by a set of independent macroscopic variables, which can be expressed in state space using the fine-grained density function (similar to the gas phase description in terms of transported probability density function, Sec. 3.3.5).

$$f(\boldsymbol{\psi};t) = \sum_{n=1}^{N_p} \prod_{i=1}^{M} \delta[\psi_i - \phi_i^n] \tag{2.53}$$

The sample space ψ_i corresponds to quantity ϕ_i, and M is the number of macroscopic variables that describe the particle state. The subscript n denotes the n-th particle. The probability density function of $f(\boldsymbol{\psi};t)$ can be obtained by taking its expectation, i.e., taking the average in the limit of $N_p \to \infty$ over independent realizations. In the next step, this PDF is convoluted with the LES filter to obtain the filtered PDF:

$$\bar{P}(\boldsymbol{\psi},t) = \int_{\mathcal{D}} E[f(\boldsymbol{\psi};\boldsymbol{x'},t)]G(\boldsymbol{x},\boldsymbol{x'};\Delta)d\boldsymbol{x'} \tag{2.54}$$

By differentiating in time, the transport equation for the filtered PDF is obtained:

$$\frac{\partial}{\partial t}\bar{P} + \frac{\partial}{\partial \psi_i}[E(\dot{\psi}_i|\boldsymbol{\Psi} = \boldsymbol{\Phi})\bar{P}] = 0, \tag{2.55}$$

where the expectation describes the average of the change of ψ_i conditioned on $\boldsymbol{\Psi} = \boldsymbol{\Phi}$, i.e., conditioned on the particle state being found at $\boldsymbol{\Psi} = \boldsymbol{\Phi}$ within the filter volume. The LES spray equation can now be deduced by selecting appropriate macroscopic variables. Similarly, a 'LES coal equation' can be deduced. For coal, the macroscopic variables of choice are the velocity (vector), temperature, diameter, mass of volatile matter and mass of char, for which the transport equation can be written as:

$$\frac{\partial}{\partial t}\bar{P} + \nabla_{\boldsymbol{v}} \cdot (\boldsymbol{a}\bar{P}) + \frac{\partial}{\partial \mathcal{D}}\langle \dot{D}|\boldsymbol{\Psi} = \boldsymbol{\Phi}\rangle + \frac{\partial}{\partial \mathcal{T}}\langle \dot{T}|\boldsymbol{\Psi} = \boldsymbol{\Phi}\rangle +$$
$$+ \frac{\partial}{\partial M_{\mathrm{devol}}}\langle \dot{m}_{\mathrm{devol}}|\boldsymbol{\Psi} = \boldsymbol{\Phi}\rangle + \frac{\partial}{\partial M_{\mathrm{char}}}\langle \dot{m}_{\mathrm{char}}|\boldsymbol{\Psi} = \boldsymbol{\Phi}\rangle = 0, \tag{2.56}$$

where $\boldsymbol{a}$ is the conditional acceleration. The sample space of temperature, diameter, mass of volatile matter and mass of char is denoted by $\mathcal{T}$, $\mathcal{D}$, M_{devol} and M_{char}, respectively. The conditional averages appearing in Eq. 2.56 are modeled such that they are split into a deterministic and stochastic contribution, i.e., the rate of changes of the macroscopic particle quantities are split into a part that is determined by filtered flow field quantities and a part that represents the subgrid influence on the rate of change of the macroscopic quantities. Following Bini & Jones [12], the stochastic contribution is modeled by means of an isotropic Wiener diffusion process with the diffusion coefficient b depending on the SGS velocity fluctuations, a model constant (with a value of unity) and a time scale characterizing the interaction of particle and turbulence: $b = (C_0 k_{\mathrm{SGS}}/\tau_t)^{1/2}$. This diffusion coefficient is multiplied with the Wiener term $d\mathbf{W}$, which represents a three-dimensional Gaussian-distributed random variable with zero mean and a variance of dt (with the

dimension of $s^{1/2}$). Bini & Jones [13] developed an expression for τ_t that leads to an appropriate non-Gaussian PDF:

$$\tau_t = \frac{\tau_p^{2\alpha}}{(\Delta/\sqrt{k_{\mathrm{SGS}}})^{2\alpha-1}}, \text{ with } \alpha = 0.8. \tag{2.57}$$

In the direct numerical simulation, discussed in Chapter 8, all turbulent scales are resolved and hence the last term in Eq. 2.52 disappears. After evaluating the particle velocity from Eq. 2.52, the particle position can be obtained by:

$$d\mathbf{x_p} = \mathbf{u}_p dt. \tag{2.58}$$

While the equation for the particle acceleration includes a stochastic contribution to describe the influence of subgrid fluctuations, it has not been attempted to include such a term in the equations for particle temperature, mass, etc., as it is omitted in literature. However, subgrid temperature fluctuations, for example, might have an influence on the evolution of particles.

   Particle and gas phase are fully coupled (i.e., 'two-way coupling') such that particles feed back and affect the gas phase. This is facilitated through source terms in the balance/conservation equations of the gas phase (either in the large eddy or direct numerical simulation context). These source terms comprise the acceleration/deceleration of the gas phase due to interaction with the particle, the change in enthalpy due to heat transfer between gas phase and particle, and due to the enthalpy going along with mass emitted by the particle and the change in mass itself.

   Formally, the source terms from the particle phase can be written in terms of projection $\mathcal{P}$ of a Dirac delta function at the particle location onto the Eulerian location $\mathbf{x}$ by (see [21, 82]; shown here for momentum):

$$\mathcal{F}_{\mathrm{momentum}}(\mathbf{x}) = \sum_{n=1}^{N_p} \mathcal{P}(\delta(\mathbf{x}_{p,n} - \mathbf{x}))\mathbf{F}_{D,n}. \tag{2.59}$$

However, such definitions are ultimately tied to the numerical method since the numerical method usually provides the projection. Different approaches to eliminate grid dependence exist, e.g., based on explicit filtering [21, 82]. The types of projection used in this work are presented in Chapter 4 and more details on the different exchange terms are mainly given in Chapter 5.

   Similar to the particle coupling term for the momentum equation, source terms exist for the species mass fraction, mixture fraction and enthalpy equations. These equations follow the form of Eq. 2.59 and are also given in Chapter 4 and 5.

2.6   Coal Combustion

Parts of this thesis deal with the simulation of pulverized coal combustion. While the aspects important for the simulations are given in Chapters 5 through 8, the physical basics of pulverized coal combustion are summarized here briefly for completeness. Many

more details can, for example, be found in the text books by Smith and Smoot [217], Smoot and Pratt [216] and in the review article by Williams et al. [257], which most of the description given in this section is based on. In addition, more details can be found in the works by Rabaçal [190], Franchetti [52] and Cavallo Marincola [22], on which parts of this work are based on.

The composition of coal varies significantly from one type of coal to another, and coals are oftentimes classified, e.g., by their rank, which describes the carbon content of the coal [257]. Based on relating the ratios of C-to-H and C-to-O content in the coal, e.g., in the so-called van Krevelen diagram [235], coals can be classified into lignite, sub-bituminous, high volatile, bituminous, low volatile and anthracite coals. Combustion characteristics of coals of different types vary significantly, hence an understanding of the coal burned is indispensable for any successful modeling attempt. Experimental characterization techniques include proximate analyses, which provide the coal composition in terms of moisture, volatile matter, fixed carbon and ash, and ultimate analyses, which provide the coal composition in terms of atomic mass fractions. Aside from the composition, particle sizes or the particle size distribution are important quantities that need to be known for the simulation. In pulverized coal combustion, the coal is first milled into particles of sizes typically between 5 and $400\mu m$ [257], before it is transported to the burner by an air stream.

Coal combustion can be described as a sequence of processes coal naturally undergoes as being heated up, a good overview can for example be found in the work by Williams et al. [257]. Upon entering the furnace, the coal particle is subject to radiation and hot gases, both heating up the particle. At first, moisture is evaporating from the coal, also referred to as the drying step. Subsequently, volatile matter is released during the devolatilization process, which includes processes such as breaking of labile bonds in the coal structure. Devolatilization releases mostly light gases and tars with typical species being CH_4, C_2H_4, CO or C_6H_6. The volatile gases ignite and further increase the coal temperature. In addition, the heating rate of the coal particle influences the volatile composition and the devolatilization rate. The latter affects convective heat transfer. After the volatile matter has been emitted, the coal particle is mainly composed of remaining carbon and ash, and is referred to as char. This char particle undergoes char combustion generally at slower rates than devolatilization. During char combustion, oxygen diffuses into the porous coal structure and reacts with the carbon, forming CO or CO_2. Char combustion is usually controlled by either mass transfer rates or chemical conversion rates, or both [257]. The CO released during char combustion subsequently burns to form CO_2. Besides the char oxidation mechanism, char may also be converted by gasification reactions, especially in hot oxygen-depleted regions with large amounts of steam present.

All of the aforementioned processes are modeled in this work, with the exception of drying and gasification. To treat these processes, a set of models is applied, which are outlined here. A detailed description is given in the later chapters. Before simulation, the computational coal and volatile composition has to be determined. This usually includes the assumption of specific heating conditions, where the volatile release is higher than the amount of volatile matter given in the proximate analysis [217]. Based on the higher volatile yield, and the assumption that only carbon and ash are left in the coal after devolatilization, the atomic composition of the volatile gas can be obtained

by removing the remaining carbon from the proximate analysis. In this work, these atoms are distributed among species commonly found in volatile gas, as described in Chapter 5 on page 53. The coal thermal properties (i.e., heat capacity and enthalpy) are modeled based on the coal composition using models by Merrick and Brewster et al. [18, 133], as described on page 58. The coal density is set to a fixed value obtained from the experiment and changes during devolatilization, assuming that the coal particle size remains unchanged during devolatilization. Devolatilization is treated by different models in this work: a) a single rate model by Badzioch & Hawksley [2], applied in Chapter 7; b) a competing rate model by Kobayashi [108], applied in Chapters 5 through 8; and c) the Chemical Percolation for Devolatilization model [48, 49, 64], applied in Chapter 7. Smith's intrinsic model is applied for char combustion [215], as described in Section 5.2.5 on page 55. Convective heat exchange of the particle with its surroundings is accounted for by means of the Ranz-Marshall model [193], as illustrated in Chapter 5 on page 57. An equation for the particle temperature balance is solved, which includes the effects of devolatilization, char combustion, convection as well as radiation. Drag acting on the particles included in the equation for acceleration is accounted for by the Schiller-Naumann correlation [209], as given on page 52. An important modification to the standard empirical laws describing convective heat transfer and drag is the inclusion of Stefan flow by means of a so-called blowing correction [216]. This is accounted for by modifying the particle relaxation time and Nusselt number [223], as detailed on page 58. The coal models are implemented in the Lagrangian framework described in the preceding section, and details are given in Chapters 5 through 8.

Chapter 3

Turbulent Combustion Modeling

In this chapter, methods and models for turbulent combustion simulation are introduced. First, the different modes of combustion are presented. This is followed by the description of the straightforward approach of directly modeling combustion with an appropriate chemical mechanism. However, this approach is only limited to direct numerical simulation, where all scalar and flow scales are resolved, leading to extensive computational requirements currently out of reach for engineering applications. For the application to engineering flows with large eddy simulation (LES), reduced-order models are mainly employed that oftentimes rely on a conserved scalar approach and the flamelet assumption. Both of these assumptions are employed in large parts of this work. A description for situations of single and multiple conserved scalars is given in this chapter.

3.1   Modes of Combustion

3.1.1   Premixed Combustion

Laminar Premixed Flame

In premixed combustion, oxidizer and fuel are mixed before being supplied to the reaction zone. To achieve ignition and maintain combustion, the mixture needs to be within its flammability limits. If this is the case, a premixed flame front propagates through the unburned mixture. The speed at which the flame front propagates is referred to as the burning velocity or flame speed, and constitutes a major quantity for the description of premixed flames. In the laminar case, the burning velocity depends on the temperature of the unburned mixture and its composition, as well as on the pressure at which the conversion to burned gases occurs. To compare the flame speeds for a mixture of a certain fuel and oxidizer, the equivalence ratio is a helpful quantity. It relates the ratio of fuel to oxidizer to the ratio at stoichiometric conditions (all in the unburned state):

$$\phi = \frac{(Y_\mathrm{f}/Y_\mathrm{ox})_\mathrm{u}}{(Y_\mathrm{f}/Y_\mathrm{ox})_\mathrm{u,st}}. \tag{3.1}$$

Different definitions of flame speed exist, one of them is the speed at which the flame front moves towards the unburned gases in direction normal to the flame surface. Differ-

ent theories exist to theoretically derive flame speeds based on certain assumptions and simplifications, such as the theories by Mallard and Le Chatelier or Zeldovich, Frank-Kamenetskii and Semenov [60]. Nowadays, flame speeds can easily be computed using codes such as Cantera [62] or Chemkin [93], where the accuracy of the flame speed calculations is limited by the accuracy of the chemical mechanism, the model applied for molecular transport and the thermodynamic data. Similar to flame speed, different definitions of flame thickness exist. A frequently used definition is the thermal flame thickness, which is defined as the temperature difference (between unburned and burned side) divided by the steepest temperature gradient found in the flame (in one dimension).

The laminar structure of premixed flames is well understood and usually divided into three zones with distinct characteristics: the *preheat zone*, *reaction zone* and *recombination zone* (e.g., [60]). The understanding of the laminar flame structure is important for a conceptual understanding of the interaction of turbulence with the premixed flame. The *preheat zone* can be found on the unburned side of the premixed flame. In this zone, the chemistry is slow and the mixture is heated up by thermal diffusion from the flame front. Some species diffuse from reaction zone to preheat zone and some low-temperature reactions occur. However, important reactions forming radicals that can break up the fuel, e.g., the chain branching reaction, do not occur at these temperatures. In the reaction zone, however, temperatures are high enough for radicals such as OH to form, which in turn rapidly convert fuel. Behind the fuel consumption layer still within the reaction layer one can find a zone where intermediates are consumed and where a conversion of CO to CO_2 takes place, which is the source of large parts of the heat release in a premixed hydrocarbon flame. The recombination zone owes its name to radicals recombining, which occurs without significant heat release as the radical concentrations are low in the post-flame [60].

Turbulent Premixed Flame

Turbulent premixed flames can effectively be investigated by coupling the characteristic laminar flame quantities, flame speed and flame thickness, to the characteristic turbulence scales, velocity fluctuation and turbulent length scale (i.e., eddy size). This coupling can conveniently be visualized in regime diagrams such as the ones proposed by Borghi [15] and Peters [163]. A detailed description of the regime diagram is omitted here, but the important points are outlined. The *corrugated flamelet regime* corresponds to the situation where eddies are not strong and small enough to perturb the laminar flame structure on spatial scales of the order of that of the flame. With increasing turbulence intensity, i.e., velocity fluctuations, eddies are able to alter the flame structure. This regime is called *thin reaction zones*. Here, the smallest eddies are able to penetrate into the laminar flame structure. However, they are unable to alter the inner layer but rather affect the preheat zone, and hence mainly thermal diffusion. At even higher turbulence intensities, in the *broken/distributed reaction zone regime*, eddies are able to disrupt and perturb the inner layer of the flame, leading to broken reaction layers.

3.1.2 Non-premixed Combustion

In non-premixed combustion, fuel and oxidizer are not mixed before being supplied to the reaction zone. Furthermore, the rate at which fuel is converted is tied to the rate at which oxidizer and fuel mixes. Often, it is argued that chemical reactions occur on much smaller time scales than the mixing and hence the progress of conversion is solely determined by the mixing of fuel and oxidizer. Some of the concepts to describe non-premixed flames in a turbulent (or laminar) environment are discussed in the following sections.

Mixture Fraction

Since mixing between fuel and oxidizer is of predominant importance in the description of non-premixed flames, a scalar that can quantify the mixing of fuel and oxidizer is particularly useful. The scalar that has become the basis for modeling of non-premixed flames is the so-called mixture fraction [166]. It tracks how much fluid originating from a particular stream contributes to a mixture. For a steady system with two inlet streams, a fuel stream with a mass flow of $\dot{m}_\mathrm{f}$ and an oxidizer stream with the mass flow of $\dot{m}_\mathrm{ox}$, this can be expressed as:

$$Z = \frac{\dot{m}_\mathrm{f}}{\dot{m}_\mathrm{f} + \dot{m}_\mathrm{ox}}. \tag{3.2}$$

Similarly, multiple mixture fractions can be defined, which is shown in Chapter 5.

3.1.3 Mixed-Mode/Stratified Combustion

Typically, turbulent combustion appears in a mode that is neither purely premixed nor non-premixed. Such situations are observed in the carrier-phase direct numerical simulation (CP-DNS) in Chapter 8 and are reported for the flame studied in Chapter 9. From a practical viewpoint, the simultaneous occurrence of premixed and non-premixed zones poses difficulties for classical turbulent combustion modeling since the models are usually based on either one of the regimes, e.g., non-premixed and premixed flamelets. However, advanced methods such as the transported filtered density function (FDF) method applied in Chapter 9 are not limited to one of the regimes. However, some of the deficiencies may become more severe in either one of the regimes (e.g., modeling of the molecular diffusion in premixed flames).

3.2 Direct Combustion Modeling with DNS

The straightforward approach to simulate turbulent reacting flows is to resolve all scales and describe the chemistry by reaction mechanisms describing all elementary reactions occuring for the fuel and oxidizer burnt. This includes the solution of a number of mass fraction equations equaling the number of species included in the chemical mechanism as well as the solution of the coupled system of ordinary differential equations describing the reactions. To consider reactive flows, an additional restriction is added to the resolution of the numerical grid by the requirement to resolve the scalar flame structure. For premixed flames, this is usually expressed by requiring a specific number of grid points

be located within the thermal flame thickness. For non-premixed flames, criteria can be based on laminar scalar profiles of species such as OH under relevant strain conditions (e.g., [71]). Usually, these restrictions are more severe than the restrictions based on the smallest turbulent flow scales, since often the smallest flame scales are smaller than the Kolmogorov scales. Therefore, the DNS approach is only limited to small turbulent combustion problems and requires large computing resources, but is well suited for model development and understanding of combustion physics [23]. Only recently, the DNS of laboratory scale flames has been achieved [244]. Currently, the approach cannot be afforded for problems of direct engineering relevance, such as the problems described in Chapters 5 and 6. The problem depicted in Chapter 8 is a so-called carrier phase DNS, where all scales are resolved apart from scales induced by the particles (e.g., particle wakes, boundary layers).

3.3   Combustion Modeling in LES

3.3.1   Transported/Conserved Scalar

Many combustion models are built upon the concept of a conserved scalar. Such a scalar can, for example, track the fluid from a certain stream, such as the mixture fraction described in Eq. 3.2. The equation describing such a scalar is similar to the equation for mass fraction and is written here in terms of the arbitrary quantity ϕ.

$$\frac{\partial \rho \phi}{\partial t} + \frac{\partial \rho \phi u_j}{\partial x_j} = \frac{\partial}{\partial x_j}\left(\rho D_\phi \frac{\partial \phi}{\partial x_j}\right) + \rho \dot{S}_\phi \qquad (3.3)$$

In Eq. 3.3, D_ϕ denotes the diffusion coefficient of quantity ϕ and S_ϕ the source term. The source term is included here, however, if it is non-zero Eq. 3.3 is not a conserved scalar. Applying the filtering operation to Eq. 3.3 results in:

$$\frac{\partial \overline{\rho \phi}}{\partial t} + \frac{\overline{\partial \rho \phi u_j}}{\partial x_j} = \overline{\frac{\partial}{\partial x_j}\left(\rho D_\phi \frac{\partial \phi}{\partial x_j}\right)} + \overline{\rho \dot{S}_\phi}. \qquad (3.4)$$

Using similar approximations as for the filtered momentum equations, the final Favre-filtered transport equation for scalar ϕ is:

$$\frac{\partial \bar{\rho}\tilde{\phi}}{\partial t} + \frac{\partial \bar{\rho}\tilde{\phi}\tilde{u}_j}{\partial x_j} = \frac{\partial}{\partial x_j}\left(\bar{\rho}\tilde{D}_\phi \frac{\partial \tilde{\phi}}{\partial x_j} - F_{\mathrm{SGS}}\right) + \bar{\rho}\tilde{S}_\phi. \qquad (3.5)$$

In Eq. 3.5, F_{SGS} denotes the subgrid scale (SGS) scalar flux, i.e., $F_{\mathrm{SGS}} = \bar{\rho}(\widetilde{\phi u_j} - \tilde{\phi}\tilde{u}_j)$. In analogy to the eddy viscosity, this term can be modeled based on the *eddy diffusivity approach*:

$$F_{\mathrm{SGS}} = -\bar{\rho}D_t \frac{\partial \tilde{\phi}}{\partial x_j}. \qquad (3.6)$$

In this work, the SGS diffusion coefficient D_t is related to the turbulent viscosity by a turbulent Schmidt number Sc_t, such that $D_t = \nu_t/\mathrm{Sc}_t$. The turbulent Schmidt number

is assumed to be 0.7. However, D_t can also be computed using a dynamic procedure [170], similar to the one for the SGS momentum fluxes, effectively providing a turbulent Schmidt number.

The most important example of a transported quantity is the mixture fraction, which is used in all parts of this work, i.e., Chapters 5 through 9 (it is only used as a post-processing quantity and for future modeling in the CP-DNS work of Chapter 8). Its local value gives the ratio of mass of a fluid from a specific origin (e.g., stream) to the total mass. Its equation can be written as:

$$\frac{\partial \bar{\rho}\tilde{Z}}{\partial t} + \frac{\partial}{\partial x_j}\bar{\rho}\tilde{Z}\tilde{u}_j = \frac{\partial}{\partial x_j}\left(\bar{\rho}\tilde{D}_Z\frac{\partial \tilde{Z}}{\partial x_j} - F_{\mathrm{SGS}}\right) + \overline{\rho\dot{S}_Z}. \tag{3.7}$$

Besides Eq. 3.7, its variance is of importance for various turbulent combustion models. The subgrid variance of Z is defined as:

$$\widetilde{Z''^2} = \widetilde{Z^2} - \tilde{Z}^2. \tag{3.8}$$

Cook & Riley [35] reported a simple model based on scale similarity, where the subgrid variance can be computed from (here reported in terms of Favre averages, see [158]):

$$\widetilde{Z''^2} = C_{\mathrm{v}}\left[\widehat{\bar{\rho}\widetilde{Z^2}}/\hat{\bar{\rho}} - \left(\widehat{\bar{\rho}\tilde{Z}}/\hat{\bar{\rho}}\right)^2\right]. \tag{3.9}$$

Here, the hat symbol denotes a filtering operation with a filter width larger than the grid size.

Another simple model to obtain the subfilter variance of Z is the model by Branley & Jones [17]. This model assumes that the subgrid dissipation is proportional to the variance multiplied by the characteristic rate of strain $\mathcal{S}$, and that there is a local equilibrium of variance production and dissipation. The model can be written as:

$$\widetilde{Z''^2} = C_{\mathrm{v}}\Delta^2\frac{\partial \tilde{Z}}{\partial x_j}\frac{\partial \tilde{Z}}{\partial x_j}. \tag{3.10}$$

Branley & Jones theoretically obtained a model constant of $C_{\mathrm{v}} \approx 0.2$ for constant density flows and scaling following the inertial subrange of isotropic turbulence. However, they argued that this value has to be reduced, and reported a value of 0.1 being successful for the hydrogen jet diffusion flame under study [17].

While simple approaches based on scale similarity or local equilibrium may be expected to work well in cases of homogeneous turbulence, transport equations are needed to consider non-equilibrium effects as suggested by Jimenez et al. [86]. Such effects are especially important in two-phase flows where the non-gaseous phase introduces variance on the subgrid. Such transport equations can either be written in terms of $\widetilde{Z''^2}$ or $\widetilde{Z^2}$ (e.g., [94]). The variance can easily be computed from the latter by subtracting $\tilde{Z}^2$, which can readily be obtained from the transport of $\tilde{Z}$. The equations can be written as (with

the effective diffusivity $D_{\text{eff}} = \tilde{D} + D_t$):

$$\frac{\partial \bar{\rho} \widetilde{Z^2}}{\partial t} + \frac{\partial \bar{\rho} \tilde{u}_j \widetilde{Z^2}}{\partial x_j} = \frac{\partial}{\partial x_j} \left(\bar{\rho} D_{\text{eff}} \frac{\partial \widetilde{Z^2}}{\partial x_j} \right) - \bar{\rho} \tilde{\chi}_Z, \tag{3.11}$$

$$\frac{\partial \bar{\rho} \widetilde{Z''^2}}{\partial t} + \frac{\partial \bar{\rho} \tilde{u}_j \widetilde{Z''^2}}{\partial x_j} = \frac{\partial}{\partial x_j} \left(\bar{\rho} D_{\text{eff}} \frac{\partial \widetilde{Z''^2}}{\partial x_j} \right) - \bar{\rho} \tilde{\chi}_Z + 2 \bar{\rho} D_{\text{eff}} \frac{\partial \tilde{Z}}{\partial x_j} \frac{\partial \tilde{Z}}{\partial x_j}. \tag{3.12}$$

Both equations 3.11 and 3.12, contain the term for the unclosed scalar dissipation rate $\bar{\rho} \tilde{\chi}_Z$:

$$\bar{\rho} \tilde{\chi}_Z = \overline{2 \rho D_Z \frac{\partial Z}{\partial x_j} \frac{\partial Z}{\partial x_j}}. \tag{3.13}$$

There are different ways to model the scalar dissipation rate term, often it is divided into a resolved and unresolved part [40, 158]:

$$\bar{\rho} \tilde{\chi}_Z = 2 \bar{\rho} \tilde{D}_Z \frac{\partial \tilde{Z}}{\partial x_j} \frac{\partial \tilde{Z}}{\partial x_j} + 2 \bar{\rho} C_{\chi Z} D_t \frac{\widetilde{Z''^2}}{\Delta^2}. \tag{3.14}$$

The second term on the RHS of 3.14 represents a model for the unresolved part of the scalar dissipation rate. Different values of $C_{\chi Z}$ have been used in the literature. Commonly, a value of 2 is chosen. However, in the context of multiphase flows, larger values may be employed, since the non-gaseous phase introduces large gradients on the subgrid scale.

In other studies, $\bar{\rho} \tilde{\chi}_Z$ is not explicitly divided into resolved and unresolved parts but modeled together [192]:

$$\bar{\rho} \tilde{\chi}_Z = 2 \bar{\rho} \frac{D_{\text{eff}}}{\Delta^2} \widetilde{Z''^2}, \tag{3.15}$$

which is consistent with the way scalar dissipation rate or mixing frequency is usually modeled in the context of transported FDF methods. Recently, Kaul et al. [91] suggested a dynamic method to obtain the model coefficients in transported variance closures.

The equations and methods described above are used to obtain the variance of conserved scalars. If the scalar is not conserved, additional terms arise in the variance transport equations. One example is the progress variable, which is usually defined as a linear combination of product species mass fractions, such as CO and CO_2, often simply defined as $Y_p = Y_{CO} + Y_{CO_2}$. The transport of the progress variable and its square, $\widetilde{Y_p^2}$, is written as:

$$\frac{\partial}{\partial t} \bar{\rho} \tilde{Y}_p + \frac{\partial \bar{\rho} \tilde{u}_j \tilde{Y}_p}{\partial x_j} = \frac{\partial}{\partial x_j} \left(\bar{\rho} D_{\text{eff}} \frac{\partial \tilde{Y}_p}{\partial x_j} \right) + \bar{\rho} \tilde{\dot{S}}_{Y_p}, \tag{3.16}$$

$$\frac{\partial \bar{\rho} \widetilde{Y_p^2}}{\partial t} + \frac{\partial \bar{\rho} \tilde{u}_j \widetilde{Y_p^2}}{\partial x_j} = \frac{\partial}{\partial x_j} \left(\bar{\rho} D_{\text{eff}} \frac{\partial \widetilde{Y_p^2}}{\partial x_j} \right) + 2 \bar{\rho} \widetilde{Y_p \dot{S}_{Y_p}} - \bar{\rho} \tilde{\chi}_{Y_p}. \tag{3.17}$$

Compared to the transport of the (squared) conserved scalar mixture fraction, this equation involves an additional variance production term due to chemical reactions, $2 \bar{\rho} \widetilde{Y_p \dot{S}_{Y_p}}$.

The scalar dissipation rate is modeled in the same way as for mixture fraction. Another example is a mixture fraction containing a source term, as for the multiphase flows studied in Chapter 5 to 7. The modeling of the variance in this case is described in Chapter 5.

In this work, Dirac PDFs for enthalpy and scalar dissipation rate are used in Chapters 5 to 7, whereas Chapter 9 relies on a two-dimensional top-hat PDF for mixture fraction and progress variable, and the transported PDF approach. Hence, equations to obtain the variance of scalar dissipation rate or enthalpy are not solved.

3.3.2 Flamelet Model in Non-Premixed Combustion

The flamelet model is based on the idea that a turbulent flame can be thought of as an ensemble of laminar flames, so-called flamelets. This implies that locally, the flame structure is still laminar and that the flame is simply embedded in a flow field that wrinkles the flame on scales larger than the thickness of the flame. Equivalently, a condition for the flamelet assumption to hold is that the size of the Kolmogorov eddy is much larger than the size of the reaction layer (inner layer) that is responsible for fuel conversion.

The flamelet concept goes back to Williams [260] by establishing the idea that a turbulent non-premixed flame can be understood as an ensemble of stretched laminar flames. Peters [165] and Kuznetsov [115] subsequently derived the flamelet equations using mixture fraction as independent variable and scalar dissipation to describe mixing. The flamelet equations can be derived by different means, i.e., asymptotic analysis and coordinate transformation with the application of boundary layer arguments [70]. The latter approach is presented here briefly. The starting point is the transport equation of species mass fraction, Eq. 2.3, transformed into non-conservative form (i.e., by applying the chain-rule to accumulation and convection term and substituting mass conservation) and using Fick's law:

$$\rho \frac{\partial Y_\alpha}{\partial t} + \rho u_j \frac{\partial Y_\alpha}{\partial x_j} = \frac{\partial}{\partial x_j} \left(\rho D_\alpha \frac{\partial Y_\alpha}{\partial x_j} \right) + \dot{\omega}_\alpha. \tag{3.18}$$

Now, the coordinates are transformed from the Cartesian reference frame into a frame that is attached to the stoichiometric mixture fraction (Z_{st}) surface, which identifies the reaction layer. The Cartesian coordinates are arranged such that x_1 is located normal to the stoichiometric mixture fraction, which is now replaced by the mixture fraction Z while the tangential coordinates are expressed by Z_y and Z_z, respectively. The derivatives in the new coordinate system are given by the following transformation rules:

$$\frac{\partial}{\partial t} = \frac{\partial}{\partial \tau} + \frac{\partial Z}{\partial t} \frac{\partial}{\partial Z},$$
$$\frac{\partial}{\partial x_1} = \frac{\partial Z}{\partial x_1} \frac{\partial}{\partial Z},$$
$$\frac{\partial}{\partial x_\beta} = \frac{\partial}{\partial Z_\beta} + \frac{\partial Z}{\partial x_\beta} \frac{\partial}{\partial Z}, \qquad \beta = y, z.$$

These transformation rules are now applied to Eq. 3.18. According to Peters [162], derivatives with respect to the tangential coordinates Z_y and Z_z are negligible, which results in a one-dimensional time-dependent diffusion-reaction equation in mixture fraction space (assuming Le=1):

$$\rho\frac{\partial Y_\alpha}{\partial t} = \rho\frac{\chi}{2}\frac{\partial^2 Y_\alpha}{\partial Z^2} + \dot{\omega}_\alpha. \tag{3.19}$$

Equation 3.19 contains the scalar dissipation rate χ:

$$\chi = 2D\left(\frac{\partial Z}{\partial x_j}\right)^2. \tag{3.20}$$

The scalar dissipation rate can be seen as the inverse of a characteristic diffusion time [164]. If the scalar dissipation rate is high, radicals and energy will be transported away from the flame front without being balanced by the production of energy and radicals due to chemical reaction. This situation corresponds to a very thin reaction zone that breaks at a certain quenching scalar dissipation rate χ_q. If diffusion balances reaction, Eq. 3.19 becomes the steady flamelet equation:

$$-\rho\frac{\chi}{2}\frac{\partial^2 Y_\alpha}{\partial Z^2} = \dot{\omega}_\alpha. \tag{3.21}$$

The flamelet equation can be solved in mixture fraction space to obtain the relationship of thermo-chemical quantities and mixture fraction. However, this requires the specification of a scalar dissipation rate profile. Alternatively, the state relationship can be obtained by solving density, momentum, energy and species equations in physical space, and then mapping the thermo-chemical quantities onto mixture fraction. The latter approach is taken in this work.

The flamelet equations can be extended to multiple dimensions, i.e., to more than one mixture fraction, such as presented by Hasse [70] and Hasse & Peters [68]. In this work, multi-dimensional flamelets have been applied in Chapters 5 to 7. However, flamelet tables have been obtained by solving laminar flames in physical space only. Flamelet tables with multiple fuel streams can be generated by solving multiple single laminar flames, each with a different fuel composition. This approach shall be illustrated at the example of mixture fractions for volatile Z_{vol} and char off-gases Z_{char} as used in Chapters 5 and 6. First, it has to be recognized that all possible thermo-chemical states lie within a triangle in Z_{vol}-Z_{char}-space, bound between $Z_{\mathrm{vol}} = 0$, $Z_{\mathrm{char}} = 0$ and $Z_{\mathrm{vol}} + Z_{\mathrm{char}} = 1$, which poses numerical difficulties for the interpolation of thermo-chemical states as a function of Z_{vol} and Z_{char}. Hasse [70] proposed to conduct a coordinate transformation to the mixture fraction sum Z and a mixing parameter Z_2:

$$\begin{aligned} Z &= Z_{\mathrm{vol}} + Z_{\mathrm{char}}, \\ Z_2 &= Z_{\mathrm{char}}/(Z_{\mathrm{vol}} + Z_{\mathrm{char}}). \end{aligned} \tag{3.22}$$

The domain in $Z - Z_2$-space is rectangular. The flamelet table can now be generated from 1D-laminar flames for different values of Z_2, representing a mixture of the fuels from the two streams. The results of the individual flames can easily be interpolated onto a two-dimensional grid in Z and Z_2 space. However, for a full description, additional parameters may be required, such as enthalpy and scalar dissipation rate (see Chapters 5 to 7), which increases the dimensionality of the flamelet table.

3.3.3   Subgrid PDF Modeling

The purpose of computing the variance of mixture fraction (or other scalars the combustion model is based upon) is usually to construct a presumed probability density function for the dependent scalars. Givi [59] was the first to suggest using presumed or transported PDFs in LES, and Pope introduced the notion of a filtered density function (FDF) [177]. Subsequently, Madnia & Givi [123] reported the application of a presumed FDF to LES. Cook & Riley [35] further refined this concept by employing the beta-PDF as a model for the FDF, which is widely used nowadays.

The probability density function describes how the transported scalar is distributed within the subgrid. These presumed probability density functions are usually obtained from the first two moments of a scalar, i.e., its average and variance. A dependent Favre-filtered quantity $\tilde{\psi}$ can then be obtained from convolution with the Favre subgrid PDF $\tilde{P}$ as:

$$\tilde{\psi} = \int_0^1 \psi(Z)\tilde{P}(Z; \tilde{Z}, \widetilde{Z''^2})dZ. \tag{3.23}$$

The Favre subgrid PDF in Z-space is parametrized using $\tilde{Z}$ and $\widetilde{Z''^2}$. A widely used subgrid PDF is the beta-PDF, first introduced to LES by Cook & Riley [35]. It has been shown that the beta-PDF can be used for both, Reynolds- and Favre PDFs [241]. It can be computed from $\tilde{Z}$ and $\widetilde{Z''^2}$ by (here written in terms of the Favre PDF):

$$\begin{aligned}
\tilde{P}(Z; \tilde{Z}, \widetilde{Z''^2}) &= Z^{a-1}(1 - Z)^{b-1}\Gamma(a + b)(\Gamma(a)\Gamma(b)), \text{ with:} \\
a &= \tilde{Z}c, \\
b &= (1 - \tilde{Z})c, \\
c &= (\tilde{Z} - \tilde{Z}^2 - \widetilde{Z''^2})/\widetilde{Z''^2}.
\end{aligned} \tag{3.24}$$

In Eq. 3.24, Γ denotes the gamma function. The beta-PDF has been shown to be able to very well reproduce the subgrid PDF obtained from DNS data in many situations. However, as described by Floyd et al. [50], there are situations where the beta-PDF does not work well, e.g., in situations of multi-stream mixing. Floyd et al. proposed a simpler model, namely the top-hat PDF, which assumes a constant gradient of Z within a finely resolved LES cell (or the density-weighted gradient for Favre filtering). Such a top-hat PDF has been applied in Reynolds-averaged Navier-Stokes simulations before [16], but is much more suitable in the LES [50]. This leads to all values between an upper and a lower limit of Z being equally likely to occur within the subgrid (or with uniform density-weighted probability for the Favre filter), such that the Favre PDF has the shape of the top-hat between these limits. This is expressed as:

$$\tilde{P}(Z; \tilde{Z}, \widetilde{Z''^2}) = \begin{cases} t_0 & Z_a \leq Z \leq Z_b \\ 0 & \text{all other } Z. \end{cases} \tag{3.25}$$

The limits Z_a, Z_b and the width t_0 are computed from $\tilde{Z}$ and $\widetilde{Z''^2}$ by:

$$
\begin{aligned}
Z_a &= \tilde{Z} - \frac{1}{2}\sqrt{12\widetilde{Z''^2}}, & (3.26) \\
Z_b &= \tilde{Z} + \frac{1}{2}\sqrt{12\widetilde{Z''^2}}, \\
t_0 &= 1/(Z_b - Z_a).
\end{aligned}
$$

3.3.4   Extension to Multiple Scalars

Multiple tracking scalars may be necessary to accurately predict the state of the gas phase. This might, for example, be multiple mixture fractions (described in Section 3.3.2 and used in Chapters 5 to 7) or a variable describing the overall progress of chemical reactions (discussed in detail in Chapter 9). The subgrid modeling in a situation with multiple scalars could be treated by solving separate variance transport equations and use of a multi-dimensional joint subgrid PDF. A simpler approach is not to employ a joint subgrid PDF but to assume statistical independency between the transported scalars, which often is further simplified by assuming a Dirac distribution for one of the involved scalars. Another approach is to combine the transported scalars, i.e., if they are both mixture fractions such as in Chapters 5 through 7 and base the subgrid PDF modeling on their sum. This approach has been employed in Chapters 5 through 7, nonetheless, also the other approaches are discussed here.

The modeling of a joint beta-PDF for multi-scalar mixing in the Reynolds-averaged Navier-Stokes (RANS) context has been presented by Girimaji [58] and applied by Hasse [68] in the context of RANS modeling of a two mixture fraction model for split Diesel injections. The two-dimensional beta-PDF for mixture fractions $\tilde{Z}_1$ and $\tilde{Z}_2$ is written as:

$$
\begin{aligned}
\tilde{P}(Z_1, Z_2; \tilde{Z}_1, \widetilde{Z_1''^2}, \tilde{Z}_2, \widetilde{Z_2''^2}) &= Z_1^{a-1} Z_2^{b-1}(1 - Z_1 - Z_2)^{c-1} \cdot & (3.27) \\
&\quad \frac{\Gamma(a+b+c)}{(\Gamma(a)\Gamma(b)\Gamma(c))}, \text{ with:} \\
a &= \tilde{Z}d, \\
b &= \tilde{Z}_2 d, \\
c &= (1 - \tilde{Z}_1 - \tilde{Z}_2)d, \\
d &= \frac{1-e}{f} - 1, \\
e &= \tilde{Z}_1^2 + \tilde{Z}_2^2 + (1 - \tilde{Z}_{\text{sum}})^2, \\
f &= \widetilde{Z_1''^2} + \widetilde{Z_2''^2} + \widetilde{Z_{\text{sum}}''^2}, \\
Z_{\text{sum}} &= Z_1 + Z_2.
\end{aligned}
$$

To the author's knowledge, using a two-dimensional beta-PDF has not been attempted in LES yet. One reason is that there are not many LES studies yet that use multiple mixture fractions. Some examples are the studies by Ihme & See [81] or Lamouroux et al. [116]. The other reason is that the memory requirement strongly increases by using a joint PDF. The thermo-physical data that is dependent on Z_1 and Z_2 needs to be pre-integrated

such that it can be efficiently accessed by supplying $\tilde{Z}_1$, $\widetilde{Z_1''^2}$, $\tilde{Z}_2$ and $\widetilde{Z_2''^2}$, leading to a four-dimensional look-up table, which still might be tractable. However, typical combustion models require more than just mixture fractions to be properly parametrized, e.g., the flamelet model requires scalar dissipation rates to include the local mixing rate in the thermo-physical state. Building a look-up table with more than four dimensions quickly becomes intractable since the memory requirement is too high and access is not computationally cheap anymore. Hence, the approach of using a two-dimensional joint beta-PDF for the mixture fractions has not been attempted in this work, given that scalar dissipation and enthalpy had to be included as additional parameters.

The aforementioned situation of look-up table dimensionality becoming intractable is far less severe if the top-hat PDF approach is used, since using the top-hat PDF does not increase the dimensionality. Olbricht et al. [152] used a joint top-hat PDF for mixture fraction and progress variable. The joint subgrid PDF of the mixture fractions can be calculated as:

$$
P(Z_1, Z_2; \tilde{Z}_1, \widetilde{Z_1''^2}, \tilde{Z}_2, \widetilde{Z_2''^2}) = \begin{cases} t_0 & Z_{1,a} \leq Z_1 \leq Z_{1,b}, \quad Z_{2,a} \leq Z_2 \leq Z_{2,b} \\ 0 & \text{all other } Z_1, Z_2. \end{cases} \tag{3.28}
$$

The limits $Z_{1,a}$, $Z_{1,b}$, $Z_{2,a}$ and $Z_{2,b}$ are obtained analogously to Eq. 3.26 and t_0 is obtained by:

$$
t_0 = \frac{1}{(Z_{1,b} - Z_{1,a})(Z_{2,b} - Z_{2,a})}. \tag{3.29}
$$

The approach taken in this work is to sum up the mixture fractions $\tilde{Z} = \tilde{Z}_1 + \tilde{Z}_2$, to solve a transport equation only for $\widetilde{Z''^2}$ and to apply the subgrid PDF only for $\tilde{Z}$, such that essentially Eqs. 3.25 and 3.26 are used in a two mixture fraction situation. The implications of such an approach are that subgrid fluctuations cannot be treated independently, which, however, is not as severe in coal combustion due to the mixture fractions coming from consecutive processes. However, a two-dimensional top-hat PDF is used for the hybrid method presented in Chapter 9.

As mentioned earlier, the chemical state relationship might be based on more than a single or two mixture fractions. If no subgrid distribution in some of these scalars is assumed then this corresponds to a Dirac PDF. Formally, this can be expressed by first re-writing the joint PDF as a product of a marginal PDF and a conditional PDF (with Y being an arbitrary parameter to follow a Dirac PDF, such as enthalpy or scalar dissipation rate discussed in Chapters 5-7):

$$
\tilde{P}(Z, Y) = \tilde{P}(Z)\tilde{P}(Y|Z). \tag{3.30}
$$

The PDF of Y conditional on Z is expressed as a Dirac PDF (representing an infinite peak at $Y = \widetilde{Y|Z}$):

$$
\tilde{P}(Y|Z) = \delta(Y - \widetilde{Y|Z}). \tag{3.31}
$$

One property of the Dirac PDF is such that $\int f(x)\delta(x - x_0)dx = f(x_0)$ (which is referred to as the sifting property, see [178]) and hence it follows (for the integration of an arbitrary

quantity ψ which depends on Z and Y):

$$\tilde{\psi} \; = \; \int_0^1 \int_0^1 \psi(Z,Y)\tilde{P}(Z;\tilde{Z},\widetilde{Z''^2})\delta(Y - \widetilde{Y|Z})dZdY \qquad (3.32)$$

$$= \; \int_0^1 \psi(Z,Y = \widetilde{Y|Z})P(Z;\tilde{Z},\widetilde{Z''^2})dZ.$$

Assuming statistical independence finally allows $\widetilde{Y|Z} = \tilde{Y}$, such that $\tilde{\psi}$ is only a function of $\tilde{Z}$, $\widetilde{Z''^2}$ and $\tilde{Y}$. Such an approach is widely adopted, for example, for the progress variable in combination with a mixture fraction [80, 169] or scalar dissipation rate in combination with a mixture fraction [96].

3.3.5   Transported FDF Approach

Instead of assuming a subgrid PDF, an equation for the subgrid PDF may also be solved. This has the advantage that the shape of the PDF does not need to be known but evolves within the simulation. However, this comes at additional cost and requires special methods such as the Monte Carlo method. Transported PDF methods for reacting flows have been established as standalone methods or in combination with RANS by Dopazo & O'Brien [42], Pope [179], O'Brien [148], Janicka [84] and others. However, the suggestion of using a Monte Carlo method to solve for the transport of the PDF [180] turned the method into a tractable tool for practical combustion simulations. A detailed overview is given by Pope [178].

   After the suggestion to use subgrid PDFs in LES by Givi [59] and the introduction of the notion of a filtered density function (FDF) by Pope [177] and his proposition to transport such FDF in LES, Gao & O'Brien [55] were the first to provide closure of the terms in the FDF transport equation in LES. First applications of the LES-FDF method have then been reported for non-reactive and reactive cases by Colucci et al. [34] and Jaberi et al. [83], respectively. The main advantages of the PDF being transported and not being needed to be prescribed, and of the reaction source term appearing in closed form eventually led to the application of the LES-FDF method to realistic laboratory flames by Sheikhi et al. [211] and Raman et al. [192]. These first applications did not employ the LES-FDF method to its full potential but used the flamelet model such that the transported FDF method basically provided the subgrid PDF closure. The first application with a reaction mechanism was by Raman & Pitsch [191], showing very good results for Sandia flames D & E [5]. A recent review of probability density function methods is given by Haworth [72].

   The transported FDF approach in this work centers around the scalar filtered mass density function (SFMDF), which is defined as:

$$F_t(\boldsymbol{\Psi};\boldsymbol{x},t) = \int_{-\infty}^{+\infty} \rho(\boldsymbol{x'},t)f_t(\boldsymbol{\Psi},\phi(\boldsymbol{x'},t))G(\boldsymbol{x'} - \boldsymbol{x})d\boldsymbol{x'}. \qquad (3.33)$$

This FDF is a convolution of the LES grid filter function G, the fluid density ρ in physical space and the (fine-grained) PDF f_t in composition space [178], where $\boldsymbol{\Psi}$ is

the composition sample space vector. For brevity, the SFMDF will simply be referred to as FDF in the following.

The FDF approach relies on the concept of the so-called fine grained density [178]. This concept expresses the PDF f_t as a Dirac delta function of the dimensionality of the number of scalars n_s (i.e., mass fractions and enthalpy) required to describe the chemistry or correspondingly, as a product of n_s scalar delta functions, and reads:

$$f_t(\boldsymbol{\Psi}, \boldsymbol{\phi}(\boldsymbol{x'}, t)) = \delta(\boldsymbol{\Psi} - \boldsymbol{\Phi}(x, t)) = \prod_{\alpha=1}^{n_s} \delta[\psi_\alpha - \phi_\alpha(x, t)]. \tag{3.34}$$

In Eq. 3.34, Φ is the composition vector and ϕ_α a composition vector component. The FDF transport equation can be deduced by taking the time derivative of equation (3.33) [34], which after some manipulation eventually leads to:

$$\frac{\partial F_t}{\partial t} + \frac{\partial \widetilde{u}_i F_t}{\partial x_i} = -\frac{\partial}{\partial x_i}(\overline{[u_i|\boldsymbol{\Psi}} - \widetilde{u}_i]F_t) \tag{3.35}$$
$$+ \frac{\partial}{\partial \psi_\alpha}\left[\overline{\frac{1}{\rho}\frac{\partial J_i^\alpha}{\partial x_i}\Bigg|\boldsymbol{\Psi}}\, F_t\right] - \frac{\partial S_\alpha F_t}{\partial \psi_\alpha}.$$

The convective flux has been split into resolved and subgrid parts in Eq. 3.35. Equation 3.35 expresses the exact FDF transport, but involves unclosed terms (i.e., the first two terms on the RHS). The first term of the RHS describes the SGS convective flux and is usually closed by a gradient-diffusion approach [34] corresponding to the LES closure:

$$-\frac{\partial}{\partial x_i}(\overline{[u_i|\boldsymbol{\Psi}} - \widetilde{u}_i]F_t) = \frac{\partial}{\partial x_i}\left(\bar{\rho}D_t\frac{\partial F_t/\bar{\rho}}{\partial x_i}\right). \tag{3.36}$$

The second term on the RHS describes the SGS diffusive fluxes and is closed by a mixing model such as the interaction-by-exchange-with-the-mean (IEM) model [41, 239] or the (modified) Curl's model [37, 84]. With the IEM model, $J_i^\alpha = -\rho D \partial\phi_\alpha/\partial x_i$, and minor modifications (see [83]), the second term on the RHS becomes:

$$\frac{\partial}{\partial \psi_\alpha}\left[\overline{\frac{1}{\rho}\partial J_i^\alpha/\partial x_i\Bigg|\boldsymbol{\Psi}}\, F_t\right] = \frac{\partial}{\partial x_i}\left(\bar{\rho}\tilde{D}\frac{\partial F_t/\bar{\rho}}{\partial x_i}\right) + \frac{\partial}{\partial \psi_\alpha}\left[\Omega(\psi_\alpha - \tilde{\phi}_\alpha)F_t\right], \tag{3.37}$$

where Ω describes the mixing frequency and is discussed later.

The last term of Eq. 3.35 is the closed chemical reaction source term, which can be computed by solving the system of ODEs described in Chapter 2. The final modeled FDF transport equation is

$$\frac{\partial}{\partial t}F_t + \frac{\partial}{\partial x_i}\widetilde{u}_i F_t = \frac{\partial}{\partial x_i}\left(\bar{\rho}(\tilde{D} + D_t)\frac{\partial F_t/\bar{\rho}}{\partial x_i}\right)$$
$$+ \frac{\partial}{\partial \psi_\alpha}\left[\Omega(\psi_\alpha - \tilde{\phi}_\alpha)F_t\right] - \frac{\partial S_\alpha F_t}{\partial \psi_\alpha}. \tag{3.38}$$

Since solving this transport equation with standard Eulerian methods is intractable, the transport of the FDF is not solved directly but evolves based on a Monte-Carlo method

[178], where the FDF is represented by a number of notional Lagrangian particles. It should be noted that equivalently an Eulerian Monte-Carlo method can be used to solve for the FDF transport (e.g., [24]), which has not been attempted in this work.

The notional particles evolve in physical and composition space, and each of the particle evolutions can be seen as a representation of a single realization of the turbulent scalar field. The equation governing the particle evolution in physical space is:

$$dx_i^+ = \left(\tilde{u}_i + \frac{1}{\bar{\rho}} \frac{\partial \bar{\rho}(\tilde{D} + D_t)}{\partial x_i} \right) dt + (2(\tilde{D} + D_t))^{1/2} dW_i(t). \qquad (3.39)$$

Equation 3.39 describes the evolution of particle position x_i^+ and depends on the molecular and turbulent diffusivity, D and D_t, respectively, the filtered velocity $\tilde{u}_i$ and a three-dimensional Wiener term dW_i. The diffusivities are obtained in the same way as for the Eulerian transport equations and are mapped onto the particles. It should be noted that from a physical point of view, molecular diffusivity should not appear in the expression multiplied with the Wiener term. Modeling the particle evolution in physical space with Eq. 3.39 can lead to spurious variance production, e.g., in well-resolved regions of the flow field [229]. Recent mixing model developments provide an improvement by treating laminar diffusion in the equation governing the evolution in composition space instead of physical space [128, 229]. This has been tested in this work, but only minor differences have been found compared to the standard approach (e.g., [191, 242]) for the case studied in Chapter 9. However, it is important to note that the treatment of mixing needs to be consistently represented in the variance transport equations if transported and assumed FDF methods are used within the same simulation, such as presented in Chapter 9.

The mixing (here: IEM) and chemistry models govern the particle evolution in composition space, described by Eq. 3.40.

$$d\psi_\alpha = -C_\phi \tau_{\mathrm{mix}}^{-1} (\psi_\alpha - \tilde{\phi}_\alpha) dt + S_\alpha(\boldsymbol{\psi}) dt \qquad (3.40)$$

Besides the IEM model, the Modified Curl's mixing model [37, 84] has been applied in this work, in a formulation that supports particles with unequal weights as reported by Nooren et al. [147]. With this model, particles interact in pairs. First, particles within one cell are assigned into pairs. Then, a probability of mixing is computed as $P_{\mathrm{mix}} = w_p/w_e \beta C_\phi \tau_{\mathrm{mix}}^{-1} N_e \Delta t$ with the mean weight of the pair w_p, the weight of the particle ensemble in the cell w_e, the number of particles in the cell N_e and a factor $\beta = 3$. A uniform random number between 0 and 1 is generated. If its value is smaller than P_{mix}, the particles in the pair mix with each other, such that the two particles move towards their weighted average in composition space to a random extent. The random mixing extent corresponds to a uniform distribution between no mixing and full mixing, i.e., equal composition after the mixing event. The (expected) variance decay between MC and IEM is the same.

The mixing frequency $\omega = \tau_{\mathrm{mix}}^{-1}$ is closely related to the dissipation rate modeling described earlier through

$$\omega = \tau_{\mathrm{mix}}^{-1} = \chi / \widetilde{Z''^2}. \qquad (3.41)$$

However, the mixing frequency model usually employed in LES-FDF methods reads [83]:

$$\omega = \tau_{\text{mix}}^{-1} = \frac{D_{\text{eff}}}{\Delta^2}. \tag{3.42}$$

Recent improvements of mixing models include the IEM model with mean drift implementation [128], which gives a better prediction of molecular diffusion. This model had been tested in this work, but is not applied in the transported FDF study in Chapter 9.

Chapter 4

Numerical Methods

4.1 Finite Volume Method

The equations presented in the preceding Chapters, 2 and 3, are solved in the finite volume framework, where the solution domain is discretized into a finite number of non-overlapping volumes. The transport and conservation equations can be solved for each of these finite volumes. Local values are computed for cell centers and appropriate interpolation schemes need to be used to obtain values at the volume surfaces to compute fluxes.

The starting point of the discretization of the transport and conservation equations is to write these equations in *integral form*, i.e., to integrate them over an arbitrary finite volume ΔV (here, for the arbitrary scalar ϕ):

$$\int_{\Delta V} \frac{\partial \rho \phi}{\partial t} dV + \int_{\Delta V} \frac{\partial}{\partial x_j} \rho \phi u_j dV = \int_{\Delta V} \frac{\partial}{\partial x_j} \left(\rho D_\phi \frac{\partial \phi}{\partial x_j} \right) dV + \int_{\Delta V} \rho \dot{S}_\phi dV. \qquad (4.1)$$

Then, the *Gauß theorem* is applied to conveniently rewrite transport terms in terms of fluxes over the volume surface (i.e., to relate a volume integral of a divergence of a field to the flux normal to the volume's surface, $\int_{\Delta V} \nabla \cdot \boldsymbol{\phi} dV = \int_{\Delta A} \boldsymbol{\phi} \cdot \mathbf{n} dA$). Applying this theorem yields:

$$\int_{\Delta V} \frac{\partial \rho \phi}{\partial t} dV + \int_{\Delta A} \rho \phi u_j n_j dA = \int_{\Delta A} \left(\rho D_\phi \frac{\partial \phi}{\partial x_j} \right) n_j dA + \int_{\Delta V} \rho \dot{S}_\phi dV. \qquad (4.2)$$

Equation 4.2 can be integrated on a numerical grid. In this work, the numerical grid is composed of equally sized cubic cells. A sketch of the setup of a representative cell and its neighbors is given in Fig. 4.1 exemplarily in 2D.

The equations are solved for each of the finite volume cells. The computed value of a quantity is hence volume-averaged over the cell volume, and this averaged value is equal to the value at the cell center. The task of the discretization methods is to approximate derivatives and cell face values of the terms of the transport/conservation equations.
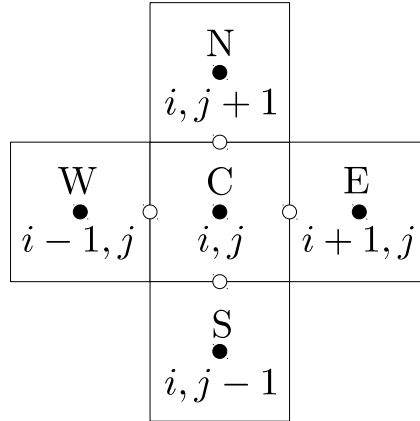
Figure 4.1: Sketch of the setup of a cell and its neighbors in 2D.

4.1.1   Discretization of Volume Integrals

The computation of source terms and the accumulation term requires the evaluation of an integral over the cell volume. Generally, computed cell values of ϕ are assumed to be equal to the value at the cell center. Hence, volume integrals are simply computed as (here at the example of the source term in Eq. 4.1 for cell C):

$$\int_{\Delta V} \rho \dot{S}_\phi dV = \rho_C \dot{S}_{\phi,C} \Delta^3. \tag{4.3}$$

4.1.2   Discretization of the Convective Fluxes

The convective flux is described as an integral over a cell's surfaces. Using cubic cells, this integral can hence be approximated by a sum over all six cell faces, which can be written as:

$$\int_{\Delta A} \rho \phi u_j n_j dA \approx \sum_f \rho_f \phi_f u_f n_f \Delta A_f. \tag{4.4}$$

The main task of the discretization schemes is to give an approximation to the cell face value of $\rho_f \phi_f$. There are different methods to choose from and commonly there has to be a trade-off between accuracy, stability and cost. The different methods used in this work are presented in the following discussion.

Central Differencing Scheme

The central differencing scheme approximates cell face values from cell center values of neighboring cells, such that:

$$\phi_{i+1/2,j,k} = \frac{1}{2} \left(\phi_{i+1,j,k} + \phi_{i,j,k} \right), \tag{4.5}$$

for the eastern face of cell i,j,k. The central differencing scheme is used to compute convective fluxes of momentum. The scheme is of second order but prone to oscillations

if the fields are not smooth enough. This requires scalars in the large eddy simulation (LES) to be treated with a different scheme that ensures that no oscillations evolve. In the direct numerical simulation (DNS), as the fields are well resolved, the central differencing scheme (CDS) is used for convective fluxes of all scalars. In the LES, treating momentum fluxes with the central differencing scheme is appropriate since the pressure solver is able to remove oscillations.

Total Variation Diminishing Scheme

The total variation diminishing (TVD) scheme ensures that no oscillations evolve. It is used for convective fluxes of scalars in the LES. The TVD scheme blends CDS and the upwind differencing scheme (UDS) such that the accurate CDS is used where possible (i.e., where the solution is smooth enough) to maintain accuracy and the UDS where required to ensure a bounded non-oscillating solution. The TVD flux is computed as:

$$\phi_{i+1/2,j,k} = \phi_{i+u,j,k} + \frac{1}{2}B(r)\left(\phi_{i+u,j,k} - \phi_{i+uu,j,k}\right). \tag{4.6}$$

The function $B(r)$ is called the flux limiter function that requires the input of r:

$$r = \frac{\phi_{i+d,j,k} - \phi_{i+u,j,k}}{\phi_{i+u,j,k} - \phi_{i+uu,j,k}}. \tag{4.7}$$

In the above equations u and uu indicate the two upstream cell centers (uu indicating the farther upstream cell), and d indicates the downstream cell center. If the velocity on the cell face is positive, u takes the value of 0, uu of -1 and d of 1. If the velocity on the cell face is negative, u takes the value of 1, uu of 2 and d of 0. The so-called CHARM limiter [269] has been applied in this work, based on earlier investigations of different limiter functions [95, 220].

4.1.3   Discretization of the Diffusive Fluxes

The computation of diffusive fluxes requires the approximation of derivatives on the cell faces. In this work, all diffusive fluxes are treated by a central differencing scheme. First, the diffusive flux is written as a sum of the fluxes over all faces:

$$\int_{\Delta A} \left(\rho D_\phi \frac{\partial \phi}{\partial x_j}\right) n_j dA = \sum_f \left[\rho D_\phi \frac{\partial \phi}{\partial x_j}\right]_f n_f \Delta A_f. \tag{4.8}$$

The expression within brackets containing the derivative then needs to be approximated at the cell face:

$$\left[\rho D_\phi \frac{\partial \phi}{\partial x_j}\right]_{i+1/2,j,k} \approx \frac{1}{2}([\rho D_\phi]_{i+1,j,k} + [\rho D_\phi]_{i,j,k})\frac{\phi_{i+1,j,k} - \phi_{i,j,k}}{\Delta}. \tag{4.9}$$

4.1.4 Pressure Correction

As outlined in Chapter 2, the governing equations solved in this work are based on a low-Mach approximation (see [125]). This means that density and pressure are treated in a decoupled manner (see [28] for incompressible flows). All computations involving pressure assume a constant specified thermodynamic *background* pressure, which in all investigations reported in this work is equal to the atmospheric pressure. The only exception to this is the pressure gradient term in the momentum equations, which represents the gradient of the dynamic pressure. In the low-Mach context, this pressure gradient term can be understood as the pressure gradient required for the velocities to satisfy continuity [45] and has to be obtained to accurately solve the momentum equations.

An equation for the pressure and hence for the pressure gradient can be obtained by discretizing the momentum conservation equations to solve for a predicted momentum field first. This predicted momentum contains the yet unknown pressure gradient term. Substituting the difference of predicted momentum and pressure gradient term (i.e., the corrected momentum at the new time step) into the continuity equation allows to write an equation of Poisson type for the pressure [95, 220]. This equation can then be solved by iterative methods, for example, such as the Gauß-Seidel method with successive over-relaxation used in this work.

Defining momentum and pressure in a collocated fashion, and computing pressure gradients at cell centers gives rise to a velocity-pressure decoupling and *checkerboarding* [155]. This is alleviated by applying the momentum interpolation method by Rhie & Chow [196], such that the pressure gradient is computed on the cell faces to correct the cell face-based velocities that enter the flux computation in the discretized momentum equations. More information on the pressure correction algorithm can be found in the work by Proch [185].

4.1.5 Time Discretization

The time-advancement of the flow fields is done exclusively by a Runge-Kutta scheme of third order in a low-storage implementation in this work. However, operator splitting is employed in some parts of this work (Chapter 8) such that chemical source terms are integrated in time using a different scheme. The time integration of the flow solver and chemistry solvers is described in the following.

Runge-Kutta Scheme for Time-Advancement

The Runge-Kutta scheme is based on consecutive explicit Euler steps. To describe an explicit Euler step, Eq. 4.2, is re-arranged such that everything except the accumulation term is on the RHS of the equation:

$$\int_{\Delta V} \frac{\partial \rho \phi}{\partial t} dV = \text{RHS}^*(\rho \phi). \tag{4.10}$$

With the volume integral approximation discussed above and including Δ^3 into RHS* to give RHS, this yields:

$$\frac{\partial \rho \phi}{\partial t} = \text{RHS}(\rho \phi). \tag{4.11}$$

Using the explicit Euler integration, Eq. 4.11, the value of $\rho\phi$ at the new time step $[\rho\phi]^{n+1}$ can be computed from the old time step $[\rho\phi]^n$ by:

$$[\rho\phi]^{n+1} \approx [\rho\phi]^n + \Delta_t \text{RHS}([\rho\phi]^n). \tag{4.12}$$

This approximation is only of first order and not suitable for LES let alone DNS. The Runge-Kutta scheme combines explicit Euler steps to yield higher-order time integration. A third-order scheme is applied, which combines three explicit Euler steps in a low-storage fashion [261], meaning that not all sub-steps have to be stored in the memory. The three consecutive steps (the three sub-step levels indicated by the subscripts a,b and c) are:

$$
\begin{aligned}
[\rho\phi]_a^n &= [\rho\phi]^n + \Delta_t \left[\alpha_a \text{RHS}([\rho\phi]^n) \right] \\
[\rho\phi]_b^n &= [\rho\phi]_a^n + \Delta_t \left[\alpha_b \text{RHS}([\rho\phi]_a^n) + \beta_b \text{RHS}([\rho\phi]^n) \right] \\
[\rho\phi]^{n+1} &= [\rho\phi]_b^n + \Delta_t \left[\alpha_c \text{RHS}([\rho\phi]_b^n) + \beta_c \left[\text{RHS}([\rho\phi]_a^n) + \frac{\beta_b}{\alpha_b} \text{RHS}([\rho\phi]^n) \right] \right]
\end{aligned}
\tag{4.13}
$$

The coefficients can, for example, be found in the work by Kempf [95].

Implicit and Semi-Implicit Schemes for Combustion Chemistry

The system of ordinary differential equations (ODE) describing chemistry usually involves stiffness. Hence, integrating the system in time with the same method as the flow solver would often require time steps much smaller than that of the flow solver, especially in the context of low-Mach flows dealt with in this work. Implicit or semi-implicit methods can relax the time step restriction and in combination with operator splitting permit to solve flow and chemistry at a large time step (governed by the Courant–Friedrichs–Lewy (CFL) criterion of the flow).

The implicit method used in this work is the method by Hindmarsh et al. based on a backward differentiation formula [74]. The equations describing the chemical system can be written as:

$$\dot{Y}_\alpha = \dot{\omega}_\alpha(Y_\gamma, H) = RHS(Y_\gamma, H), \text{ with } \gamma \in [1, .., N_s]. \tag{4.14}$$

Applying the backward difference to this system yields a non-linear algebraic system that is solved using the Newton–Raphson method.

For smaller time steps, the full implicit method might incur an unnecessary penalty on the computational cost. To reduce this, a semi-implicit method can be used. In this work, the point implicit ODE solver [90, 266] has been applied. This solver decomposes the RHS of Eq. 4.14 into a production, P_α, and destruction part, D_α, such that:

$$\dot{Y}_\alpha = P_\alpha - D_\alpha. \tag{4.15}$$

This equation can be discretized based on the explicit Euler scheme with an additional introduction of implicity by multiplying D_α by the ratio of $Y_\alpha^{n+1}/Y_\alpha^n$ [117]:

$$Y_\alpha^{n+1} - Y_\alpha^n = \Delta_t \left(P_\alpha^n - D_\alpha^n \frac{Y_\alpha^{n+1}}{Y_\alpha^n} \right). \tag{4.16}$$

Re-arranging this to give the new mass fraction Y_α^{n+1} yields:

$$Y_\alpha^{n+1} = \frac{Y_\alpha^n + \Delta_t P_\alpha^n}{1 + \frac{\Delta_t D_\alpha^n}{Y_\alpha^n}}. \tag{4.17}$$

The new mass fraction at $n+1$ can then be solved iteratively, solving from one iteration step m to the next $m+1$ by (starting from $Y_\alpha^{n,m} = Y_\alpha^n$ for $m = 1$):

$$Y_\alpha^{n,m+1} = \frac{Y_\alpha^n + \Delta_t P_\alpha^{n,m}}{1 + \frac{\Delta_t D_\alpha^{n,m}}{Y_\alpha^{n,m}}}. \tag{4.18}$$

This is done until the change from m to $m+1$ is smaller than a specified tolerance, which here is the same as in the work by Yang et al. [267]. The new mass fractions Y_α^{n+1} are then the mass fractions of the last iteration, i.e., $Y_\alpha^{n+1} = Y_\alpha^{n,m=\text{last}}$. This scheme proved to work well if overall small time steps are employed (i.e., $\approx 0.1\mu$s), such as in the direct numerical simulation presented in Chapter 8.

4.2   Numerical Treatment of Lagrangian Particles

4.2.1   Time Advancement

The numerical solution of the equations describing the evolution of the Lagrangian particles is done consistently with that of the Eulerian quantities. The stochastic differential equations (SDEs) describing the evolution of the particle position in the context of the transported FDF method, or the particle velocity in the context of solid particles in LES are solved by the Euler-Maruyama approximation [105]. This first-order approximation is embedded into the Runge-Kutta scheme. For the position of a transported FDF particle this yields:

$$x_i^+(t^{n+1}) = x_i^+(t^n) + \left[\tilde{u}_i^+ + \left[\frac{\partial}{\partial x_i}(\tilde{D} + D_t) \right]^+ \right] \Delta t + \sqrt{2(\tilde{D} + D_t)}^+ \sqrt{\Delta t}\, \xi_i, \tag{4.19}$$

where $^+$ indicates that the quantity is either a particle quantity (in case of x_i^+), or a quantity interpolated onto the particle position (in case of the other quantities) and ξ_i is the three-dimensional Gaussian distributed random variable with zero mean and unity variance. The latter is obtained by the Box-Muller transformation [105] using uniformly distributed random variables. Equivalently, the equation describing the change of velocity of a solid particle is described by:

$$d\mathbf{u}_p(t^{n+1}) = d\mathbf{u}_p(t^n) + \frac{\tilde{\mathbf{u}} - \mathbf{u}_p}{\tau_p}\Delta t + \left(1 - \frac{\bar{\rho}}{\rho_p}\right)\mathbf{g}\Delta t + \underbrace{\sqrt{C_0 \frac{k_{sgs}}{\tau_t}}\sqrt{\Delta t}\, \xi_i}_{=0 \text{ for CP-DNS}}. \tag{4.20}$$

Particles are not considered for determining the numerical time step width. However, instabilities may occur if τ_p drops below Δt. In the simulations performed in this work,

this occurs only very occasionally. Hence, τ_p is simply limited to Δt such that particles are not allowed to adjust their velocity to the gas phase within less than one time step, preventing particles to over-shoot. Another possibility is to treat particles as tracers, i.e., neglecting inertial forces and setting their velocity to that of the gas phase. However, this would result in an undefined subgrid dispersion term and thus, is undesirable.

The equation describing the temperature evolution (described in detail in Chapter 5) of a solid particle is solved in a similar fashion but without stochastic term (as ordinary differential equation). All terms appearing in this equation are discretized in an explicit fashion except for the convective heating term. As the associated time scale may be below the numerical time step width dictated by the Eulerian solver, an implicit scheme is adopted based on the assumption that the gas phase is 'frozen' during the particle temperature increment.

4.2.2   Interpolation in the Solid Particle Context

A key element in combined Eulerian-Lagrangian methods is the interpolation between Lagrangian and Eulerian phase, and *vice versa*. This is accomplished by a linear interpolation or linear projection scheme that takes into account the cell centers of the particle's eight nearest neighbors (e.g., [39]). To perform the interpolation either from particle to grid, or from grid to particle, weights for the cell center contributions have to be found. This first requires finding the cell centers within which the particle is located, in all three Cartesian directions. Then, the distance to one of the cell centers in each direction is computed, from which the weights can be obtained. For the direction in x, this can be written as $w(i^-) = (x_c^+ - x_p)/\Delta$, where $w(i^-)$ is the weight for the contribution to/from the next closest cell center in negative x direction, x_c^-; and x_c^+ is the distance to the next closest cell center in positive x direction. The weight for latter can then be computed simply by $w(i^+) = 1 - w(i^-)$. The other directions are treated equivalently, resulting in the weights $w(j^-)$, $w(j^+)$, $w(k^-)$ and $w(k^+)$, respectively. The 3D interpolation from grid to particle can then, for example, be written as:

$$\phi_p = \sum_{i \in [i^-, i^+]} \sum_{j \in [j^-, j^+]} \sum_{k \in [k^-, k^+]} w(i)w(j)w(k)\phi(i, j, k). \tag{4.21}$$

Equivalently, a particle's contribution to the neighboring cells can be written as:

$$\phi(i^-, j^-, k^-) = w(i^-)w(j^-)w(k^-)\phi_p, \tag{4.22}$$
$$\phi(i^-, j^-, k^+) = w(i^-)w(j^-)w(k^+)\phi_p, \tag{4.23}$$
$$\phi(i^-, j^+, k^-) = w(i^-)w(j^+)w(k^-)\phi_p, \tag{4.24}$$
$$\phi(i^-, j^+, k^+) = w(i^-)w(j^+)w(k^+)\phi_p, \tag{4.25}$$
$$\phi(i^+, j^-, k^-) = w(i^+)w(j^-)w(k^-)\phi_p, \tag{4.26}$$
$$\phi(i^+, j^-, k^+) = w(i^+)w(j^-)w(k^+)\phi_p, \tag{4.27}$$
$$\phi(i^+, j^+, k^-) = w(i^+)w(j^+)w(k^-)\phi_p, \tag{4.28}$$
$$\phi(i^+, j^+, k^+) = w(i^+)w(j^+)w(k^+)\phi_p. \tag{4.29}$$

A special case is the interpolation close to immersed boundaries. Particles are assumed to not directly interact with the walls, such that the interpolation near walls only considers
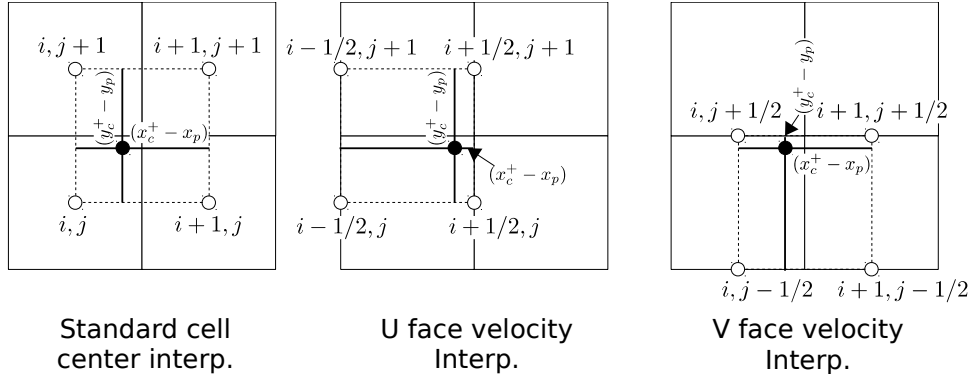
Figure 4.2: Sketch of the different types of interpolation (from cell centers/cell faces).

fluid cells but not immersed boundary cells. This is achieved by modifying the particle weights by a factor f, which is obtained as:

$$f^{-1} = \sum_{i \in [i^-, i^+]} \sum_{j \in [j^-, j^+]} \sum_{k \in [k^-, k^+]} w(i)w(j)w(k)I_{IB}(i, j, k), \qquad (4.30)$$

where $I_{IB}(i, j, k)$ is the immersed boundary indicator. This indicator is 1 in fluid cells and 0 in immersed boundary cells. This factor ensures that the weights are properly re-normalized when cells are taken out of the interpolation. The interpolation accounting for the immersed boundaries is:

$$\phi_p = \sum_{i \in [i^-, i^+]} \sum_{j \in [j^-, j^+]} \sum_{k \in [k^-, k^+]} f \cdot w(i)w(j)w(k)\phi(i, j, k)I_{IB}(i, j, k). \qquad (4.31)$$

The interpolation from a particle to the neighboring cells is treated correspondingly (RHS of Eqs. 4.22 is multiplied with f and $I_{IB}(i, j, k)$). The interpolation is sketched in 2D in Fig. 4.2 (left).

4.2.3   Interpolation in the Transported FDF Context

The interpolation procedure in the preceding section is modified in the transported FDF context. Here, in addition to the interpolation of cell center values, diffusivity gradients and velocities from the cell faces need to be interpolated onto the particles. This is accommodated by modifying the interpolation procedure such that the nearest cell faces are found in the three Cartesian directions and the weights are based on the distances to the cell faces. This requires the computation of weights and the interpolation for each of the three velocity components individually. For example, in the direction of x for velocity u only cell faces in x need to be considered whereas cell centered values are taken for the other directions. This is illustrated in 2D in Fig. 4.2 at the example of u and v velocities. Compared to the cell centered interpolation, the interpolation kernel is shifted by $\Delta/2$ in x and y direction for u and v, respectively. The interpolation of cell face values is necessary because in the transported FDF method the interpolation of velocities has a different significance than for solid particles due to the density feedback. Hence, in the transported FDF method pseudo-staggering has to be considered appropriately.

4.2.4   Pressure Correction in the Transported FDF Method

The density treatment in the transported FDF method follows that of Popov et al. [182, 183] using an additional specific volume transport equation, as described in more detail in Chapter 9. The density coupling has to consistently be included in the pressure correction scheme of the low-Mach flow solver. This is achieved by the following scheme, which is performed during every Runge-Kutta sub-step (unless otherwise stated). Operations on particle fields are denoted by 'P' and operations on Eulerian fields by 'E', where applicable.

I **Predictor**

  1) E: Advance scalar transported quantities, including specific volume and density

  2) P: Seed new particles, only during first Runge-Kutta sub-step

  3) P: Split and merge particles as necessary

  4) P: Mixing

  5) P: Reaction

  6) P: Particle movement

  7) P: Map specific volume source term onto predicted Eulerian transported specific volume

  8) P: Map laminar viscosities and diffusivities onto Eulerian grid

  9) P: Reset particle positions and velocities

II **Poisson solver**

  1) Use the reciprocal value of the transported specific volume and the transported density from the predictor step to construct the density time-derivative and solve the Poisson equation

III **Corrector**

  1) P: Move particles with corrected velocities

  2) P: Map specific volume source term onto Eulerian transported specific volume

  3) P: Map laminar viscosities and diffusivities onto Eulerian grid

  4) E: Advance all transported quantities using corrected velocities

4.3   Special Numerical Treatment

4.3.1   Initialization of Furnace Simulations

The initialization of furnace simulations such as the ones presented in Chapters 5 and 6 requires significant computational effort due to the flow establishing slowly, especially in regions like the domain corners. To reduce the cost of establishing a statistically

stationary flow, a grid interpolation strategy has been applied such that the large scale features of the flow could be established in a coarse simulation that is then mapped onto the finer grid. Without such a treatment, the computational effort to perform a simulation like shown in Chapter 6 would be prohibitive. In addition to mapping from a coarse to fine grid, a parcel splitting strategy was used such that the coarse initialization run could be performed with fewer computational particles. Particle splitting is described in the next sub-section.

4.3.2   Particle Number Density Control

Stochastic Lagrangian solution methods usually require methods to control the statistical error (which scales as $N_p^{-1/2}$, where N_p is the number of particles). If the particle number density drops below a certain prescribed value, computational particles are split. In the transported FDF method this is done by taking the 'heaviest' (based on particle weight) particle, halving its weight and cloning it such that instead of one particle, two exist with the same properties but half of the original weight. This procedure is repeated until the particle number density reaches a satisfactory level.

In order to improve load balancing, a particle merging algorithm is applied. This algorithm takes the 'lightest' two particles and merges them together by deleting the 'lightest' one and assigning the weighted average properties of the two particles to the second lightest particle (except for the weight, which is summed up). Since merging affects the statistics (i.e., artificially reduces the subgrid variance), it is not applied frequently.

While especially splitting needs to be done frequently in the transported FDF method, it is only applied in the solid fuel simulations when simulation results are mapped onto a finer grid.

Chapter 5

Flamelet LES of a Semi-Industrial Pulverized Coal Furnace [202]

This chapter including all text, figures and tables is published in Combustion and Flame 'Rieth, M., Proch, F., Rabaçal, M., Franchetti, B. M., Cavallo Marincola, F. , Kempf, A.M. (2016). Flamelet LES of a semi-industrial pulverized coal furnace. Combustion and Flame, 173, 39-56.' [202] and is reprinted with permission from Elsevier. The author of this thesis contributed the code extension and development (including the incorporation of the combustion model and the devolatilization model and updates/optimization of other coal models), running of simulations, post-processing and paper writing. The authors M. Rabaçal, B.M. Franchetti & F. Cavallo Marincola contributed previous code development for coal combustion and radiation, and discussions. The author F. Proch contributed the basic CFD code. The author A.M. Kempf contributed discussions, proof-reading, corrections, and developed the original version of the PsiPhi code.

Abstract

The goal of this work is to introduce the flamelet model into large eddy simulation (LES) of realistic coal furnaces. A flamelet table based on two mixture fractions (for volatile and char-off gases) and enthalpy is generated and used in a massively parallel LES of the semi-industrial IFRF coal furnace [250, 251] for which comprehensive experimental data is available enabling the validation of the flamelet model under realistic conditions. Comparison between experiment and simulation is shown by means of averaged quantities of velocities, species concentrations and temperature. Overall good agreement between experiment and simulation could be obtained, giving evidence for the suitability of the flamelet model. The results of the LES are further analyzed, focussing on instantaneous particle and gas phase data to gain additional insight into the coal conversion process inside the furnace.

5.1   Introduction

Pulverized coal combustion (PCC) is currently among the major sources of energy supply and is expected to play an important role in the future due to coal being the most abundant fossil fuel. However, its combustion releases large amounts of carbon dioxide due to the high carbon content of the coal. Efforts being made to reduce the emissions of PCC, e.g. carbon capture and storage with oxy-coal combustion or co-firing coal with biomass, go along with penalties in power plant efficiency. This requires the combustion to be as efficient as possible and a highly optimized combustor design, supported by a comprehensive set of experimental and numerical data. However, comprehensive experimental studies of full scale combustors are infeasible. Even laboratory scale experiments suffer from some gas flame diagnostics being infeasible in PCC, e.g. due to scattering of laser light at coal particles and soot. Simulations promise to provide additional data which cannot be obtained from experiments, giving further insight into the physics of PCC. Large eddy simulation (LES), a technique successfully applied to gaseous flames, is a very promising approach for the simulation of PCC as the effect of unclosed terms is small compared to Reynolds-averaged Navier-Stokes simulations (RANS). However, further research effort is still needed, particularly on the description of the gas phase, on which this work concentrates by introducing tabulated flamelet chemistry into realistic LES of PCC.

Large eddy simulation of PCC has emerged around a decade ago with a study of a hypothetical solid fuel flame by Kurose and Makino [114]. This study employed a conserved scalar approach with an idealized single-step reaction. Subgrid turbulence-chemistry interaction was modeled by a β-pdf for the species mass fractions, with the variance calculated with an algebraic model. Successive LES studies of coal flames have been mainly employing the eddy break-up model (EBU) or the eddy dissipation concept (EDC) to describe the gas phase [26, 30, 43, 53, 57, 153, 189, 221, 245]. These studies considered two or three reactions, of which one describes the conversion of volatiles to CO and H_2 or H_2O, and another the conversion of CO to CO_2. A third reaction is used to describe the conversion of a pilot gas such as CH_4 [53] or an intermediate species such as H_2 [26]. The volatile gas is treated as a postulate substance in these studies, since the exact composition of the volatile gases is unknown, and since a postulate substance can easily be used in the EBU/EDC framework.

Different to the commonly employed EBU or EDC description are the studies by Yamamoto et al. [264], Pedel et al. [156, 157] and Muto et al. [140], where a relaxation model towards equilibrium, a mixture fraction based equilibrium approach and the scale similarity filtered reaction rate model is used, respectively. Yamamoto et al. argued that in their particular ignition experiment pyrolysis is more important than gaseous combustion to predict the flame.

Only recently, Watanabe & Yamamoto [248] introduced the flamelet model with volatile and char-off gases for the simulation of PCC. A two-dimensional jet was studied with direct numerical simulation and the flamelet model was compared to finite rate chemistry. Despite having been only tested on a very simplified case, the flamelet model promises significant improvement of the description of the gas phase when applied to the LES of real PCC configurations. Previously, Williams et al. [257] reported the use of the

flamelet model for volatile combustion and recently, Vascellari et al. [238] and Xu et al. [263] investigated flamelet approaches for resolved single coal particle simulations. They obtained very good agreement between finite rate chemistry and flamelet approaches.

The flamelet model, mainly developed by Peters [162], has been applied in the LES of gaseous flames with great success, as illustrated by the reviews by Pitsch [174] and Janicka & Sadiki [85]. The flamelet model assumes the chemical time scales to be small compared to the turbulent time scales, such that reactions occur only in thin layers embedded in the turbulent flow field [162]. These thin layers maintain their structure in the turbulent flow field and can be described one-dimensionally as a function of mixture fraction. The interaction between the turbulent flow field and the flamelet structure is described by the scalar dissipation rate, which acts as a diffusion coefficient in the flamelet equations.

This study applies the flamelet model to the LES of PCC in a semi-industrial coal furnace experiment by Weber et al. [250, 251], which is a test case that features a good compromise between realistic PCC conditions and comprehensive experimental measurements to validate the approach. The furnace has only recently been studied by means of LES by Olenik et al. [153], who employed the EBU model to describe the gas phase reactions. Flamelet solutions for the reaction of the three streams of oxidizer, pyrolysis gases and char-off gases are tabulated and additionally parameterized by enthalpy and the variance of the sum of the mixture fractions. To our knowledge, this is the first LES of PCC employing the flamelet model.

The remainder of this work is structured as follows. A description of the solid phase, coal and radiation modeling is given in the next sections, which is followed by the description of the combustion modeling approach employing the flamelet model. This is followed by the description of the numerical method and an outline of the experiment. Finally, results from the computations conducted will be presented and the work concluded in the summary.

5.2   Coal Particle and Radiation Modeling

Coal particles are treated in a Lagrangian manner following the laws of motion for dispersed flow and the fundamental processes of heat exchange with their surroundings. However, specific models are required to describe the processes coal undergoes as it is being converted in a combustion system. The conversion of coal is mainly governed by the two steps of devolatilization and char combustion, where first matter bound in the coal volatilizes and combusts in the gas phase. In the second step, the remaining porous char structure further combusts with oxygen diffusing into the pores and oxidizing the carbon left in the coal. Both processes are of fundamental importance for the gas phase combustion model since they provide the source terms in the equations governing the gaseous phase.

5.2.1   Particle Motion

The coal particles are treated in a Lagrangian manner, their motion being described by the balance of the particle's inertial forces with the forces acting on it. Similar to previous

LES studies of PCC or particle-laden flows [149, 221], simplifications are made regarding the forces acting on the particles. This leaves only drag, gravity and buoyancy forces and a force representing the influence of the unresolved flow scales acting on the particle in Eq. 5.1:

$$d\mathbf{u}_p = \frac{\tilde{\mathbf{u}} - \mathbf{u}_p}{\tau_p}dt + \left(1 - \frac{\bar{\rho}}{\rho_p}\right)\mathbf{g}dt + \sqrt{C_0\frac{k_{sgs}}{\tau_t}}d\mathbf{W}. \tag{5.1}$$

In this equation, $\mathbf{u}_p$ is the particle velocity vector, $\tilde{\mathbf{u}}$ the filtered Eulerian phase velocity vector at the particle location, τ_p the particle relaxation time, $\bar{\rho}$ the filtered Eulerian phase density at the particle location, ρ_p the density of the particle, $\mathbf{g}$ the gravitational acceleration, C_0 a model constant, k_{sgs} the subgrid kinetic energy of the Eulerian flow field, τ_t the particle-turbulence interaction time scale and $\mathbf{W}$ a Wiener vector process. The particle relaxation time τ_p represents the time scale on which the particle is able to adjust to the flow field, as modeled by Eq. 5.2 depending on the particle Reynolds number $\mathrm{Re}_p = \bar{\rho}|\tilde{\mathbf{u}} - \mathbf{u}_p|D_p/\mu$, with μ being the dynamic viscosity of the gas phase and D_p being the particle diameter.

The calculation of τ_p is based on the analytical solution for Stokes flow, $\tau_{p,\mathrm{St}}$ (derived for Re_p approaching zero). The Schiller-Naumann correlation [31, 209] is used for the drag coefficient, incorporated in the calculation of τ_p. The correlation is valid up to $\mathrm{Re}_p = 1000$, which is sufficient in this case.

$$\begin{aligned}
\tau_p &= \frac{\tau_{p,\mathrm{St}}}{f_1} \\
\tau_{p,St} &= \frac{\rho_p D_p^2}{18\mu} \\
f_1 &= 1 + 0.15\mathrm{Re}_p^{0.687}, \quad \mathrm{Re}_p \leq 1000
\end{aligned} \tag{5.2}$$

The last term in Eq. 5.1 represents the force due to the interaction of subgrid motion and particle, modeled as a Wiener process [12]. The subgrid kinetic energy is estimated following Bini & Jones [12], Eq. 5.3, with the turbulent kinematic viscosity ν_{sgs}, the filtered strain rate tensor $\tilde{S}_{i,j}$, the Smagorinsky model constant C_S and the cell width Δ.

$$k_{\mathrm{sgs}} = (2\Delta\nu_{\mathrm{sgs}}\tilde{S}_{ij}\tilde{S}_{ij})^{2/3} = \left(\frac{\nu_{\mathrm{sgs}}}{C_S^{4/3}\Delta}\right)^2 \tag{5.3}$$

The particle-turbulence interaction time scale, used in Eq. 5.1, is calculated by Eq. 5.4 [12] with $\alpha = 0.8$ [88]. The modeling constant C_0 is set to unity [12].

$$\tau_t = \frac{\tau_p^{2\alpha}}{(\Delta/\sqrt{k_{\mathrm{sgs}}})^{2\alpha-1}} \tag{5.4}$$

The particle position $\mathbf{x_p}$ evolves according to $d\mathbf{x_p} = \mathbf{u}_p dt$.

5.2.2 Coal Composition and Volatile Gas Properties

As the coal particle is heated up, matter bound in the coal breaks down and is released as volatile gas [217]. The process of devolatilization is complex and involves processes

Table 5.1: Properties of the Saar hvBb coal fired in the experiment [250].

Ultimate Analysis (daf)	
C	79.3%
H	4.7%
N	1.3%
S	1.0%
O	13.7%
LHV	32.32 MJ/kg [161]
Proximate Analysis	
ash	8.3%
volatiles	37%
fixed carbon	52.5%
moisture	2%

of cracking of labile bonds inside the coal structure, formation and re-attachment of metaplast and vaporization of light gases and tars. The products of devolatilization are light gases, tars and the char remaining in the coal particle. The exact composition of the gases released during devolatilization is unknown, but can be modeled under mass balance considerations using the data from proximate and ultimate analysis and assuming that the coal is pure carbon and ash after devolatilization. The ultimate and proximate analysis of the Saar hvBb coal fired in the experiment is given in table 5.1 [250]. In the computation, coal is solely composed of volatile matter (VM), fixed carbon (FC) and ash. The low moisture content of 2% and sulphur content of 1% was neglected. The yield of volatile gases is usually higher than the amount of volatiles obtained by proximate analysis under rapid heating conditions, reflected in a higher initial amount of volatile matter of the particles in the computation, $m_{\mathrm{VM,0}} = m_{\mathrm{VM,0}}^{\mathrm{prox}} \cdot Q$ [217]. Devolatilization measurements for the Saar hvBb coal are given by Weber et al. [250] and Knill et al. [107]. The experimentally obtained high temperature volatile yield amounts to 0.646 on a daf basis. The same value is used here with a resulting Q-factor of approximately 1.6.

Similar to the approach taken by Stöllinger et al. [223], we used the formulas presented by Petersen & Werther [167] to obtain the volatile composition. First, the remaining carbon resulting from the high temperature volatile yield is removed from the ultimate analysis, which provides the atomic composition of the volatile gases. This atomic composition is distributed among species by specifying three splitting factors while ensuring that the atomic composition is preserved. The splitting factors were set to: $\xi_{\mathrm{CO}} = 1.0$, $\xi_{\mathrm{C_2H_4}} = 0.23$ and $\xi_{\mathrm{tar}} = 0.05$ corresponding to high CO instead of CO_2 and low tar yield. The splitting factors cannot be chosen independently, but have to be chosen under the constraint to result in positive mass fractions. The resulting volatile composition is (in mass fractions): $Y_{\mathrm{CH_4}} = 0.005472$, $Y_{\mathrm{C_6H_6}} = 0.224332$, $Y_{\mathrm{C_2H_4}} = 0.370435$, $Y_{\mathrm{CO}} = 0.376965$, $Y_{\mathrm{H_2}} = 0.002356$ and $Y_{\mathrm{N_2}} = 0.020440$. Currently, we do not include tars in the modeled gas but replace it by C_2H_2, which has the same C/H-ratio as benzene (C_6H_6). Although elemental mass fractions are represented correctly by the modeled volatile gas composition, the lower heating value may deviate from the experimental value with this approach.

The heating value of the modeled volatile gas and the fixed carbon weighted by the respective mass fractions on dry-ash-free (daf) basis needs to match the experimental coal heating value of 32.32 MJ/kg given by Peters & Weber [161]. In the present case, the heating value of the modeled coal is 32.70 MJ/kg, which is sufficiently close to the value of 32.32 MJ/kg.

5.2.3 Particle Mass and Size Balance

The particles are represented as parcels due to the large amount of several billions of coal particles in the furnace. Particle properties are the same within each parcel. The diameter of the particles inside a parcel injected at the inlet is obtained randomly from the experimental weight-based cumulative size distribution CDF [250]. A uniform random variable with values between 0 and 1 is used to obtain the initial diameter of the particles inside the parcel from the experimental CDF. The number of particles per parcel is obtained such that each parcel contains the same mass, which results in the correct particle diameter CDF at the inlet. In the present simulation, each parcel contains particles with a total initial mass (sum of all particle masses in the parcel) of approximately 10^{-8} kg leading to a variable number of particles within each parcel depending on the randomly obtained diameter. All particles have a density of 1000 kg/m^3, which corresponds to the value used by Weber et al. [250]. The mass balance of the coal particle after injection is governed by Eq. 5.5.

$$dm_p = -(\dot{m}_{\mathrm{char}} + \dot{m}_{\mathrm{devol}})dt \qquad (5.5)$$

In Eq. 5.5, m_p is the coal particle mass and $\dot{m}_{\mathrm{char}}$ and $\dot{m}_{\mathrm{devol}}$ the mass flow rates of char combustion and devolatilization, respectively. The equations to obtain these mass flows are given in the next sections.

The composition of the numerical parcels at the inlet of the furnace is: $Y_{p,\mathrm{FC},0} = 0.325$, $Y_{p,\mathrm{VM},0} = 0.592$ and $Y_{p,\mathrm{ash},0} = 0.083$, where $Y_{p,\mathrm{FC},0}$, $Y_{p,\mathrm{VM},0}$ and $Y_{p,\mathrm{ash},0}$ are the initial mass fractions of fixed carbon, volatile matter and ash in the coal, respectively. This is obtained from the proximate analysis considering the high heating volatile yield and neglecting sulphur and moisture.

Initially, the density is decreasing due to devolatilization, which is assumed to not change the particle diameter. Conversely, the coal particle density remains unchanged during char combustion while the coal particle is shrinking and its diameter decreases. Devolatilization reduces the mass of volatile matter, char combustion the mass of fixed carbon. The mass of ash contained in a coal particle does not change throughout the computation.

5.2.4 Devolatilization

The rate of devolatilization can be obtained by detailed phenomenological network models, such as CPD developed by Grant et al. [64], FGDVC developed by Solomon et al. [218] or FLASHCHAIN developed by Niksa & Kerstein [146]. However, these approaches might be too expensive in LES, hence simpler models are usually used. The method we chose to represent the devolatilization is known as the Kobayashi model [108]. This

Table 5.2: Parameters used for the Kobayashi model.

A_1	A_2	E_1	E_2	α_1	α_2
s^{-1}	s^{-1}	J/kmol	J/kmol		
$3.7 \cdot 10^4$	$1.46 \cdot 10^{12}$	$5.16 \cdot 10^7$	$3.07 \cdot 10^8$	0.39	0.8

model splits up the rate of devolatilization into two Arrhenius type expressions. The temperature dependent mass flow of volatile gases can be calculated as follows, Eq. 5.6.

$$\dot{m}_{\text{devol}} = k_{\text{devol}}(m_{\text{VM},0} - m_{\text{VM}}) \tag{5.6}$$

$$k_{\text{devol}} = \alpha_1 A_1 e^{-E_1/RT_p} + \alpha_2 A_2 e^{-E_2/RT_p} \tag{5.7}$$

The mass flow due to devolatilization $\dot{m}_{\text{devol}}$ is expressed as the devolatilization rate k_{devol} multiplied with the difference between volatile yield after an infinite amount of time $m_{\text{VM},0}$ (or the initially available volatile matter in the computational particle) and current volatile yield m_{VM}. This difference corresponds to the remaining volatile matter left in the coal. It is assumed that the mass loss from devolatilization does not alter the size of the particle but only its density. [108]. The pre-exponential constants A_1 and A_2 and activation energies E_1 and E_2 are fitted to the experimental pyrolysis characteristics of this coal (Saar hvBb, Göttelborn) obtained by Knill et al. [107]. The constants used are summarized in table 5.2 and the fitting procedure outlined in 5.8. The volatile gases that leave the coal particle are assumed to be at the same temperature as the particle with an enthalpy $h_{\text{vol},\text{T}_p}$.

5.2.5 Char Combustion

The coal particles undergo char combustion once devolatilization has finished, which is the process of the remaining carbon burning out with oxygen diffusing into the porous coal structure. Char combustion is described by the intrinsic model by Smith [215] in this work. The equations presented here for completeness can mostly be found in other recent PCC studies, such as by Stöllinger et al. [223], Schaffel et al. [208] and Backreedy et al. [1]. The carbon is assumed to be converted to CO only, which is the dominant reaction in high temperature char combustion. The overall char(=carbon) conversion rate is given by Eq. 5.8.

$$\dot{m}_{\text{char}} = X_{O_2} p_0 \pi D_p^2 \frac{R_{\text{ox}} \cdot R_{\text{char}}}{R_{\text{ox}} + R_{\text{char}}} \tag{5.8}$$

In Eq. 5.8, R_{ox} and R_{char} are the bulk molecular mass diffusion coefficient of oxygen and the chemical reaction rate coefficient, respectively. Further, X_{O_2} and p_0 are molar fraction of O_2 and atmospheric pressure, respectively. The bulk molecular mass diffusion of oxygen is calculated by Eq. 5.15.

$$R_{\text{ox}} = C_{\text{diff}} \frac{T_m^{0.75}}{D_p} \tag{5.9}$$

In Eq. 5.9, $C_{\text{diff}} = 5 \cdot 10^{-12} \text{ s/K}^{0.75}$ is the mass diffusion limited rate constant and T_m the mean temperature between particle and bulk gas, $T_m = (\tilde{T} + T_p)/2$. The reaction

rate coefficient R_{char} is calculated by Eq. 5.10, with η, S_a and k_i being the effectiveness factor, the specific internal surface area and the intrinsic reactivity, respectively.

$$R_{\text{char}} = \eta \rho_p S_a \frac{D_p}{6} k_i \tag{5.10}$$

The effectiveness factor η is used to account for pore diffusion resistance and can be calculated by Eq. 5.11.

$$\eta = \frac{3}{\phi^2}(\phi \coth \phi - 1) \tag{5.11}$$

The effectiveness factor is a function of the Thiele modulus ϕ only, which is calculated by Eq. 5.12.

$$\phi = \frac{D_p}{2} \left(\frac{S_{O_2} S_a \rho_p k_i X_{O_2} p_0}{D_e \rho_g Y_{O_2}} \right)^{1/2} \tag{5.12}$$

In Eq. 5.12, S_{O_2} is the stoichiometric oxygen mass requirement for the heterogeneous reaction considered (i.e. $S_{O_2} \approx 1.33$) and D_e the effective pore diffusion coefficient. The effective pore diffusion coefficient is calculated from bulk and Knudsen diffusion, Eq. 5.13, under the assumption that both processes proceed in parallel.

$$D_e = \frac{\theta}{\tau^2} \left(\frac{1}{D_{\text{Kn}}} + \frac{1}{D_{\text{ox}}} \right)^{-1} \tag{5.13}$$

Here, θ, τ and D_{Kn} are the porosity of the coal, the tortuosity of the pores and the Knudsen diffusion coefficient, calculated with Eq. 5.14.

$$D_{\text{Kn}} = C_{\text{Kn}} \, \bar{r}_{\text{pore}} \sqrt{T_p / M_{O_2}} \tag{5.14}$$

In Eq. 5.14, $\bar{r}_{\text{pore}}$ is the mean pore radius, which is calculated from the coal porosity, tortuosity, specific area and density: $\bar{r}_{\text{pore}} = 2\theta\sqrt{\tau}/(S_a \rho_p)$, and M_{O_2} the molecular weight of oxygen in kg/kmol and C_{Kn} a dimensional constant of the value $97 \text{kg}^{0.5}\text{m K}^{-0.5}\text{kmol}^{-0.5}\text{s}^{-1}$ [215]. The tortuosity is assumed to be $\tau = \sqrt{2}$ and the porosity $\theta = 0.7$. The internal surface area of the coal particle is calculated as a function of the char burnout b_{char} and the initial surface area $S_{a,0}$: $S_a = (1 - b_{\text{char}})\sqrt{b/\theta + (1 - b_{\text{char}})}S_{a,0}$ with $b_{\text{char}} = 1 - m_{p,FC}/m_{p,FC,0}$ where $m_{p,FC}$ is the current fixed carbon content and $m_{p,FC,0}$ the initial carbon content. The initial surface area is approximated by $S_{a,0} = [1.5463Y_{\text{char}}^2 - 2.8349Y_{\text{char}} + 1.3017] \cdot 10^6 \text{ m}^2/\text{kg}$ [256], with Y_{char} being the char mass fraction from the proximate analysis on daf basis.

The diffusion coefficient D_{ox} is calculated by Eq. 5.15 [8].

$$D_{\text{ox}} = D_0 (T_m / T_0)^{1.75} \tag{5.15}$$

Following Baum and Street [8], the molecular diffusion coefficient of the oxygen is approximated by the binary diffusion coefficient for O_2 in N_2, where D_0 is given as $3.13 \cdot 10^{-4} \text{m}^2/\text{s}$ at a reference temperature of 1500 K and a reference pressure of one atmosphere. The temperature T_m represents the mean temperature between particle and gas.

Finally, the intrinsic reactivity k_i is obtained as an Arrhenius type expression by Eq. 5.16, with the pre-exponential factor of A_i and the activation energy E_i.

$$k_i = A_i \, e^{-\frac{E_i}{RT_p}} \tag{5.16}$$

The pre-exponential factor and activation energy are $A_i = 0.052\,\text{kg}/(\text{m}^2\,\text{s}\,\text{Pa})$ and 161500 J/mol in this work, which are the same values as used by Stöllinger et al. [223] in a similar setup with a similar coal.

5.2.6 Particle Heat Balance

The heat conduction inside a coal particle is usually assumed to be much faster than the heat exchange with the surroundings. Correspondingly, the coal particles are treated as having a homogeneous temperature distribution neglecting internal temperature gradients. The change of the particle temperature in PCC is mainly due to convective heat exchange with the gas, radiative emission and absorption, and heat of char combustion and devolatilization. The equation describing the change of particle temperature can be derived from balancing the heat transfer on the particle surface and the change of thermal energy of the coal particle, Eq. 5.17.

$$\begin{aligned} \frac{dT_p}{dt} = {} & \frac{1}{\tau_{\text{con}}}(\tilde{T} - T_p) + \frac{\epsilon_p A_p \sigma}{m_p c_{p,p}}(\Theta_r^4 - T_p^4) \\ & + \frac{\dot{q}_{\text{char}}}{m_p c_{p,p}} + \frac{\dot{q}_{\text{devol}}}{m_p c_{p,p}} \end{aligned} \tag{5.17}$$

Equation 5.17 depends on the convective time scale τ_{con}, the Eulerian phase temperature at the particle location $\tilde{T}$, the particle temperature T_p, the particle emissivity ϵ_p, the projected area A_p of the particle, the particle mass m_p, the particle heat capacity $c_{p,p}$, the Eulerian phase radiation temperature Θ_r, the heat flux due to char combustion $\dot{q}_{\text{char}}$ and the heat flux due to devolatilization $\dot{q}_{\text{devol}}$. The latter is the latent heat of devolatilization and set to zero in Eq. 18 [161]. The first term of the RHS represents the change of particle temperature due to convective heat transfer. The convective time scale τ_{con} is calculated using the Nusselt number Nu, correlated to the particle Reynolds number according to Ranz-Marshall [193], and the Prandtl number Pr, Eq. 5.18. The Prandtl number is set constant to $\text{Pr} = 0.7$.

$$\tau_{\text{con}} = \tau_{p,\text{St}} \frac{3\text{Pr}}{\text{Nu}} \frac{c_{p,p}}{c_p} = \frac{1}{6} \frac{\text{Pr}}{\text{Nu}} \frac{c_{p,p}}{c_p} \frac{\rho_p D_p^2}{\mu} \quad \text{with} \quad \text{Nu} = 2 + 0.552\text{Re}_\text{p}^{1/2}\text{Pr}^{1/3} \tag{5.18}$$

The second term of the RHS of Eq. 5.17 describes the effect of radiation on the particle temperature. The last two terms in Eq. 5.17, represent the change of temperature due to devolatilization and char combustion. The heat flux due to char combustion $\dot{q}_{\text{char}}$ is calculated based on the assumption that the heat of partial oxidation from C to CO is absorbed by the particle and that the CO leaves the particle at gas phase temperature. Hence, the particle absorbs the enthalpy change in the gas phase due to char combustion as well as the sensible enthalpy of the reacting char, i.e. $\dot{q}_{\text{char}} =$

$-\dot{m}_{\text{char}}[(S_{O_2}+1)h_{CO} - S_{O_2}h_{O_2} - h_{\text{char}}]$, where h_{CO} and h_{O_2} are the enthalpies of CO and O_2 at gas phase temperature and h_{char} is the enthalpy of char at particle temperature.

An important parameter for the behavior of the coal heat up and heat exchange is the particle heat capacity. We followed Stöllinger et al. [223] to model the coal specific heat based on the composition of volatile matter, char and ash according to Merrick and to Brewster et al. [18, 133] with the volatile matter mean atomic weight being $W_{\text{VM}} \approx 6.83$ kg/kmol in the present case, obtained from the volatile gas composition. The particle heat capacity is computed by Eq. 5.19.

$$c_{p,p} = Y_{p,\text{VM}}c_{p,\text{VM}} + Y_{p,\text{FC}}c_{p,\text{FC}} + Y_{p,\text{ash}}c_{p,\text{ash}} \tag{5.19}$$

In Eq. 5.19, $Y_{p,\text{VM}}$, $Y_{p,\text{FC}}$ and $Y_{p,\text{ash}}$ are the mass fractions of volatile matter, fixed carbon and ash in the coal particle and $c_{p,\text{VM}}$, $c_{p,\text{FC}}$ and $c_{p,\text{ash}}$ the respective heat capacities. Volatile matter and fixed carbon heat capacities are computed by Eq. 5.20, where γ denotes either volatile matter ($\gamma = \text{VM}$) or fixed carbon ($\gamma = \text{FC}$) [133].

$$c_{p,\gamma} = \frac{R_{\text{uni}}}{W_\gamma}\left[g_1\left(\frac{380}{T_p}\right) + 2g_1\left(\frac{1800}{T_p}\right)\right] \tag{5.20}$$

The function $g_1(x)$ is evaluated as $g_1(x) = e^x/\frac{e^x-1}{x}^2$, R_{uni} the universal gas constant in J kmol^{-1}K^{-1} and W_γ the mean atomic weight ($W_{\text{VM}} \approx 6.83$ kg/kmol and $W_{\text{FC}} \approx 12$ kg/kmol). The ash heat capacity is obtained as $c_{p,\text{ash}} = 539.9 + 0.586T_p$ in J kg^{-1}K^{-1} [18].

5.2.7   Blowing Correction

The effect of the rapid devolatilization on the processes of momentum- and convective heat transfer is usually accounted for by applying a blowing correction [216, 223]. Following Stöllinger et al., the blowing correction B can be calculated by Eq. 5.21 [223].

$$B = \frac{\text{Pr}}{2\pi D_p \mu}\dot{m}_{\text{devol}} \tag{5.21}$$

The blowing correction is applied to the particle relaxation time τ_p and the Nusselt number Nu, as given by Eqs. 5.22 and 5.23.

$$\tau_p^* = \tau_p(1+B) \tag{5.22}$$

$$\text{Nu}^* = \text{Nu}\, e^{-0.6B} \tag{5.23}$$

The corrected values of τ_p and Nu, τ_p^* and Nu*, respectively, are used in all of the above equations although not explicitly stated for simplicity.

5.2.8 Radiation

Radiation represented by the radiative transfer equation (RTE) is solved using the discrete ordinates method [29, 47, 231]. The order of discretization follows the S-8 approximation, hence the RTE is solved in 80 directions.

Gas phase spectral properties are approximated with the grey weighted sum of grey gases model (GWSGG) with coefficients provided by Kangwanpongpan et al. [89]. Particle absorption, scattering and emission of radiation is considered with the particle emissivity ϵ_p being calculated from a linear function of the particle char burnout, being $\epsilon_p = 0.9$ for an unreacted particle and $\epsilon_p = 0.5$ for an ash particle [223].

5.3 Combustion Modeling

5.3.1 Mixture Fraction Approach and Transport Equations

A flamelet model for two fuels/mixture fractions has been introduced by Hasse and Peters to deal with split injections in direct injection Diesel engines [68, 69]. A similar approach is adopted in this work. Mixture fractions for the two fuels, volatile gas Z_{vol} and char-off gas Z_{char}, are introduced to describe a three-feed mixing system with the oxidizer (similarly to the studies by Watanabe & Yamamoto [248] and Stöllinger et al. [222, 223], the latter being a RANS/PDF with tabulated equilibrium chemistry). Like in the work by Watanabe & Yamamoto, the flamelet model is based on one-dimensional flames without solving the full two-dimensional flamelet equations.

The mixture fractions are defined by the ratio of the mass flux originating from the given fuel stream (volatile gas: $\dot{m}_{\mathrm{devol}}$, char-off gas: $\dot{m}_{\mathrm{char}}^*$) to the total mass flux in the view of a steady three-feed system, as described by Eqs. 5.24, and with $\dot{m}_{\mathrm{ox}}$ being the mass originating from the oxidizer stream. Here, $\dot{m}_{\mathrm{char}}$ is the mass of carbon supplied to the system by char combustion and $\dot{m}_{\mathrm{char}}^*$ the mass of CO/N_2, i.e. reacted carbon and participating oxidizer from the heterogeneous reaction.

$$
\begin{aligned}
Z_{\mathrm{vol}} &= \frac{\dot{m}_{\mathrm{devol}}}{\dot{m}_{\mathrm{devol}} + \dot{m}_{\mathrm{char}} + \dot{m}_{\mathrm{ox}}} \\
Z_{\mathrm{char}} &= \frac{\dot{m}_{\mathrm{char}}^*}{\dot{m}_{\mathrm{devol}} + \dot{m}_{\mathrm{char}} + \dot{m}_{\mathrm{ox}}}
\end{aligned}
\tag{5.24}
$$

The evolution of the mixture fraction for either of the two fuel streams (volatile gas: $\alpha = \mathrm{vol}$, char-off gas: $\alpha = \mathrm{char}$) is described by a Favre-filtered scalar transport equation in the LES, Eq. 5.25.

$$
\frac{\partial}{\partial t}\bar{\rho}\tilde{Z}_\alpha + \frac{\partial}{\partial x_j}\bar{\rho}\tilde{u}_j\tilde{Z}_\alpha = \frac{\partial}{\partial x_j}\left(\bar{\rho}D_{\mathrm{eff}}\frac{\partial \tilde{Z}_\alpha}{\partial x_j}\right) + \bar{\rho}\dot{S}_{\tilde{Z}_\alpha}
\tag{5.25}
$$

In Eq. 5.25, $\bar{\rho}$ is the filtered density, $\tilde{u}_j$ is the Favre-filtered velocity in direction j, D_{eff} the effective diffusivity containing molecular and subgrid diffusion ($D_{\mathrm{eff}} = D_{\mathrm{turb}} + D_{\mathrm{lam}}$) and $\dot{S}_{\tilde{Z}_\alpha}$ the source term for Favre-filtered mixture fraction $\tilde{Z}_\alpha$. In contrast to the usual

approach in gas flames, Eq. 5.25 requires a source term describing the mass transfer from particle to gas phase. Hence, Z_α is generally not a conserved quantity.

The treatment of the source terms for the continuity equation, Eq. 5.26, differs from the treatment for the mixture fraction equations, which is due to the char conversion consuming oxygen. Details on the source terms are given in the next section, Sec. 5.3.2.

$$\frac{\partial}{\partial t}\bar{\rho} + \frac{\partial}{\partial x_j}\bar{\rho}\tilde{u}_j = \bar{\rho}\dot{S} \tag{5.26}$$

In addition to the mixture fractions, a Favre-filtered transport equation for enthalpy is being solved, Eq. 5.27.

$$\frac{\partial}{\partial t}\bar{\rho}\tilde{h} + \frac{\partial}{\partial x_j}\bar{\rho}\tilde{u}_j\tilde{h} = \frac{\partial}{\partial x_j}\left(\bar{\rho}D_{\text{eff}}\frac{\partial\tilde{h}}{\partial x_j}\right) + \bar{\rho}\dot{S}_{\tilde{h}} \tag{5.27}$$

Here, $\tilde{h}$ describes the Favre-filtered sum of sensible and chemical enthalpy ($\tilde{h} = \Delta h_f^0 + \int_{T_0}^{\tilde{T}} c_p dT$, obtained using NASA polynomials) and hence is not altered by chemical reactions. The effective diffusivity D_{eff} in Eqs. 5.25 and 5.27 is taken to be equal, meaning that enthalpy and mixture fractions diffuse at the same rate, which is commonly referred to as unity Lewis number assumption.

The turbulent diffusivity is obtained from an eddy-viscosity approach, the Smagorinsky model and assuming a constant turbulent Schmidt number. The Smagorinsky model constant is $C_S = 0.173$ and the turbulent Schmidt number $\text{Sc}_{\text{turb}} = 0.7$.

Since only filtered quantities are solved by the LES, the chemical state cannot be obtained directly using the filtered mixture fractions and enthalpy. With the common assumption of the subgrid distribution of mixture fraction following the shape of a β-pdf, the mixture fraction variance is required as an additional parameter. In this work, we use a transport equation to model the subgrid variance of the sum of mixture fractions, $Z = Z_{\text{vol}} + Z_{\text{char}}$. The transport equation of the Favre-filtered subgrid variance of the sum of mixture fractions $\widetilde{Z''^2}$, defined as $\widetilde{Z''^2} = \widetilde{Z^2} - \tilde{Z}^2$, is given by Eq. 5.28, similar to the one given by Pera et al. [158] and used for spray flame LES before [204].

$$\frac{\partial}{\partial t}\bar{\rho}\widetilde{Z''^2} + \frac{\partial}{\partial x_j}\bar{\rho}\tilde{u}_j\widetilde{Z''^2} = \frac{\partial}{\partial x_j}\left(\bar{\rho}D_{\text{eff}}\frac{\widetilde{Z''^2}}{x_j}\right)$$
$$+2\bar{\rho}D_{\text{turb}}\left(\frac{\partial\tilde{Z}}{\partial x_j}\right)^2 - \quad 2\bar{\rho}\bar{S}_{\chi_{\tilde{Z}}} + \bar{\rho}\widetilde{\dot{W}}^+ \tag{5.28}$$

The second term of the RHS of Eq. 5.28 represents the resolved part of the scalar dissipation rate, providing a source term in the transport equation of the Favre-filtered subgrid variance. The unresolved scalar dissipation rate, third term on the RHS of Eq. 5.28, on the other hand is a sink term. It can be modeled as in Eq. 5.29.

$$\bar{S}_{\chi_{\tilde{Z}}} = C_{\chi_{\tilde{Z}}} D_{\text{turb}} \frac{\widetilde{Z''^2}}{\Delta^2} \tag{5.29}$$

The subgrid scale dissipation rate model constant $C_{\chi_{\tilde{Z}}}$ is set to 8.0 in this work, following previous LES studies of spray flames [38, 204]. The last term of the RHS of Eq. 5.28 represents the subgrid variance source assuming that the particles release their mass on the subgrid scales. It is modeled according to Pera et al.:

$$\bar{\rho}\widetilde{\dot{W}}^{+} = \alpha\widetilde{Z''^2}\frac{\bar{\rho}\dot{S}_{\tilde{Z}}}{\tilde{Z}}.$$ (5.30)

The model constant α is set to 0.5, according to Tillou et al. [227]. Note that the mixture fraction source term $\dot{S}_{\tilde{Z}}$ appearing in Eq. 5.30 is the sum of the source terms appearing in the transport equation of the volatile gas and char-off gas mixture fractions (Eq. 5.25), i.e. $\bar{\rho}\dot{S}_{\tilde{Z}} = \bar{\rho}\dot{S}_{\tilde{Z}_{\text{vol}}} + \bar{\rho}\dot{S}_{\tilde{Z}_{\text{char}}}$, and is obtained from the coal particles, as described in Sec. 5.3.2.

5.3.2 Gas Phase Source Terms

The coal particles interact with the gas phase through exchange of mass, momentum and enthalpy. The source terms for the Eulerian transport equations described in Sec. 5.3 are obtained by summing up particle contributions in each computational cell of size Δ^3. The mass source term arising in the mixture fraction transport equations is calculated by Eqs. 5.31.

$$\bar{\rho}\dot{S}_{\tilde{Z}_{\text{vol}}} = \frac{1}{\Delta^3}\sum_{p=1}^{N_p}\dot{m}_{p,\text{devol}}$$

$$\bar{\rho}\dot{S}_{\tilde{Z}_{\text{char}}} = \frac{1}{\Delta^3}\sum_{p=1}^{N_p}\dot{m}_{p,\text{char}}(1 + S_{\text{O}_2} + S_{\text{N}_2})$$ (5.31)

In case of the pyrolysis gas mixture fraction, the source described by Eq. 5.31 is used in the mass and momentum conservation equations, the transport equation for the pyrolysis gas mixture fraction, Eq. 5.25, and the subgrid variance transport equation, Eq. 5.28. In the case of the char-off gas mixture fraction, only the char released by the coal is added to the continuity equation, but the corresponding CO and N_2 mass is added to the transport equation of the mixture fraction, expressed by the stoichiometric mass based oxygen requirement $S_{\text{O}_2} \approx 1.33$ and the corresponding nitrogen mass $S_{\text{N}_2} \approx 4.387$. The source term for the continuity equation $\bar{\rho}\dot{S}$ in Eq. 5.26 is expressed as Eq. 5.32, which considers only the mass actually released by the particle.

$$\bar{\rho}\dot{S} = \frac{1}{\Delta^3}\sum_{p=1}^{N_p}\dot{m}_{p,\text{devol}} + \frac{1}{\Delta^3}\sum_{p=1}^{N_p}\dot{m}_{p,\text{char}}$$ (5.32)

The source term for the enthalpy transport equation is given by Eq. 5.33.

$$\begin{aligned}\bar{\rho}\dot{S}_{\tilde{h}} &= \frac{1}{\Delta^3}\sum_{p=1}^{N_p}[-m_p c_{p,p}\frac{dT_{p,\text{con}}}{dt} + \dot{m}_{p,\text{devol}}h_{\text{vol}} \\ &+ \dot{m}_{p,\text{char}}h^*_{\text{char}}] + \nabla \cdot q_{\text{rad}}\end{aligned}$$ (5.33)

Equation 5.33 contains the contributions of the change of thermal energy of the particle due to convective heat transfer, with $dT_{p,\text{con}}/dt$ corresponding to the first term on the RHS of Eq. 5.17, and the release of volatile and char-off gases, with h_{vol} being the enthalpy of the volatile gases at particle temperature. As described earlier, the determination of the char-off gas enthalpy h_{char}^* is based on the assumption that the CO leaves the particle at the temperature of the gas surrounding the particle, hence h_{char}^* is calculated as $h_{\text{char}}^* = (S_{\text{O}_2}+1)h_{\text{CO}} - S_{\text{O}_2}h_{\text{O}_2}$ with the enthalpies determined at gas phase temperature. This corresponds to the absorbed heat by the particle $\dot{q}_{\text{char}}$ in Eq. 5.17. It should be noted that h_{char} and h_{char}^* are different quantities. The former is the sensible enthalpy of solid char matter while the latter is the enthalpy of the char-off gases. The term $\dot{q}_{\text{devol}}$ in Eq. 5.17 is neglected. The last term, $\nabla \cdot q_{\text{rad}}$, is the radiative enthalpy source obtained from the DOM.

The source term for the momentum equation contains the momentum of the mass released by the particles as well as the effect of drag. The treatment is the same as in the study by Rittler et al. [204] for spray flame LES.

5.3.3 Flamelet Modeling

The flamelet model employed in this work relies on single one-dimensional steady non-premixed flamelets. The use of one-dimensional flamelets in a three-feed system corresponds to neglecting the interaction between the streams in flamelet space and is justified if this interaction is weak as outlined by Ihme & See [81] and implicitly assumed by Watanabe & Yamamoto [248]. The weakness of this interaction will be assumed in this work and a fully two-dimensional flamelet solution investigated in the future. This can be justified by the fact that volatile and char combustion are consecutive processes and usually not taking place locally at the same time.

The mixture fraction Z_{vol} describes the gas originating from devolatilization. The mixture fraction Z_{char} represents the char-off gas and needs appropriate modeling to correctly treat the oxygen consumption during the heterogeneous char reactions [248]. The heterogeneous reaction considered in this work is $\text{C} + 0.5\,\text{O}_2 \rightarrow \text{CO}$. To ensure overall conservation of elemental masses, the fuel for the char-off gas mixture fraction $\tilde{Z}_{\text{char}}$ needs to contain not only the CO resulting from the heterogeneous reaction but also the amount of nitrogen that goes along with the consumed oxygen. The amount of nitrogen is given by the molecular nitrogen to oxygen ratio ν_{N_2} in the oxidizer stream. Hence, the composition of the fuel for Z_{char} consists of the two species CO and N_2 with the corresponding mass fractions $Y_{\text{CO}} = M_{\text{CO}}/(M_{\text{CO}} + 0.5\nu_{\text{N}_2}M_{\text{N}_2})$ and $Y_{\text{N}_2} = 0.5\nu_{\text{N}_2}M_{\text{N}_2}/(M_{\text{CO}} + 0.5\nu_{\text{N}_2}M_{\text{N}_2})$.

To achieve an equidistant spacing in the flamelet table, Hasse proposed a transformation of the two mixture fractions into their sum and the ratio of one of them to their sum [70]. This transformation is adopted here. One-dimensional counter-flow flames are calculated for a fuel composition corresponding to a specific ratio of $Z_2 = Z_{\text{char}}/(Z_{\text{vol}}+Z_{\text{char}})$. These flames are then tabulated over the sum of the mixture fractions $Z = Z_{\text{vol}} + Z_{\text{char}}$. The calculations are performed with Cantera [62] using a unity Lewis number transport model [184]. We used the GRI-3.0 mechanism [214] to describe the reactions for volatile and char-off gases. Cantera solves the equations in physical space, the solution is mapped onto the Z-Z_2 space for the tabulation.

In PCC, adiabatic flamelet solutions cannot be used without introducing significant errors, mainly due to large convective heat exchange between solid and gas phase and due to radiation to the walls. In this work, we include enthalpy as an additional look-up parameter and adopt a method to incorporate heat losses in one-dimensional flames proposed by Proch & Kempf [184]. This method is based on scaling the reaction source term in the temperature equation solved by Cantera, such that the flame temperature can be successively lowered. Each of the flames in the discretized $Z_2 = Z_{\mathrm{char}}/(Z_{\mathrm{vol}} + Z_{\mathrm{char}})$-space was 'cooled down' by scaling the source term, until a stably burning flame could not be obtained anymore. The composition of the coldest burning flame was frozen and further cooled down to ambient temperature. To obtain an appropriate accessible range in the enthalpy direction and ensure burning one-dimensional flames, the fuel and oxidizer inlet temperatures were set to $800\,\mathrm{K} - 1200\,\mathrm{K}$ ($800\,\mathrm{K}$ for volatile gas and $1200\,\mathrm{K}$ for char-off gas) and $1400\,\mathrm{K}$, respectively. The table is stored as a function of the normalized enthalpy h^n. The normalization is based on the minimum ($h_{\min}$) and maximum ($h_{\max}$) enthalpy values for a given combination of Z and Z_2, $h^n = (\tilde{h} - h_{\min})/(h_{\max} - h_{\min})$, where the minimum corresponds to the flame cooled down to ambient conditions and the maximum to the flame without heat loss.

The final four-dimensional flamelet look-up table is obtained by β-integrating the solution for the three variables Z, Z_2, h^n in Z direction, with the mean and variance of the β-pdf correspondingly being based on the sum of the mixture fractions $Z = Z_{\mathrm{char}} + Z_{\mathrm{vol}}$. Note that Z and Z_2 are within 0 and 1 but the maximum and minimum enthalpy values are a function of Z and Z_2 and hence need to be stored appropriately in the look-up table. The four-dimensional flamelet table is accessed with the transported quantities transformed into Z, Z_2 and the normalized enthalpy and variance. No subgrid distribution is assumed for Z_2 and the normalized enthalpy. Flames required for the table have been calculated with strain rates of approximately 0.0025 (at $Z_2 = 0.9$, 90% char-off gas in the fuel) to 0.2 s^{-1} (at $Z_2 = 0.0$, pure volatile flame) and linearly interpolated in between, which corresponds to mean scalar dissipation rates of the order of 10^{-2} observed at locations 85 cm downstream of the quarl inlet. Such low scalar dissipation rates are similar to what has been observed in flamelet simulations of moderate and intense low oxygen dilution (MILD) combustors [32].

Exemplary plots of temperature and carbon dioxide mass fraction as obtained from the flamelet table are shown in Fig. 5.1.

5.4 Numerical Method and Setup

The code used in this study is our in-house code PsiPhi, which has been developed for combustion LES. PsiPhi has been successfully used for gas flame LES [97, 126, 168, 187], as well as for LES of PCC [53, 189] and LES of spray flames [204].

PsiPhi solves the Favre-filtered transport/conservation equations of mass, momentum and arbitrary scalars with a variable density low-Mach number formulation. The equations are discretized with a finite volume framework on an equidistant and orthogonal grid. A prediction-correction scheme with the resulting Poisson equation solved by either a Jacobi-preconditioned conjugated gradient solver or a Gauss-Seidel solver with succes-
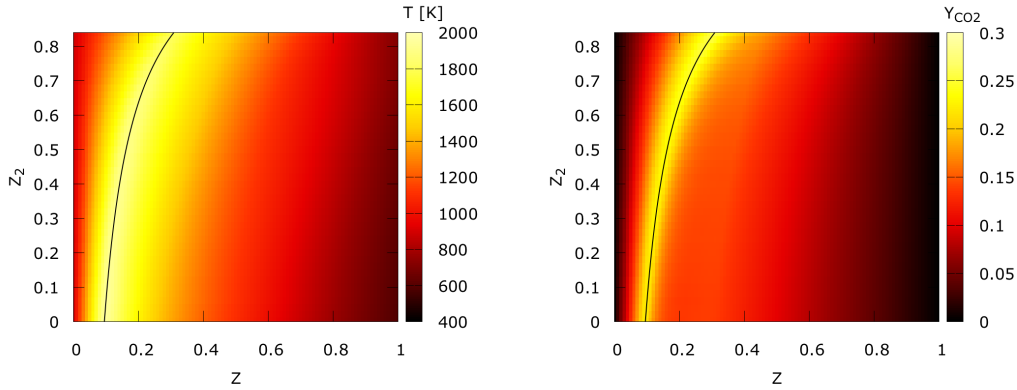
Figure 5.1: Contour plots of temperature (left) and carbon dioxide mass fraction (right) in the $Z - Z_2$ plane extracted from the flamelet table with a normalized enthalpy of 0.5 and a normalized variance of 0. The line corresponds to the stoichiometric mixture.

sive over relaxation is used to enforce continuity. Diffusive fluxes are spatially discretized with a central differencing scheme (CDS) of second order, which is also used for the convective flux of momentum, whereas a total variation diminishing scheme with CHARM limiter [269] is used for density and scalars. A low-storage third order Runge-Kutta scheme is used for explicit time discretization. The message passing interface (MPI) is used for distributed memory domain decomposition. The same decomposition is used for particle and Eulerian fields.

Equations 5.1 and 5.17 are embedded in the Runge-Kutta time integration scheme. The Wiener term in Eq. 5.1 is obtained from uniformly distributed random variables with the Box-Muller transformation [105] and the random contribution is added only once per time step. The interaction between Eulerian and particle fields is facilitated by a trilinear interpolation scheme.

For all transported variables a zero-gradient boundary condition is used at the outlet domain, whereas a Dirichlet condition is set at the inlet. Pseudo-turbulence is set for the velocities at the inlet using the method proposed by Klein et al. [103] with the efficient implementation proposed by Kempf et al. [98], with a length-scale of 20 mm and a fluctuation magnitude of 0.1 of the local mean flow velocity.

Walls are described by the immersed boundary method. The wall temperature is set to 1300 K and its emissivity to 0.6. Conductive heat transfer to the walls is neglected since radiative heat transfer is dominant in such furnaces. At the walls, particles are treated such that their position is reset to the closest fluid-wall interface in each time step if they are found to have crossed the solid boundaries. No slagging model is used.

The simulations have been conducted on two different grids with uniform cell sizes of 10 and 5 mm resulting in roughly 27 and 220 M cells. Simulations of confined geometries and of coal furnaces in particular require a long initialization phase in which the large and slow recirculation zones need to form and in which the furnace needs to be filled with flue gas and particles. To reduce the cost associated with a long initialization phase on the fine grid, we mapped the data from the coarse grid simulation onto the fine grid

to obtain a proper initial field. This approach has been successfully applied by Moureau et al. [139] to successively refine the mesh of a premixed swirl flame from large eddy to direct numerical simulation resolution. In this work, a first simulation on the coarse grid was run up to around 12 s of physical time. The fine simulations were run for 1.5 more seconds, until the turbulent structures had been established. Another 1.5 s of runtime were simulated to obtain enough samples for statistics. After the full physical time of around 15 s around 46 M parcels were present inside the domain. The simulations were performed on SuperMUC with 640 and 2048 cores and cost around 30 k and 252 k core hours (based on 3 s physical run time) for the coarse and fine grid, respectively.

5.5   Experiment

The experimental test case is a 2.5 MW flame studied by Weber et al. at the International Flame Research Foundation (IFRF) in the IFRF furnace No. 1 employing the swirled Aerodynamically Air Staged Burner (AASB) [250, 251]. The furnace was fired with Saar hvBb coal, for which the properties are summarized in table 5.1.

The coal particles are pulverized with around $75\%_{wt}$ of the coal particles being smaller than 75μm in diameter. The furnace dimensions are approximately $6.25 \times 2 \times 2\,\text{m}^3$. The coal is supplied with transport air through an annular injector surrounding a bluff-body. The coal injector has an inner and outer diameter of 108 mm and 134 mm, respectively. A wall of 3 mm thickness is separating the coal feed from the annular combustion air supply, which has an inner and outer diameter of 140 mm and $D = 234$ mm, respectively. The quarl has an exit diameter of 468 mm$(= 2D)$ and a length of 234 mm$(= D)$.

Coal is being supplied at a rate of 263 kg/h carried by 421 kg/h of transport air. The combustion air is swirled with a swirl number of 0.93 and its mass flow amounts to 2670 kg/h. Transport and combustion air are preheated to 70°C and 300°C, respectively.Velocity of the coal particles has been measured by laser Doppler velocimetry (LDV) and gas temperature and composition by probes equipped with thermocouples and different analyzers (paramagnetic, infared and chemiluminiscent).

Weber et al. provided RANS results of the quarl near region of this case along with the experimental results [250, 251]. The first LES of this case has been presented recently by Olenik et al. [153], who obtained good results without tuning the models. An extensive comparison between LES and experiment is provided in the next section.

5.6   Results

5.6.1   Instantaneous Results

Figure 5.2 presents instantaneous fields of the two mixture fractions for volatile and char-off gases, respectively. Regions dominated by either of the two mixture fractions can be clearly distinguished. High volatile gas mixture fractions can only be found inside the quarl or in the quarl near region. In this region, coal particles rapidly devolatilize and mass originating from devolatilization is being recirculated. Further downstream the volatile gas mixes with fresh air. Char oxidation and the formation of char-off gases
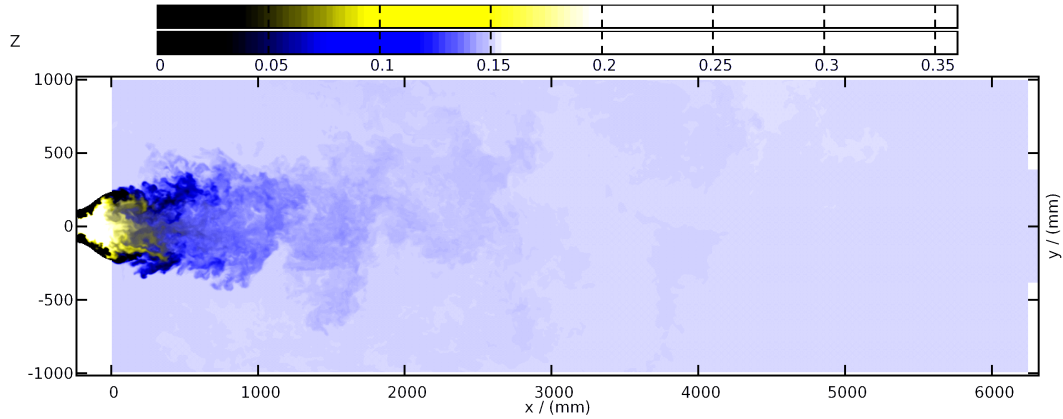
Figure 5.2: Instantaneous images of volatile gas mixture fraction (yellow scale) and char-off gas mixture fraction (blue scale) for the simulation on the 5 mm grid.

starts in a region downstream of the quarl where the volatile gas mixture has been diluted with combustion air enough to allow for a hot environment with oxygen excess. Further oxidation of the char-off gases results in additional heat release and subsequent char oxidation. No significant mixing can be observed anymore downstream of around $x = 3$ m.

Figure 5.3 shows instantaneous and temporal mean axial velocity, temperature, oxygen molar fraction and equivalence ratio fields.

The axial velocity field illustrates the highly turbulent quarl region and the internal and external recirculation zones. The combustion air enters the domain with around 40 m/s through the outer annular gap at the quarl inlet. Due to the strong swirl the combustion air is pushed outwards and closely follows the curved quarl wall towards the quarl exit. The swirling flow breaks down approximately one quarl inlet diameter downstream of the quarl exit and a strong recirculation zone is formed inside the quarl. An external recirculation zone (ERZ) is formed in the corner of the domain at the left wall.

The temperature field shows that up to 2300 K are reached at the quarl exit. Further downstream the high temperature region becomes more narrow due to the interaction with the colder fresh combustion air stream. Even further downstream, the high temperature region broadens where volatile gases are well mixed with the combustion air and where char conversion takes place. The temperature field from the center of the furnace towards the exit can be characterized as being relatively homogeneous with a decreasing temperature to around 1300 K at the outlet of the furnace. The temperature in the ERZ is relatively homogeneous as well, with temperatures being slightly higher than at the outlet of the furnace.

The oxygen is entirely consumed inside the IRZ upstream of the quarl exit, where a very rich volatile gas mixture is present. The oxygen that is not consumed and passes the IRZ is transported into the furnace by the strongly swirling combustion air flow. Downstream of the IRZ it mixes and reacts with the volatile gases and subsequently

with the char left in the coal particles after devolatilization. Roughly 2 m downstream of the quarl exit, the oxygen molar fraction field becomes mostly homogeneous since char conversion slows down due to moderate temperatures and since mixing is mostly completed.

The equivalence ratio field demonstrates the very rich quarl region. Equivalence ratios of locally up to around $\phi \approx 7$ are reached where the particles rapidly devolatilize and where flue gas is recirculated. The IRZ is surrounded by lean regions with equivalence ratios below 0.6, consisting mostly of combustion air with diluted volatile gases. The stoichiometric iso-contour shown corresponds to the global equivalence ratio of around $\phi_{gl} \approx 0.74$, considering the inlet fuel (volatile matter and carbon in the coal) and air streams. The iso-line divides the plot into regions that are lean or rich compared to the global equivalence ratio. The low-equivalence ratio region due to the dilution of fuel with combustion air extends to approximately 2 m in axial direction and may get close to the walls in radial direction. Further downstream the equivalence ratio is slightly higher than the global equivalence ratio.

Figure 5.4(top) presents particles in the quarl near region and inside the quarl in the horizontal plane containing the quarl center (15 cm below the meridional plane) of 25 mm thickness. Particles rapidly heat up upon entering the domain and release most of their volatile matter before exiting the quarl. Some particles are being trapped in the recirculation zone just downstream of the bluff-body, which gives them enough time to release all their volatile mass and to convert some of the char. Downstream of the quarl exit, only a low amount of particles can be found close to the centerline in the internal recirculation zone. This is possibly due to the recirculation not being strong enough to overcome the particle inertia and to advect the particles back towards the quarl. Small ash particles can be found outside of the internal swirling flow region in the ERZ and correspondingly the average particle size drops rapidly in radial direction across the shear layer between flue gas from the ERZ and fresh swirling air with suspended unreacted large particles.

Figure 5.4(bottom) shows that a large number of particles with intermediate temperatures and high burnout can be identified inside the quarl at small radii (approximately corresponding to the quarl inlet radius). With the information obtained from Fig. 5.3, it can be observed that these particles have not been entrained in the combustion air flow, neither have they experienced the volatile flame that is formed in the shear layer between the recirculating flow and combustion air. The particles with the highest temperatures can be found at the quarl exit between radii of one and two quarl inlet diameters, corresponding to the hot main volatile flame region. Further downstream, some small particles can be observed that still have low temperatures below 1000 K. These particles are mostly relatively large and hence have due to their inertia not been entrained in the hot volatile flame at the shear layer of IRZ and combustion air stream. Particles in the ERZ have uniformly temperatures of around 1400 K.

Figure 5.5 shows instantaneous scatter plots of particle (a)-(b) and gas phase (c)-(f) data. Figures 5.5(a) and 5.5(b) show every hundredth particle randomly selected of a total of 46 M, excluding burned out particles (with an ash content of $> 99 \%$). Figures 5.5(c)-5.5(f) show every 250th cell value randomly selected from the total of around 220 M (5 mm grid).
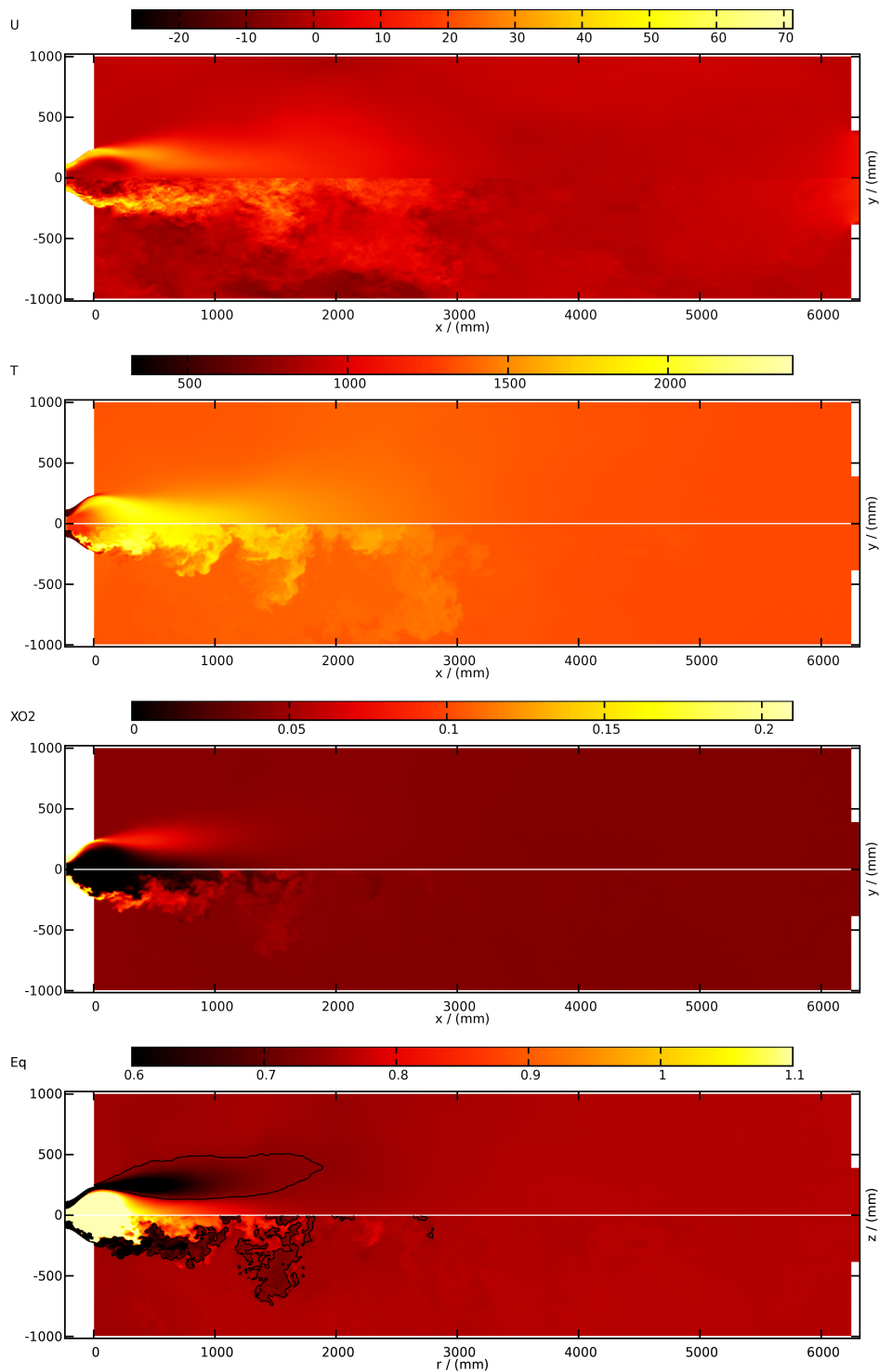
Figure 5.3: Mean and instantaneous images of axial velocity, temperature, oxygen molar fraction and equivalence ratio for the simulation on the 5 mm grid. The equivalence ratio figure contains the iso-line for the global equivalence ratio based on the fuel and air entering the furnace ($\phi_{\mathrm{gl}} \approx 0.74$); the equivalence ratio values are clipped in the figure and and reach up to around $\phi \approx 7$.
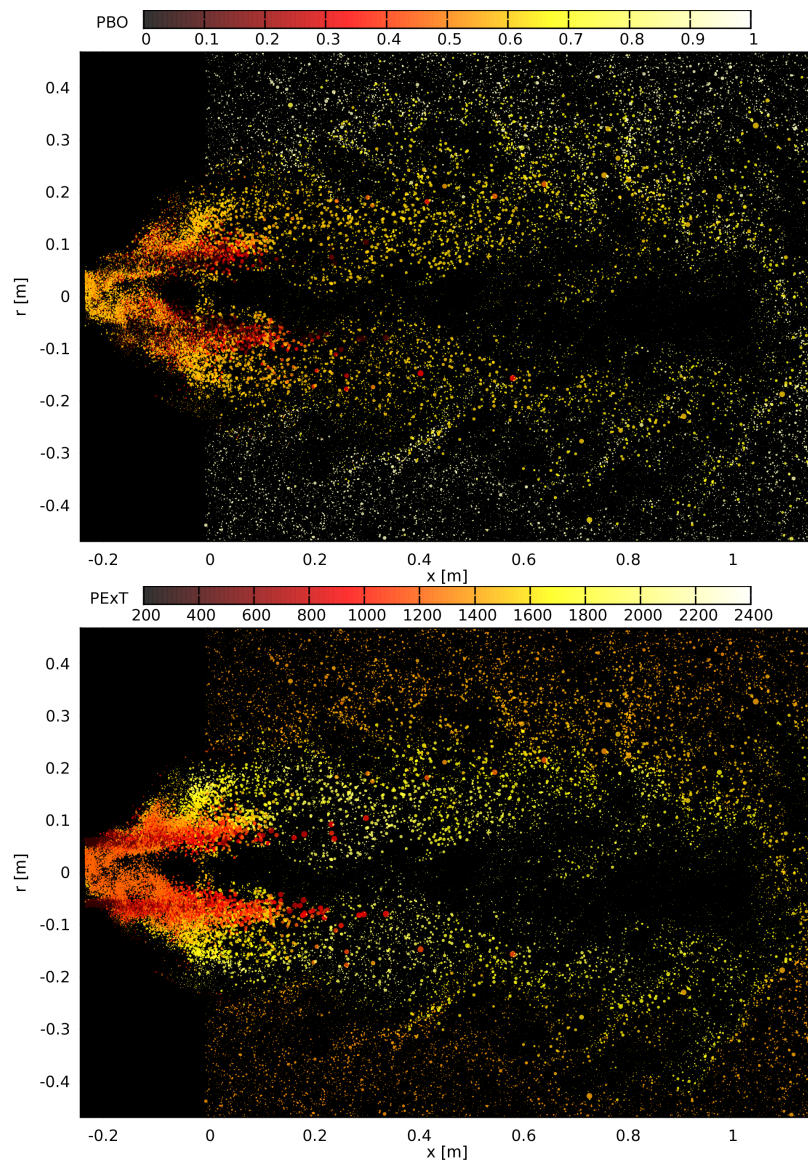
Figure 5.4: Particles in the quarl region scaled by diameter and colored by burnout (top) and by temperature (bottom) for the simulation on the 5 mm grid.

In Fig. 5.5(a), the mixture fraction ratio $Z_2 = Z_{\text{char}}/(Z_{\text{vol}} + Z_{\text{char}})$ versus the mixture fraction sum $Z = Z_{\text{vol}} + Z_{\text{char}}$ as seen by the particle are shown. A line corresponding to the stoichiometric $Z_{\text{vol}} - Z_{\text{char}}$-mixture is plotted as well, dividing the plot in a lean (left of the line) and rich (right of the line) part. There are mainly three characteristic regions that can be observed. The first region is characterized by high values of Z and low values of Z_2, hence being rich with respect to the volatile mass fraction. Such states only occur inside the quarl or in the near quarl region, where most of the volatiles are being released but almost no char combustion is occurring and correspondingly, most particles are not fully burnt out yet. The second region is characterized by low values of Z and Z_2, where particles are still mostly surrounded by air and have released no or low amounts of volatiles. Particles that have passed the volatile flame can be found in the third region, where a mixture of intermediate Z and high Z_2 values is present. This region is lean and corresponds to the slow char combustion burnout of the coal in the post volatile flame region. Particles with high burnout tend to cluster around a slightly lean mixture of $Z = 0.2$ and $Z_2 = 0.75$, which corresponds to a global equilibrium mixture of the fuel and air entering the furnace.

Figure 5.5(b) illustrates the thermal (dis-)equilibrium between gas and particle phase depending on particle diameter and burnout. Naturally, unreacted particles tend to have a lower temperature than the gas phase as they need to be heated by the hot gases, which directly goes along with an increase of their burnout due to the release of volatiles. Contrarily, some particles with intermediate to high burnout can be found with substantially higher temperatures than their surrounding gas. These particles have been heated in the volatile flame but got entrained in the colder air stream before completing devolatilization. However, most particles with a burnout of > 0.3 are close to thermal equilibrium with the gas phase, mainly because of a slower mixing process downstream of the IRZ and because of the slow char oxidation process that does not induce rapid changes in gas or particle temperature. Similar observations have been made by Olenik et al. [153].

Figure 5.5(c) presents gas phase temperature vs. the mixture fraction sum Z with points colored by the mixture fraction ratio Z_2. The maximum temperatures observed correspond to the volatile flame, where temperatures up to around 2350 K are reached. Compositions rich in the char-off gas mixture fraction are characterized by temperatures of around 1500 K. Since volatile and char combustion are consecutive processes with different time scales, the rich volatile flame ($Z > 0.2$ and $Z_2 < 0.3$) is first diluted in flue gases and air before char oxidation takes place which slowly enriches the mixture again to the final state with $Z \approx 0.2$ and $Z_2 \approx 0.8$.

Figure 5.5(d) shows the CO_2 mass fraction vs. the mixture fraction sum Z. Similarly to Fig. 5.5(c), volatile combustion and char oxidation regions can be differentiated. Up to $Z \approx 0.15$, the CO_2 mass fraction increases with the mixture fraction, independently of whether the mixture consists of volatiles or char-off gas. Beyond $Z \approx 0.15$, the volatile flame is rich, hence the CO_2 mass fraction decreases due to the formation of CO becoming dominant. The CO_2 mass fraction however keeps increasing if the fuel mixture consists of mostly char-off gas until a mixture corresponding approximately to global stoichiometry is reached. From Fig. 5.5(d), it can be observed that the mixture in the volatile flame is diluted before being enriched with CO_2 when char oxidation is progressing.

Table 5.3: Numerical and experimental [250] flue gas properties.

	X_{O_2}	X_{CO}	X_{CO_2}	part. burnout	temperature
	-	ppm	-	%	K
experiment	0.03	30	0.156	99.4	1353
simulation	0.041	44	0.155	100.0	1307

Figure 5.5(e) presents the O_2 mass fraction vs. the mixture fraction sum Z. With increasing mixture fraction Z, the O_2 mass fraction decreases. The decrease with respect to Z is larger if the gas is composed mainly of volatile instead of char-off gas. This is due to the higher stoichiometric oxygen requirement of the volatile gas. Corresponding to Fig. 5.5(a), gas with fuel mostly being char-off gas is mostly lean and contains unreacted oxygen.

Figure 5.5(f) shows the CO mass fraction vs. the mixture fraction sum Z. High CO mass fractions can be found in rich volatile gas mixtures inside the quarl, whereas mixtures with a high char-off gas content usually feature low CO mass fractions, such as can be observed at the outlet of the domain where the composition reaches the global stoichiometry. Although the char-off gas consists solely of CO, the CO is mostly directly consumed since it is only released in regions with oxygen availability.

5.6.2 Averaged Results

Table 5.3 provides a comparison of the molar fractions of O_2, CO and CO_2 as well as particle burnout and temperature at the outlet of the computational domain versus the experimentally measured results at the chimney. A discrepancy in the O_2 molar fraction can be observed, the numerically obtained oxygen molar fraction exceeds the experimentally obtained value clearly. However, Peters & Weber [161] found a similar discrepancy and pointed out that the experimentally obtained value is most likely erroneous. The agreement for CO is quite good given that this species is difficult to predict with a steady flamelet approach. The computed CO_2 molar fraction at the outlet of the furnace corresponds well to the experimentally obtained value. The particle burnout in the simulation reaches complete burnout, while the experiment suggests almost complete burnout. The temperature prediction is satisfactory, but indicates excessive heat extraction through radiation in the simulation, which however is consistent to the prediction by Peters & Weber [161].

An energy balance calculation is done for validation and to compare to the data from Peters & Weber [161]. The enthalpy supplied to the furnace consists of the sensible enthalpy of the combustion and transport air (212 kW), the sensible enthalpy of the coal (3.7 kW) and the heat released by the combustion of the coal (2191 kW) totalling 2407 kW. The enthalpy leaving the system consists of the radiation of particles and gas to the walls (1291 kW), the sensible enthalpy of the flue gas (1041 kW) and the sensible enthalpy of the ash particles leaving the domain (6.5 kW) totalling 2339 kW. The radiative heat loss of 1289 kW is calculated by integrating the radiative heat loss over all cells and particles and agrees well with the total heat extraction predicted by
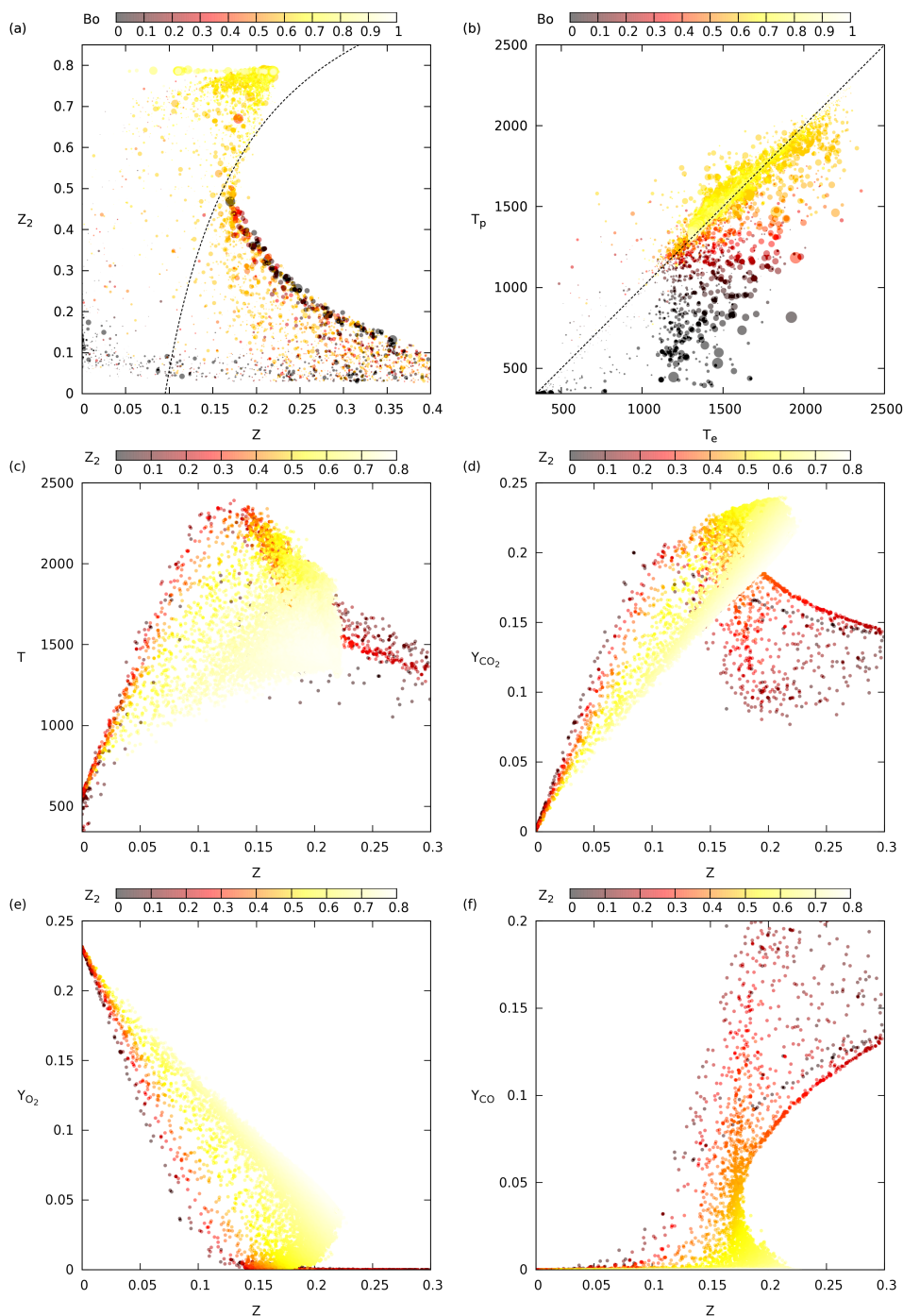
Figure 5.5: Scatter plots for the simulation on the full 5 mm grid; (a)-(b) from particle and (c)-(f) from Eulerian data. (a): Mixture fraction ratio Z_2 vs. mixture fraction sum Z as seen by particle colored by particle burnout, (b): particle temperature vs. gas temperature as seen by particle colored by burnout, (c): gas temperature vs. Z colored by Z_2, (d): CO_2 mass fraction vs. Z colored by Z_2, (e): O_2 mass fraction vs. Z colored by Z_2, (f): CO mass fraction vs. Z colored by Z_2.

Peters & Weber [161]. The discrepancy of around 3% between the enthalpy flow supplied to the furnace and leaving the furnace might be due to not fully stationary conditions during the computations, in spite of an overall simulation time of around 15 s and around 3 s of sampling for the energy balance statistics.

Figures 5.6 to 5.9 show the averaged results for the simulations on the 10 mm and 5 mm grids by means of radial profiles at different axial locations.

Figure 5.6 presents the results for the O_2 and CO_2 molar fractions. Some differences between experiment and LES can be observed mainly in the quarl near region. In the experiment, some of the O_2 has not been consumed at the exit of the quarl ($x = 0$ cm), whereas the LES shows complete consumption. The experiment shows a maximum CO_2 molar fraction on the centerline at the quarl exit and a drop in radial direction towards zero at the radial location of the quarl wall. The LES however shows an almost uniform CO_2 distribution across the quarl exit plane and a rapid drop at the air stream, which however is slightly shifted towards larger radii. The agreement between LES and experiment improves strongly further downstream with a mostly better agreement on the fine grid.

The mixing of flue gases in the outer recirculation zones with fresh gases and the decrease of the oxygen peak due to char combustion and mixing appears to be predicted well. However, an over-consumption of oxygen can be observed close to the centerline up to $x = 85$ cm. It should be noted that the scalar dissipation rate used to construct the flamelet table corresponds to the conditions observed at $x = 85$ cm, which results in a good agreement at this location as well as further downstream.

Figure 5.7 shows the profiles for the molar fraction of CO and temperature. High CO molar fractions can be observed at the quarl exit, which is due to the rich volatile gas mixture. However, the LES clearly over-predicts the CO molar fraction, which might be due to the fact that recirculating product gases cannot be captured correctly with the current approach. This is due to the lack of a variable that allows for the distinction between burnt and unburnt gases in the steady non-premixed flamelet approach and has been previously observed in gas flames by e.g. Lamouroux et al. [116]. Further downstream, the molar fraction of CO is only slightly over-predicted and under-predicted beyond $x = 125$ cm. Noteworthy is the fact that CO levels are higher on the fine grid, which corresponds to the higher pyrolysis gas mixture fractions at this location on the fine grid (cf. Fig. 5.10). The temperature profile from the LES shows a narrow flame at locations up to $x = 50$ cm, whereas the experimental temperature profile is almost flat, indicating a much stronger mixing of the combustion air with flue and volatile gas in the experiment. Close to a radius approximately corresponding to the quarl outlet, the temperature is over-predicted at $x = 25$cm and $x = 50$cm, which again is probably due to the treatment of recirculating flue gases in the flamelet model. Both the over-predicted temperature and CO can also be partially attributed to the single scalar dissipation rate used, which is below the values observed in the shear layers between volatile gas and combustion air stream, which in turn strongly affects the composition inside the quarl. Further downstream, the agreement close to the centerline is good. However, the temperatures are under-predicted significantly in the region of the combustion air stream, but only up to $x = 50$ cm. Further downstream the temperatures are generally slightly under-predicted.

Figure 5.8 presents axial and swirling velocities with a comparison between experimental particle LDV measurements and the gas phase velocities from the LES. Axial velocities are over-predicted by the LES. In the quarl near region, this is due the discrepancy between particle and gas phase velocity. Further downstream, particle and gas phase velocities correspond to each other according to Weber et al. [250]. The predictions of the swirling velocity show again some discrepancies at the quarl exit, which can be attributed to the slip between particle and gas phase. At x = 25 cm, the peak of the swirling velocity cannot be reproduced and the LES swirling velocity does not go to zero at higher radii as measured in the experiment. The swirling velocity profiles are predicted well further downstream. Generally, the simulation on the fine grid shows a significantly better agreement than the simulation on the coarse grid.

Figure 5.9 shows the axial and swirling velocity fluctuations, which are generally predicted well by the LES. However, discrepancies can be found in the shear layer between the swirling fresh air flow and the ERZ.

Figure 5.10 compares the profiles of the volatile gas (Z_{vol}) and char-off gas (Z_{char}) mixture fractions, respectively, for the two different grids used. A higher volatile gas mixture fraction at the quarl exit and up to a downstream position of $x = 25$ cm is predicted on the fine grid. This might be due to the differences in the axial velocity predictions at $x = 25$ cm possibly leading to a stronger accumulation of Z_{vol} on the fine grid. At a position of $x = 195$ cm, both simulations show the same flat Z_{vol} profile. Similarly, the Z_{char} profile deviates at upstream locations, indicating differences of the resolution having an effect on the particle char conversion at locations where strong mixing is present.
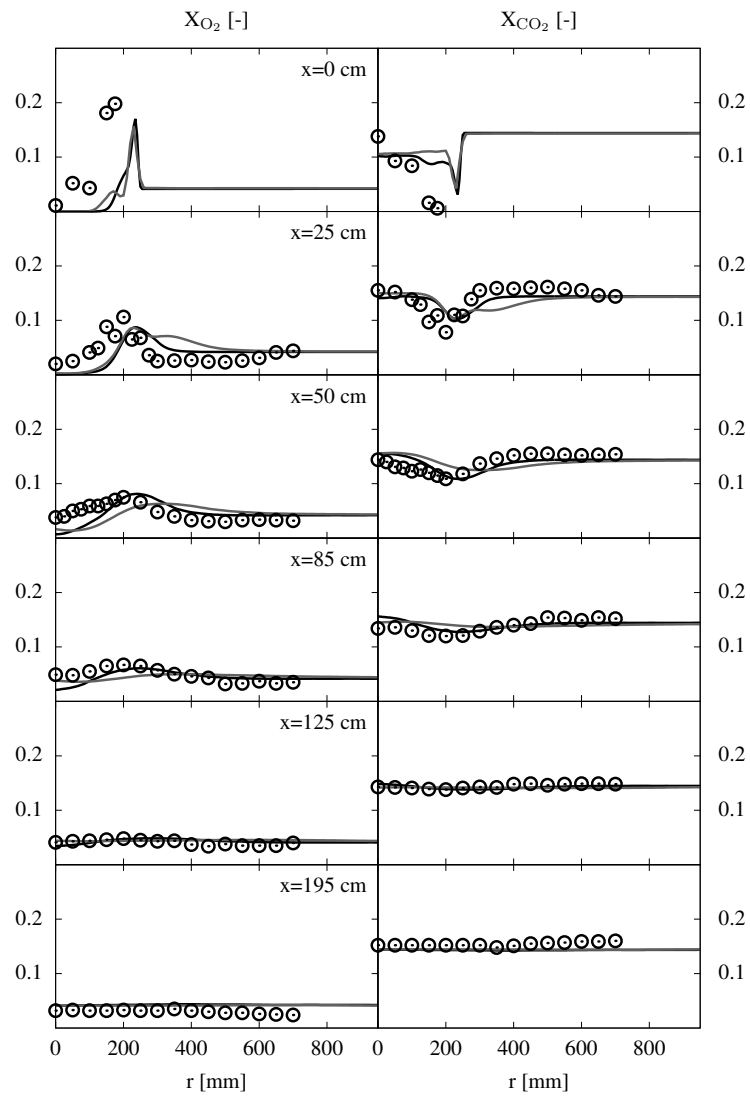
Figure 5.6: Mean oxygen (left) and carbon dioxide molar fractions (right) for the simulations on the 10 mm (—) and 5 mm (—) grid.
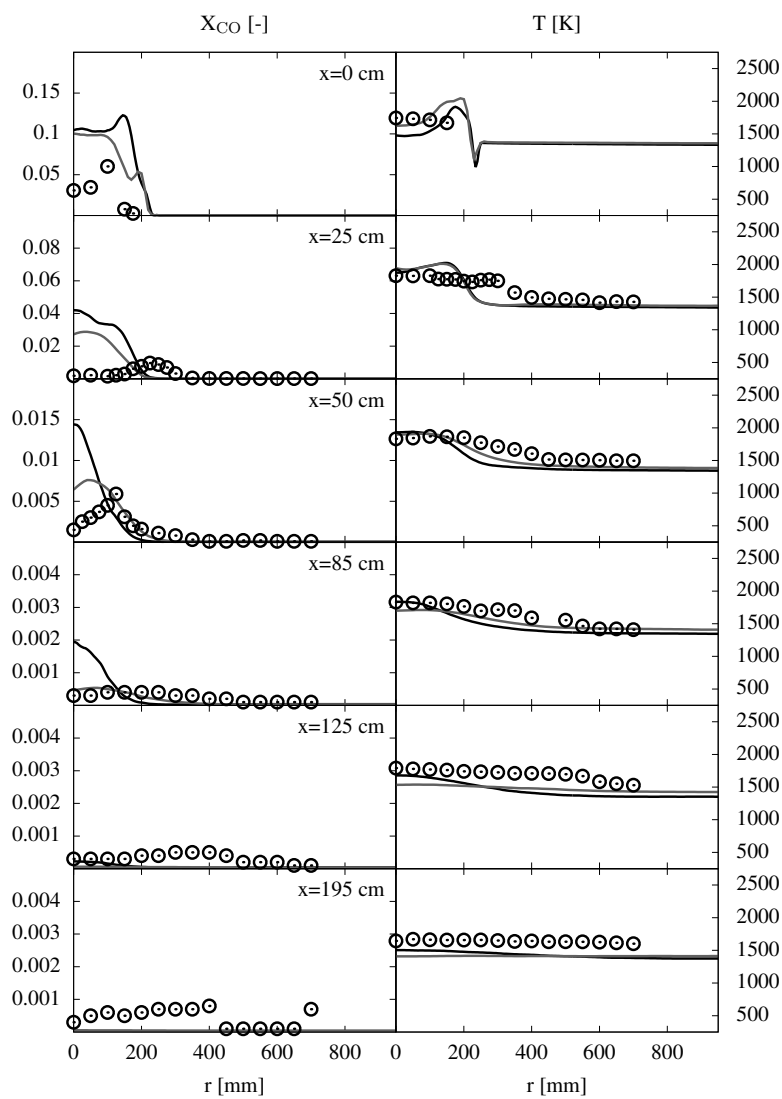
Figure 5.7: Mean carbon monoxide molar fraction (left) and temperature (right) for the simulations on the 10 mm (—) and 5 mm (—) grid.
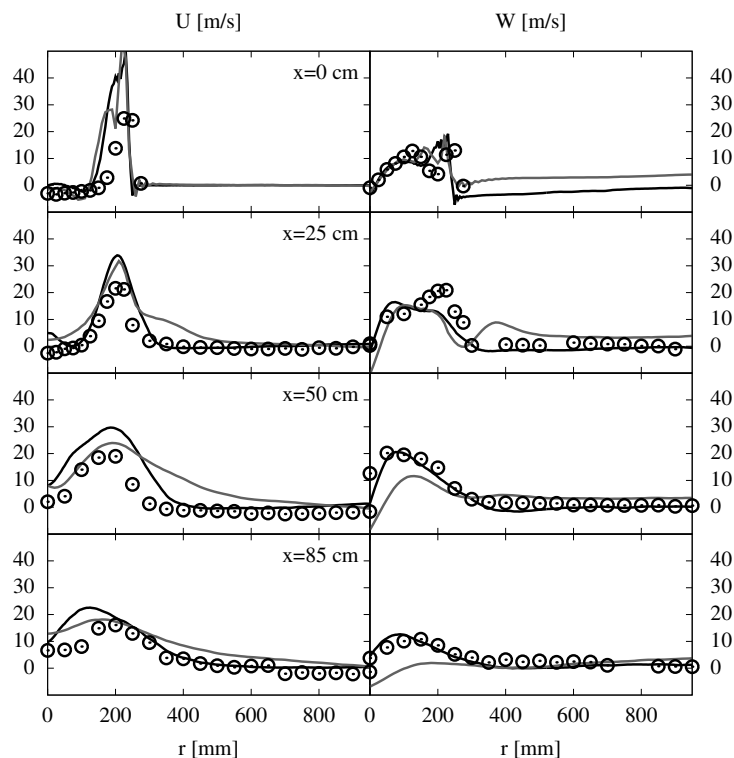
Figure 5.8: Mean axial (left) and swirling velocities (right) for the simulations on the 10 mm (—) and 5 mm (—) grid.

5.7 Conclusions

A flamelet LES of a semi-industrial coal furnace has been presented. The current flamelet model is based on one-dimensional steady counter-flow flames with four parameters for the volatile and char-off gas mixture fractions, enthalpy and the variance of the sum of the mixture fractions. The flamelet model performs well in the PCC context with an overall good agreement between simulation and experiment validating the flamelet model for further use for the LES of realistic PCC configurations. However, differences can be found in the quarl region, where recirculated flue gas cannot be treated correctly with the current steady flamelet approach relying on a tabulation based on the two mixture fractions and enthalpy only. Additionally, more work is necessary to eliminate the differences in the regions of large radii and far downstream, which are characterized by very low scalar dissipation rates and where the flamelet assumption might not be valid anymore. Finally, more elaborate flamelet tabulation approaches than the current one based on pure gaseous one-dimensional flames should be investigated, such as the tabulation based on laminar one-dimensional flows with suspended coal particles.
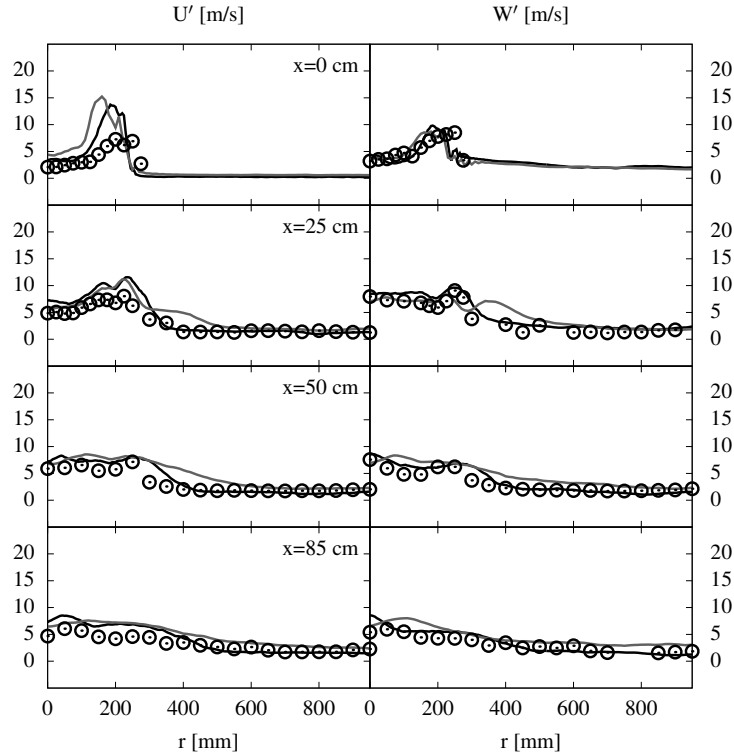
Figure 5.9: Fluctuations of the axial (left) and swirling velocities (right) for the simulations on the 10 mm (—) and 5 mm (—) grid.

Acknowledgements

5.8   Appendix - Fitting of the devolatilization model parameters

The kinetic parameters of the Kobayashi model [108] are fitted to the experimentally obtained pyrolysis data [107] of the coal fired. The present fit is based on the values presented by Ubhayakar et al. [234]. Compared to the parameters by Ubhayakar et al., the pre-exponential factors for low temperature and high temperaure reactions, A_1 and
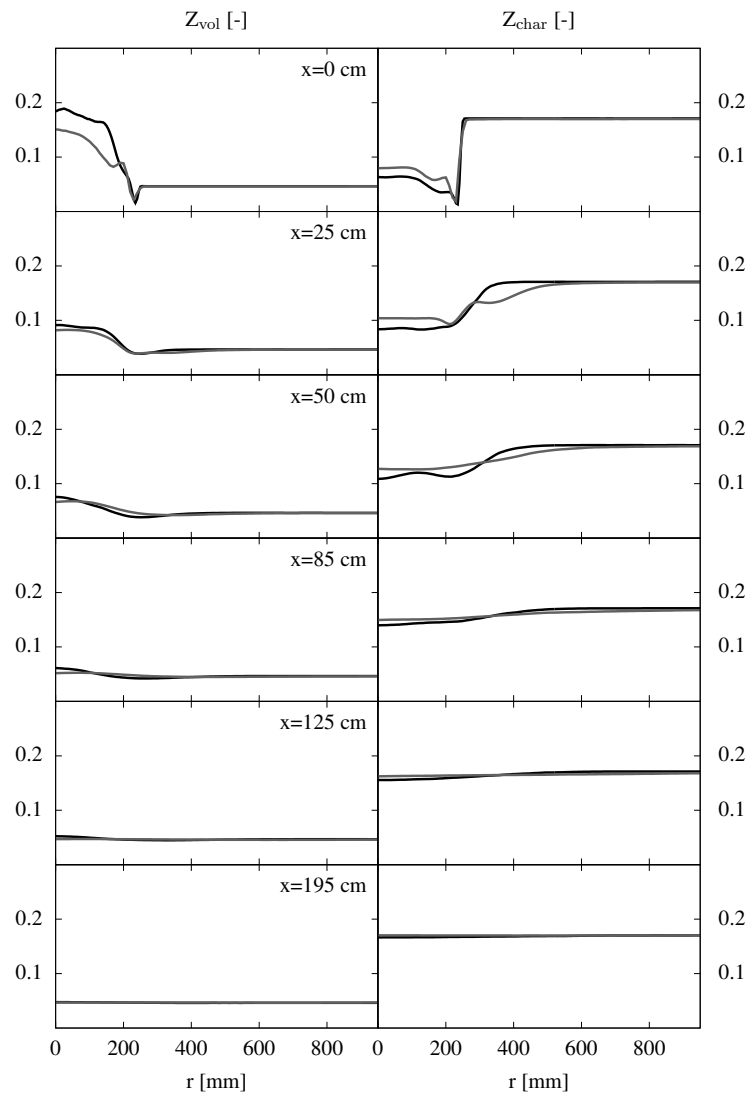
Figure 5.10: Volatile (left) and char-off mixture fractions (right) for the simulations on the 10 mm (—) and 5 mm (—) grid.
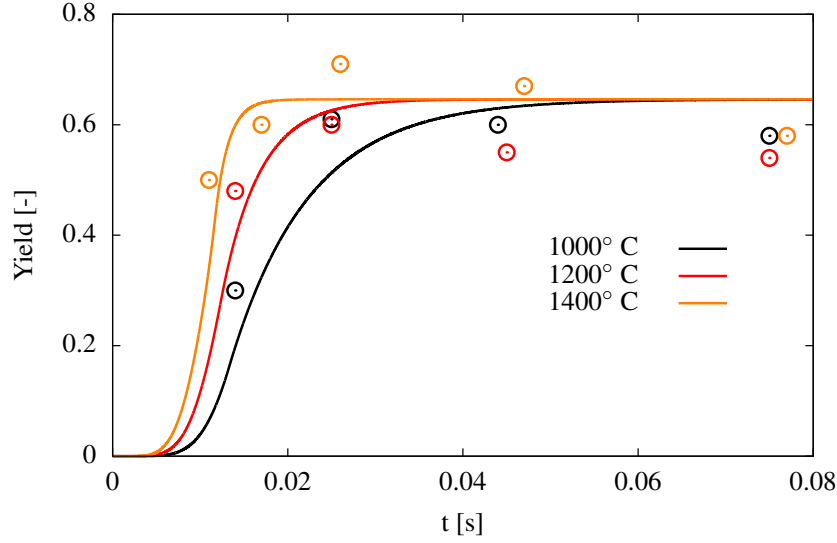
Figure 5.11: Volatile yield vs. residence time for the Saar coal obtained experimentally (circles)[107] and for the fitted Kobayashi model with parameters given in table 5.4.

A_2, have been reduced by one order of magnitude. The activation energies, E_1 and E_2 have been reduced by 30% and increased by 20%, respectively. The parameters α_1 and α_2 have been remained unchanged. The results of the fitting are presented in table 5.4 along with the original parameters and the ones given by Ubhayakar et al.

The experimental conditions used for the fitting are obtained from Knill et al. [107], considering only $80\,\mu$m particles subjected to environments of 1000, 1200 and 1400 °C at mean heating rates of $0.73 \cdot 10^5$, $0.95 \cdot 10^5$ and $1.17 \cdot 10^5$ K/s, respectively. The results obtained with the present fit compared to the experiment are shown in Fig. 5.11.

Table 5.4: Kobyashi model parameters.

Source	A_1 s^{-1}	A_2 s^{-1}	E_1 J/kmol	E_2 J/kmol	α_1	α_2
original [108]	$2.0 \cdot 10^5$	$1.3 \cdot 10^7$	$1.05 \cdot 10^8$	$1.67 \cdot 10^8$	0.3	1.0
Ubhayakar [234]	$3.7 \cdot 10^5$	$1.46 \cdot 10^{13}$	$7.37 \cdot 10^7$	$2.51 \cdot 10^8$	0.39	0.8
present work	$3.7 \cdot 10^4$	$1.46 \cdot 10^{12}$	$5.16 \cdot 10^7$	$3.07 \cdot 10^8$	0.39	0.8

Chapter 6

Highly Resolved Flamelet LES of a Semi-Industrial Coal Furnace [201]

This chapter including all text, figures and tables is published in the Proceedings of the Combustion Institute 'Rieth, M., Proch, F., Clements, A.G., Rabaçal, M., Kempf, A.M. (2017). Highly resolved flamelet LES of a semi-industrial scale coal furnace. Proceedings of the Combustion Institute, 36(3), 3371-3379.' [201] and is reprinted with permission from Elsevier. The author of this thesis contributed the code extension and development (including the incorporation of the combustion model and the devolatilization model and updates/optimization of other coal models), running of simulations, post-processing and paper writing. The author A.G. Clements contributed optimization of the radiation routines and the author F. Proch the basic CFD code. The authors A.G. Clements, M. Rabaçal and A.M. Kempf contributed discussions, proof-reading and corrections. The author A.M. Kempf developed the original versions of the PsiPhi code.

Abstract

A highly resolved large eddy simulation (LES) of the semi-industrial IFRF coal furnace [250, 251] employing the steady flamelet model is presented. The flamelet table is based on mixture fractions of volatile and char-off gases as well as on enthalpy and scalar dissipation rate. Turbulence-chemistry interaction is treated with an assumed pdf approach, with the variance obtained from a transport equation. Radiation is computed by the discrete ordinates method and the grey weighted sum of grey gases model. The simulation is conducted with the massively parallel 'PsiPhi' code on up to 1.7 billion cells and with 40 million particles. Results are processed and compared against the comprehensive set of experiments to i) validate the new flamelet model and the simulation method and to ii) gain further insight into the combustion process that is not available from the experiment. The simulation results show that the flamelet LES approach can successfully describe the flow field and combustion inside the furnace; major species and velocities are found in good agreement with the experiment.
The results are further analyzed with a focus on the processes of particle heating, devolatilization, char combustion and flame stabilization in a highly turbulent environment.

Additionally, the relative importance of scalar dissipation rate is highlighted, showing a large separation of mixing scales between volatile and char-off gas combustion due to the long residence time and generally much lower scalar dissipation rates than typical for lab-scale experiments.

6.1   Introduction

World's energy demand relies and will rely on burning fuels in the foreseeable future, with coal remaining attractive due to its abundance. The move towards more efficient and less polluting plants drives research efforts into fields like oxy-coal or biomass combustion [27].

Experiments are invaluable for the design and validation of efficient combustion systems, but are increasingly supported by simulations. One of the most promising tools for accurately predicting pulverized coal combustion (PCC) is large eddy simulation (LES). It offers superior predictions of flow and scalar fields, accurately considering gas phase combustion and turbulent transport. This has become the weakest link in (RANS) coal simulations, since advanced coal sub-models have become available. The first application of LES to coal combustion has been reported by Kurose & Makino [114] followed by several studies on lab-scale jet flames [53, 140, 156, 157, 221, 252, 264], lab- and pilot-scale furnaces and test facilities ($\leq 1.0\,\mathrm{MW_{th}}$) [26, 30, 43, 57, 189, 245] and semi-industrial furnaces [153] like the 2.5 $\mathrm{MW_{th}}$ swirled IFRF experiment [250, 251] studied in this work. Although we find that LES is the most promising tool for predictive PCC simulations, there are several recent Reynolds-averaged/transported probability density function (RANS/PDF) based studies that were capable of reproducing PCC experiments very well [20, 161, 208, 223, 268], but usually in simulations with non-swirled flow fields.

Most of the reported LES studies rely on early turbulent combustion models (eddy break-up and eddy dissipation), but there is a need to advance the gas combustion models in PCC LES to the state-of-the-art as in pure gas flames to capture turbulence-chemistry interaction phenomena, which are important for flame stabilization and pollutant formation. The flamelet model [162] is particularly promising for PCC applications due to its numerical efficiency and wide success in the field of turbulent combustion LES [85, 174]. After the first application of the flamelet model to volatile combustion by Williams et al. [257], Vascellari et al. [238] and Xu et al. [263] investigated flamelet methods for resolved single coal particle simulations. Recently, Watanabe & Yamamoto [248] presented a flamelet model that can be applied to turbulent PCC simulations taking volatile and char combustion into account. Their testing in a two-dimensional simulation of a coal jet showed a good agreement compared to data obtained with finite rate chemistry.

This work applies the flamelet model to the LES of the semi-industrial IFRF coal furnace studied experimentally by Weber et al. [250, 251], introduces efficient subgrid modeling and validates the model under realistic conditions and against a comprehensive set of measurements.

6.2 Gas Phase and Radiation Modeling

The flamelet model is based on two mixture fractions, similar to previous work on split injection in Diesel engines [68, 69], RANS/PDF of PCC [223] and the recently introduced flamelet model for PCC [248].

The two mixture fractions are defined by the amount a respective mass flow contributes to the mixture in a three-feed system expressed in terms of mass flows of oxidizer ($\dot{m}_{\mathrm{ox}}$), volatiles ($\dot{m}_{\mathrm{vol}}$) and char-off gas ($\dot{m}_{\mathrm{char}}$: pure carbon released, $\dot{m}_{\mathrm{char}}^*$: CO/N_2 released from char combustion) in steady state:

$$
\begin{aligned}
Z_{\mathrm{vol}} &= \quad \dot{m}_{\mathrm{vol}}/(\dot{m}_{\mathrm{vol}} + \dot{m}_{\mathrm{char}} + \dot{m}_{\mathrm{ox}}) \\
Z_{\mathrm{char}} &= \dot{m}_{\mathrm{char}}^*/(\dot{m}_{\mathrm{vol}} + \dot{m}_{\mathrm{char}} + \dot{m}_{\mathrm{ox}}).
\end{aligned}
\tag{6.1}
$$

Both mixture fractions evolve by Favre-filtered transport equations containing source terms for the mass leaving the coal particles, Eq. 6.2, with $\alpha = \mathrm{vol}, \mathrm{char}$.

$$
\frac{\partial}{\partial t}\bar{\rho}\tilde{Z}_\alpha + \frac{\partial}{\partial x_j}\bar{\rho}\tilde{u}_j\tilde{Z}_\alpha = \frac{\partial}{\partial x_j}\left(\bar{\rho}D_{\mathrm{eff}}\frac{\partial \tilde{Z}_\alpha}{\partial x_j}\right) + \bar{\rho}\dot{S}_{\tilde{Z}_\alpha}
\tag{6.2}
$$

Subgrid fluxes are closed with the Smagorinsky model [213] ($C_S = 0.173$), assuming a turbulent and laminar Schmidt number of 0.7. The fact that char combustion consumes oxygen is considered in the definition of the mixture fractions, Eq. 6.1, and source terms, Eqs. 6.3, as further discussed in Section 6.3.

Instead of solving two-dimensional flamelet equations to provide the flamelet table, the present approach relies on one-dimensional steady non-premixed counter-flow flames solved in physical space. This is justified if the fuel streams interact only weakly in flamelet space [81], which can be assumed to be the case here, where volatile and char combustion are mainly consecutive processes, as illustrated in Fig. 6.1 and discussed in Section 6.5.

We use scalar dissipation rate as a steady flamelet table parameter, as opposed to a progress variable [248]. This is motivated by the fact that the unstable branch of the S-curve does not play a role in most of the furnace, since char-combustion occurs in high-temperature low-scalar dissipation rate regions. Additionally, ignition is believed to mostly depend on devolatilization [264].

It should be noted that the flamelet model applied here (and [248]) includes the simplification that particle source terms do not affect the flamelet structure. Recent publications on spray combustion show that evaporation terms may become important [154] and suggest to include these terms as an additional dimension in the flamelet table. Similarly, coal flamelet equations would have to be extended to account for the effect of devolatilization and char combustion on the flamelet structure. However, as this is a first attempt to employ flamelets in PCC LES, these terms are neglected, following common practice for spray flame LES [121, 137, 204].

One scalar dissipation rate is considered for the sum of the mixture fractions ($Z = Z_{\mathrm{char}} + Z_{\mathrm{vol}}$), which is modeled by: $\chi = 2D_{\mathrm{eff}}(\partial Z/\partial x_i)^2$, with D_{eff} being the sum of laminar (D_{l}) and turbulent (D_{t}) diffusivity. The variance $\widetilde{Z''^2}$ of the sum of the mixture

Table 6.1: Properties of the Saar hvBb coal [250] fired in the experiment and mass fractions of the modeled volatile gas.

Ultimate Analysis (daf)		Proximate Analysis	
C	79.3%	ash	8.3%
H	4.7%	volatiles	37.0%
N	1.3%	fixed carbon	52.5%
S	1.0%	moisture	2.0%
O	13.7%		
LHV	32.32 MJ/kg [161]		

Modeled gas composition (mass fractions)					
CH_4	C_2H_2	C_2H_4	CO	H_2	N_2
0.005	0.224	0.370	0.377	0.002	0.020

fractions is obtained from a transport equation developed for spray combustion [158], using parameters that have been tested for spray flame LES [204, 227].

An enthalpy equation is solved to consider the radiative heat losses to the walls and the heat exchange between the phases. The set of quantities solved in the LES to obtain the thermo-chemical state of the gas phase is: volatile gas mixture fraction, char-off gas mixture fraction, enthalpy and scalar dissipation rate.

The flamelet table is based on the transformed mixture fractions $Z = Z_{\text{char}} + Z_{\text{vol}}$ and $Z_2 = Z_{\text{char}}/(Z_{\text{char}} + Z_{\text{vol}})$ and is obtained by solving steady one-dimensional counter-flow flames for varying fuel ratio Z_2 with Cantera [62]. To obtain solutions for different enthalpies, a method is employed that relies on scaling the source term in the energy equation solved by Cantera by a factor $(1 - f_L)$, where f_L represents the relative heat loss [184]. Solutions for different scalar dissipation rates are obtained by varying the strain rate. A unity Lewis number is assumed to avoid additional complexity [248].

The final four-dimensional flamelet table for laminar flames is pre-integrated to be used with the assumed top-hat pdf for turbulence-chemistry interaction modeling [50, 152], which has the following advantages over a β-pdf assumption: i) it is more accurate on very fine LES grids, ii) shows the correct behavior with mixing between more than two streams and iii) requires no additional table dimensions.

Radiation is incorporated by means of the discrete ordinates method [47, 231] using the S8 quadrature set. The radiative properties of the gas are described by the grey weighted sum of grey gases model (GWSGG) using parameters from Kangwanpongpan et al. [89].

6.3   Coal Particle Modeling

The properties of the coal are summarized in table 6.1 [250]. Instead of a postulate substance, a 'real' composition is required for the flamelet model. The exact composition depends on the heating rate and temperature conditions the coal particle is subjected to. To obtain a reasonable volatile gas composition, the elements are distributed among species commonly found in volatile gas under high heating rate conditions, under the

constraint that the elemental masses are conserved [167, 223]. The composition obtained is given in table 6.1. The tar species (C_6H_6) is replaced by C_2H_2, following previous PCC simulations [63, 238], with the same C/H-ratio and to be able to use the GRI 3.0 mechanism [214] to obtain the flamelet table. With a unity Lewis number assumption a replacement of C_6H_6 with C_2H_2 has only negligible influence on the main flame properties including ignition [63]. However, additional to preserving the elemental mass fractions, the heating value of the volatile gas needs to be close to the experimental value to prevent a strong over-prediction of temperatures. Here, the heating value for the modeled gas is 32.7 MJ/kg, which is close to the value of this specific coal [161] and hence no correction of the heat release is necessary. Composition and heating value calculations are based on the assumption that the maximum volatile yield is 0.646 on a daf basis, which has been measured by Knill et al. [107, 250].

Devolatilization is modeled using the Kobayashi model [108] with constants fitted to the measurements by Knill et al. [107]. Only a single yield has been used for both rates to ensure elemental mass preservation without increasing the flamelet table dimensionality.

Char combustion is treated with Smith's intrinsic model [208, 215, 223]. The pre-exponential factor and activation energy of the intrinsic reaction are the same as in the study by Stöllinger et al. [223] due to a similar coal applied. The initial surface area of the char is approximated as suggested by Williams et al. [256] and changes as a function of char burnout based on a pore tree model [212].

Only a single char reaction is considered, $C + 0.5\,O_2 \rightarrow CO$. To be stoichiometrically consistent, the fuel composition for the char-off gas mixture fraction needs to consider that oxygen is consumed from the oxidizer stream, hence the char-off gas composition consists of CO and N_2 [248]. The mass of CO and the N_2, which corresponds to the consumed oxygen from the N_2/O_2 ratio in the air, is added to the transport equation of the char-off gas mixture fraction Z_{char}, and only the mass of the consumed C is added to the continuity equation, ensuring consistency with respect to stoichiometry. The source terms are described by Eqs. 6.3, with mass flows due to devolatilization $\dot{m}_{p,vol}$ and char combustion $\dot{m}_{p,char}$ (carbon) summed up over the N_p particles in each cell, the stoichiometric mass based oxygen requirement S_{O_2} and the corresponding nitrogen mass S_{N_2}. Correspondingly, the relationship between $\dot{m}_{char}^*$ and $\dot{m}_{char}$ in Eq. 6.1 is $\dot{m}_{char}^* = \dot{m}_{char} \cdot (1 + S_{O_2} + S_{N_2})$.

$$\bar{\rho}\dot{S}_{\tilde{Z}_{vol}} = \frac{1}{\Delta^3} \sum_{p=1}^{N_p} \dot{m}_{p,vol}$$

$$\bar{\rho}\dot{S}_{\tilde{Z}_{char}} = \frac{1}{\Delta^3} \sum_{p=1}^{N_p} \dot{m}_{p,char}(1 + S_{O_2} + S_{N_2})$$

(6.3)

Coal particles are accelerated by the forces of drag, gravity and buoyancy [221]. The particle relaxation time is based on the Schiller-Naumann correlation [143]. The influence of the subgrid turbulence is modeled by a Wiener process [12, 88], with the particle-turbulence interaction time scale calculated from the particle relaxation time and the subgrid kinetic energy [88].

Heat transfer occurs by convection, radiative absorption and emission and enthalpy change due to char combustion and volatile release. Heat conductivity inside the particles is neglected due to their small size [135]. The modeling of the convective heat transfer relies on a Ranz-Marshall correlation for the Nusselt number and a constant Prandtl number of 0.7. A heat of devolatilization is neglected in the particle temperature balance, implying that devolatilization does not alter the particle temperature. However, the enthalpy of the volatile gas released is considered as a source term in the LES enthalpy equation. The heat of char combustion is assumed to be absorbed by the particle (and thus raises the particle's temperature). Particle absorption, emission and radiation is considered with the particle emissivity calculated based on particle burnout [223].

A blowing correction is applied to the momentum- and convective heat transfer based on the volatile release rate [216, 223].

Please refer to our earlier study [202] for further reading, where an LES of this case with less sophisticated resolution and subgrid/flamelet modeling is presented.

6.4   Experiment and Numerical Setup

The test case is a swirled 2.5 MW_{th} coal flame studied by the International Flame Research Foundation (IFRF) experimentally by Weber et al. [250, 251] and numerically by Peters & Weber [161]. The furnace dimensions are approximately $6.25 \times 2 \times 2\,\mathrm{m}^3$, the quarl inlet consists of a bluff-body surrounded by an annular coal injector which is surrounded by the annular swirled combustion air inlet. Coal, transport air and combustion air is supplied at rates of 263 kg/h, 421 kg/h (at 343 K) and 2670 kg/h (at 573 K) respectively. Measurements applied Doppler velocimetry (LDV) and gas and particle probing.

The simulation domain contains the furnace from the quarl inlet to furnace outlet with walls being modeled as immersed boundaries (1300 K, emissivity of 0.6).

The solution is obtained with our low-Mach in-house code 'PsiPhi', which has been successfully used for PCC LES [53, 189] and many other combustion systems [97, 184, 187] before, it is based on methods used for combustion LES since 2000 [99]. Two different Cartesian grids with uniform cell sizes of $(5\,\mathrm{mm})^3$ and $(2.5\,\mathrm{mm})^3$ have been used, corresponding to 220 million and 1.7 billion cells, permitting a grid independence test. To reduce the cost associated with the long initialization phase, coarse grid solutions were mapped onto the final grids [139]. This enables a proper statistically converged flow in the slow external recirculation zones in the furnace corners, which requires physical run-times of more than 10 s. Statistics were obtained over at least 1 s, after at least 1 s past the mapping from the coarse grid. All simulations were run on SuperMUC using 2048 (180 k core-h) and 16384 cores (3.4 M core-h) for coarse and fine runs, respectively. The 220M cell simulation took 5.6 times the compute time of the earlier OpenFOAM LES with 1 million cells [153]; such simulations may be standard in few years from now.

Physical particles are lumped into parcels, such that each parcel contains the same mass , and are injected with a stochastically determined size from the particle size distribution given by the experiment [250]. Around 40 million parcels are present inside the furnace at the time statistics are taken.

6.5 Results

Figure 6.1 shows a superposition of both mixture fractions on the fine grid. The volatiles being rapidly released inside the quarl are recirculated by the strong recirculating flow. The volatile combustion products are diluted by the combustion air stream, providing the lean high-temperature conditions for char combustion. As can be seen, char and volatile combustion interact only weakly with each other due to being separated in space. The char-off gas mixture fraction interacts strongly with the combustion air stream.

6.5.1 Validation

Figures 6.2 to 6.5 show the axial and circumferencial velocity mean and rms values, O_2 and CO_2 molar fractions and temperature. In Figs. 6.2 and 6.3, LES gas phase and particle velocities are compared to the LDV measurements. The LES is capable of predicting the turbulent circumferencial flow field reasonably well, with a slight over-prediction of mean axial velocities, a shift of the peak circumferencial velocity towards the centerline at x=25 cm and an under-prediction of the strength of the inner recirculation. It can be seen that particle velocities are generally close to gas phase velocities, but tend to be closer to the experimental values, which is expected due to the measurements having been obtained by LDV. The discrepancy for the particle circumferencial velocity at the centerline at x=85 cm is due to only absolute circumferencial velocities ($\langle |W| \rangle$) being used for the particle velocity statistics, which results in a non-zero circumferencial velocity at the centerline.

Figure 6.4 shows the comparison for O_2 and CO_2 molar fractions. Simulations and experimental measurements show good agreement. In comparison to the experiment, more oxygen is consumed at locations up to x=85 cm close to the centerline. The agreement improves further downstream, with a good prediction from x=125 cm downstream. The dilution of the volatile flame with combustion air and the oxygen consumption and CO_2 production by char combustion is predicted well.

Figure 6.5 shows mixture fractions and temperature. The temperature profile shows a good agreement with the experiment, the major difference is an under-prediction at a radial location close to the combustion air inlet, possibly due to an under-prediction of the mixing between volatile gas and combustion air stream. Further downstream, temperatures are under-predicted, which might be due to an over-prediction of radiative heat losses. However, the predicted mean furnace outlet temperature is 1314 K, which agrees well with the experimental value of 1353 K [161].

The mixture fraction profiles illustrate how the volatile gas mixture fraction peaks close to the centerline due to recirculation and rapid devolatilization inside the quarl. Further downstream, the volatile gas mixture fraction shows a flat profile. In contrast, the char-off gas mixture fraction shows a flat profile in the external recirculation zones and a decrease to low values in the inner recirculation zone. It should be noted that discrepancies in the CO prediction exist, which result from the steady flamelet approach not correctly describing minor species when flue gas and fresh gas mix.   Figure 6.6 presents particle burnout statistics from the LES and the work by Peters & Weber [161]. They outlined that the major difficulties for the comparison are that in the experiment
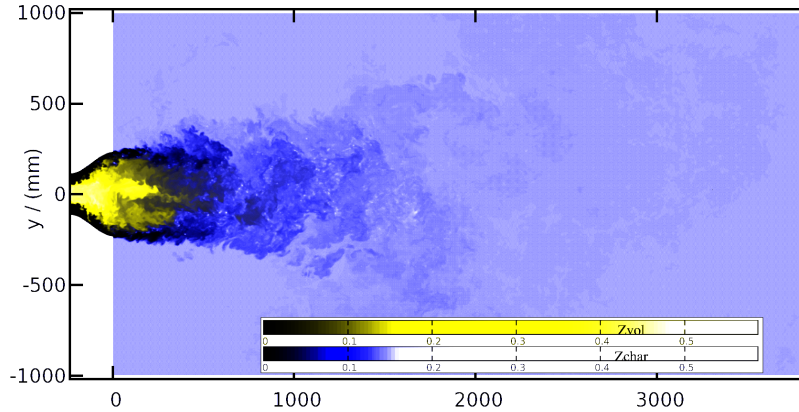
Figure 6.1: Mixture fraction for volatile (yellow) and char-off gases (blue) on the 2.5 mm grid showing approximately half of the domain in axial direction (1600 × 816 of a total of 2624 × 816 cells).
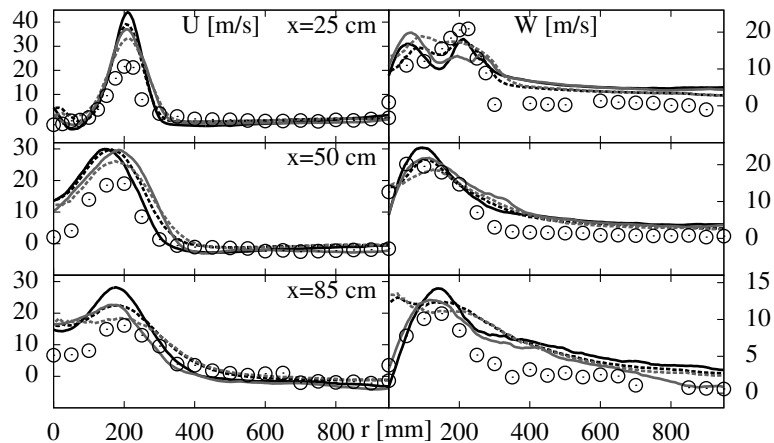
Figure 6.2: Mean axial (left) and circumferencial velocities (right) for the simulations on the 5 mm (—) and 2.5 mm (—) grid. Dashed lines represent particle mean axial and absolute circumferencial ($\langle |W| \rangle$) velocities. Scales are adjusted to each subplot.

particles are collected with a probe facing the upstream direction, explaining the large discrepancies between their RANS solutions and the experimental measurements . In the present LES we obtained the burnout statistics by collecting i) all particles and ii) only particles with an axial velocity of greater than -2 m/s, respectively. As can be seen, the conditional average slightly improves the prediction at the most upstream location. However, an over-prediction of the burnout at this location still remains, but a good agreement could be obtained further downstream. However, char combustion is over-predicted in the region between x=125 cm and x=195 cm. The burnout statistics are mostly independent of the grid resolution.

With the satisfactory overall agreement, further details can be explained in the next section.
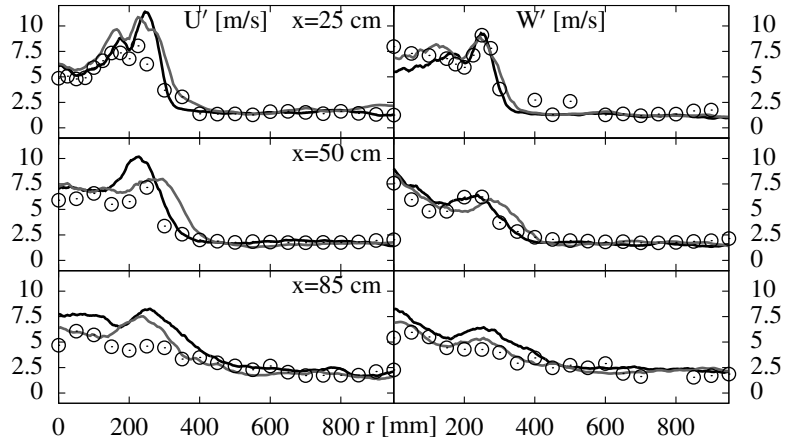
Figure 6.3: Fluctuations of the axial (left) and circumferencial velocities (right) for the simulations on the 5 mm (—) and 2.5 mm (—) grid. Scales are adjusted to each subplot.
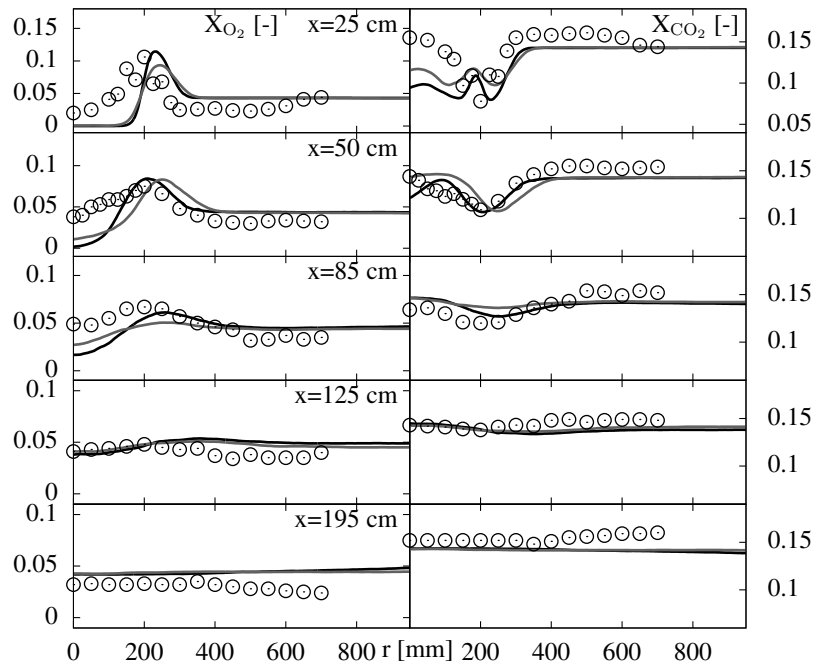
Figure 6.4: Mean oxygen (left) and carbon dioxide molar fractions (right) for the simulations on the 5 mm (—) and 2.5 mm (—) grid. Scales are adjusted to each subplot.
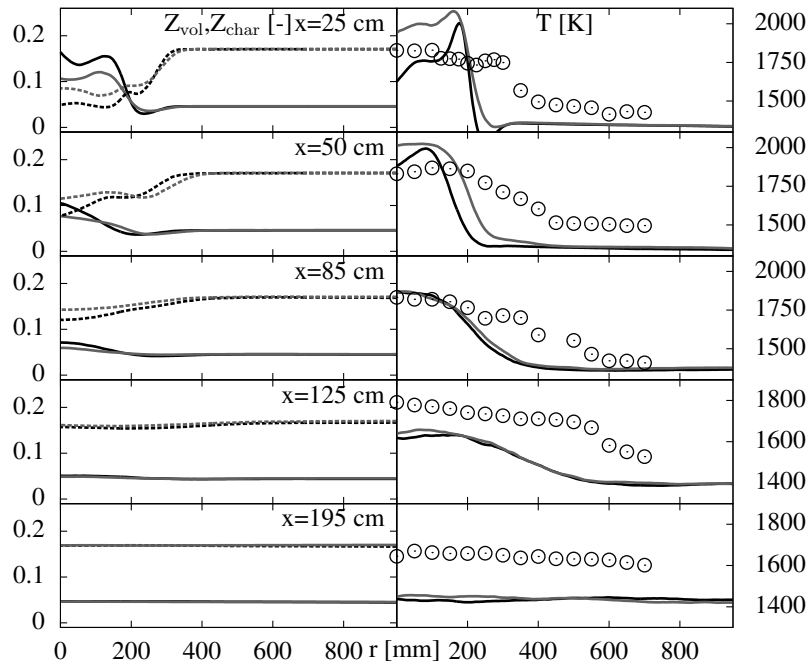
Figure 6.5: Mean volatile (—) and char-off gas mixture fractions (- -) (left) and temperature (right) for the simulations on the 5 mm (—) and 2.5 mm (—) grid. Scales are adjusted to each subplot.
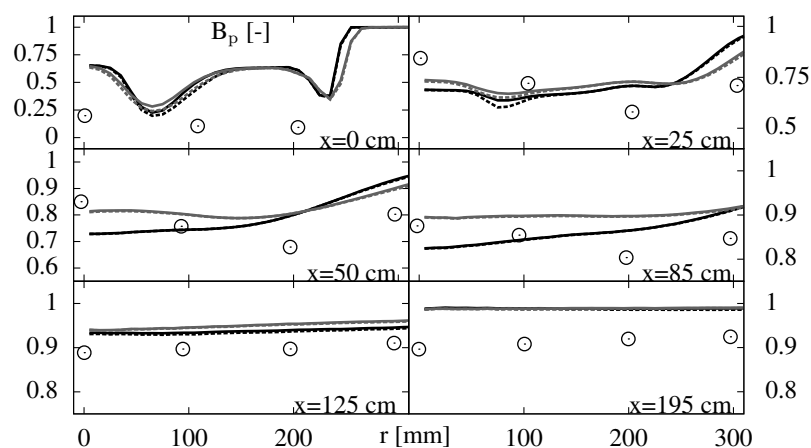
Figure 6.6: Mean particle burnout for the simulations on the 5 mm (—) and 2.5 mm (—) grid, dashed lines represent the conditioning on the probe suction velocity. Scales are adjusted to each subplot.
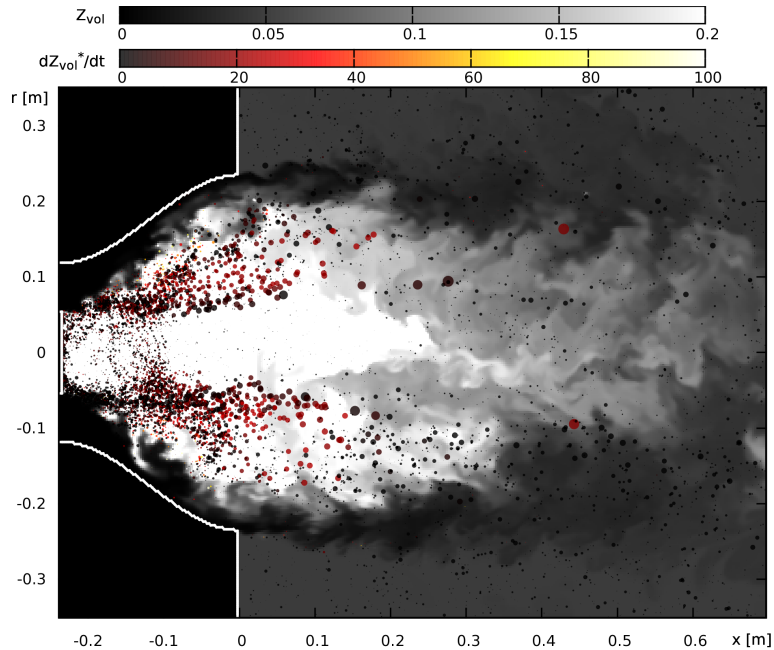
Figure 6.7: Particle volatile mixture fraction source normalized by initial particle mass and volatile gas mixture fraction field in the quarl region for the 2.5 mm grid simulation. Points are scaled by particle size.

6.5.2 Further Analysis

Figures 6.7 shows a combined plot of particle mixture fraction source term normalized by the initial particle mass and the Eulerian mixture fraction field for volatile gas, in a slice of one LES cell width in the quarl region. Particles are transported into the rich volatile gas region by the transport air, mostly without being entrained in the swirling combustion air flow. As they encounter reverse or stagnating flow, they are decelerated and deflected outwards, where they devolatilize further and more rapidly in the mixing layer of volatile gases and combustion air. After devolatilization, they are entrained in the combustion air flow, which transports them into the furnace. In the center region and in the recirculation zone at the bluff body, only a low amount of small recirculated particles can be seen. Larger particles have sufficient inertia to overcome the reverse flow. Figure 6.8 allows for a more detailed assessment of the processes in the furnace on the particle level by presenting mean heating rates of the different processes governing the particle heat balance. All particles in a tube with a diameter corresponding to the quarl exit in one instant in time are considered for averaging.

Upon entering the simulation domain, particles are heated up rapidly by convective heat transfer. While convective heating plays the dominant role in the quarl area, radiative cooling starts after only a few centimeters downstream of the inlet. This confirms the character of the flame stabilization relying on recirculation rather than radiation found in this and similar low-No_x burners [230, 250]. As can be observed in Fig. 6.7, particles move in axial direction where they are subjected to a hot reverse flow, heating them up significantly. The point where the particles are deflected outwards and are entrained by
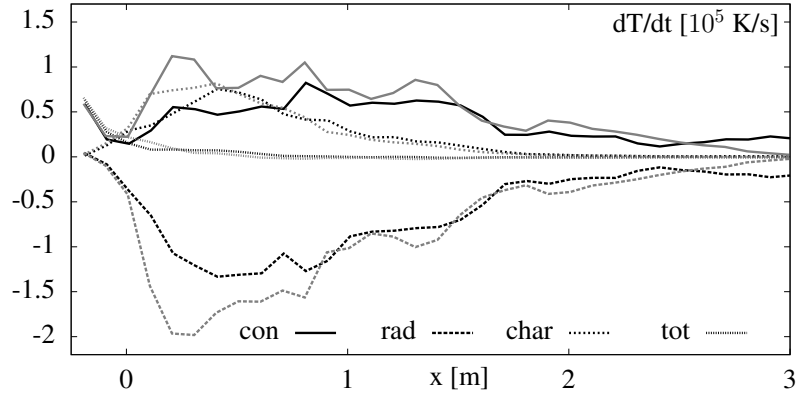
Figure 6.8: Mean particle heating rate for convective and radiative heat transfer and char combustion for the simulations on the 5 mm (—) and 2.5 mm (—) grid.

the swirling combustion air flow can be seen by the start of the heating through char combustion, as the hot devolatilized particles leave the oxygen depleted region. Up to around one to two quarl exit diameter downstream of the quarl exit, char combustion plays a similarly dominant role in the particle heating as convection. Overall, particles heat up slowly downstream of the quarl exit since heating due to char combustion and convection is balanced by radiative cooling. At approximately 1.5 m downstream of the quarl exit, the total heating rate becomes negative, with very low rates of the order of 100 K/s. Even further downstream, the particle heat exchange mechanism constitutes radiative loss of thermal energy to the walls with a fast return to thermal equilibrium through convective heating.

Figure 6.9 shows a scatter plot of temperature vs. the sum of the mixture fractions ($Z = Z_{\mathrm{char}} + Z_{\mathrm{vol}}$) colored by the mixture fraction ratio ($Z_2 = Z_{\mathrm{char}}/(Z_{\mathrm{char}} + Z_{\mathrm{vol}})$) and illustrates characteristics of the flamelet modeling in PCC. The two branches of volatile and char combustion can clearly be distinguished. The volatile flame is represented by an envelope with the highest temperatures. The temperatures are close to an exemplary adiabatic flamelet solution with inlet temperatures of 573 K and 343 K for air and volatile gas, respectively. The branch corresponding to the char burnout region however shows lower temperatures of around 1500 K featuring strong heat losses. The visible gap between volatile and char-off envelopes demonstrates the consecutive nature of volatile and char combustion, where the rich volatile flame first is diluted with combustion air, the resulting hot mixture with oxygen availability provides conditions for char oxidation to occur which subsequently enriches the mixture again.

Figure 6.10 presents the mean laminar and turbulent contributions to the scalar dissipation rate. As can clearly be seen, scalar dissipation rates are generally very low and show a strong separation between volatile and char combustion regions. As expected, the contribution of the resolved part increases with grid refinement. However, also the subgrid contribution increases slightly with grid refinement, which might be due to a slightly shifted flow field or the particle sources inducing larger mixture fraction gradients on the fine grid counteracting the lower turbulent viscosity.
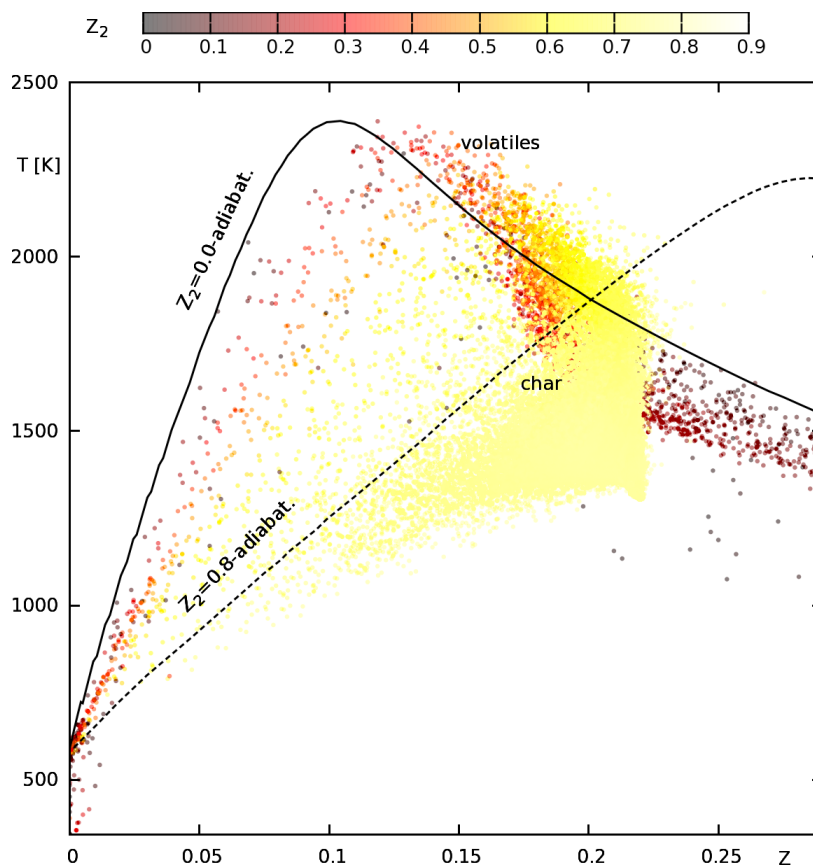
Figure 6.9: Temperature vs. mixture fraction sum colored by mixture fraction ratio ($Z_2 = Z_{\mathrm{char}}/(Z_{\mathrm{char}} + Z_{\mathrm{vol}})$) for the 2.5 mm grid. The lines represent an adiabatic volatile flame and an adiabatic flame with $Z_2=0.8$.
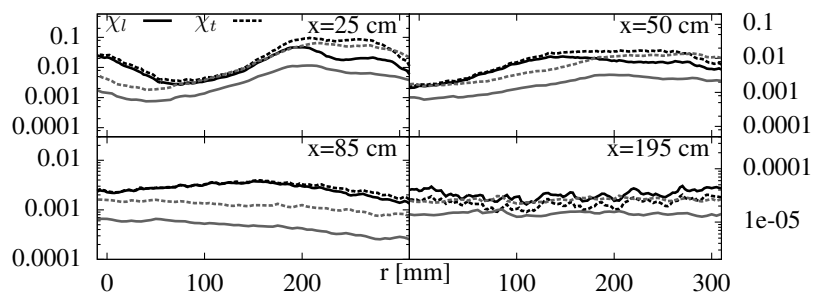
Figure 6.10: Laminar (χ_l) and turbulent (χ_t) contributions to the scalar dissipation rate on the 5 mm (—) and 2.5 mm (—) grid.

6.6   Conclusion

A massively parallel flamelet LES of a semi-industrial coal furnace has been conducted. The flamelet LES approach is validated against the comprehensive set of experimental data and a good agreement between LES and measurement is found. A subsequent analysis gave further qualitative and quantitative insight into the heating, devolatilization and char combustion processes in the turbulent environment. In particular, the averaged particle heating rates could confirm that the stabilization mechanism relies on swirl and recirculation. We will further investigate the present large data set in the future to further to assess the interactions of particles and turbulence.

An improvement of the modeling strategy should mainly be directed towards the description of the recirculation zone, the inclusion of tar species in the volatile gas, devolatilization and the prediction of CO. Additionally, a validation on other test cases is planned.

Acknowledgement

Chapter 7

Flamelet LES Modeling of Coal Combustion with Detailed Devolatilization by Directly Coupled CPD [199]

This chapter including all text, figures and tables is published in the Proceedings of the Combustion Institute 'Rieth, M., Clements, A.G., Rabaçal, M., Proch, F., Stein, O.T., Kempf, A.M. (2017). Flamelet LES modeling of coal combustion with detailed devolatilization by directly coupled CPD, Proceedings of the Combustion Institute, 36(2), 2181-2189.' [199] and is reprinted with permission from Elsevier. The author of this thesis contributed the code extension and development (including the incorporation of the combustion model and the devolatilization models and updates/optimization of other coal models), running of simulations, post-processing and paper writing. The author A.G. Clements contributed the basic CPD code and the author F. Proch the basic CFD code. The authors A.G. Clements, M. Rabaçal, O.T. Stein and A.M. Kempf contributed discussions, proof-reading and corrections. The author A.M. Kempf developed the original versions of the PsiPhi code.

This paper was awarded with the Distinguished Paper Award by the Combustion Institute in the Solid Fuel Combustion Colloquium at the 36th International Symposium on Combustion.

Abstract

A large eddy simulation (LES) with direct CPD devolatilization modeling and gas phase combustion modeling through a new flamelet approach is presented for the CRIEPI flame [77]. The devolatilization rates are directly determined from CPD for each coal particle. The flamelet is generated from non-premixed one-dimensional gaseous flames and is based on mixture fractions for volatiles and methane as well as on enthalpy and scalar dissipation rate. A transport equation for mixture fraction variance is combined with an assumed pdf approach for modeling turbulence-chemistry interaction. Special emphasis is put on

the influence of devolatilization, with a comparison of LES with direct CPD coupling to empirical models with fitted and standard rate constants. The results are further analyzed by scatter plots and phase space trajectories of the quantities of interest. The results show that large deviations between CPD and the fitted model exist on the instantaneous particle level. It is shown that the direct use of CPD in the LES is feasible and that the flamelet model is able to perform well. Some weaknesses specific to the CRIEPI flame are also discussed.

The results show that even with the detailed devolatilization modeling the volatile release is over-predicted but same trends can be observed as with the fitted empirical model. The conclusion that can be drawn from the results is that a) a fitted empirical model for the devolatilization is sufficient for predicting the mean quantities of this flame (and supposedly for other flames as well) and b) that the steady flamelet model as applied in this study is not sufficient for this particular flame and that further work is required on the gas phase and particle flame interaction modeling.

7.1   Introduction

Large eddy simulation (LES) is a promising tool for simulating pulverized coal combustion (PCC), due to its capability of predicting velocity fields and mixing well, which has become the weakest link in Reynolds-averaged simulations (RANS) with the advancement of the coal sub-models. This work aims at advancing the LES of PCC by a) employing the flamelet model, which has been successfully validated for predictions of gaseous and spray combustion LES [85, 162, 174] and recently extended for PCC simulations and tested on simplified cases [238, 248, 263] but not been applied to LES yet and by b) the direct incorporation of the Chemical Percolation model for Devolatilization (CPD) [48, 49, 64].

Since the first application of PCC LES [114] by Kurose & Makino, several studies have followed, mainly in the past five years [26, 30, 43, 53, 57, 140, 153, 156, 157, 189, 221, 245, 252, 264]. These studies mostly relied on a much simplified description of the gas phase combustion using the eddy breakup and eddy dissipation models, which struggle to take into account detailed chemistry and turbulence-chemistry interaction effects. The flamelet model, combined with an assumed PDF, incorporates these effects at a low cost and high numerical efficiency. The first application of the flamelet model to PCC is reported by Williams et al. [257] for volatile combustion, followed by Vascellari et al. [238] and Xu et al. [263], who investigated flamelet methods for resolved single coal particle simulations. A flamelet model that takes volatile and char combustion into account has recently been presented by Watanabe & Yamamoto [248], who tested the approach on a two-dimensional simulation of a coal jet, showing good agreement with data from finite rate chemistry.

The LES and the majority of RANS of PCC (e.g. [153, 189, 245]) have employed simple empirical models to treat devolatilization, often relying on a single or two competing Arrhenius-type rates to describe the volatile yield as a function of coal particle temperature. Some of the studies apply standard rates that have been adjusted to a general set of coals and operating conditions, while other studies use rates fitted to either

experimental measurements [153] or to predictions from more detailed devolatilization models, such as the CPD model [189, 236]. However, the empirical fitting of these rates can only represent a specific heating rate profile - which may not be appropriate for an LES, as a wide range of particle trajectories will typically be resolved, spanning over a wide range of particle heating rates. Assuming a constant heating rate would provide an artificial constraint on the modelling. The more general and predictive but costly approach is to use the detailed CPD model directly in the LES, which is investigated in this work; as far as we know for the first time. The CRIEPI jet flame experiment [77, 78, 79] has been chosen as the test case for the validation of the approach due to the small and simple setup that permits parameter and grid studies and for the flame being dominated by volatile release and gaseous combustion. The results of previous numerical studies of this burner [10, 20, 53, 66, 67, 221, 252, 268] are summarized in Sec. 7.5 along with the results of the present study.

7.2 Gas Phase and Radiation Modeling

The flamelet model is based on two mixture fractions for volatile gas and methane from the supporting pilot. The approach is similar to previous work on split injection in Diesel engines [68, 69], RANS/PDF of PCC [223] and the recently introduced flamelet model for PCC [248]. The mixture fractions are described by Favre-filtered transport equations. While the methane transport equation does not contain a source term, there is one in the volatile gas mixture fraction for the mass released during devolatilization.

The current approach relies on one-dimensional steady non-premixed counter-flow flame calculations to generate the flamelet table. This corresponds to the approach by Watanabe & Yamamoto [248] and assumes a weak interaction between the two streams in mixture fraction space [81].

The flamelet table is stored based on the transformed mixture fractions $Z = Z_{CH_4} + Z_{vol}$ and $Z_2 = Z_{CH_4}/(Z_{CH_4} + Z_{vol})$ and normalized enthalpy and scalar dissipation rate. The table is obtained from computing non-premixed flames with Cantera [62] with a different mixture fraction ratio $Z_2 = Z_{CH_4}/(Z_{CH_4} + Z_{vol})$, enthalpy and strain rate. The radiative and convective heat transfer requires the solution of an enthalpy transport equation. The variation in enthalpy is achieved by scaling the source term in the energy equation by a factor of $(1 - f_L)$, where f_L represents the relative heat loss [184]. A Lewis number of unity is assumed in all calculations.

Effects of strain on the flamelets are incorporated by employing the scalar dissipation rate as a flamelet parameter, of which only one is considered for the sum of mixture fractions ($Z = Z_{CH_4} + Z_{vol}$). Assuming an equilibrium between production and dissipation, the scalar dissipation rate can be obtained by: $\chi = 2D_{eff}(\partial Z/\partial x_i)^2$, where D_{eff} is the sum of laminar (D_l) and turbulent (D_t) diffusivity. The influence of turbulence on the flamelets is treated with the assumed top-hat pdf approach [50, 152], which is especially advantageous over the β-pdf assumption for the present study because it can yield correct mixing behaviour in a multi-stream situation and does not require an additional table dimension. The variance of the sum of mixture fractions is obtained from a transport equation [158] that is often used in spray flame LES [204, 227].

Table 7.1: Properties of the Newlands bituminous coal fired in the experiment [77] and the modeled gas composition.

Ultimate Analysis (dry)		Proximate Analysis	
C	71.9%	ash	15.2%
H	4.4%	volatiles	26.9%
N	1.5%	fixed carbon	57.9%
S	0.44%	moisture	2.0%
O	6.53%		
LHV	28.1 MJ/kg		

Modeled gas composition (mass fractions)					
CH_4	C_2H_2	C_2H_4	CO	H_2	N_2
0.082	0.595	0.088	0.052	0.009	0.034
CO_2	H_2O				
0.041	0.010				

Pre-integration of the table for the use with the assumed top-hat pdf allows for efficient data retrieval from the flamelet table, which remains four-dimensional. The table dimensions are $201 \times 11 \times 11 \times 11$ in mixture fraction sum, mixture fraction ratio, enthalpy and scalar dissipation rate directions, respectively.

Radiative heat transfer is solved with the discrete ordinates method [47, 231] using the S8 quadrature set. The grey weighted sum of grey gases model (GWSGG) is used to model radiative properties of the combustion environment with parameters from Kangwanpongpan et al. [89].

7.3   Coal Particle Modeling

The coal properties are summarized in Table 7.1 [77]. The flamelet model requires the specification of the volatile gas that can be associated with detailed kinetics, instead of a postulate substance, which is often used in the eddy break-up or eddy dissipation models. The volatile gas composition is obtained by distributing the elements among common species found in the volatile gas under high heating rate conditions [167, 223] instead of using CPD to obtain the composition (e.g. [66]). The approach by Petersen & Werther [167] was extended to also incorporate H_2O. Different from CPD this approach ensures elemental mass conservation. The composition obtained is given in Table 7.1. The GRI 3.0 mechanism (53 species, 325 reactions) [214] is used to create the flamelet table, and the tar species (C_6H_6) is replaced by C_2H_2 [63, 238]. The enthalpy solved by the LES and based on the modeled composition is corrected during the flamelet table access by a scaled heat release, such that the correct heating value is recovered to eliminate the difference between experimental heating value and the heating value of the modeled volatile gas. The models used to describe devolatilization are the single first order reaction (SFOR) model by Badzioch & Hawksley [2], the CPD model developed by Fletcher and co-workers [48, 49, 64] and the Kobayashi model with two competing rates [108] (CRM*, the star indicates that this model is, unlike the other two, not adjusted for this coal and conditions). The two empirical devolatilization models (SFOR and CRM*)
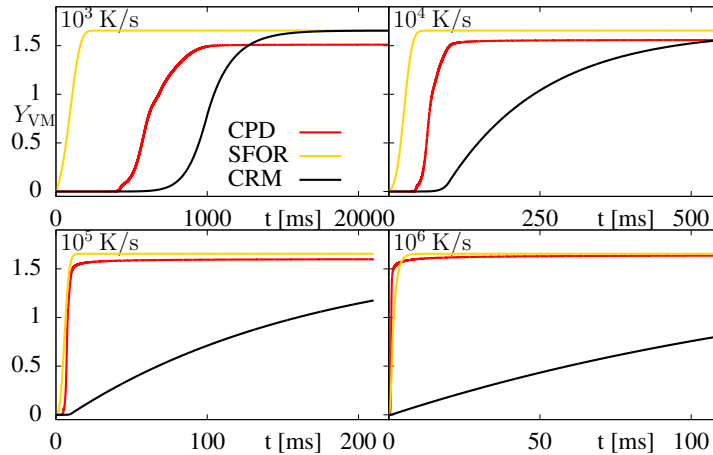
Figure 7.1: Volatile yield normalized by the volatile matter from proximate analysis as a function of time for different heating rates and devolatilization models.

describe the devolatilization with one or two fitted Arrhenius expressions. In the case of the SFOR we apply the fitted rates by Franchetti et al. [53], in the case of CRM* we apply the standard rates. Both models have been tested in previous simulations of the CRIEPI jet flame [20, 53, 252, 268] and hence been chosen here for the comparison. The same volatile composition based on the high temperature volatile yield is used for all three cases. This implies that only a single yield is used for CRM* and that the gas composition is independent of heating rate for the CPD model. Any heating rate dependent composition increases the table size by at least one dimension.

Figure 7.1 illustrates the large differences between the models for zero-dimensional devolatilization calculations at different constant heating rates (heating from 300 to 1300 K with subsequent hold at 1300 K). The phenomenological CPD model describes the devolatilization based on a network model and lattice statistics, which describe the devolatilization process by the breaking of bonds between aromatic clusters in the coal and the subsequent formation of light gas, tar, metaplast and char. The model is based on three reaction rates for the evolution of labile bridges, chain ends and char from which quantities such as the volatile release rate can be derived.

The high heating rate volatile yield is assumed to be $VM_{hhr} = 0.525$, which was obtained from a CPD calculation with a heating rate of 10^6 K/s and applied to the runs with all models for better comparison. A run with CPD and without the constraint of a maximum volatile yield has been performed, which showed a slightly higher maximum value of $VM_{hhr} = 0.54$ due to some (small) particles experiencing higher heating rates. At these high heating rate/temperature conditions, variations in heating rates have only a small impact on the final yield [108].

Smith's intrinsic model has been applied for char combustion [208, 215, 223]. However, the impact of char combustion on the gas phase has not been taken into account (unlike the effect on the particles), due to the memory constraint associated with the multidimensional flamelet table. This issue only arises with natural gas assisted PCC, necessitating the inclusion of a third mixture fraction for the pilot flame. However, the char-off gas mixture fraction has been added as a tracer to confirm the small importance

on the numerical results: the maximum char-off gas mixture fractions were of the order of 10^{-3} and 10^{-5} for CRM* and CPD/SFOR, respectively, which is in agreement to previous numerical studies [53, 221, 268] and can be neglected.

7.4   Experiment and Numerical Setup

The simulated coal jet flame was developed by the Japanese Central Research Institute of Electric Power Industry (CRIEPI) [77, 78, 79]. The Newlands bituminous coal is supplied by a pipe of 6 mm diameter, which is surrounded by a 0.5 mm thick wall and an annular methane supply of 0.5 mm width. The feed rates of coal, air and methane are $1.49 \cdot 10^{-4}$ kg/s, $1.8 \cdot 10^{-4}$ m^3/s and $2.33 \cdot 10^{-5}$ m^3/s, respectively. The Reynolds-number based on the central jet is 2544. The thermal inputs of coal and methane are 4.19 and 0.83 kW, respectively. Measurements were taken with Laser Doppler Velocimetry, Shadow Doppler Particle Analyzer, two-color radiation pyrometers and sampling probes.

The simulation domain is a rectangular box of 200 mm length and a cross-section of 50 mm × 50 mm. The air and coal inlet velocity follow a power law, such that the centerline velocity and mass flow match with the experiment. Only a low inflow turbulence level of 5% is prescribed, using Klein's inflow generator [98, 103]. The particle diameter at the inflow is determined by stochastic sampling from a measured size distribution [66]. Our low-Mach finite volume in-house code PsiPhi is used to obtain the simulation results, which has been successfully used for PCC LES [53, 189] and many other combustion systems before [97, 184, 187], relying on methods used for combustion LES since 2000 [99]. The discretization relies on a total variation diminishing scheme of (up to) second order for advective fluxes of scalars and on a second order central difference scheme for all other fluxes. A predictor-corrector scheme is employed with the Poisson equation solved by a Gauss-Seidel solver with successive over-relaxation. The influence of the grid resolution has been tested on grids with cubic cells of 0.5 and 0.25 mm edge-length, resulting in approximately 4 and 36 million cells, respectively . The simulations were performed on 576 and 2048 cores on SuperMUC and cost around 4k and 40k core-h, respectively, for a physical run-time of overall 0.4 s.

The direct use of CPD did not increase the cost of the simulations significantly. On the coarse grid, where each computational core contained the largest number of simulated coal particles on average, the fraction of the cost of devolatilization compared to the overall computation is 5.9% and 1.1% for CPD and SFOR, respectively. It should be noted though, that the particle loading per core is low in this case. The overall cost of the CPD compared to the particle part of the code is around 20% (including mapping operations between Eulerian and Lagrangian phase). The overall number of particles present in the computational domain is approximately 450k for SFOR/CPD and 420k for CRM*.

7.5 Results

7.5.1 Experimental and Previous Numerical Findings

The CRIEPI jet flame has been previously simulated with RANS [10, 67], RANS/PDF [20, 268], LES [53, 221, 252] and recently DNS [66]. One of the major common findings among these studies is that the oxygen consumption is too rapid, often associated with an accelerated rate of production of carbon dioxide concentrations. This behavior might be linked to the observation that only a small amount of coal is burned: only 44.6% of the volatile matter from the proximate analysis, or approximately 12% of the coal mass, was emitted as volatiles [78], which is often over-predicted by simulations. The studies by Bermudez et al. [10], Zhao & Haworth [268] and Cai et al. [20] address this problem explicitly. The latter study emphasizes the importance of the devolatilization model while other studies, e.g. by Stein et al. [221] attribute the differences in oxygen consumption to the simplistic turbulence-chemistry interaction modeling (eddy break-up). However, given the large scatter between the different numerical results, the behavior of the flame and the importance of the different sub-models is not yet fully understood.

7.5.2 Results

Figure 7.2 shows the instantaneous particle devolatilization rates normalized by the initial particle mass and the volatile gas mixture fraction for the simulations with CPD, SFOR and CRM*; Fig. 7.3 illustrates the corresponding devolatilization rate PDFs. The first observation is that devolatilization rates vary by an order of magnitude between the SFOR/CPD and standard CRM* model, which significantly affects the volatile gas mixture fraction field. Correspondingly, CRM* shows a narrow PDF with low devolatilization rates. SFOR and CRM* show a similar behavior of broader PDFs towards higher values of up to approx. 250 s^{-1}. Only CRM* predicts rates above this value. For the CRM* simulation, an inner and outer volatile flame can clearly be distinguished even at an axial distance of 100 mm as well as further downstream, whereas with the CPD and SFOR model the inner volatile flame merges at an axial distance of 50-60 mm.

While CPD and SFOR simulations show a similar behavior regarding the volatile flame, CPD shows a much broader distribution of devolatilization rates.

Figure 7.4 shows the PDFs of particle heating rate for particles between 1 and 99% of completion of devolatilization. The earlier onset of devolatilization shifts the SFOR results towards the higher heating rates, which is similarly demonstrated with the CPD model results. The behavior of the simulation with CRM* does not show the tail towards high heating rates, which can be explained by devolatilization starting at high temperatures only.

The stoichiometric methane mixture fraction iso-line in Fig. 7.2 illustrates the significant role of the methane pilot for the particle heat-up and ignition. Table 7.2 quantifies the difference in devolatilization rates observed in terms of the fractions of the (dry) coal mass released as volatiles in the three different simulations obtained from mass averaged values from the particles leaving the simulation domain. In accordance with Figs 7.2 and 7.3, the amount of volatiles released differs significantly between CPD/SFOR and CRM*.
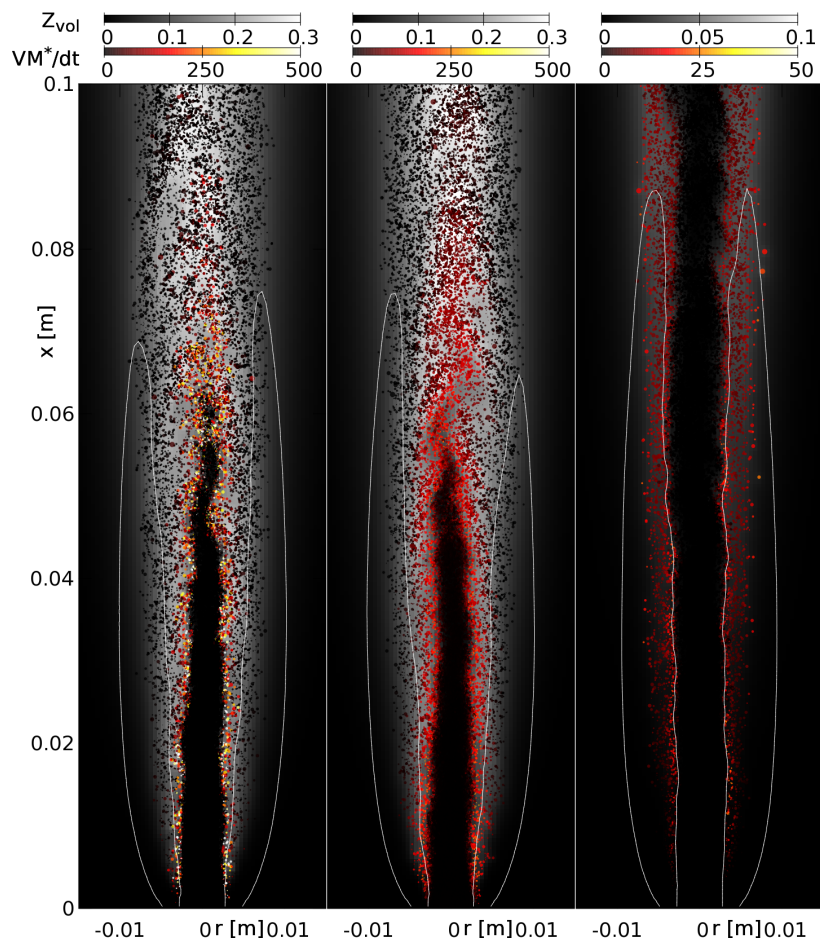
Figure 7.2: Particle devolatilization rate normalized by initial particle mass and gas phase volatile mixture fraction. Left: CPD, middle: SFOR, right: CRM*. The white iso-lines correspond to $Z_{CH_4} = Z_{CH_4,st}$.
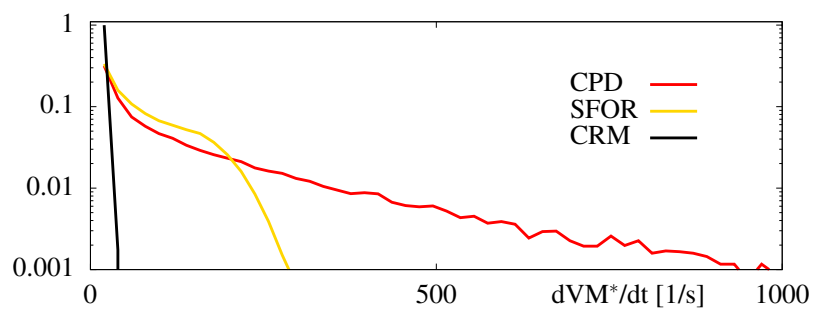
Figure 7.3: PDFs of normalized particle devolatilization rates.
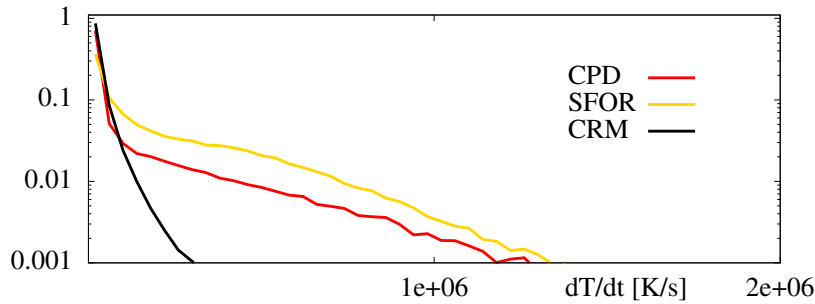
Figure 7.4: PDFs of particle heating rates for particles between 1 and 99% of completion of devolatilization.

Table 7.2: Fraction of particle mass released as volatiles (dry). Experiment: 0.12 [78].

	CPD	SFOR	CRM*
coarse	0.424	0.445	0.100
fine	0.428	0.445	0.109

While SFOR/CPD predict full/almost full loss of volatile matter (0.445), only around 0.1 of the particle matter is released as volatile gas for CRM* due to the one order of magnitude lower devolatilization rates. However, this is close to the experimental value of 0.12. Figure 7.5 presents the species molar fractions along the centerline for the three simulations. In accordance to the significant over-estimation of volatile release, CPD and SFOR show a strong under-prediction of N_2 and O_2, which is the exact behavior of previous studies relying on fitted devolatilization rate constants [53, 221, 252]. The direct comparison of CPD and SFOR both applied in the LES shows that a 'well fitted' SFOR model is able to predict the global properties of this flame with good agreement to the CPD model. This result is consistent with observations from RANS by Saha et al. [205], but might not hold in LES of more turbulent cases. Generally, results on the fine grid show slightly better results than on the coarse grid, indicating that the results are almost grid independent for the grids tested here.

The fact that the simulation with the CRM* model with standard rates appears to predict the species profiles well is somewhat surprising, but in accordance to previous studies that applied this model [20, 268]. The cause for this behavior might be compensating errors; an incorrect representation of the methane flame lift-off, and its interaction with the particles or missing effects that may become dominant with the advancement of sub-models for processes such as devolatilization (e.g. thermophoresis). The experimental results (OH-LIF images) [77] indicate that the outer methane flame is attached while the inner methane flame may be lifted and that volatile ignition may occur at an axial distance to the nozzle of around 20-30 mm. With the steady flamelet model based on scalar dissipation rate, the methane flame burns anchored at the nozzle, leading to volatile ignition occurring right downstream of the nozzle. The feedback of volatile combustion and devolatilization eventually leads to an over-prediction of volatile release. With an anchored methane flame the slow CRM* rates are compensated by too early particle heat-up. A correct lift-off prediction would delay the volatile ignition and result in a lower amount of volatiles released.
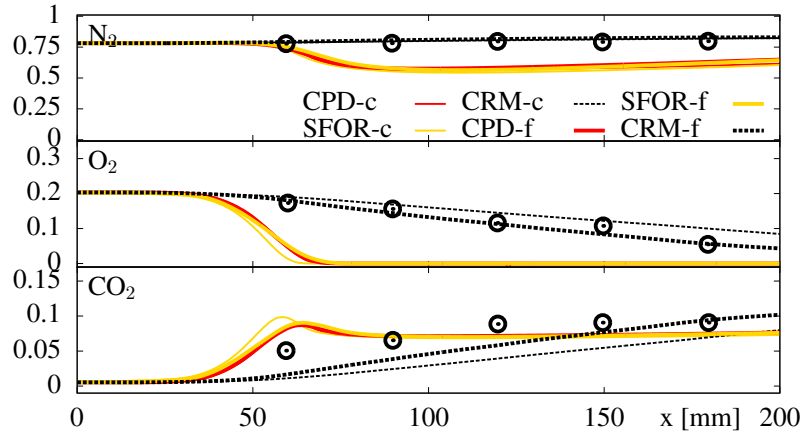
Figure 7.5: Species molar fractions (dry) along the centerline. Top: N_2, middle: O_2, bottom: CO_2 for fine (f) and coarse (c) runs.
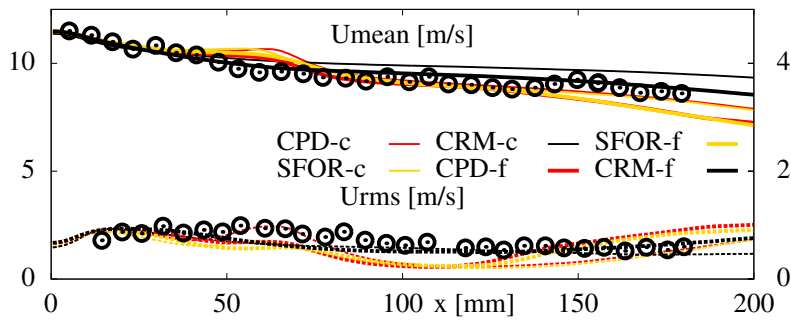
Figure 7.6: Axial mean and rms particle velocity along the centerline.

However, it should be noted that a fitted CRM or a set of different (faster) rates could be used (e.g. [234]), which would result in the CRM prediction being much closer to SFOR/CPD.

The results indicate that if the overall amount of volatiles released is matched by the simulation, the flamelet is able to predict the volatile combustion well, despite this flame showing non-premixed as well as premixed behavior [66].

Figure 7.6 presents the mean and rms axial velocity along the centerline, and Fig. 7.7 presents these values along the radius for the three axial locations x=60, 120 and 180 mm downstream of the nozzle. All simulations are able to predict the axial velocity on the centerline well. The profiles along the radius show an under-prediction of axial velocities for axial distances of 120 and 180 mm. The velocity differences can partially be attributed to the differences in heat and mass release through devolatilization and volatile combustion but the trend is the same for all simulations. A comparison with the gas phase velocities (not shown) illustrates that particle and gas phase are in kinetic equilibrium close to the centerline. Particle velocities are slightly higher than the gas phase velocities for larger radii due to particle interia.
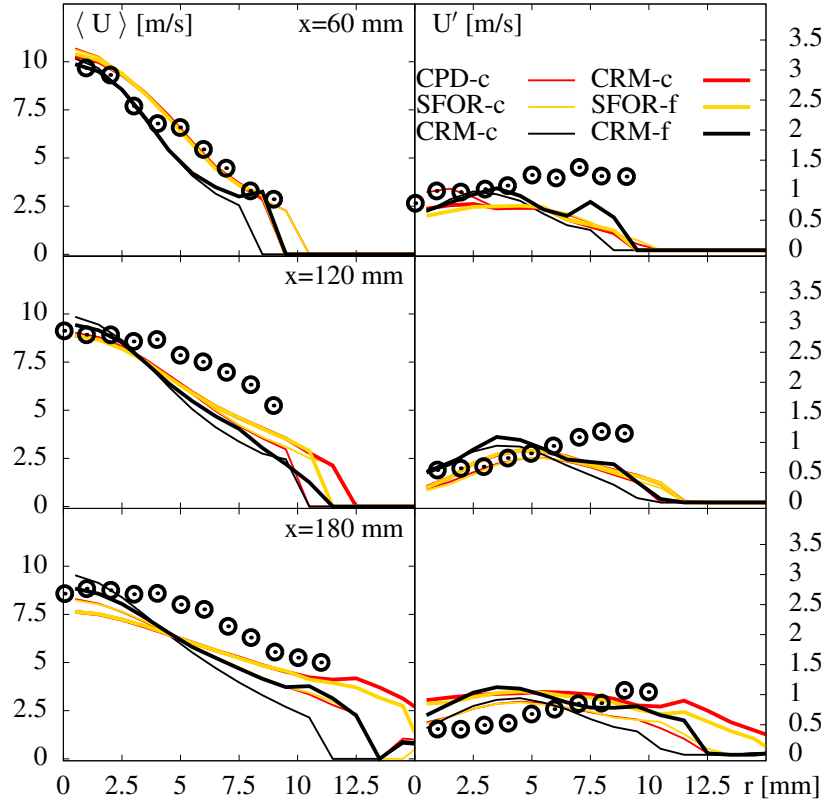
Figure 7.7: Axial mean and rms particle velocity along the radial direction at the axial positions x=60, 120, 180 mm.

7.5.3   Further Analysis

Figure 7.8 shows scatter plots of CO_2 against the sum of mixture fractions, $Z = Z_{vol} + Z_{CH_4}$, colored by the mixture fraction ratio, $Z_2 = Z_{CH_4}/(Z_{vol} + Z_{CH_4})$. It can be observed that the methane flame features the lower envelope accessed in CO_2-Z space and extends from Z=0 to Z=1 due to pure methane being supplied at the pilot inlet. The volatile flame represents the upper envelope due to its higher C/H-ratio. The space accessed in Z direction depends on the amount of volatiles released, hence the CRM* simulation shows much lower peak values of Z of around 0.1 instead of values of 0.3 to 0.4 for CPD and SFOR, respectively. Figure 7.9 presents particle trajectories in volatile yield-particle temperature space. The volatile yield is normalized by the amount of volatile matter from the proximate analysis and the color indicates the particle residence time. In accordance to the results described above, the trajectories for CRM* are shifted towards higher temperatures. The SFOR simulation shows a much earlier start of devolatilization, even below 600 K, and a rapid evolution towards the maximum volatile yield within less than 10 ms. Compared to SFOR, the CPD results show a later start of devolatilization, i.e. for temperatures around 800 K. Particles devolatilize within a similar amount of time as with the SFOR model. However, a portion of the particles do not reach the final high heating rate volatile yield due to heating up less rapidly, e.g. due to a larger particle size.

A striking difference is that with direct CPD, the correlation between particle tem-
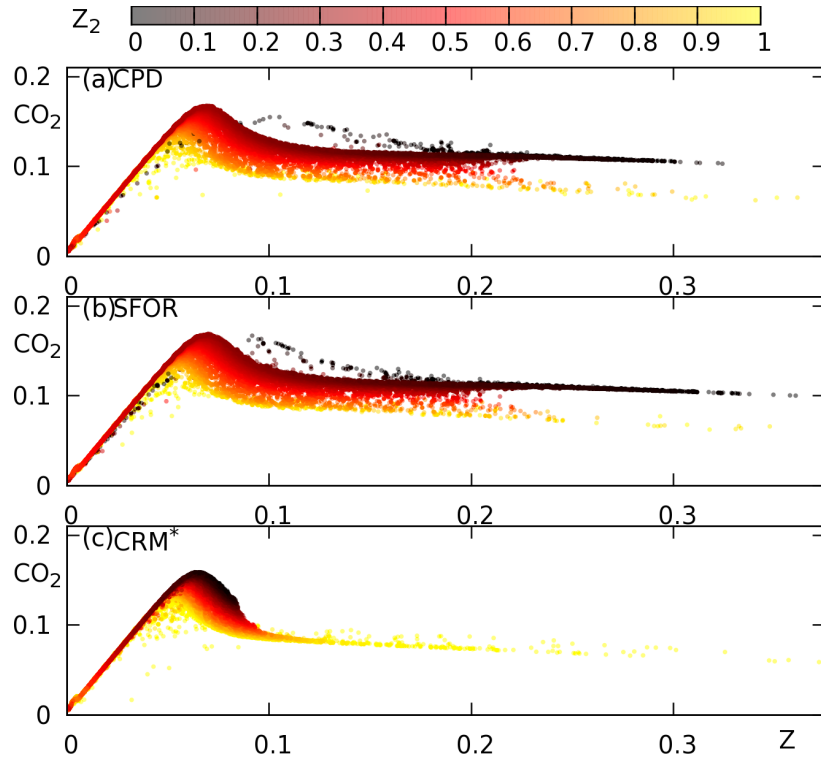
Figure 7.8: Scatterplot of CO_2 vs. mixture fraction sum $Z = Z_{vol} + Z_{CH_4}$ colored by the mixture fraction ratio $Z_2 = Z_{CH_4}/(Z_{vol} + Z_{CH_4})$. (a): CPD, (b): SFOR, (c): CRM*.

perature and volatile yield is much higher than for CRM* and SFOR. In the SFOR, the particle temperature is the only input parameter for evaluating the devolatilization rate, which means that for a specific temperature that the particle has reached, a large scatter in volatile yield can be observed. The input to the CPD model is the particle's structural information, which incorporates the particle's heating history and the current temperature and which apparently results in particles behaving more alike in volatile yield-particle temperature space.

In possession of this result for this particular flame, a better fit than the Arrhenius-type used in the SFOR could be found to describe the temperature dependent volatile yield. Alternatively, an initial coarse LES (or RANS) with direct CPD could be employed to obtain a fit for SFOR or CRM (or related models), following the idea presented by Rabaçal et al. [189], where (0D-)CPD and LES are coupled indirectly in an iterative optimization procedure to obtain fitted rates.

The low amount of scatter for the CPD results shown in Fig. 7.9 is in contrast to the broad distribution of devolatilization rates as observed in Figs. 7.2 and 7.3 and in Fig. 7.10, which shows the particle volatile yield evolution as a function of residence time. Fig 7.10 shows that the individual particle devolatilization histories look significantly different between CPD and SFOR, but for both models devolatilization on average essentially occurs within similar time frames, with the CPD model allowing for more scatter with respect to the timescales of devolatilization. Figure 7.10 also illustrates again the large deviation in devolatilization timescales between SFOR/CPD and CRM*.
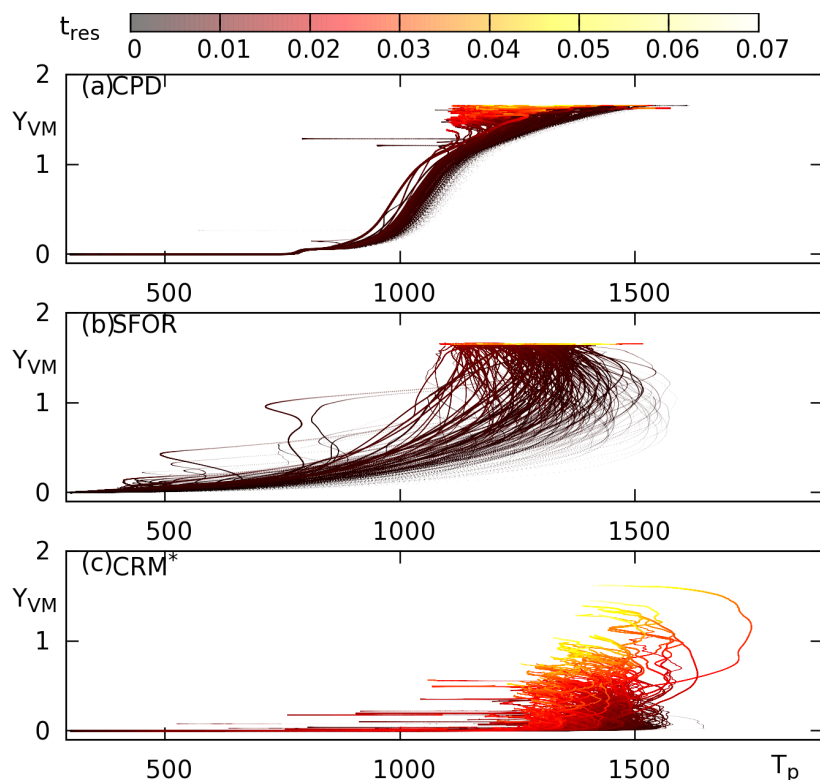
Figure 7.9: Particle trajectories in volatile yield-particle temperature space colored by particle residence time. (a): CPD, (b): SFOR, (c): CRM*. Volatile yield is normalized by the volatile matter given by the proximate analysis.

7.6 Conclusion

A new direct-CPD-flamelet model for LES has been tested for the CRIEPI flame; comparisons were presented for three different devolatilization models. The direct CPD model shows a significant effect on the individual particle level, but a cheaper SFOR model can yield similar averaged species concentrations if the SFOR model is fitted well. The CRM* model achieved the apparent agreement with experimental data, which was also observed in previous simulations of the flame – in spite of CRM* being fitted to a different coal. This apparent agreement is likely due to compensating effects of the under predicted devolatilization rate and the under predicted pilot lift-off height – a peculiarity of the investigated jet flame that is of little relevance for real, unassisted coal flames. Overall, the new direct-CPD-flamelet model provides results that are consistent with previous work, while correctly including individual particle heat-up histories. The direct CPD coupling avoids the need for tuning devolatilization model constants and may yield better results where different particles experience very different heat-up rates — which may even affect flame stabilization, for example in large low-NOx burners that will be the focus of future testing.
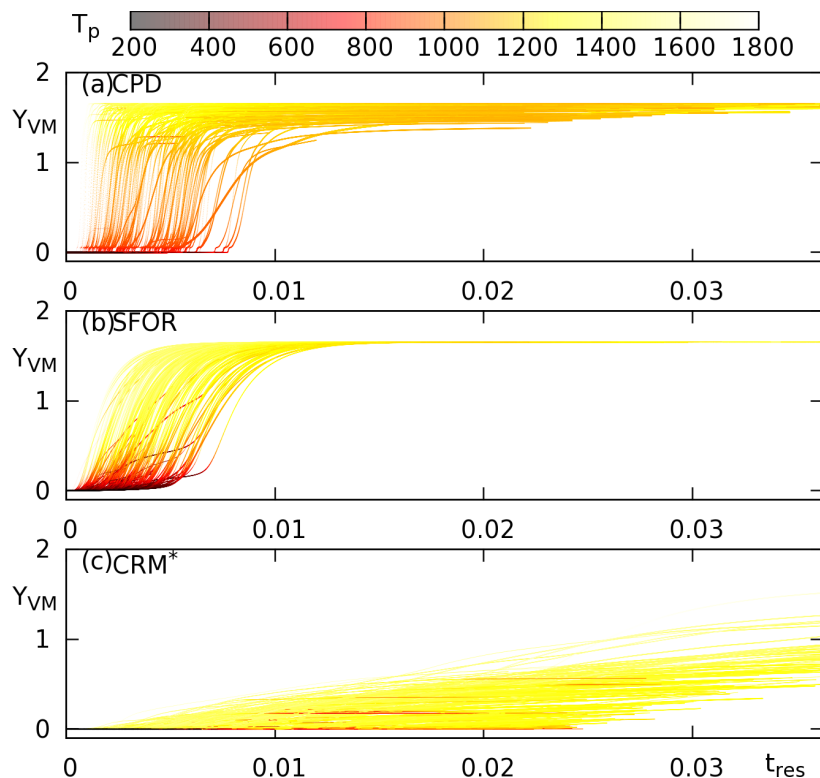
Figure 7.10: Particle trajectories in volatile yield-residence time space colored by particle temperature. (a): CPD, (b): SFOR, (c): CRM*. Volatile yield is normalized by the volatile matter given by the proximate analysis.

Acknowledgement

Chapter 8

Carrier-Phase DNS of Pulverized Coal Particle Ignition and Volatile Burning in a Turbulent Mixing Layer [200]

This chapter including all text, figures and tables is published Fuel 'Rieth, M., Kempf, A.M., Kronenburg, A., Stein, O.T. (2018). Carrier-phase DNS of pulverized coal particle ignition and volatile burning in a turbulent mixing layer, Fuel, 212, 364-374.' [200] and is reprinted with permission from Elsevier. The the author of this thesis contributed the code extension and development (including finite rate chemistry, detailed transport and the required solvers), running of simulations, post-processing and large parts of the paper writing. The author O.T. Stein contributed most of the introduction section. The authors O.T. Stein, A. Kronenburg and A.M. Kempf contributed discussions, proof-reading and corrections. The author A.M. Kempf developed the original versions of the PsiPhi code.

Abstract

Direct numerical simulations (DNS) of a three-dimensional turbulent mixing layer are performed, where coal particles seeded in an air stream mix with hot lean combustion products in a second stream. This case mimicks conditions of a pulverized coal flame stabilized by hot products such as found in industrial furnaces. Particles are heated up by the hot gases and devolatilize, followed by volatile combustion in the gas phase. The carrier-phase DNS resolves all relevant scales of the fluid phase except the boundary layers around individual particles. The simulation results are assessed in terms of instantaneous contour plots of relevant quantities, spatially averaged statistics, scatter plots and (pseudo-)flamelets. The analysis provides insight into the mechanisms of solid particle ignition and burning stabilized by hot combustion products, as well as the flame structure and combustion mode. It is shown that ignition initially occurs at very lean conditions when particles are entrained in the hot gases. Subsequently volatile combustion proceeds in non-premixed as well as premixed combustion modes, characterized by means of the

flame index, with an overall higher heat release in non-premixed zones. At late times two flames can be clearly distinguished, an upper flame burning into the air carrying the particles and a lower flame burning into the lean products. The latter flame shows a pure non-premixed behavior, while the former illustrates a complex flame structure with both premixed and non-premixed modes, as well as flame quenching. The DNS database and initial analysis lay the foundation for future systematic studies in similar configurations and support the development of models suitable for the combustion of solid fuel particles.

8.1   Introduction

Pulverized coal combustion (PCC) is still the principal technology for producing electrical base load power, as it can be implemented with known technology and is supported by a reliable supply chain. However, PCC is a major source of pollution and the environmental issues associated with pollutants like NO_x, SO_x or mercury-containing species, as well as the CO_2 footprint of PCC warrant a thorough investigation to achieve improvements. Despite recent progress on experimental techniques for studying PCC [4, 9, 73, 111, 138, 225], detailed, non-intrusive measurements of coal flames remain difficult, which is mainly caused by the hostile environment in PCC boilers and limited optical access. Numerical simulations provide an alternative source of information and allow for insights into the underlying physical and chemical processes. The flow environment in industrial PCC boilers is turbulent and traditionally Reynolds-averaged Navier Stokes (RANS) approaches have been used to model turbulent PCC. While RANS offers a cost-effective (time-averaged) description of PCC it requires major modeling assumptions which limit its predictive capability. Recently large eddy simulation (LES) has been employed to study PCC, which is a more costly turbulence modeling approach than RANS, but offers more accurate simulation results. LES resolves the largest scales of turbulence and requires modeling of the small scales only. Initially PCC-LES has been used to simulate simplified jet-type configurations [53, 114, 156, 199, 221, 264], but the past 5 years have seen a number of more realistic simulations of swirl-stabilized coal flames [26, 57, 76, 140, 153, 189, 246]. The implication of applying LES to PCC is that all processes near the particle surface remain unresolved and comprehensive LES subgrid models are required. A modeling approach of particular interest for PCC is the flamelet model [248] and current research efforts focus on finding LES subgrid closures based on flamelets [201, 202, 247, 255]. Subgrid closures would ideally be obtained from (full) direct numerical simulations (DNS), subject to the paradigm of resolving all turbulence scales from integral to Kolmogorov and all near- and intra-particle processes. Such full DNS of PCC is impossible at present, but fundamental insights can be obtained from alternative resolved flow simulation approaches like one-dimensional models, resolved laminar flow simulations (RLS), and direct numerical simulations of the carrier phase (CP-DNS). Goshayeshi, McConnell and Sutherland performed one-dimensional studies and compared various devolatilisation and homogeneous chemistry models [63], as well as different char conversion approaches [127]. Vascellari, Tufano et al. carried out RLS of single coal particle ignition and studied ignition delay times in various gas atmospheres [233]. They also used RLS to assess flamelet modeling of homogeneous ignition and volatile burning

[237, 238]. Farazi, Sayadi et al. used RLS to study both single char particle and char particle array combustion for various gas atmospheres and particle Reynolds numbers [44, 207]. The cited RLS studies resolve the particle boundary layers and the associated resolution requirements do not permit their application to real burners. Messig et al. [134] and Wen et al. [254] simulated PCC stabilized on laminar counterflow burners and performed detailed flame structure analyses for flamelet modeling. Similarly, Knappstein et al. studied flamelet modeling for burner-stabilized coal particle ignition and burning in laminar flow [106]. Turbulent PCC stabilized on jet burners was studied by Luo, Bai et al. [3, 120] and Hara et al. [66] by means of CP-DNS. It was found that within a PCC jet, three distinctly different flame zones can be discriminated [3] and that both premixed and non-premixed burning modes can be identified [66]. This finding was confirmed in the CP-DNS study by Brosh et al. [19] who studied forced ignition of coal particle clouds in decaying turbulence and analyzed the effects of equivalence ratio, turbulence level and particle diameter on particle ignition. The subsequent process of heterogenous char conversion was studied in the CP-DNS of particles in isotropic forced turbulence by Krüger et al. [112]. The authors found a significant impact of turbulence on char conversion, where particle clustering can lead to significant reductions of the conversion rate. Muto et al. [141] performed CP-DNS of coal particle clouds in a two-dimensional mixing layer, where radiative particle heating was represented by injecting preheated particles. For this configuration the authors found particle ignition to occur on the rich side due to the initial particle preheating, whereas volatile combustion subsequently proceeded on the lean side. This study provided significant insights into PCC, but a further generalization beyond the limits of two-dimensional turbulence and assumed particle preheating seems warranted. The objectives of the present study are therefore as follows:

- To perform CP-DNS of coal particle cloud ignition and combustion in a turbulent mixing layer.

- To extend the work of Muto and co-workers [141] to include particle heating due to mixing and three-dimensional turbulence.

- To analyze the structure of the resulting coal flame in the context of flamelet modeling.

- To provide a database for the community and ourselves, for future analysis of pulverized coal ignition and combustion.

8.2   Modeling

8.2.1   Gas Phase Description

The (carrier-)gas phase is described by the full instantaneous governing equations in their variable-density formulation. The balance equations of total mass and momentum are solved, which contain additional source terms due to mass and momentum exchange with the solid phase. Gas phase species transport and conversion is described by balance

equations for the species mass fractions Y_α:

$$\frac{\partial}{\partial t}\rho Y_\alpha + \frac{\partial}{\partial x_j}\rho u_j Y_\alpha = \frac{\partial}{\partial x_j}\left(\rho D_\alpha \frac{\partial Y_\alpha}{\partial x_j}\right) + \rho \dot{\omega}_{Y_\alpha} + \rho \dot{S}_{Y_\alpha}, \tag{8.1}$$

with the diffusion coefficient D_α of species α, the source/sink term due to chemical reaction $\rho \dot{\omega}_{Y_\alpha}$, the source/sink term due to mass transfer from the coal particles $\dot{S}_{Y_\alpha}$, and otherwise standard nomenclature applies. Following Tufano et al. [232] who found negligible effects of differential diffusion during coal particle ignition, the diffusivity is obtained from the standard unity Lewis number assumption ($D_\alpha = D = k(\rho c_p)^{-1}$), with thermal conductivity k and gas heat capacity c_p. Homogeneous chemistry is described by a reduced mechanism with 52 species and 452 reactions, derived from the CRECK primary reference fuel mechanism [36, 194, 219]. The same mechanism has previously been used for coal particle ignition [233] and coal particle burning in laminar counterflow flames [134]. For two-phase coupling a Lagrangian point particle model is adopted, see Sec. 8.2.2, where the gas-particle transfer term $\dot{S}_{Y_\alpha}$ is obtained from the summation of all particle source terms within each computational cell:

$$\rho \dot{S}_{Y_\alpha} = Y_{\alpha,\text{vol}}\frac{1}{\Delta^3}\sum_{p=1}^{N_p}\dot{m}_{p,\text{devol}} + Y_{\alpha,\text{char}}\frac{1}{\Delta^3}\sum_{p=1}^{N_p}\dot{m}_{p,\text{char}}. \tag{8.2}$$

In Eq. (8.2) $Y_{\alpha,\text{vol}}$ and $Y_{\alpha,\text{char}}$ denote the mass fraction of species α in the volatile and char off-gas, respectively, Δ is the edge length of a computational cell, and $\dot{m}_{p,\text{devol}}$ and $\dot{m}_{p,\text{char}}$ are the volatile/char off-gas release rates of a coal particle p within the cell, which contains N_p particles. The transport equation for the total enthalpy h (chemical + sensible) reads:

$$\frac{\partial}{\partial t}\rho h + \frac{\partial}{\partial x_j}\rho u_j h = \frac{\partial}{\partial x_j}\left(\rho D \frac{\partial h}{\partial x_j}\right) + \rho \dot{S}_h, \tag{8.3}$$

where the source term due to gas enthalpy exchange with the particles and radiation is given by:

$$\begin{aligned}\rho \dot{S}_h \;\; = \;\; & \frac{1}{\Delta^3}\sum_{p=1}^{N_p}[-m_p c_{p,p}\frac{dT_{p,\text{con}}}{dt} + \dot{m}_{p,\text{devol}}h_{\text{vol}} \\ + \;\; & \dot{m}_{p,\text{char}}h_{\text{char}}] + \nabla \cdot q_{\text{rad}}.\end{aligned} \tag{8.4}$$

In Eq. (8.4) m_p is the particle mass, $c_{p,p}$ the particle heat capacity, $dT_{p,\text{con}}/dt$ the temperature change of an individual coal particle due to convective heat transfer, h_{vol} and h_{char} the enthalpies of the volatiles and char off-gases, and $\nabla \cdot q_{\text{rad}}$ is the radiative enthalpy source term. Radiation is solved by the discrete ordinates method [29, 47, 231], where the gas phase radiative properties are obtained by the grey weighted sum of grey gases model (grey WSGGM) with the coefficients suggested by Kangwanpongpan et al. [89]. In addition to total and species mass, momentum and enthalpy a gas phase transport equation for mixture fraction is solved for post-processing, as will be detailed in Sec. 8.3.2.

8.2.2 Solid Phase Description

Modeling of the solid phase in this work largely corresponds to our recent work on PCC-LES [199, 201, 202], but now considering the resolved gas phase information without the need of subgrid modeling in the present CP-DNS context. A brief outline is given here for completeness and the reader is referred to our previous work (e.g., [202]) and the references therein for a more detailed description. The coal particles are treated in a Lagrangian framework and interact with the gas phase by transfer of momentum, heat and mass. The two-phase flow is assumed to be dilute, such that the only force acting on a coal particle is drag and the particle momentum balance reduces to:

$$d\mathbf{u}_p = \frac{\mathbf{u} - \mathbf{u}_p}{\tau_p}dt, \tag{8.5}$$

where $\mathbf{u}$ is the gas phase velocity at the particle position, $\mathbf{u}_p$ the particle velocity and τ_p the particle relaxation time obtained from the Schiller-Naumann correlation [209] for $\mathrm{Re}_p \leq 1000$:

$$\tau_p = \frac{\tau_{p,\mathrm{St}}}{f_1}, \ \ \tau_{p,St} = \frac{\rho_p D_p^2}{18\mu}, \ \ f_1 = 1 + 0.15\mathrm{Re}_p^{0.687}. \tag{8.6}$$

In Eq. 8.6, ρ_p is the particle density and Re_p is the particle Reynolds number calculated as $\mathrm{Re}_p = \rho|\mathbf{u} - \mathbf{u}_p|D_p/\mu$, with the particle diameter D_p and the dynamic gas viscosity μ. After solving Eq. (8.5) the particle position $\mathbf{x_p}$ is obtained from:

$$d\mathbf{x_p} = \mathbf{u}_p dt. \tag{8.7}$$

The mass of a particle changes as it undergoes devolatilization and char conversion:

$$dm_p = -(\dot{m}_{p,\mathrm{devol}} + \dot{m}_{p,\mathrm{char}})dt. \tag{8.8}$$

During devolatilization, the diameter is assumed to be constant and the particle density changes, whereas during char combustion the density is assumed to remain constant while the particle shrinks (assumption of zone III char conversion). Devolatilization is modeled with the Kobayashi model, relying on two kinetic rates to approximate the particle temperature dependence of devolatilization [108]. While the model allows for two different volatile compositions, only a single composition is used here, to facilitate flamelet modeling and to aid the analysis of this configuration. The volatile matter release rate is calculated as:

$$\dot{m}_{\mathrm{p,devol}} = k_{\mathrm{devol}}(m_{p,\mathrm{VM},0} - m_{p,\mathrm{VM}}), \tag{8.9}$$
$$k_{\mathrm{devol}} = \alpha_1 A_1 e^{-E_1/RT_p} + \alpha_2 A_2 e^{-E_2/RT_p}. \tag{8.10}$$

In Eq. 8.9 k_{devol} is the devolatilization rate coefficient, $m_{\mathrm{p,VM},0}$ the initially available volatile matter in the coal particle and $m_{\mathrm{p,VM}}$ the current volatile yield. The kinetic constants are $A_1 = 3.7 \cdot 10^4 \mathrm{s}^{-1}$, $A_2 = 1.46 \cdot 10^{12}\mathrm{s}^{-1}$, $E_1 = 5.16 \cdot 10^7 \mathrm{J/kmol}$ and $E_2 = 3.07 \cdot 10^8 \mathrm{J/kmol}$ and the splitting constants are set to $\alpha_1 = 0.39$ and $\alpha_2 = 0.8$ [202]. In this work char conversion is modeled by Smith's intrinsic model [215]. However, as will be shown in the results section, char conversion only plays a minor role in the present

simulation due to oxygen depletion in the region of devolatilized particles. It should be noted that in hot oxygen-depleted regions, gasification reactions might dominate char conversion [127]. However, as it occurs on similarly large or even larger time scales than the oxidation reactions considered here, gasification is expected to be negligible. Particles are assumed to have a homogeneous internal temperature distribution and the particle temperature is assumed to be affected by convective heat exchange with the gas, radiative emission and absorption, and the heats of char combustion and devolatilization. Consequently, the balance equation for the particle temperature reads:

$$
\begin{aligned}
\frac{dT_p}{dt} = &\frac{1}{\tau_{\mathrm{con}}}(T - T_p) + \frac{\epsilon_p A_p \sigma}{m_p c_{p,p}}(\Theta_r^4 - T_p^4) \\
&+ \frac{\dot{q}_{\mathrm{char}}}{m_p c_{p,p}} + \frac{\dot{q}_{\mathrm{devol}}}{m_p c_{p,p}}.
\end{aligned}
\tag{8.11}
$$

In Eq. 8.11 τ_{con} is the convective heat transfer time scale, T the gas temperature at the particle location, T_p the particle temperature, ϵ_p the particle emissivity, A_p the projected area of the particle, Θ_r the Eulerian phase radiation temperature calculated by DOM, $\dot{q}_{\mathrm{char}}$ the heat flux due to char combustion and $\dot{q}_{\mathrm{devol}}$ the heat of pyrolysis. The heat of char conversion is modeled such that the heat released by partial oxidation of C to CO is absorbed by the particle, while the heat released by further oxidation to CO_2 is absorbed by the gas, which is in accordance with the assumption that only partial oxidation occurs within the particle boundary layer [202]. The particle emissivity ϵ_p is calculated based on char burnout [222], such that it is 0.9 during devolatilization and linearly decreases from 0.9 to 0.5 with the progress of char combustion. Convective heat transfer (first term on the RHS of Eq. 8.11) is calculated based on the Ranz-Marshall model [193] and the convective time scale τ_{con} is calculated as:

$$
\tau_{\mathrm{con}} = \tau_{p,\mathrm{St}} \frac{3\mathrm{Pr}}{\mathrm{Nu}} \frac{c_{p,p}}{c_p} = \frac{1}{6} \frac{\mathrm{Pr}}{\mathrm{Nu}} \frac{c_{p,p}}{c_p} \frac{\rho_p D_p^2}{\mu},
\tag{8.12}
$$

$$
\text{with} \quad \mathrm{Nu} = 2 + 0.552 \mathrm{Re_p}^{1/2} \mathrm{Pr}^{1/3}.
$$

In Eq. 8.12, Nu and Pr $(=0.7)$ are the Nusselt and Prandtl number, respectively. The particle heat capacity is modeled according to Merrick [133] and Brewster et al. [18]:

$$
c_{p,p} = Y_{p,\mathrm{VM}} c_{p,\mathrm{VM}} + Y_{p,\mathrm{FC}} c_{p,\mathrm{FC}} + Y_{p,\mathrm{ash}} c_{p,\mathrm{ash}}.
\tag{8.13}
$$

In Eq. 8.13, $Y_{p,\mathrm{VM}}$, $Y_{p,\mathrm{FC}}$ and $Y_{p,\mathrm{ash}}$ are the mass fractions of volatile matter, fixed carbon and ash in the coal particle, respectively and the corresponding heat capacities are $c_{p,\mathrm{VM}}$, $c_{p,\mathrm{FC}}$ and $c_{p,\mathrm{ash}}$. Volatile matter and fixed carbon heat capacities are computed by Eq. 8.14, where γ denotes either volatile matter ($\gamma = \mathrm{VM}$) or fixed carbon ($\gamma = \mathrm{FC}$) [132]:

$$
c_{p,\gamma} = \frac{\overline{\mathrm{R}}}{W_\gamma} \left[g_1 \left(\frac{380}{T_p} \right) + 2g_1 \left(\frac{1800}{T_p} \right) \right].
\tag{8.14}
$$

In Eq. 8.14 $\overline{\mathrm{R}}$ is the universal gas constant and W_γ the mean atomic weight ($W_{\mathrm{VM}} \approx$ 6.83 kg/kmol and $W_{\mathrm{FC}} \approx 12$ kg/kmol). The function $g_1(x)$ is computed as $g_1(x) =$

Table 8.1: Properties of the Saar hvBb coal employed in this study (cf. [249]).

Ultimate Analysis (daf)		Proximate Analysis	
C	79.3%	ash	8.3%
H	4.7%	volatiles	37%
N	1.3%	fixed carbon	52.5%
S	1.0%	moisture	2%
O	13.7%		
LHV	32.32 MJ/kg [160]		

$e^x/(\frac{e^x-1}{x})^2$, where the argument x is either $380/T_p$ or $1800/T_p$, see Eq. 8.14. The ash heat capacity is calculated from $c_{p,\text{ash}} = 539.9 + 0.586 T_p$ [18]. Rapid devolatilization affects coal particle momentum- and heat transfer. A blowing correction is applied to account for the effect of devolatilization [216, 222]:

$$B = \frac{\text{Pr}}{2\pi D_p \mu} \dot{m}_{\text{devol}}. \tag{8.15}$$

This correction is applied by modifying the particle relaxation time and Nusselt number, i.e. by using:

$$\tau_p^* = \tau_p(1 + B) \quad \text{and} \quad \text{Nu}^* = \text{Nu}\, e^{-0.6B}, \tag{8.16}$$

in all equations where τ_p and Nu appear.

8.2.3 Coal Properties

The coal employed in this DNS study is a high-volatile bituminous coal for which measurements are reported by Weber et al. [250] and Knill et al. [250] and which has also been used in our earlier PCC-LES studies [201, 202]. The coal properties are given in Table 8.1. The density of the coal is $\rho_p = 1000\,\text{kg/m}^3$. The computational coal particle is only composed of volatile matter, fixed carbon and ash as given by the proximate analysis, and by neglecting moisture and sulphur, but considering a correction for the high temperature volatile yield. The high temperature volatile yield on dry-ash-free basis amounts to 0.646, which corresponds to a Q-factor of approximately 1.56 [250]. The procedure to obtain the volatile composition is based on the work by Petersen & Werther [167] and is the same as in our earlier work [201, 202], with the exception that C_6H_6 is considered as tar species instead of C_2H_2, since the former is available in the employed kinetic mechanism. After removing the remaining carbon obtained using the experimental value for high temperature volatile yield, the composition is obtained by distributing the atoms among species commonly found in coal volatile gas. The procedure allows one to set splitting factors which determine how much oxygen reacts to CO and how much carbon reacts to tar and C_2H_4, respectively. The splitting factors are set such that high values of CO and relatively low values of tar are obtained to yield a volatile gas with a heating value close to the experimental value. The composition of the volatile gas is given in Table 8.2. After the above procedure, the initial mass fractions of volatile content, fixed char and ash in the coal particle are 0.592, 0.325 and 0.083, respectively. The heat of pyrolysis $\dot{q}_{\text{devol}}$ is set to zero in this work, as appropriate for this type of coal [161].

8.3 Computational Configuration

8.3.1 Computational Setup and Numerical Procedure

The computational domain spans $L_x = L_y = 22.4\,\text{mm}$ and $L_z = 10.4\,\text{mm}$ in x-, y- and z-direction, respectively. A total of $5.4\,\text{M}$ cuboid cells with a constant edge length $\Delta = 100\,\mu\text{m}$ is used for discretization. A justification of the employed grid resolution is provided in Sec. 8.3.2. A three-dimensional setup is used in this work to provide a realistic turbulent energy cascade and small scale mixing, such that the database can be used for the development of LES subgrid models in the future. To evaluate the effect of three-dimensionality, the same setup has been run in 2D (x and y) for comparison. As expected, significantly less small scale mixing was observed and as a result only approximately 50% of the volatiles were converted compared to the three-dimensional case, and the latter was used to produce all data in the present work. The initial flow field consists of two streams, separated at $y = L_y/2$. The upper stream, corresponding to $y > L_y/2$, initially consists of air preheated to 600 K at a velocity of 2.4 m/s. The lower stream consists of an equilibrated mixture of volatile gas and air with a mixture fraction of $Z = 0.043$ and a velocity of -17.6 m/s. This mixing layer setup mimicks conditions that particles face upon entering the furnace in a swirled pulverized coal flame, such as in the experiments by Weber et al. [250], extracted from previous LES [201, 202]. Particles initially 'see' mixing of transport and combustion air with recirculating gas from the volatile flame. This is reasonably well reproduced by coal particles entrained in hot air, mixing with hot lean products. The equilibrated mixture composition is given in Table 8.2, along with the compositions of the air and volatile gas streams. Velocities have been selected such that the momentum is equal in both streams, jointly considering gas and particle phase. To support the rapid growth of shear layer instabilities, small isotropic velocity perturbations of $u'u' = v'v' = w'w' = 0.5\,\text{m}^2/\text{s}^2$ with a length scale of $0.5\,\text{mm}$ are generated using the methods by Klein et al. [103] and Kempf et al. [98] and introduced at initialization. A total number of $3 \cdot 10^5$ coal particles with equal diameter $D_p = 25\,\mu\text{m}$ is randomly distributed in the upper stream. The particle diameter was chosen at the lower end of a realistic particle diameter spectrum for PCC, which is in line with published work [141] and required for CP-DNS with the employed grid spacing. Additionally, small particles are expected to play the dominant role for ignition. The initial particle distribution corresponds to a particle number density of $1.15 \cdot 10^{11}$ particles/m^3 in the upper stream, or $0.58 \cdot 10^{11}$ particles/m^3 in the entire computational domain, which is representative of typical PCC conditions [188] and also used in other CP-DNS studies, e.g. [19]. No particles are introduced to the lower stream at $t = 0$ for simplicity, to facilitate the analysis and to fix the origin of the fresh volatiles. Periodic boundary conditions are set in x- and z-directions and a zero-gradient BC is applied in y-direction to allow for fluid to leave the domain due to thermal expansion.

The code used in this work is the massively parallel finite volume combustion LES/DNS code PsiPhi [97, 186] in its low-Mach version. All convective terms are discretized using a fourth-order central differencing scheme (CDS), whereas diffusive terms are discretized with a second-order CDS. A third-order accurate Runge-Kutta scheme is used for time integration. Chemical source terms and fluid properties for the 52 species are evaluated

Table 8.2: Composition of the mixing layer streams and the assumed volatile gas. Only species mass fractions exceeding 10^{-7} are given for the equilibrated lower stream, which contains additional (smaller) amounts of minor species.

Volatile gas				Upper stream		Lower stream			
Y_{CH_4}	0.0055	Y_{CO}	0.3770	Y_{N_2}	0.767	Y_{N_2}	0.734	Y_{CO}	$1.26 \cdot 10^{-5}$
$Y_{C_6H_6}$	0.2243	Y_{H_2}	0.0024	Y_{O_2}	0.233	Y_{O_2}	0.128	Y_{OH}	$1.37 \cdot 10^{-4}$
$Y_{C_2H_4}$	0.3704	Y_{N_2}	0.0204			Y_{H_2O}	0.028	Y_O	$7.67 \cdot 10^{-6}$
						Y_{CO_2}	0.108		
T	particle			T	600 K	T	1693 K		
Z	1.0			Z	0.0	Z	0.043		

by Cantera [62], which is also used to obtain the initial conditions of the equilibrated lower stream. The semi-implicit ODE solver ODEPIM is used to integrate chemical source terms [90, 266] in each Runge-Kutta substep using the Cantera Fortran interface. The pressure Poisson-equation is solved by a successive over-relaxed Gauss-Seidel solver. A constant time step of 10^{-7} s has been employed, which has been verified to sufficiently resolve the flow and kinetics in time. The adequacy of the solver and time step width has been tested by comparing results for one-dimensional premixed flames and zero-dimensional auto-igniting reactors to reference solutions from Cantera. The semi-implicit solver requires around 1-10 sub-iterations to obtain a sufficiently accurate solution. The simulations are run on 1536 Xeon E5-2650 cores on the magnitUDE supercomputer for approximately 5 days, resulting in a cost of approximately 200k core-h.

8.3.2   Post-Processing Analysis

This section outlines the procedures and equations employed for post-processing, which are used for the results analysis in Sec. 8.4. Full 3D gas and particle data from the transient evolution of the mixing layer, ignition and volatile burning is gathered for times separated by 1 ms up to a time of 14 ms. Statistical quantities are obtained through spatial averaging over the homogeneous directions x and z. Spatially averaged quantities are thus evaluated as:

$$\langle \phi \rangle (y, t) = \frac{1}{L_x L_z} \int_0^{L_x} \int_0^{L_z} \phi(x, y, z, t) \, dx \, dz, \tag{8.17}$$

where ϕ is an arbitrary quantity suitable for averaging. In order to assess the resolution of the DNS, Kolmogorov length scales are estimated. First, the instantaneous velocities are averaged based on Eq. 8.17, which are then used to obtain local velocity fluctuations, i.e. $u_i' = u_i - \langle u_i \rangle$, where u_i' is the local fluctuation of velocity component i. The fluctuations are used together with the viscous stress tensor τ_{ij} to obtain the averaged dissipation as $\epsilon = \langle \tau_{ij} \partial u_i' / \partial x_j \rangle / \langle \rho \rangle$. The Kolmogorov length scale is then calculated by $\eta = (\nu^3/\epsilon)^{1/4}$ as a function of y for different t, where ν is the averaged kinematic viscosity. The evaluation of η results in a minimum value of $\eta = 120 \, \mu$m, which is larger than the grid size of $\Delta = 100 \, \mu$m. The ability of this grid spacing to resolve the Kolmogorov scale

has been confirmed by running a finer mesh with $\Delta = 50\,\mu m$ (43M cells) for non-reacting conditions. This test is considered to be more restrictive regarding the resolution of the Kolmogorov scale, as in non-reacting conditions the fluid viscosity is lower, the Reynolds number higher and therefore even smaller turbulent scales can be expected. The test run resulted in an estimation of $\eta = 116\,\mu m$, thus confirming the adequacy of the employed $\Delta = 100\,\mu m$. The turbulent Reynolds number is calculated as $\mathrm{Re}_t = k^{1/2}L/\nu$, where the turbulent kinetic energy is $k = u_{i,\mathrm{rms}}^2/2$, with $u_{i,\mathrm{rms}} = \langle[u_i - \langle u_i\rangle]^2\rangle^{1/2}$, and the integral length scale of turbulence is given by $L = k^{3/2}/\epsilon$. Peak values of around $\mathrm{Re}_t = 110$ have been found in the present configuration, just before large amounts of volatiles ignite, which subsequently dampens turbulent velocity fluctuations. Based on estimations for a premixed flame corresponding to the initial conditions in the lower stream (volatile-air-mixture at an unburned temperature of 600 K -before equilibration- and mixture fraction of 0.043) the grid resolves the flame front with at least 6 grid points across the thermal flame thickness. A further test of the adequacy of the grid resolution to resolve the flame front has been conducted along the lines of Hawkes et al. [71]: Steady non-premixed flamelet simulations of volatile-air mixtures for ranges of strain rates representative of the present DNS have been conducted. The resolution of the OH reaction rate $\dot{\omega}_{\mathrm{OH}}$ was taken as a quality indicator for the grid resolution and the number of cells across the half-width of the normalized $\dot{\omega}_{\mathrm{OH}}$-profile was evaluated. It was found that the half-width is resolved by at least 7 cells at strain rates near flamelet extinction and by approximately 10 cells for the (lower) strain rates mostly prevalent in the DNS.

An additional transport equation is solved to track the volatile gas mixture fraction. This mixture fraction is defined by its transport equation [173]:

$$\frac{\partial}{\partial t}\rho Z + \frac{\partial}{\partial x_j}\rho u_j Z = \frac{\partial}{\partial x_j}\left(\rho D\frac{\partial Z}{\partial x_j}\right) + \rho \dot{S}_Z. \tag{8.18}$$

Equation 8.18 does not have any effect on the simulation and is solved purely for post-processing purposes. The source term $\rho\dot{S}_Z$ represents the mass released by the particles during devolatilization. The transport equation is initialized such that its value is 0 in the upper stream and 0.043 in lower stream. An alternative definition of mixture fraction, $Z_{\mathrm{v,fresh}}$, is solely used for an a-priori analysis of ignition delay times, cf. Fig. 8.2. It only considers fresh volatiles by excluding the burned volatiles present in the lower stream at initialization. A further useful quantity to describe the extent of mixing between upper and lower stream is the oxidizer split λ, which describes the ratio of the mass originating from hot products (lower stream) to the combined mass originating from pure air (upper stream) and hot products (lower stream), i.e. $m_{\mathrm{LS}}/(m_{\mathrm{LS}} + m_{\mathrm{US}})$, where m_{LS} and m_{US} is the mass originating from the lower stream and upper stream, respectively. This quantity is used to describe ignition delays by means of homogeneous reactors representative of the range of gas mixtures that can occur across the mixing layer, cf. Fig. 8.2, and to analyze flamelets, cf. Fig. 8.9.

The progress variable used in the present analysis is defined as (cf. [134]):

$$Y_C = Y_{\mathrm{CO}} + Y_{\mathrm{CO_2}}. \tag{8.19}$$

The normalized progress variable C is computed as:

$$C = \frac{Y_C - Y_{C,\text{min}}}{Y_{C,\text{eq}} - Y_{C,\text{min}}}. \tag{8.20}$$

In Eq. 8.20, $Y_{C,\text{min}}$ and $Y_{C,\text{eq}}$ are the minimum and the equilibrium progress variable, respectively. Both quantities can be expressed as a function of the mixture fraction Z and the enthalpy h. Since (here) devolatilization releases CO, $Y_{C,\text{min}}$ is non-zero. In this work, $Y_{C,\text{min}}$ is taken to be $Y_{C,\text{min}} = Z \cdot (Y_{\text{CO,vol}} + Y_{\text{CO}_2,\text{vol}})$, where $Y_{\text{CO,vol}}$ and $Y_{\text{CO}_2,\text{vol}}$ are the mass fractions of CO and CO_2 in the volatile gas. Here, $Y_{\text{CO}_2,\text{vol}}$ is 0, since the volatile composition does not contain any CO_2, see Table 8.2. The expression for $Y_{C,\text{min}}$ does not strictly provide the minimum value of Y_C for a given mixture fraction, since some reactions can potentially decrease Y_C from its value in the unburned state (e.g. $H_2 + CO(+M) \longleftrightarrow CH_2O(+M)$). However, values below 0 have not been observed. Since there only is a very limited amount of char conversion in the present setup, its small contribution to CO production and therefore to C has been neglected. The parameters Z, C (and additionally a measure of enthalpy h to account for solid-gas heat transfer) are expected to be sufficient to discuss the majority of phenomena occurring in the reactive coal mixing layer in the present study in a meaningful way. Additionally, these parameters are expected to constitute the minimum set of variables necessary for flamelet modeling of this problem.

To study the mechanisms of ignition and burning in premixed and diffusion-dominated zones, the flame index is used [265]:

$$\text{FI} = \nabla Y_F \cdot \nabla Y_{O_2}. \tag{8.21}$$

In Eq. 8.21, Y_F contains all species from the volatile gas except N_2, i.e. $Y_F = Y_{\text{CH}_4} + Y_{\text{C}_6\text{H}_6} + Y_{\text{C}_2\text{H}_4} + Y_{\text{CO}} + Y_{\text{H}_2}$ (cf. [141]). Negative values of the FI indicate non-premixed combustion, positive FI corresponds to premixed combustion, whereas FI values around zero 0 refer to homogeneous ignition events (if reactions take place simultaneously). It is noted, however, that the FI analysis should be interpreted with some care: in CP-DNS, the gradients in the boundary layers around the particles are not resolved and the present analysis refers to the scales of Kolmogorov size and above. This is similar to existing CP-DNS studies cited in Sec. 8.1.

Analogous to the progress variable used to characterize the progress of chemical reactions, Eq. 8.20, a progress variable characterizing the extent of devolatilization is introduced:

$$C_{\text{dev}} = \frac{m_{\text{VM},0} - m_{\text{VM}}}{m_{\text{VM},0}}. \tag{8.22}$$

The definition according to Eq. 8.22 was found useful for the present work, where only limited char conversion occurs and all particle processes are readily described by tracking the devolatilization progress. Finally, Stokes numbers are evaluated as $St = \tau_p/\tau_L$ with τ_p from Eqns. (8.6) and (8.16), and the large eddy turnover time calculated as $\tau_L = L/(2/3k)^{1/2}$.

8.4   Results

8.4.1   Mixing, Ignition and Volatile Burning

Figure 8.1 shows the gas phase temperature and particle devolatilization progress. Every subfigure shows contours in the x-y-plane extracted at $L_z/2$ (left part of each subfigure) and in the y-z-plane at $L_x/2$ (right part of each subfigure). Initially particles and hot gas are separated, where the upper stream contains cold gas and particles and the lower stream hot gas only. As the simulation progresses, the turbulent mixing layer between the cold upper stream and the hot lower stream evolves, and a mixing zone develops between the two streams. Initially, there is limited entrainment of particles from the upper stream into the mixing zone. In the x-y-plane view, clockwise rotating vortices develop that move from right to left, as indicated by visualisations of flow streamlines (omitted here for brevity). Particles are accelerated upwards at the leading side (in the x-y view) of the vortices and then accelerate downwards on the trailing side. At $t = 5\,\mathrm{ms}$ the mixing layer has widened due large scale momentum exchange between the upper and lower stream. In addition to this bulk motion, i.e. the mixing by the larger eddies, small scale turbulence could lead to entrainment of particles into the lower stream. However, most particles seem to follow the bulk motion (upward in the upper stream), but their inertia prevents them from following the small scale mixing which could drive them downward. As a net result, a number of particles clusters at locations slightly above $L_y/2$, whereas only a few particles get entrained into the mixing zone and are surrounded by hot gas. An additional analysis of eddy turnover times and particle response times (not shown for brevity) reveals that large scale eddies have typical turnover times τ_L of around 4 ms and that this times cale is smaller in the lower stream than in the upper stream. Similarly, particle response times τ_p are smaller in the hot stream, due to its higher viscosity. A comparison of the two time scales shows that, at early times, the effect of smaller τ_p in the hot stream is stronger and particles adjust more readily to the hot gas velocity than the cold flow. This results in upward acceleration dominating particle motion during the initial shear layer development and leads to the observed particle clustering above $L_y/2$. However, already at the early time of $t = 5\,\mathrm{ms}$, some particles have been entrained into the hot gas and locally increased temperatures can be observed around them, indicating that they have started to devolatilize and burn, see for example the bottom left particle in the y-z plane. This trend continues at $t = 7\,\mathrm{ms}$ where streaks of particles have entered the lower stream, which have, however, mostly not devolatilized yet. The first significant rise in gas temperature can be observed at $t = 9\,\mathrm{ms}$ within the lower stream. At this time, a considerable amount of volatile gases has ignited, leading to temperatures higher than the initial lower stream temperature over a wide region. At $t = 11\,\mathrm{ms}$ large hot regions spanning the full width of the mixing layer are produced within the mixing zone and lower stream, which keep increasing in size until the last reported time of $t = 13\,\mathrm{ms}$ due to the combined effect of heat release and devolatilization. At $\mathrm{t} = 11\,\mathrm{ms}$, particles cluster in the flame region. This is because of the flame expanding and accelerating the gas phase, with particles responding to the acceleration more quickly close to the flame front (low τ_p) than in the cold gas (high τ_p). Between $t = 11 - 13\,\mathrm{ms}$ a large amount of particles is entrained into the hot region and has attained substantial devolatilization
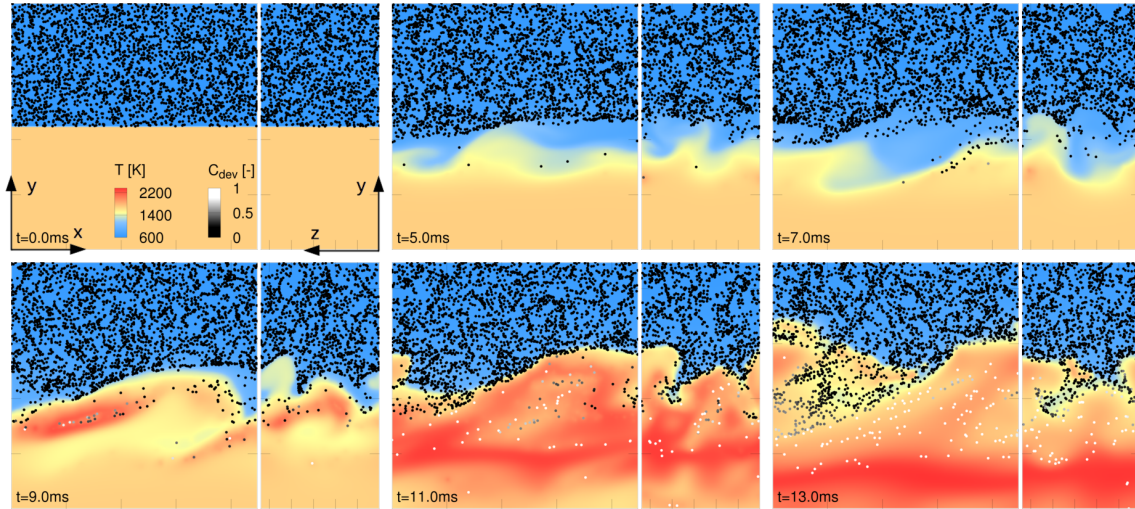
Figure 8.1: Gas phase temperature and particles colored by their devolatilization progress C_{dev} in the x-y-plane at $L_z/2$ and in the y-z plane at $L_x/2$ for selected times during the simulation.

progress, as indicated by the values of C_{dev} approaching unity. However, in the top left region of the lower stream a considerable amount of particles has still not devolatilized at this stage. This is investigated further in the discussion of Fig. 8.6.

To obtain a better understanding of how particles can be expected to ignite in this configuration, it is useful to study homogeneous ignition delay times of possible mixtures of volatiles, air (from the upper stream) and lean hot product gas (from the lower stream). Figure 8.2 shows the ignition delay of different combinations of these three components constituting possible gas mixtures in the present configuration. The x-axis shows the mixture fraction of (fresh) volatiles $Z_{\mathrm{v,fresh}}$ such that $1-Z_{\mathrm{v,fresh}}$ represents the amount of oxidizer in the mixture, where oxidizer can either be pure air or lean hot gas. The different lines represent different oxidizer compositions distinguished by the oxidizer split λ, which quantifies the mixture of lean product gas (lower stream) with the air stream (upper stream) as described in Sec. 8.3.2. The oxidizer split λ can also be interpreted as the normalized progress variable of the oxidizer (mixture of upper stream and lower stream). The ignition delay is measured as the time from the start of the calculation until the maximum positive OH mass fraction growth rate is reached in Cantera batch reactor simulations. Figure 8.2 illustrates that any particle that is entrained in the bottom stream of the mixing layer ($\lambda = 1$) will experience ignition very shortly after devolatilization (t_{ign} of the order of 0.01 to 0.1 ms). Conditions where isolated coal particles enter the hot stream are most favorable for a quick devolatilization and conversion of the volatile gas. Naturally, particles experiencing an environment consisting of mixtures of air and hot products will show slower ignition due to the decreased temperature of the air stream. Similarly, devolatilizing particle clouds will provide rich conditions that show slower ignition as well.

Figure 8.3 presents contours of mass fractions of CH_4, O_2 and OH, the heat release rate and flame index at selected times towards the end of the simulation. Particles are
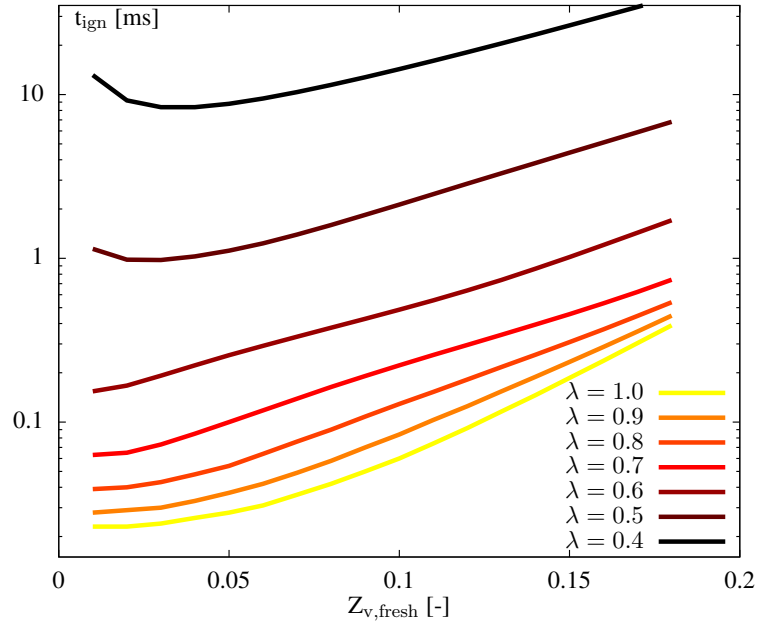
Figure 8.2: Ignition delay of homogeneous mixtures of fresh volatiles and oxidizer vs. fresh volatile mixture fraction ($Z_{v,fresh}$, excluding the initial hot products). Different lines represent different oxidizer compositions where λ is the split between lean hot product gas (bottom stream) and air (top stream). A value of $\lambda = 1.0$ corresponds to the oxidizer consisting of pure hot products and $\lambda = 0.0$ to pure air.

colored by their devolatilization progress C_{dev} and iso-lines for mixture fraction values of $Z = Z_{st}/2$, Z_{st} and $2 \cdot Z_{st}$ are shown for reference.

At $t = 8$ ms, volatile clouds have formed in the lower stream with mixture fraction values above $Z_{st}/2$. In these clouds, CH_4 is formed (among the other volatile gas species) due to devolatilization, but is rapidly consumed by chemical reactions, such that the CH_4 contour retains near-zero values. However, the O_2 contour indicates that volatile gases have been present in the mixing zone, which have been consumed by homogeneous reactions. Corresponding to the chemical conversion of volatiles in a lean and hot environment, OH and heat release can be found within the volatile clouds, but mostly around individual particles or clouds with only a few particles. This initial heat release is (mainly) associated with the non-premixed combustion mode as illustrated by the flame index.

As coal conversion proceeds, the volatile cloud in the mixing zone rapidly grows due to the interaction of devolatilization and volatile combustion. At $t = 10$ ms, regions with mixture fractions above the stoichiometric value can be observed. At this stage, large amounts of O_2 have been consumed within the volatile cloud. OH can mostly be found around the iso-line of stoichiometric mixture fraction, indicating diffusion-dominated combustion. However, it can also be observed that some volatile gas has mixed with air from the upper stream such that partially premixed regions exist. This corresponds to mixtures of relatively long ignition delay in Fig. 8.2 due to low temperatures of the

mixture. In the slice shown in Fig. 8.3, lean premixed combustion dominates the heat release at $t = 10\,\text{ms}$. This premixed flame front forms at the upper side of the mixing zone, where volatiles and O_2 have mixed, forming flammable pockets and elongated layers around $Z_{st}/2$. The flame index indicates a correlation of premixing near $Z_{st}/2$ and the highest HRR. At $t = 11\,\text{ms}$, O_2 has mostly been consumed within the mixing zone and rich pockets with unburned volatile fuel start to form. At this time, an upper flame (burning into the upper stream) and lower flame (burning into the lower stream) can be distinguished, as indicated by the OH and FI contours. The lower flame burns in non-premixed mode, shows comparatively little heat release due to burning into products with only small amounts of O_2 left to burn, but high values of OH around the stoichiometric mixture fraction iso-line. This flame appears to burn very stably and at low scalar dissipation rates (not shown for brevity). The upper flame shows a more complicated mixed burning mode and flame structure, where some regions are dominated by premixed and some by non-premixed modes. On the left side of the images at $t = 11\,\text{ms}$ for example, a large lean premixed pocket has formed, which is consumed by a premixed flame. This premixed flame burns under lean conditions, such that some oxygen is left, which is then consumed in non-premixed mode under stoichiometric conditions. At other locations near the upper stream, a similar behavior can be observed, but with premixed and diffusion flame having moved much closer together.

At the final reported time at $t = 13\,\text{ms}$, the rich regions have grown rapidly and only small amounts of O_2 are left with almost all of the oxygen consumed in the lower stream. The lower diffusion flame has moved further downwards. Comparing to $t = 11\,\text{ms}$, it can be seen that this flame exhibits low scalar dissipation rates (not shown) and a slow conversion of oxygen and volatiles. The downward movement of the lower flame can partially be attributed to displacement by mass added to the gas phase by devolatilizing particles and slow burning in diffusion mode towards the remaining O_2 in the lower stream. The upper flame at this stage shows partial extinction. On the left, a premixed/diffusion flame structure can still be observed (cf. $t = 11\,\text{ms}$, see OH and HRR contours) but on the right, the flame has extinguished. To better understand this behavior, a 2D test of premixed flame propagation into a lean particle-laden mixture of volatiles and air (upper stream) has been performed under similar conditions as present in the turbulent case. It was observed that the premixed flame cannot propagate into the particle-laden mixture due to a significant amount of heat extracted from the preheat zone due to particle heat-up. However, this premixed flame that is eventually quenched by heat losses can generate a diffusion flame in the premixed flame products. This diffusion flame forms due to particles devolatilizing in the premixed flame before it extinguishes. The extraction of the thermal energy necessary to heat up the particles is expected to be the main driver of extinction in the upper flame in this configuration. This effect is augmented by particle clustering near the flame front, which appears to be higher around the extinguished region of the upper flame than near the burning part.

Figure 8.4 shows spatially averaged gas phase quantities, Eq. 8.17, as a function of y for different times. As can be observed from the temperature plot (Fig. 8.4a), the temperature profile broadens as the mixing layer develops and at early times the profiles remain monotonic. The average temperature does not exceed the initial temperature of the hot stream at any location until around $t = 10\,\text{ms}$. However, a change of the
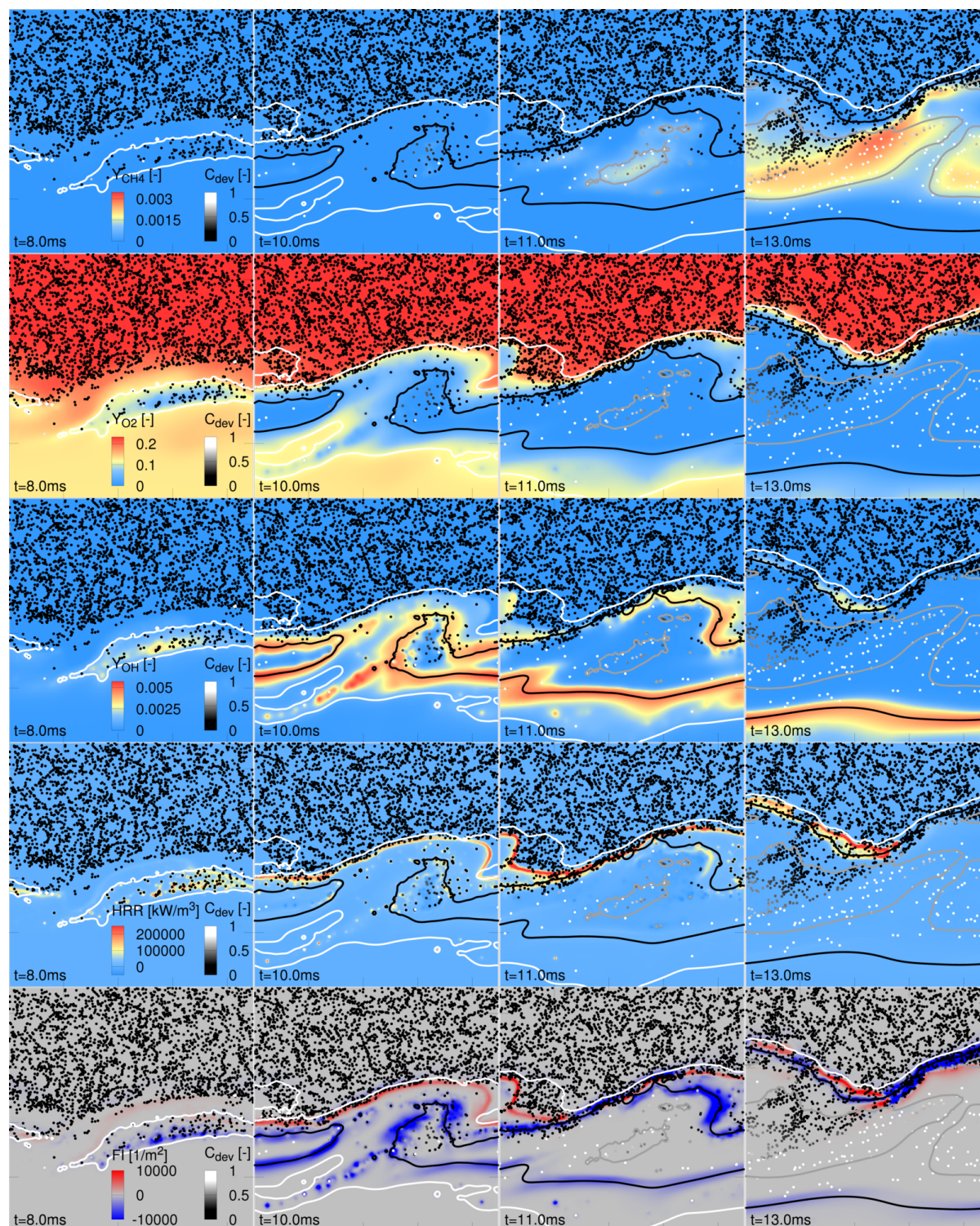
Figure 8.3: Mass fractions of CH_4, O_2, OH, heat release rate and flame index (from top to bottom) in the x-y-plane at $L_z/2$. Iso-lines correspond to volatile mixture fractions Z of $Z_{st}/2$ (white), Z_{st} (black) and $2 \cdot Z_{st}$ (grey). The stoichiometric value Z_{st} is obtained based on pure air as oxidizer. Particles are colored by C_{dev}.

broadening of the profile starts to occur at $t = 8\,\text{ms}$, where the temperature in the region between y/L_y=0.35 and 0.55 forms an intermediate peak which reaches the initial hot gas temperature at approximately y/L_y=0.38 and $t = 9\,\text{ms}$. At later times, the temperature increases rapidly across a broad range of y/L_y reaching approximately 2300 K at $t = 13\,\text{ms}$. The temperature peak moves towards lower values of y as the simulation progresses due to displacement by fresh volatiles and by the flame burning into the lean products.

Figure 8.4b shows the time evolution of the mixture fraction. Non-zero values of mixture fraction appear even on the upper end of the upper stream $(y/L_y \rightarrow 1)$ from the beginning of the simulation since the initial temperature of 600 K is sufficient for (limited extents of) devolatilization to occur. The lower stream initially has a uniform (pre-set) mixture fraction of $Z = 0.043$. The mixture fraction rises near the center around y/L_y=0.5 first, which then shifts towards lower values of y/L_y into the hot stream due to hot conditions leading to rapid devolatilization. At $t = 10\,\text{ms}$, the average mixture fraction exceeds its stoichiometric value (approx. 0.095) for the first time, beyond which it increases to form peak values of up to 0.25 and rich mixtures across a broad region at late times.

Figure 8.4c shows the evolution of the progress variable according to Eq. 8.19. Initially, the evolution of the progress variable illustrates pure mixing between upper stream and lower stream due to the absence of devolatilization and chemical reactions at very early times. The onset of ignition of significant amounts of volatiles and the localised increase of Y_C can be observed around $t = 8\,\text{ms}$ (analogous to the temperature profile) close to $y/L_y = 0.4 - 0.5$. From this time onwards, Y_C increases until the last reported time. The increase of Y_C is partially due to CO being released by devolatilization (around 37% of the volatiles released is CO) and due to chemical reactions. At late times (from $t = 12\,\text{ms}$ to $14\,\text{ms}$), the peak value of Y_C increases only slightly, although the volatile mass fraction increases at this position (cf. Fig. 8.4b). This behavior is due to the production rates of Y_C decreasing drastically as the mixture becomes richer, which is discussed in more detail for Fig. 8.7.

Figure 8.4d shows the averaged heat release rate. It can be observed that low levels of heat release are already present early on in the simulation, due to isolated particles devolatilizing and igniting. The heat release rate increases up to $t = 10\,\text{ms}$ and its peak shifts from lower values of y/L_y to higher values, indicating the propagation of the upper flame burning into the upper stream. Consistent with Fig. 8.3, only low averaged values of heat release are observed at the lower flame. At $t = 11\,\text{ms}$, negative averaged heat release rates can be observed around $y/L_y = 0.2 - 0.45$ within the mixtures well above stoichiometry due to destruction of products such as CO_2. At times later than $t = 11\,\text{ms}$, the maximum heat release rate decreases due to partial flame quenching.

Figure 8.4e shows the averaged velocity in x-direction. As the mixing layer develops, the initial sharp velocity profile broadens as turbulent flow structures form and mix the two streams. The velocity in the lower stream shows a much stronger change, with velocities changing even at $y/L_y = 0$ at late times. This is due to the decelerating impact of particles and volatile gases on the lower stream.

Velocity fluctuations are presented in Fig. 8.4f. The initial perturbations are quickly dampened, but a fluctuation level increase in the mixing zone can be observed starting
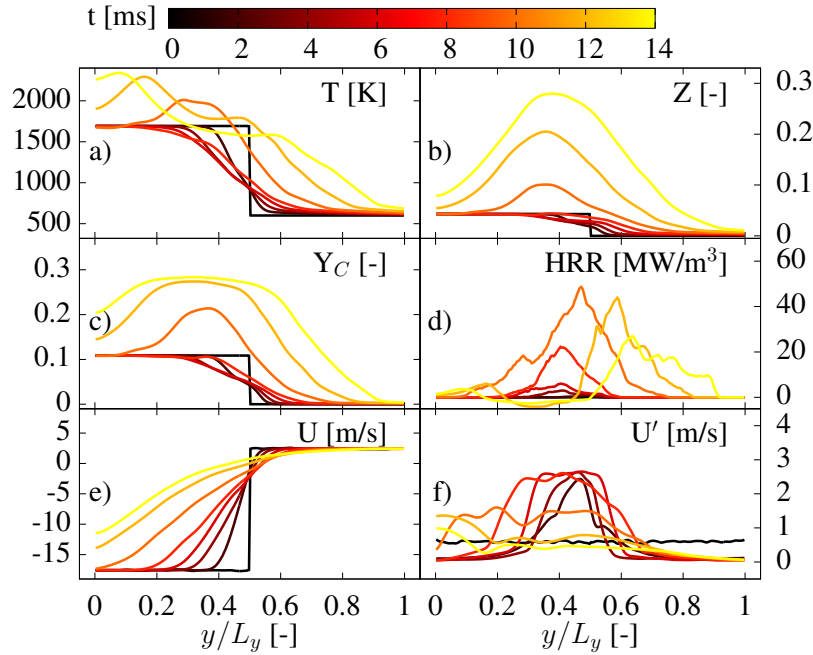
Figure 8.4: Spatially averaged temperature, volatile mixture fraction, progress variable, heat release rate, mean and fluctuating velocity as a function of the cross-stream coordinate y for different times.

at early times as the mixing layer develops. Largest fluctuation levels of around $2.5\,\mathrm{m/s}$ are observed before strong burning in the mixing zone occurs (around $t = 8\,\mathrm{ms}$). The volatile flame strongly dampens the turbulence in the mixing zone such that the velocity fluctuation drops to values of the order of the initial perturbations at late times.

Figure 8.5 presents volume-integrated mass released by devolatilization and char combustion (obtained by volume-integrating volatile and char off-gas mixture fractions, respectively) and volume-integrated heat release rate as a function of time. The overall devolatilization rate increase accelerates at around $t = 8\,\mathrm{ms}$ as the gas starts to heat up rapidly due to chemical reactions and the particles are in turn heated up by the volatile flame. At the same time the heat release rate starts to increase rapidly. The peak heat release is reached at $t = 10\,\mathrm{ms}$. The heat release is split into premixed and diffusion parts by integrating the heat release only where the flame index is positive and negative, respectively. It should be noted, however, that the conclusions drawn from this part of the analysis need to be treated with some caution, since the processes in the boundary layers around individual particles remain unresolved in CP-DNS. Overall, there is a balance between heat release associated with premixed and diffusion-dominated burning up to $t = 9\,\mathrm{ms}$. Then, burning in diffusion mode starts to dominate the overall heat release, but decreases rapidly after $t = 10\,\mathrm{ms}$ while the premixed heat release shows only a small decrease. This can be related to an initially steady flame burning into the premixed gas forming on the colder side of the mixing zone, and a very rapid diffusion-dominated heat release in the hot region of the mixing zone, which rapidly consumes oxygen and then extinguishes. The available O_2 mass starts to decrease rapidly at around $t = 8 - 9\,\mathrm{ms}$. At
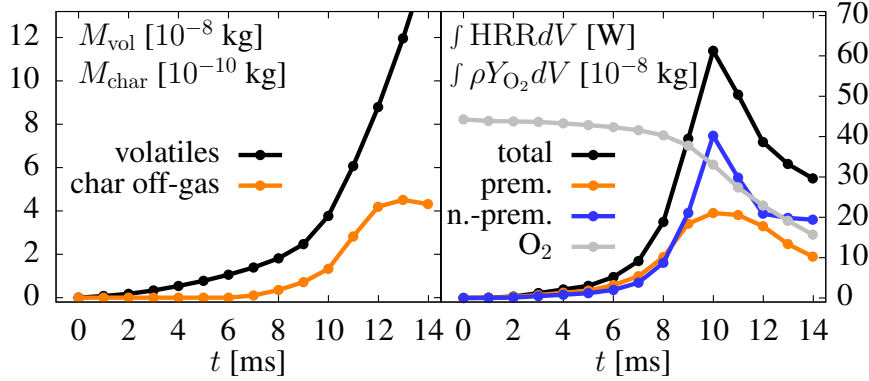
Figure 8.5: Volume-integrated mass of devolatilization and char conversion products vs. time (left), volume-integrated heat release (total, diffusion and premixed zones), and volume-integrated mass of O_2 vs. time (right).

$t = 13\,\text{ms}$, less than half of the initially present oxygen is left, mainly located in the upper part of the domain, cf. Fig. 8.3. At late times, the premixed flame fronts show some extinction leading to a decrease of heat release in the premixed zones. The overall heat release due to diffusion-dominated burning stabilizes at $t = 12\,\text{ms}$ and remains almost constant until $t = 14\,\text{ms}$.

Char conversion starts at $t = 7\,\text{ms}$ and increases up to $t = 13\,\text{ms}$. Contour plots of the char conversion progress (not shown) indicate that in the present setup char conversion only occurs near the bottom boundary of the domain, and for particles that have rapidly devolatilized in the mixing zone and were carried into the few remaining regions, where even at late times some O_2 is left to drive char combustion. Also note that the units of M_{vol} and M_{char} in Fig. 8.5 (left) differ by a factor of 100, indicating that only limited char conversion occurs.

Figure 8.6 presents the devolatilization progress C_{dev} of all particles as a function of y for different times. The points representing individual particles are colored by the gas temperature the particle is exposed to (interpolated onto the particle position). Initially, particles devolatilize at y/L_y=0.5, see $t = 3\,\text{ms}$. At $t = 5\,\text{ms}$, a significant increase of devolatilization progress can be observed for particles that are exposed to high gas temperatures within the mixing zone and towards the lower stream. This process continues such that a few particles reach fully devolatilized states at $t = 7\,\text{ms}$, even before heat release starts to increase rapidly, cf. Fig. 8.5. As the volatiles ignite and burn, a significant portion of particles below y/L_y=0.5 rapidly devolatilizes between $t = 9\,\text{ms}$ and $t = 13\,\text{ms}$. Fully devolatilized particles can be observed far in the upper stream up to y/L_y=0.8. However, there are still particles that are not fully devolatilized even when exposed to temperatures around 1400 K at $t = 11 - 13\,\text{ms}$. This is due to the fact that even at gas temperatures of 2000 K, particles require around 3 ms to heat up and reach a devolatiliztion progress of 99%. At 1400 K the time to heat and devolatilize the particles exceeds the $t = 14\,\text{ms}$ of simulation time.

Figure 8.7 presents the normalized progress variable C vs. mixture fraction with scatter points colored by temperature. Up to $t = 3\,\text{ms}$, the mixture fraction does not
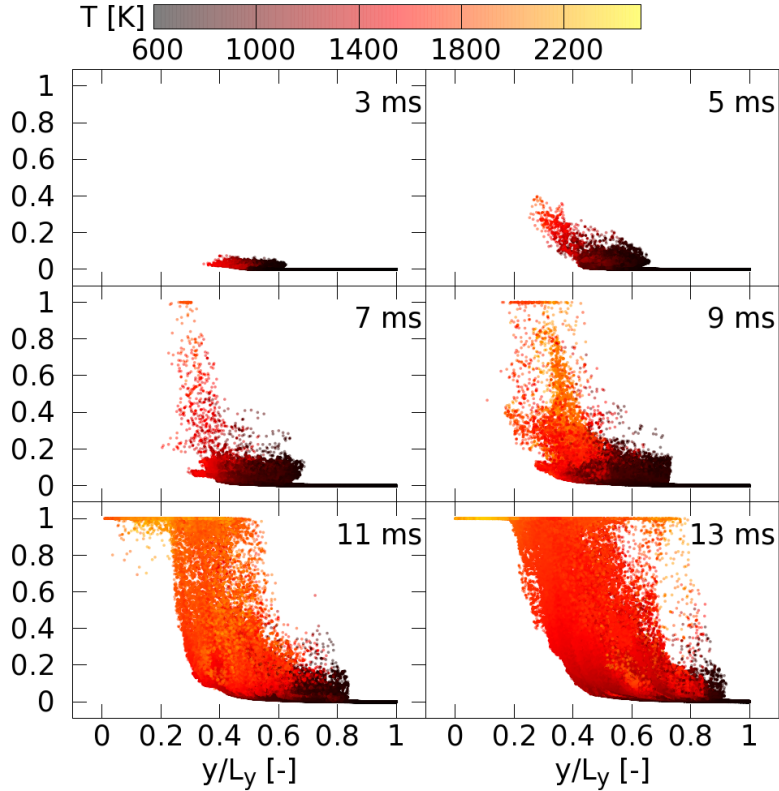
Figure 8.6: Scatterplot of devolatilization progress C_{dev} vs. y/L_y colored by the gas phase temperature surrounding the particle for different times.

significantly exceed the value in the lower stream imposed at initialization. At $t = 5\,\text{ms}$, states beyond $Z = 0.043$ exist that show high temperatures and large values of C. Low values of C and temperature for small mixture fractions indicate premixed regions, whereas high values of C for $Z > 0.043$ indicate regions around individual particles or small particle groups entrained in the lower stream (cf. Fig. 8.1). The picture changes more drastically from $t = 7\,\text{ms}$ to $t = 9\,\text{ms}$, where mixture fractions exceeding $Z = 0.2$ are present. Near stoichiometry, peak values of C below 1 are observed, whereas richer regions show peak values closer to unity. Tests based on 0D reactor calculations (using fresh volatiles mixed with gas corresponding to the lower stream) confirm that the time to reach equilibrium values of C is shorter for rich mixtures with Z around 0.14 than at stoichiometric conditions, which explains this behavior. The reactor simulations show that in stoichiometric regions, CO_2 and CO form relatively fast, followed by a relatively slow conversion of some of the CO to CO_2. In richer regions, CO_2 and CO form slightly more slowly, but a slow conversion of CO to CO_2 is not observed, leading to overall faster times to reach equilibrium as judged by the progress variable. Regions with mixture fractions exceeding $Z \approx 0.2$ show significantly lower values of C. This is characteristic for fresh volatiles being released into oxygen-depleted products or large amounts of volatiles released in the lower stream, where a slow production of CO takes place. At later times this trend continues, but overall more states with lower values of C are present even at
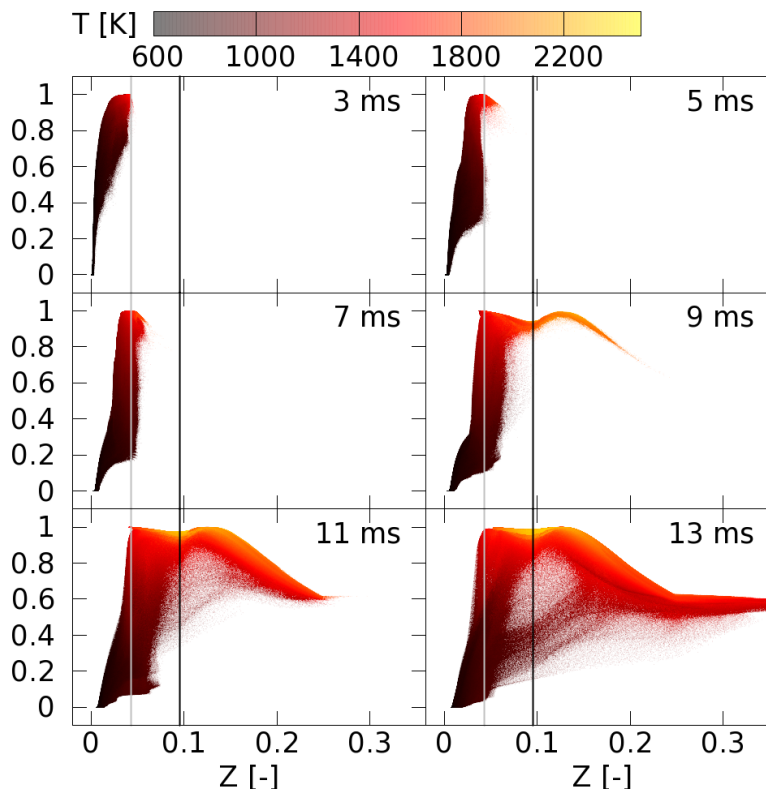
Figure 8.7: Scatterplot of normalized reaction progress variable C vs. mixture fraction Z colored by temperature. The vertical grey and black lines indicate the lower stream and stoichiometric mixture fraction, respectively.

stoichiometric conditions, which is related to partially extinguishing conditions (cf. the discussion of Fig. 8.3) at the upper flame and slow chemistry in rich regions.

8.4.2 Analysis of Combustion Modes

Figure 8.8 presents the scatter of heat release rate as a function of mixture fraction with points colored by flame index. Already at $t = 3\,\mathrm{ms}$, non-zero values of heat release rate can be observed in lean mixtures, mostly in homogeneous ignition (grey) or diffusion (blue) modes. At $t = 5\,\mathrm{ms}$, peak values of heat release rate increase, mostly associated with the diffusion combustion mode. From $t = 5\,\mathrm{ms}$ to $t = 7\,\mathrm{ms}$, a strong increase in premixed (red) heat release can be observed at lean conditions around $Z = 0.04$. This corresponds to regions in the mixing zone where fresh volatiles mix with mixtures of the upper stream and lower stream forming lean flammable mixtures. Diffusion-dominated heat release on the other hand corresponds to clouds around single or few particles within the lower stream (cf. Fig. 8.3). At $t = 9\,\mathrm{ms}$, as richer mixtures are present and large amounts of volatiles ignite, strong heat release associated with the premixed mode can be observed around $Z = 0.05$. Heat release in diffusion mode features overall slightly lower HRR values but spans a broad range of mixture fractions from $Z = 0.05$ to 0.15. This
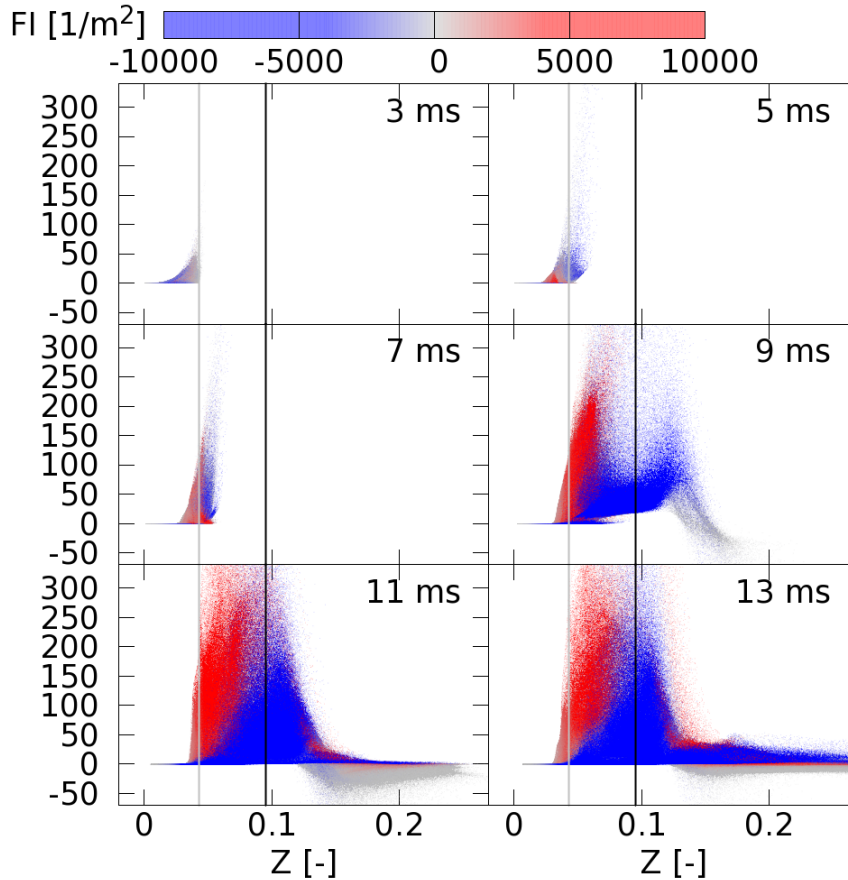
Figure 8.8: Scatterplot of heat release rate vs. mixture fraction colored by the flame index. The vertical grey and black lines indicate the lower stream and stoichiometric mixture fraction, respectively.

can be observed similarly at $t = 11\,\text{ms}$ with, however, more points showing high values of heat release. Homogeneous negative heat release is found for richer mixtures (cf. Figs. 8.3 and 8.4). This is related to fresh volatiles being released to product gas, where CO_2 is converted to CO, as observed from 0D reactor calculations of representative conditions. Time $t = 13\,\text{ms}$ shows a similar picture with an overall decreased level of heat release compared to 11 ms. Interestingly, positive heat release now extends far into rich regions.

Compared to the 2D-DNS by Muto et al. [141], differences in the ignition behavior can be observed in the present work. Muto et al. observed rich ignition due to particles being pre-heated to 2000 K, readily providing a rich, hot mixture. However, they observe a shift of the heat release to lean mixtures, mostly burning in premixed mode. This latter observation is very similar to the lean premixed zones identified in this work.

8.4.3   Flamelet Structure

Figure 8.9 shows temperature as a function of mixture fraction for pseudo-flamelets colored by the oxidizer split λ. These pseudo-flamelets are extracted along lines orthogonal

to the $Z = Z_{st}$ iso-surface and mapped onto mixture fraction. Data for a distance between -10Δ and $+10\Delta$ has been considered, where 0 indicates the iso-surface. Additional information on various limiting conditions is provided by a number of reference lines in Fig. 8.9, for cases of the adiabatic equilibrium solution, adiabatic mixing between the lower stream and fresh volatiles and adiabatic mixing between fresh volatiles and air. One observation that can be made is that all flamelets stay well below the adiabatic equilibrium solution, which is due to the heat exchange with the particle phase. Stably burning (steady) flamelets with high temperatures can be observed from $t = 8...9$ ms onwards. At later times, increasingly more unburned states can be observed even at stoichiometric mixture fractions. Additionally, different types of flamelets can be distinguished at later times. There are steady flamelets close to the equilibrium solution covering short distances in mixture fraction space. This indicates low mixture fraction gradients, since only a small mixture fraction distance is covered across a fixed distance used for flamelet extraction ($2 \cdot 10\Delta$). These flamelets consistently show large values of λ, indicating that they stem from the lower flame burning into the hot lean products. Further flamelet structures are present below these stable hot flamelets and correspond to the upper flame burning into the upper stream showing low values of λ. These flamelets mostly cover a larger range in mixture fraction space indicating larger mixture fraction gradients. Towards the end of the simulation flamelets can be observed that show very steep gradients (in T-Z-space), which indicates premixed flames in mixtures of air from the upper stream and volatiles. Overall, the analysis of pseudo-flamelets reveals that heat losses need to be accounted for in the flamelet modeling of the present mixing layer case, which, however, is to be expected and considered in recent work concerned with flamelet modeling for PCC (e.g. [106, 134, 199, 201, 202, 237, 248, 253, 254]). In addition, a progress variable approach could be adopted that is able to capture the effects of slow chemistry for detailed modeling of the ignition and burning behavior in such a configuration, as attempted in recent work [106, 134, 237, 248, 253, 254].

8.5 Conclusions

This work presents the first three-dimensional carrier-phase DNS study of pulverized coal combustion in well-defined shear-generated turbulence. The simulation includes particle heating, devolatilization, ignition, volatile combustion and (albeit limited) char conversion. The simulation is analyzed and discussed focusing on the characterization of the ignition mechanism and burning modes. The analysis reveals initial heat release at very lean conditions for particles that are entrained in the hot flow. Subsequent burning of volatiles shows both non-premixed and premixed combustion modes, where overall the non-premixed mode dominates the heat release. Complex flame structures can be observed with partially premixed zones ahead of diffusion flames as well as flame quenching likely because of significant heat losses to heat up particles. At late times an upper and lower flame can be distinguished, where the upper flame burns into the particle-laden air stream in premixed and non-premixed mode, while the lower flame burns in non-premixed mode towards the lean hot product stream, where it consumes the remaining oxygen. Between these two flames, an overall rich mixture of volatile
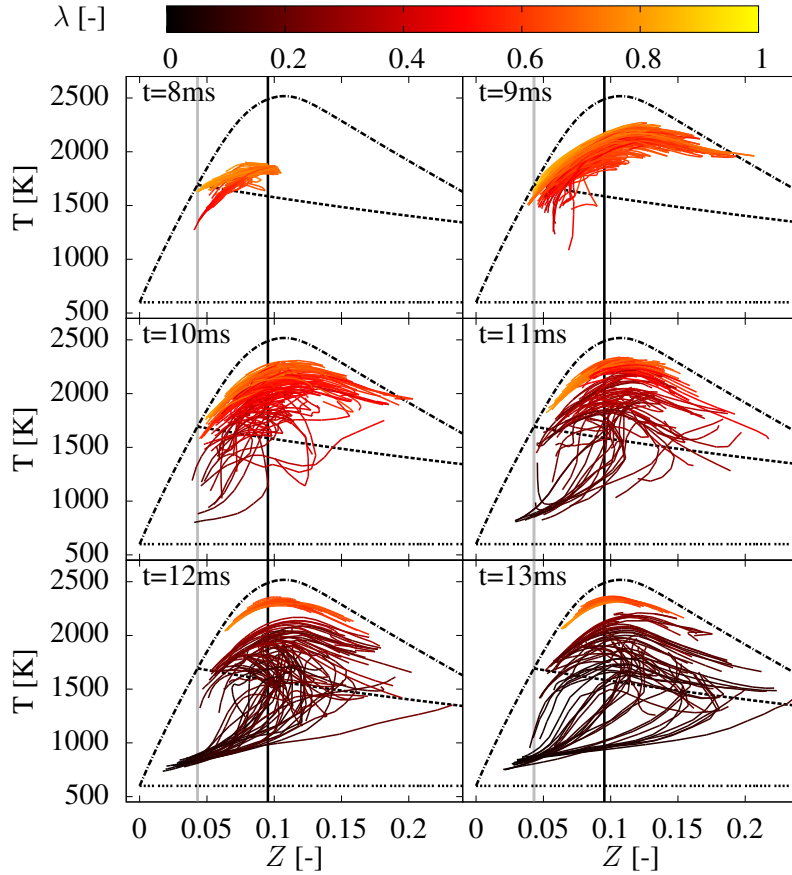
Figure 8.9: Pseudo-flamelets extracted along normals to the $Z=Z_{st}$ iso-surface showing temperature as a function of mixture fraction colored by the oxidizer split λ. Additional lines shown: $Z=Z_{LS}$ (vertical solid grey) and $Z=Z_{st}$ (vertical solid black); adiabatic equilibrium solution (dash-dotted), adiabatic mixing between lower stream and fresh volatiles (dashed), adiabatic mixing between fresh volatiles and air (dotted).

combustion products and fresh volatiles can be found. A basic flamelet analysis has been performed, showing that the lower flame can likely be modeled well by a steady non-premixed flamelet, while the upper flame requires a more sophisticated progress variable based approach that includes heat losses.

8.6   Acknowledgements

Chapter 9

A Hybrid Flamelet Finite-Rate Chemistry Approach for Efficient LES with a Transported FDF

This chapter is under preparation for submission in Combustion and Flame [198] by the authors 'Rieth, M., Chen, J.-Y., Menon, S., Kempf, A.M. The author of this thesis contributed the code extension and development (including the implementation of the standard and hybrid transported FDF method), running of simulations, post-processing and paper writing. The authors J.-Y. Chen, S. Menon and A.M. Kempf contributed discussions, proof-reading and corrections. The author A.M. Kempf developed the original versions of the PsiPhi code.

Abstract

A hybrid method combining flamelet tabulation with transported filtered density function (FDF) finite rate chemistry has been developed and applied to large eddy simulation (LES) of the Sydney/Sandia piloted turbulent flame with inhomogeneous inlets. Aiming to improve the efficiency while maintaining accuracy, the hybrid method applies the computationally expensive Lagrangian particles representing FDF transport and direct chemistry only in selected, dynamically varying locations. The rest of the domain is treated with flamelet chemistry based on the Eulerian fields and a presumed top-hat PDF closure. The method relies on consistency between Eulerian and Lagrangian fields through robust, accurate coupling and consistent modeling. The performance of the hybrid model is verified by an extensive comparison against the experiment and the 'pure' models, i.e., the a) flamelet LES with presumed FDF, b) flamelet LES with transported FDF, and c) direct chemistry LES with transported FDF. Finite rate chemistry is found to improve species predictions over flamelet chemistry and the hybrid method is found to reproduce these improvements by using particles with finite rate chemistry only at locations where the flamelet is not sufficient, promising a reduced overall computational cost.

9.1   Introduction

The LES approach has proven to be well suited for predicting turbulent reacting flow problems [85, 174]. In reacting flows, the subgrid distribution influences the flow field more strongly than in non-reacting flows, since reaction occurs on small scales unresolved by the LES. Hence, the LES of reacting flows relies on appropriate models for turbulence-chemistry interaction. The transported PDF method is an approach where the evolution of a joint probability density function (PDF) in composition and physical space is calculated and the source terms appear in closed form.

A very promising technique is the combined LES-FDF approach, where the transported PDF becomes the transported filtered density function (FDF). The composition is provided by the FDF that is transported by the velocity and turbulence fields from the LES, benefiting from the accurate flow field predicted by the LES.

Dopazo and O'Brien were the first to propose a transport equation for the PDF of reactive scalars [42], which has been developed further by Pope [179], O'Brien [148], Janicka et al. [84] and others. Pope's suggestion of using a Monte Carlo scheme for treating the PDF [180] turned the method into a tractable tool for combustion simulation. It has been presented in detail by Pope [178], and early combustion applications of the method have been reported by Chen et al. [25] and others.

The use of a PDF in LES has been proposed by Givi [59], of a transported PDF in LES (FDF) by Pope [177]. Gao and O'Brien provided a closure of the FDF transport equation in LES [55]. The first applications of the LES/FDF method have been reported by Colucci et al. [34] and Jaberi et al. [83], realistic flames have first been simulated by Sheikhi et al. [211], who studied the Sandia Flame D, and Raman et al. [192], who simulated the Sydney bluff-body flame. Both simulations used the laminar flamelet model to determine the Lagrangian Monte Carlo (LMC) particles' chemical states, so that the FDF method effectively provided a subgrid model for the mixture fraction only. Raman & Pitsch [191] were the first to directly apply finite rate chemistry with a 16-step chemical mechanism to simulate Sandia flames D and F with the LES/FDF approach.

Recent developments focus on numerical issues reported by Wang et al. [242] or Popov et al. [182], on improvements of mixing models for premixed combustion, on convergence when approaching DNS resolution or on dynamic modeling as reported by Tirunagari & Pope [228, 229] or Han et al. [65].

The flamelet model, as studied by Peters [162] for non-premixed flames, has been widely applied in LES of turbulent combustion [85, 174] and extended for unsteady effects (e.g. [169]) or to premixed flames (e.g. [151]). The success of flamelet models can be attributed to their low numerical cost and its ability to accurately predict most relevant flames, i.e., flames without significant quenching, reignition or flame-wall interaction.

The present work aims to combine the advantages of flamelet models (cost) with the advantages of transported FDF methods (detailed chemistry and accurate subgrid modelling) in a hybrid method which couples a) flamelet models with a presumed FDF and b) direct chemistry with transported FDF, so that the most suitable model is applied at each point of the flow field. The development of such a hybrid method is motivated by the fact that in technical combustors often regions exist where tabulation based combustion models work well, e.g. regions that are well resolved due to a low local Reynolds number,

Table 9.1: Nomenclature used in this work.

Acronym	FDF method
ADF	Assumed filtered density function
TDF	Transported filtered density function
HDF	Hybrid filtered Density Function
Acronym	Chemistry type
DC	Direct Chemistry
FC	Flamelet Chemistry

regions without quenching or re-ignition, or regions where the flow is non-reactive [61]. To reduce the cost of the transported FDF method, it can be constrained to locations where the simpler combustion model fails, e.g. in regions of high strain featuring local extinction or in situations where premixed as well non-premixed combustion can occur (such as in the investigated configuration).

To permit a compact discussion of the many models tested and combined in this work, we introduce the nomenclature for the different methods and models summarized in Tab. 9.1. ADF is exclusively used with FC, hence the specification of the chemistry model is omitted for ADF. TDF and HDF are used with both, FC and DC. The hybrid method relies on scalar fields obtained by both, the Eulerian based ADF and the Lagrangian based TDF. The ADF relies on the flamelet generated manifold (FGM) method with a presumed top-hat FDF. The TDF method uses DC (or FC) for the evaluation of the source terms and for obtaining the scalar fields. The TDF particles are either seeded in the whole domain (as in a conventional LES-FDF) or, in the hybrid method, just at specific locations to reduce the computational cost, where the seeding locations may vary in space and time. Filtered scalar fields in the hybrid framework (HDF) can then be obtained from the TDF where particles are present or otherwise from ADF. This hybrid method requires robust coupling of LES and particle fields, consistent seeding methods for the particles as well as consistent transport of particle and LES fields, all of which are addressed in this work.

9.2   Modeling

9.2.1   Modeling of the Flow Field

Large eddy simulation (LES) is used to obtain the flow field, which is required for the transport of the Lagrangian particles describing the TDF and the resolved scalar fields describing the ADF.

The LES solves the Favre-filtered Navier-Stokes (density weighted - $\overline{\rho\phi} = \bar{\rho}\tilde{\phi}$) and additional transport equations in a low-Mach formulation.

$$\frac{\partial \bar{\rho}}{\partial t} + \frac{\bar{\rho}\tilde{u}_j}{x_j} = 0 \tag{9.1}$$

$$\frac{\partial \bar{\rho}\tilde{u}_i}{\partial t} + \frac{\partial \bar{\rho}\tilde{u}_i\tilde{u}_j}{\partial x_j} = -\frac{\partial \bar{P}}{\partial x_i} + \frac{\partial}{\partial x_j}\left[2\bar{\mu}\tilde{S}_{ij}^d - \tau_{ij}^{\mathrm{SGS}}\right] \tag{9.2}$$

The equations include the filtered density $\bar{\rho}$, the Favre-filtered velocity vector $\tilde{u}_i$, the filtered pressure parameter $\bar{P}$, the filtered dynamic viscosity $\bar{\mu}$, the deviatoric part of the rate-of-strain tensor $\tilde{S}_{ij}^d$ based on Favre-filtered velocities and the subgrid stress tensor $\tau_{ij}^{\mathrm{SGS}} = \bar{\rho}[\widetilde{u_i u_j} - \tilde{u}_i\tilde{u}_j]$. The deviatoric part of the subgrid stresses is closed by the eddy-viscosity approach and the Germano model [56] in a localized [172] and variable density formulation [136]:

$$\tau_{ij}^{\mathrm{SGS}} - \frac{1}{3}\delta_{ij}\tau_{kk}^{\mathrm{SGS}} = -\bar{\rho}2C\Delta^2\mathcal{S}\tilde{S}_{ij}^d = -\mu_{\mathrm{t}}\tilde{S}_{ij}^d. \tag{9.3}$$

The stresses depend on the modeling constant C obtained from the dynamic procedure, to the characteristic rate-of-strain $\mathcal{S}$ and the subgrid dynamic viscosity μ_{t}. The isotropic part of the subgrid stress tensor $(\frac{1}{3}\delta_{ij}\tau_{kk}^{\mathrm{SGS}})$ is not computed explicitly but combined with pressure p to yield the pressure parameter P since a low Mach assumption is employed.

We would also like to point out that in the present case, the Germano model was chosen as it produced better results than the more cost-effective Sigma model [145] that we usually prefer [203].

9.2.2　Combustion Model A - Direct Chemistry (DC)

Direct chemistry is used in combination with the TDF approach, and reactions are described by the DRM19 mechanism for methane [92] consisting of 21 species (19 active species, and N_2 and Argon) and 84 reactions. Species source terms are obtained by solving the coupled system of ODEs for each species as well as enthalpy, using the solver CVODE [33]. The chemical kinetics library Cantera [62] is used to obtain reaction rates as well as thermodynamic properties of the gas.

9.2.3　Combustion Model B - Flamelet Chemistry (FC)

Flamelet chemistry is used with the ADF approach, relying on the DRM19 mechanism to ensure consistency with DC. The flamelet generated manifolds (FGM) [150, 151] are generated from one-dimensional premixed flames for different equivalence ratios and tabulated as a function of a normalized progress variable C and mixture fraction Z. The non-normalized progress variable is defined as $Y_p = Y_{CO_2} + Y_{H_2O} + Y_{CO} + Y_{H_2}$. Further details on the modeling and implementation are given by Proch and co-workers [186, 187].

It should be noted that FC can also be applied to individual Lagrangian particles in the TDF approach, which is useful to check consistency and to directly compare ADF, TDF and HDF.

9.2.4 FDF Model A - Transported FDF (TDF)

The FDF transported by the LES velocity and turbulence fields is the scalar filtered mass density function (SFMDF) [83, 192]:

$$F_t(\mathbf{\Psi}; \boldsymbol{x}, t) = \int_{-\infty}^{+\infty} \rho(\boldsymbol{x}', t) f_t(\mathbf{\Psi}, \phi(\boldsymbol{x}', t)) G(\boldsymbol{x}' - \boldsymbol{x}) d\boldsymbol{x}'. \qquad (9.4)$$

This FDF is a convolution of the LES grid filter function $\mathcal{G}$, the fluid density ρ in physical space and the (fine-grained) PDF f_t in composition space [178], where $\mathbf{\Psi}$ is the composition sample space vector.

The fine-grained PDF f_t [178] is described as a delta function of the dimensionality of the number of scalars n_s (i.e., mass fractions and enthalpy) required to describe the chemistry or correspondingly as a product of n_s scalar delta functions, it reads:

$$f_t(\mathbf{\Psi}, \boldsymbol{\phi}(\boldsymbol{x}', t)) = \delta(\mathbf{\Psi} - \mathbf{\Phi}(x, t)) = \prod_{\alpha=1}^{n_s} \delta[\psi_\alpha - \phi_\alpha(x, t)]. \qquad (9.5)$$

In Eq. 9.5, Φ is the composition vector and ϕ_α a composition vector component.

The transport equation of the SFMDF can be deduced by taking the time derivative of Eq. 9.4, which after some manipulations and substitutions eventually leads to [34, 55, 192]:

$$
\begin{aligned}
\frac{\partial F_t}{\partial t} + \frac{\partial \widetilde{u}_i F_t}{\partial x_i} &= -\frac{\partial}{\partial x_i}(\overline{[u_i|\mathbf{\Psi} - \widetilde{u}_i]} F_t) \\
&+ \frac{\partial}{\partial \psi_\alpha} \left[\overline{\frac{1}{\rho} \frac{\partial J_i^\alpha}{\partial x_i}} \middle| \mathbf{\Psi} \right] F_t \right] - \frac{\partial S_\alpha F_t}{\partial \psi_\alpha}.
\end{aligned}
$$

The SGS convective and diffusive fluxes are closed by a gradient-diffusion approach [34] $(\partial([\overline{u_i|\mathbf{\Psi}} - \widetilde{u}_i]F_t)/\partial x_i = -\partial[\bar{\rho}D_t\partial(F_t/\bar{\rho})/\partial x_i]/\partial x_i)$ and by the IEM mixing model [41, 239]. The last term of Eq. 9.6 is the closed chemical reaction source term and is detailed later.

The transport of the FDF is not solved directly but evolves based on a Monte-Carlo method [178], represented by notional Lagrangian particles. The notional particles evolve in physical and composition space and each of the particles can be seen as a representation of a single realization of the turbulent scalar field [177].

The following equation governs the particle evolution in physical space:

$$dx_i^+ = \left(\tilde{u}_i + \frac{1}{\bar{\rho}} \frac{\partial \bar{\rho}(\tilde{D} + D_t)}{\partial x_i} \right) dt + (2(\tilde{D} + D_t))^{1/2} dW_i(t). \qquad (9.6)$$

The change dx_i^+ in the physical position x_i^+ of the particles depends on the molecular diffusivity $\tilde{D}$ and turbulent diffusivity D_t, the filtered velocity $\tilde{u}_i$ and a three-dimensional Wiener term dW_i. The diffusivities are obtained from assuming a constant turbulent Schmidt number of $Sc_t = 0.7$ and a unity Lewis number.

The chemistry and mixing model govern the particle evolution in composition space:

$$d\psi_\alpha = -C_\phi \tau_{\mathrm{mix}}^{-1}(\psi_\alpha - \tilde{\phi}_\alpha)dt + S_\alpha(\boldsymbol{\psi})dt. \tag{9.7}$$

The mixing time scale and mixing model constant have to be matched with the LES subfilter dissipation (detailed below). The mixing frequency is set to:

$$\omega = \tau_{\mathrm{mix}}^{-1} = \frac{D_{\mathrm{eff}}}{\Delta^2}, \tag{9.8}$$

and the mixing model constant (scalar-to-mechanical time scale ratio) is set to $C_\phi = 12$. With DC, the composition vector consists of the 21 species mass fractions contained in the chemical mechanism (DRM19) and enthalpy. (With FC, the composition space would be two dimensional, simply consisting of the mixture fraction and progress variable.)

Favre-filtered quantities $\tilde{q}$ are obtained by averaging over the particles (n_p) contained in an LES cell.

$$\tilde{q} = \frac{\sum_{p=1}^{n_p} w_p q_p}{\sum_{p=1}^{n_p} w_p} \tag{9.9}$$

The averages depend on a particle weight w_p which is assigned to a particle upon generation such that the sum of particle weights within a filter volume corresponds to the mass in the local filter volume. The Reynolds-filtered density is correspondingly obtained by:

$$\bar{\rho} = \left(\frac{\sum_{p=1}^{n_p} w_p/\rho_p}{\sum_{p=1}^{n_p} w_p}\right)^{-1}. \tag{9.10}$$

9.2.5   FDF Model B - Assumed FDF (ADF)

The FC model is combined with an assumed two-dimensional top-hat FDF, which requires values of $\tilde{Z}$, $\tilde{Y}_p$, $\widetilde{Z''^2}$ and $\widetilde{Y_p''^2}$ from the respective transport equations to determine the thermo-chemical state in a filter volume.

The transport of Favre-filtered mixture fraction $\tilde{Z}$ and progress variable $\tilde{Y}_p$ is given by Eqs. 9.11 and 9.12.

$$\frac{\partial}{\partial t}\bar{\rho}\tilde{Z} + \frac{\partial}{\partial x_j}\bar{\rho}\tilde{u}_j\tilde{Z} = \frac{\partial}{\partial x_j}\left(\bar{\rho}D_{\mathrm{eff}}\frac{\partial \tilde{Z}}{\partial x_j}\right) \tag{9.11}$$

$$\frac{\partial}{\partial t}\bar{\rho}\tilde{Y}_p + \frac{\partial}{\partial x_j}\bar{\rho}\tilde{u}_j\tilde{Y}_p = \frac{\partial}{\partial x_j}\left(\bar{\rho}D_{\mathrm{eff}}\frac{\partial \tilde{Y}_p}{\partial x_j}\right) + \bar{\rho}\tilde{\dot{S}}_{Y_p} \tag{9.12}$$

The effective diffusivity D_{eff} is the sum of molecular diffusivity $\tilde{D}$ and subgrid diffusivity D_{t}, where the former is obtained by assuming a Lewis number of unity and the latter by assuming a constant turbulent Schmidt number of $\mathrm{Sc}_{\mathrm{t}} = 0.7$.

Corresponding to the transported FDF, the assumed FDF (f_a) and assumed Favre FDF (F_a) can be defined as follows.

$$F_a(\boldsymbol{\Psi}; \tilde{\boldsymbol{\phi}}, \widetilde{\phi''^2}) = \rho(\boldsymbol{\Psi})f_a(\boldsymbol{\Psi}; \tilde{\boldsymbol{\phi}}, \widetilde{\phi''^2})/\bar{\rho} \tag{9.13}$$

The quantities F_a and f_a are the Eulerian counterparts of the quantities F_t and f_t used in the transported FDF context in Sec. 9.2.4, and $\boldsymbol{\Psi}$ denotes the sample-space corresponding to Z and Y_p. However, it should be noted that f_a and F_a are averages over many realizations, while F_t and f_t describe single realizations. The ADF is parametrized by Favre-mean and variance of Z and Y_p, denoted by the vectors $\tilde{\boldsymbol{\phi}}$ and $\widetilde{\boldsymbol{\phi}''^2}$, respectively.

Filtered species mass fractions, density and progress variable source term are obtained by a convolution of the mass fraction and FDF in composition space, Eqs. 9.14-9.16.

$$\tilde{Y}(\tilde{\boldsymbol{\phi}}, \widetilde{\boldsymbol{\phi}''^2}) \qquad = \int Y(\boldsymbol{\Psi}) F_a(\boldsymbol{\Psi}; \tilde{\boldsymbol{\phi}}, \widetilde{\boldsymbol{\phi}''^2}) d\boldsymbol{\Psi} \tag{9.14}$$

$$\bar{\rho}(\tilde{\boldsymbol{\phi}}, \widetilde{\boldsymbol{\phi}''^2}) \quad = \left(\int \rho(\boldsymbol{\Psi})^{-1} F_a(\boldsymbol{\Psi}; \tilde{\boldsymbol{\phi}}, \widetilde{\boldsymbol{\phi}''^2}) d\boldsymbol{\Psi} \right)^{-1} \tag{9.15}$$

$$\bar{\rho}\tilde{\dot{S}}_{Y_p}(\tilde{\boldsymbol{\phi}}, \widetilde{\boldsymbol{\phi}''^2}) \qquad = \bar{\rho} \int \dot{S}_{Y_p}(\boldsymbol{\Psi}) F_a(\boldsymbol{\Psi}; \tilde{\boldsymbol{\phi}}, \widetilde{\boldsymbol{\phi}''^2}) d\boldsymbol{\Psi} \tag{9.16}$$

Different shapes of the ADF can be employed and classically the β PDF is used [35]. Here, the FDF is described by a two-dimensional top-hat FDF in normalized progress variable and mixture fraction space [50, 152] (which is equivalent to the work by Kuenne et al. [113] if linear interpolation is used):

$$F_a(\boldsymbol{\Psi}) = \begin{cases} t_0 & \boldsymbol{\Psi}_a \leq \boldsymbol{\Psi} \leq \boldsymbol{\Psi}_b \\ 0 & \text{all other } \boldsymbol{\Psi} \end{cases} \tag{9.17}$$

The value of t_0 is calculated from:

$$t_0 = 1/\prod_{i=1}^{2}(\Psi_{i,b} - \Psi_{i,a}) = 1/\left[(Z_b - Z_a)(C_b - C_a) \right], \tag{9.18}$$

with $Z_a = \tilde{Z} - 1/2(12\widetilde{Z''^2})^{1/2}$, $Z_b = \tilde{Z} + 1/2(12\widetilde{Z''^2})^{1/2}$, $C_a = \tilde{C} - 1/2(12\widetilde{C''^2})^{1/2}$ and $C_b = \tilde{C} + 1/2(12\widetilde{C''^2})^{1/2}$. This allows only for relatively small variances [50], which however are sufficient in the present work. No additional flame thickening or related techniques are employed in this work.

The evaluation of the ADF requires the variances of mixture fraction and progress variable. Here, Eulerian transport equations are modeled consistently with the TDF method such that both methods obtain consistent subfilter variances. To this end Eulerian equations of the square of the mixture fraction and progress variable, $\widetilde{Z^2}$ and $\widetilde{Y_p^2}$, are solved in the LES [142, 192]:

$$\frac{\partial \bar{\rho}\widetilde{Z^2}}{\partial t} + \frac{\partial \bar{\rho}\tilde{u}_j \widetilde{Z^2}}{\partial x_j} \quad = \quad \frac{\partial}{\partial x_j} \left(\bar{\rho}D_{\text{eff}} \frac{\partial \widetilde{Z^2}}{\partial x_j} \right) - \bar{\rho}\tilde{\chi}_Z, \tag{9.19}$$

$$\frac{\partial \bar{\rho}\widetilde{Y_p^2}}{\partial t} + \frac{\partial \bar{\rho}\tilde{u}_j \widetilde{Y_p^2}}{\partial x_j} \quad = \quad \frac{\partial}{\partial x_j} \left(\bar{\rho}D_{\text{eff}} \frac{\partial \widetilde{Y_p^2}}{\partial x_j} \right) + 2\bar{\rho}\widetilde{Y_p\dot{S}_{Y_p}}$$
$$\qquad - \quad \bar{\rho}\tilde{\chi}_{Y_p}. \tag{9.20}$$

Particular importance in this respect can be attributed to the modeling of scalar dissipation rate or equivalently the mixing frequency in the transported FDF method, for which

different approaches exist. Raman et al. [192] used a transport equation for the filtered square of the mixture fraction, $\widetilde{Z^2}$ and modeled the scalar dissipation rate using a model typically employed in PDF methods [34] and a fixed scalar-to-mechanical time scale ratio to obtain consistency between LES and transported FDF mixture fraction variances. Later, Raman & Pitsch [191] employed a dynamic procedure based on the assumption of local equilibrium [170], such that a scalar-to-mechanical time scale ratio can be obtained dynamically. Most of the LES-FDF studies do not solve for additional variance equations (since it is provided from the transport of the FDF) or use a dynamic procedure, and define mixing frequencies similar to Colucci et al. [34], but with a largely varying value for the model constant (e.g., $C_\phi = 3$ [83], $C_\phi = 8$ [211], $C_\phi = 12$ [101]). Han et al. [65] determined an optimum value of $C_\phi = 10$ for the prediction of a lifted hydrogen flame based on the application of a dynamic model based on the local equilibrium assumption. The approach chosen in the present work is to solve equations for the squares of mixture fraction and progress variable, use the same model for scalar dissipation for both transport equations and model the mixing consistently. The approach follows Raman et al. [192] but adds the progress variable variance, which is treated in a similar fashion as by Nambully et al. [142].

The dissipation term is modeled following Eq. 9.21, such as frequently done for the mixing frequency in LES-FDF methods [34, 192, 211] and consistent to Eq. 9.8 with $C_\chi = 2C_\phi$:

$$\bar\rho\tilde\chi_{\phi_\alpha} = C_\chi \frac{2\bar\rho D_\text{eff}}{\Delta^2} \widetilde{\phi''^2_\alpha}. \tag{9.21}$$

The subfilter mixture fraction and progress variable variance is obtained from the transported quantities as:

$$\widetilde{\phi''^2_\alpha} = \widetilde{\tilde\phi^2_\alpha} - \tilde\phi^2_\alpha. \tag{9.22}$$

A normalized progress variable mean and its variance are required for ADF. Progress variable and its variance are normalized by the values at chemical equilibrium: $\tilde C = \tilde Y_p / \tilde Y_{p,eq}$ and $\widetilde{C''^2} = \widetilde{Y^2_p / Y^2_{p,\text{eq}}} - \tilde Y^2_p / \tilde Y^2_{p,eq}$ (cf. [40]), which includes the assumptions $\widetilde{Y^2_p / Y^2_{p,\text{eq}}} \approx \widetilde{Y^2_p / \tilde Y^2_{p,\text{eq}}}$ and $\widetilde{Y_p / Y_{p,eq}} \approx \widetilde{\tilde Y_p / Y_{p,\text{eq}}}$. These assumptions can be expected to hold if the variation of $Y_{p,\text{eq}}$ within a cell is small.

9.3   Hybrid Approach

The hybrid approach presented in this work combines the models introduced above. It adds the transported FDF description with direct chemistry on top of the normal assumed FDF with flamelet chemistry, to augment accuracy in regions where the error would otherwise be large. This means that particles are introduced near such regions, and within such regions, the gas phase state and reaction progress are governed by the TDF, while regions without particles are governed by FC-ADF. Such an hybrid approach requires a) consistent modeling and b) robust coupling between LES and transported FDF as addressed in the following.

9.3.1   Particle Generation

In the standard non-hybrid LES-FDF, particles are generated at the inflow plane just downstream of the burner exit and hence used throughout the entire computational domain. In this work, particles can be generated arbitrarily in the computational domain. However, the particles generated at a specific location must reproduce the local filtered mean and variance of mixture fraction and progress variable, which is achieved by randomly sampling particles from their distribution function, the ADF. With the top-hat FDF employed, the individual particle mixture fraction and progress variable are determined by the following equations, using independent uniform random numbers ζ_Z and ζ_C between 0 and 1.

$$Z_p = \tilde{Z} + (\zeta_Z - 1/2)\sqrt{12\widetilde{Z''^2}} \qquad (9.23)$$

$$C_p = \tilde{C} + (\zeta_C - 1/2)\sqrt{12\widetilde{C''^2}} \qquad (9.24)$$

Here, the hybrid method is based on determining a volume where particles are to be used instead of the ADF based on certain switching criteria (explained below). The TDF volume is treated such that it may change in space and time. At the beginning of each time step, a buffer layer with a width of two cells around the TDF volume is determined, similar to the concept of ghost cells in the finite volume method. Particles are only seeded in this buffer layer and their weights are determined such that the sum of particle weights corresponds to the LES density with 20 particles per cell being seeded (same number as used e.g. by Tirunagari & Pope [228]). This buffer layer provides the correct boundary conditions for the TDF volume. In the next time step, the following situations may occur: a) a buffer layer cell might be outside of both the new TDF volume and buffer layer, particles within such cell are deleted and the ADF is considered to obtain the gas phase state. b), if a cell remains a buffer layer cell, new particles are generated that replace the old ones. The old particles need to be deleted and replaced to ensure that the TDF volume obtains boundary conditions that are consistent with the ADF and to ensure that particle weights are correct. Finally, c), a buffer layer cell might now be within the TDF volume and the particles are treated in the conventional way. This buffer layer treatment ensures correct particle fluxes across the faces of the particle volume.

9.3.2   Switching Criteria

The hybrid model is based on switching between TDF-DC and ADF-FC descriptions, following suitable local switching criteria. Based on standard LES-FDF calculations (presented in detail in Sec. 9.7) it could be observed that direct chemistry improves the predictions of certain species such as CO_2 in a mixture fraction range between approximately 0.04 and 0.2 as exemplarily depicted in Fig. 9.1. To evaluate the dynamic seeding method, the TDF volume is determined from a criterion based on mixture fraction. To include the reactive region and the rich region where differences can be seen, we have selected mixture fraction bounds of 0.001 and 0.18 to determine the TDF volume. Additionally, runs with more narrow criteria have been conducted, i.e., with mixture fractions bounds between 0.05 and 0.18 and 0.06 and 0.1. It should be noted that this method to
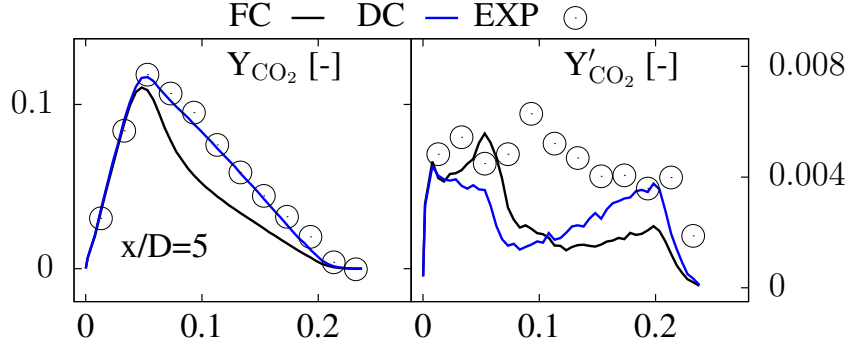
Figure 9.1: Mean and rms of the resolved CO_2 mass fraction conditioned on the mixture fraction for TDF-FC and TDF-DC.

specify the particle volume is not general, but used here to validate the dynamic seeding as a first step. Better general criteria are to be developed in the future, for example based on ideas of pure LES by Wu & Ihme [262].

9.3.3   Maintaining Consistency between TDF and ADF

A key issue of the LES-FDF method is achieving consistency between Eulerian and particle fields by feeding the TDF density to the LES flow solver. This issue has been addressed in many LES-FDF studies, e.g. [83, 182, 183, 192]. In this work, we follow Popov et al. [182, 183] to ensure coupling through the solution of an additional transport equation for the specific volume:

$$\frac{\partial \bar{\rho}\hat{v}}{\partial t} + \frac{\partial \bar{\rho}\tilde{u}_j\hat{v}}{\partial x_j} = \frac{\partial}{\partial x_j}\left(\bar{\rho}D_{\text{eff}}\frac{\partial \hat{v}}{\partial x_j}\right) + S_v + \bar{\rho}\frac{\tilde{v} - \hat{v}}{\tau_{\text{relax}}}. \tag{9.25}$$

The specific volume source S_v is due to particle reaction and micro-mixing. The last term relaxes the specific volume from the transport equation $\hat{v}$ to the specific volume $\tilde{v}$ from the particle phase to ensure that TDF and Eulerian fields do not deviate with time due to numerical errors. In the present work, it was not necessary to include this term and adequate consistency is demonstrated in Sec. 9.7.1. The use of an additional specific volume transport equation strongly reduces stochastic noise compared to direct feedback of the TDF density (obtained by Eq. 9.10).

   Essential to the numerical stability of a hybrid method where particle properties are only taken into account in parts of the domain is a robust density coupling that can combine LES transported and TDF density. In this work, the source terms in Eq. 9.25 are only applied if a certain amount of particles are present, i.e., if the particle number in a cell exceeds a quarter of the nominal particle number density $1/4N_{p,nominal}$ and if the sum of particle weights in a cell $\sum_{p=1}^{n_p} w_p/\Delta^3$ is larger than 10% of the local fluid density obtained from the specific volume transport $(\hat{v}^{-1})$ to prevent rapid density changes when hybrid seeding is applied. The transported specific volume in regions without particles is set to $\bar{\rho}\hat{v} = \bar{\rho}_t/\bar{\rho}_s$ with $\bar{\rho}_t$ being the density obtained from advancing the continuity equation and $\bar{\rho}_s$ being the density obtained from ADF. This approach is numerically

robust and ensures that LES and particle density fields evolve consistently even if regions are unoccupied by particles.

The laminar viscosity needed by the LES is either determined from the flamelet table (with ADF) or alternatively (with TDF) from the particle averages (Eq. 9) and subsequent spatial smoothing.

Post-processing quantities such as filtered temperature and mass fractions are either obtained from the tables (with ADF) or from averaging over the particles following Eq. 9.9 (with TDF-DC & TDF-FC).

9.4   Numerical Implementation

The LES equations are solved with the in-house code `PsiPhi`, which has been used in many combustion LES studies before (e.g. [97, 122, 168]). It uses the finite volume method (FVM) on an equally spaced orthogonal grid. Convective terms are discretized by a central differencing scheme (CDS) of second order for momentum and by a total variation diminishing (TVD) scheme of (up to) second order for scalars. Diffusive terms are treated with CDS of second order as well. Continuity is enforced by employing a predictor-corrector scheme in combination with a projection method. The LES equations are discretized in time by a low-storage Runge-Kutta procedure of third order.

The stochastic differential equation (SDE) governing the particle motion in physical space is discretized using an Euler-Maruyama approximation [105] and is embedded into the Runge-Kutta procedure of the LES. The semi-discrete equation for the particle position for a time $t_{n+1} = t_n + \Delta t$ reads:

$$
\begin{aligned}
x_i^+(t_{n+1}) &= x_i^+(t_n) + \left[\tilde{u}_i + \frac{1}{\bar{\rho}} \frac{\partial \bar{\rho}(\tilde{D} + D_t)}{\partial x_i} \right]^+ \Delta t \\
&+ [(2(\tilde{D} + D_t))^{1/2}]^+ \Delta t^{1/2} \, \xi_i.
\end{aligned} \tag{9.26}
$$

Quantities with the superscript $^+$ are either particle quantities like x_i^+ or quantities interpolated to the particle position. Random motion is described by $\Delta t^{1/2} \xi_i$, which is a three-dimensional Gaussian distributed random variable with zero mean and a variance equal to the time step width Δt.

The drift and Wiener term of the SDE are treated separately such that particles are moved in two consecutive steps in each Runge-Kutta substep. The drift term is computed by interpolating cell face based LES velocities and diffusivity gradients onto the particle positions by a tri-linear interpolation scheme. The Wiener term representing the stochastic motion of the particles is evaluated only in the first substep of the Runge-Kutta procedure, the same values are then used in the following substeps.

The message passing interface (MPI) is used for distributed memory domain decomposition and the same decomposition is used for particle and Eulerian fields. It should be noted that the hybrid method will not directly lead to a reduction in computational cost with this parallelization strategy. To obtain a significant decrease in computational time, strategies such as dynamic load balancing need to be applied. However, this work focuses on the feasibility and accuracy of the hybrid approach as a necessary first step.

9.5   Experimental Setup and Previous Numerical Studies

The Sydney/Sandia piloted burner with inhomogeneous inlets [6, 129, 130] consists of a main (outer) tube of 7.5 mm diameter and an inner tube of 4 mm diameter, the configuration studied in this work features fuel from the inner tube. To increase the level of premixing, the inner tube can be recessed. Different configurations have been studied experimentally, and it has been found that the blow-off velocity significantly changes when changing the recession length. In this work, we study the nearly homogeneous flame with the inner tube recessed by 300 mm ('FJ200-5GP-Lr300-59'). The main tube is surrounded by a pilot which provides hot products of a 5-gas mixture whose equilibrium temperature and composition are matched to methane at stoichiometry. The velocities of main jet, pilot and co-flow are 59 m/s, 3.72 m/s (cold) and 15 m/s, respectively. The equivalence ratio of the main jet is 4.8. This burner configuration is ideally suited to demonstrate the hybrid method, as finite rate chemistry shows strong improvements in certain regions of the flame compared to flamelet chemistry. Hence, to verify the capabilities of the hybrid method, we attempt to reproduce the improvements of finite rate chemistry by only seeding particles where such an improvement can be expected. We have also studied the inhomogeneous case ('FJ200-5GP-Lr75-80') and found that the FC is able to reproduce this flame well, due to the premixed stabilization mechanism. Hence, the inhomogeneous flame is less of an adequate case to test the hybrid method since differences between finite rate and FC are less pronounced.

The Sydney/Sandia flame with inhomogeneous inlets has been studies numerically by different groups recently. Meares et al. [129] presented results using an LES with an Eulerian stochastic fields approach employing a finite rate chemical mechanism. Their work was mainly concerned with the stabilization mechanism comparing the inhomogeneous and homogeneous flame and they found that the LES could support the conclusions on the stabilization drawn from the experiment. Kleinheinz et al. [104] and Perry et al. [159] presented LES results using advanced flamelet methods. Kleinheinz et al. based their LES on a hybrid flamelet/progress variable (FPV) method that combines premixed and non-premixed flamelets. They analyzed premixed and non-premixed regions in detail and obtained satisfactory results compared with the experiment. Perry et al. applied an FPV model based on non-premixed flames with an additional mixture fraction that tracks the premixing in the fuel tube of the burner. They showed how and additional mixture fraction to consider inhomogeneity improves the LES results compared to the experiment. Galindo et al. [54] employed an LES with sparse-Lagrangian multiple mapping conditioning (MMC). They found that the diffusion flame based MMC model performs better at predicting the homogeneous case than the inhomogeneous case due to the premixed flame stabilization in the inhomogeneous case. Maio et al. [124] compared LES results of two different approaches, artificial flame thickening and filtered tabulated chemistry, both based on premixed flamelets, to the experiment. They concluded that both premixed based methods are able to reproduce the flame characteristics for the governing quantities compared (mixture fraction and temperature). Further, Wang & Zhang [243] studied the Sydney Sandia flame with an LES-PDF approach in comparison to other tra-

ditional piloted jet flame experiments to obtain a unified view of pilot stabilized turbulent jet flames. In addition, they demonstrated that the LES-PDF method is capable of reproducing different configurations across the combustion mode spectrum. Wu & Ihme [262] applied a hybrid non-premixed FPV and premixed filtered tabulated chemistry in LES using a species-specific combustion regime indicator based on a manifold drift term. They found that CO in particular is sensitive to the combustion regime assumption of the two models applied. Johnson et al. [87] tested a Wasserstein metric based approach to quantitatively compare simulation results of the Sydney/Sandia flame. Kim & Kim [102] applied a multi-environment PDF approach and compared premixed and non-premixed based methods. A recent review on stratified turbulent flames and the influence of mixture inhomogeneities, including a discussion of the Sydney/Sandia flame, is provided by Lipatnikov [119].

9.6 Numerical Setup

All simulations have been performed on a computational grid with cubic cells of 0.5 mm edge length. Two different domains have been considered, a large one of $288 \times 88 \times 88$ mm^3 (17.8M cells) and a compact one of $108 \times 44 \times 44$ mm^3 (1.7M cells). In the case of standard non-hybrid LES-FDF, where particles are used throughout the computational domain, around 450 M and 35 M particles are present for both grid sizes, respectively. The computational domain includes a one diameter long part of the burner upstream of its outlet. Temporally and spatially resolved mixing tube simulation results from the Princeton group [159] are interpolated onto the LES inflow plane in space and time such that an accurate representation of the main fuel jet is achieved. A constant time step width of 0.3×10^{-5}s is employed such that the interpolation in time can be done prior to the simulation and the LES can efficiently cycle through the data provided. Fluctuations of 10% of the bulk pilot and co-flow velocities are set for these streams using Klein's inflow generator [103] in its most efficient implementation [98]. (The intermediate efficiency implementation [100] that also works on unstructured grids was not necessary here.)

The large domain has been simulated for validation even against measurements downstream, using the cost-effective methods ADF and TDF-FC only. For comparing the hybrid method to the pure ADF and TDF-DC methods, the small domain was sufficient as it included the challenging regions of high strain and flame stabilization. All simulations that are presented and analyzed in this paper are summarized in table 9.2.

9.7 Results

9.7.1 Validation of Standard LES-FDF Approach with FC

In this section, the consistency of the standard LES-FDF is examined by comparing results for ADF and TDF, both obtained from the same simulation (R2). As this did not couple back the viscosity and density from ADF, an additional simulation was necessary, running flamelets with ADF only (R1) for validation.

Table 9.2: Runs conducted in this work (refer to Tab. 9.1 for information on acronyms). Chemistry for ADF is always FC. ADF* indicates a pure LES, i.e., LES where all scalars are solely obtained from the ADF.

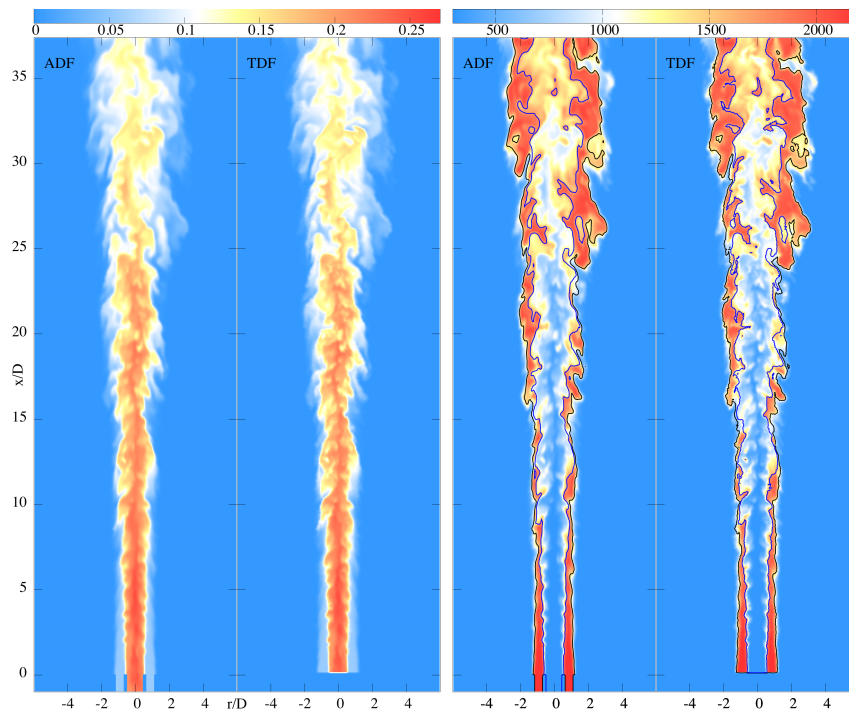| Run	Dom. size	TDF chem.	hybrid/ Z range	sub. FDF	$N_{p,tot}$ M	cost k cpu-h
R1	large	-	-	ADF*	-	7
R2	large	FC	non hyb.	TDF	445	61
R3	small	-	-	ADF*	-	0.3
R4	small	FC	non hyb.	TDF	35	1.8
R5	small	FC	0.001-0.18	HDF	9	1.5
R6	small	FC	0.05-0.18	HDF	5	1.4
R7	small	FC	0.06-0.1	HDF	3.5	1.3
R8	small	DC	non hyb.	TDF	35	129
R9	small	DC	0.001-0.18	HDF	9	119
R10	small	DC	0.05-0.18	HDF	5	123
R11	small	DC	0.06-0.1	HDF	3.5	130

Figure 9.2: Instantaneous fields from ADF and TDF, both with FC (R2). From left to right: ADF mixture fraction (i.e., Eulerian based result), TDF mixture fraction, ADF temperature, TDF temperature.

Figure 9.2 shows the filtered Eulerian (ADF) and particle mixture fraction (TDF) fields of R2. As can be seen, a relatively homogeneous mixture emanates from the central tube. The rich central jet (equivalence ratio of 4.8) is surrounded by a hot pilot gas with a stoichiometric mixture fraction. Instantaneous consistency between the fields can clearly be observed, even though both mixture fraction fields evolve independently and are only indirectly coupled through the density feedback mechanism.

Figure 9.2 additionally presents the instantaneous temperature fields for ADF and TDF of R2 and the iso-lines of the lean and rich flammability limits (mixture fractions of 0.026 and 0.093, respectively). It can be seen that the pilot flame is only weakly wrinkled in the near-field. Further downstream, the temperature field gets wrinkled as the pilot stream starts to interact with central jet and co-flowing air. Different to the mixture fraction field, the particle temperature field is more strongly affected by the subgrid mixing process and the shape of the subgrid PDF due to the chemical source terms. However, both temperature fields correspond well to each other and show instantaneous consistency. Some differences, such as the stochastic noise in the instantaneous TDF solution as well as the 'sharper' features of the TDF solution due to the lower amount of numerical dissipation going along with the transport solved in Lagrangian manner can be observed. It should be noted that the stabilization mechanism of the flame is very sensitive to the flow conditions and mixing rates, due to fresh air having to mix with the central jet without excessively diluting the pilot stream. As a consequence, locally quenched states can be observed, slightly more in the TDF than in the ADF fields (e.g., at $x/D \approx 12$).

Figures 9.3 to 9.7 show a comparison of time averaged results for ADF* of R1 as well as for ADF and TDF of R2. Figure 9.3 presents mean and rms of the resolved mixture fraction. Overall, the time-averaged mixture fraction compares very well to the experiment for ADF*, ADF and TDF. While mixture fraction predictions of R1 and R2 hardly show differences in the reactive range in the near field, small differences exist in the far field. Larger differences exist for the rms of the resolved mixture fraction. Overall, predictions based on TDF show larger fluctuations, which might be related to the particle fields being less affected by numerical diffusion, hence showing sharper features and higher fluctuations. A better comparison of mixture fraction fluctuations to the experiment can be obtained if the total rms is considered, i.e., obtained from the sum of resolved and subgrid variances, Fig. 9.6. Figure 9.4 shows density mean and rms predictions compared to the experiment. The comparison of density is particularly important to assess whether the density feedback mechanism works correctly and whether ADF and TDF results are consistent. As can be observed, the mean density behaves very consistently. Only resolved rms values show some minor discrepancies. Overall, it can clearly be seen that the density feedback mechanism employing the additional transport equation for the specific volume works well and provides consistent results. Figure 9.5 shows the progress variable mean and resolved rms predictions compared to the experiment. The experimental profiles have been computed from raw data considering the same species as in the simulation (H_2, CO, CO_2, H_2O). Again, a very good agreement between experiment and ADF*, ADF and TDF could be obtained. The simulations tend to slightly underpredict the progress variable, especially in the mixing layer of main jet and pilot gas stream, which might be related to an overprediction of flame quenching. Also, the spreading of the flame into the co-
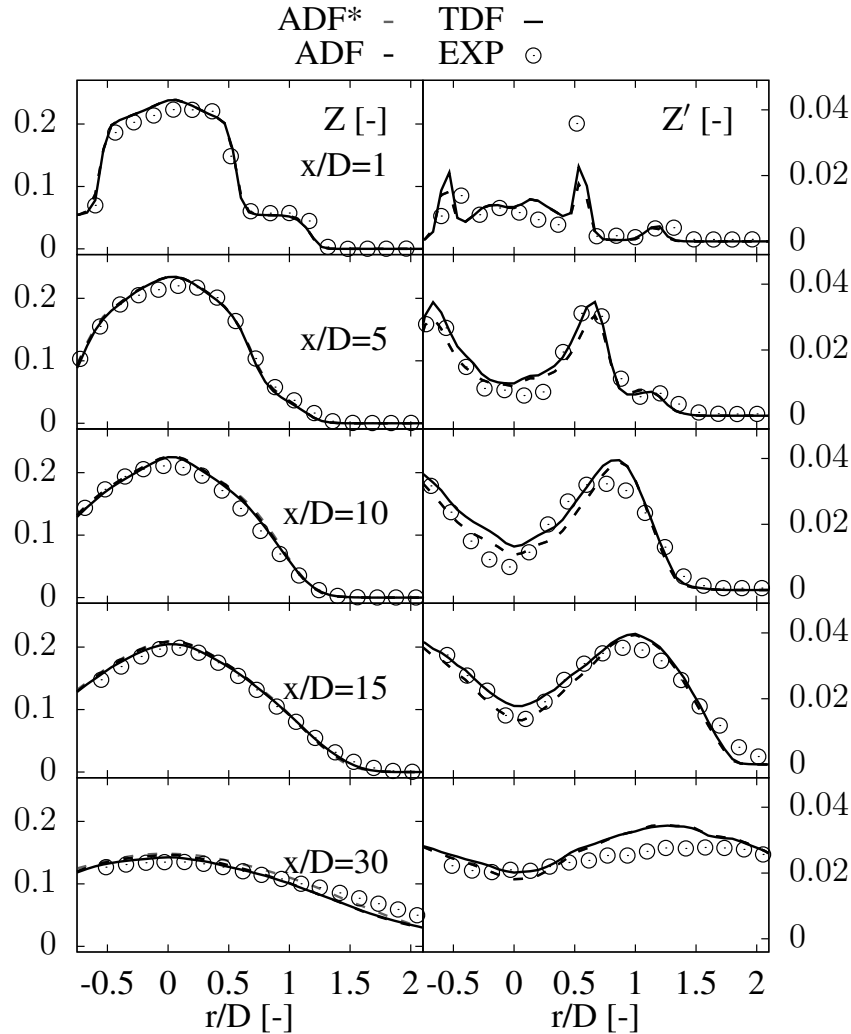
Figure 9.3: Mean and rms of the resolved mixture fraction for ADF and TDF fields (R2) and ADF* (R1).

flowing air appears to be underpredicted at the downstream locations. The resolved rms shows a good agreement to the experiment, with TDF results again having a tendency to show higher rms values than ADF and ADF* results, respectively. Figure 9.6 presents total and subgrid mixture fraction rms predictions. Ultimately, the total rms should be compared to the experiment, since the experiment considers (almost) all scales of motion (limited by diagnostics) in the evaluation of the fluctuations. It can be observed that the overall agreement is comparable to that of the resolved rms (i.e., the contribution of the unresolved scales is relatively low). However, there are some differences, e.g. a better prediction of the rms peak at $x/D = 1$, where subgrid fluctuations dominate. The comparison of the subgrid fluctuations serves the purpose of validating the LES-FDF method and to cross-check with the LES transport equations for the second moments. It can be seen that both methods produce very consistent results. Figure 9.7 shows the total and subgrid progress variable rms predictions. The total rms essentially corresponds
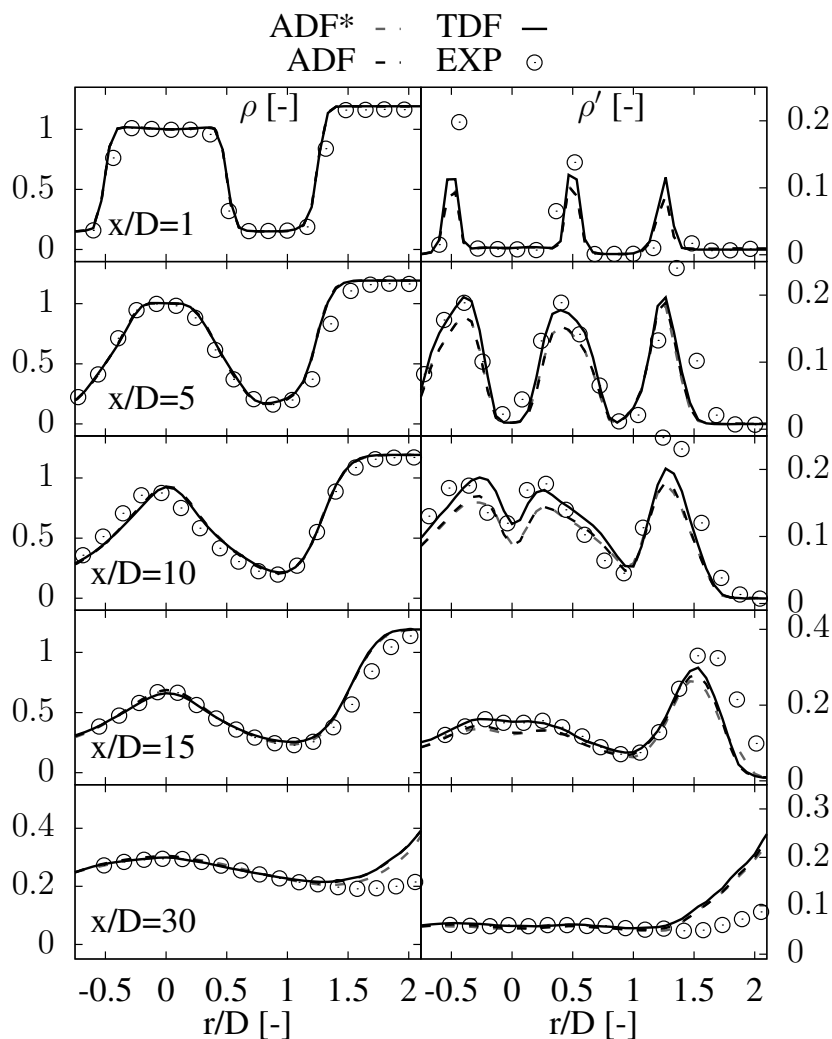
Figure 9.4: Mean and rms of the resolved density for ADF and TDF fields (R2) and ADF* (R1).

to the resolved rms since the subgrid contribution is very low, i.e., around one order of magnitude lower than the mixture fraction subgrid rms. However, again, TDF, ADF and ADF* correspond well to each other further proving the consistency of the LES-FDF method.

9.7.2 Validation of the Hybrid Method with FC

In this section, the hybrid method is validated. To this end, ADF* of R3 (pure LES), ADF and TDF of R4 (standard LES-FDF) and HDF of R5 (hybrid LES-FDF) are compared to each other. For validation purposes, all results are obtained with FC.

Figure 9.8 presents mean and rms density predictions. Here, the density of HDF corresponds only to the density obtained from TDF (unlike all other results for HDF, where TDF and ADF are combined such that ADF is used where no particles are present).
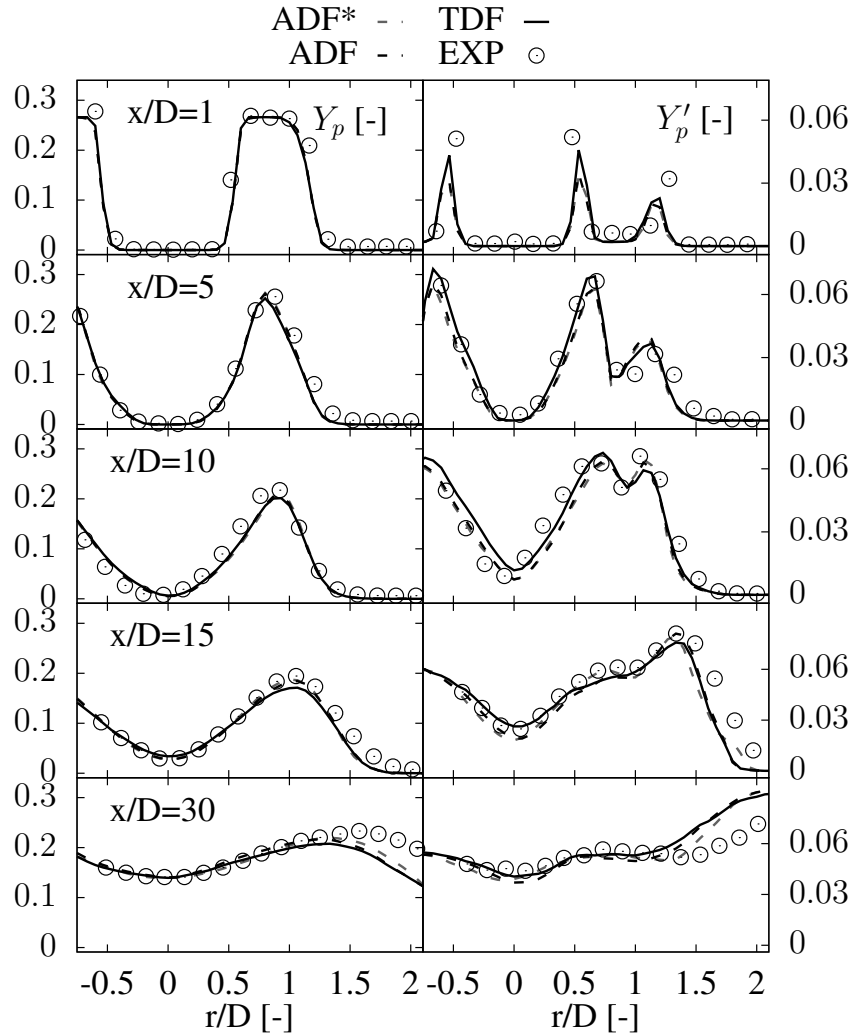
Figure 9.5: Mean and rms of the resolved progress variable for ADF and TDF fields (R2) and ADF* (R1).

Hence, this allows for examining where particles are present and whether the hybrid approach still shows consistency with respect to the density predictions. As can be observed, no particles are present beyond the pilot (in radial direction) and within the core of the main jet. Only further downstream, as the peak average mixture fraction decreases, some particles are existent on the centerline. However, in regions where particles are present, the density is consistent to the density from ADF* and ADF/TDF, which validates the consistency of the dynamic seeding method. Figure 9.9 shows the mixture fraction predictions. As can be observed, average values with the hybrid method (HDF) virtually show the same results as with the standard method (TDF). Minor differences in the rms predictions can be observed. The temperature predictions, Fig. 9.10, show similar trends as the mixture fraction, which proves that the dynamic seeding method works very well. This allows a proper examination of the hybrid method with the application of DC.
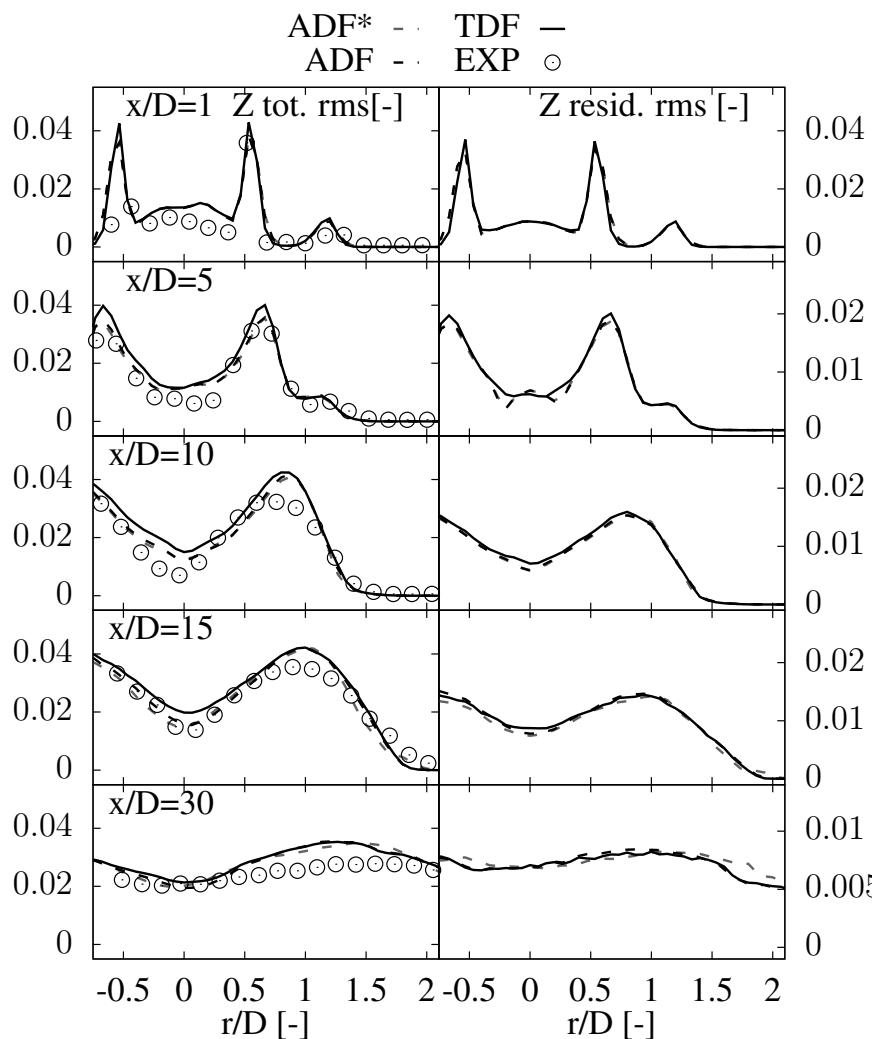
ADF* - · TDF —
ADF - · EXP ○

Figure 9.6: Total and subgrid rms of the resolved mixture fraction for ADF and TDF fields (R2) and ADF* (R1).

9.7.3 Results of LES-FDF with DC and Validation of the Hybrid Method with DC

In this section, the influence of direct chemistry and the performance of the hybrid method examined by comparing results for TDF-FC (R4), TDF-DC (R8) and HDF-DC (R9, hybrid method with a wide mixture fraction range). The goal of the hybrid method is to reproduce the results of TDF-DC as closely as possible while seeding particles only where a DC provides better results than FC. Instantaneous particle fields can be seen in Fig. 9.11 (second & third column) next to hybrid methods with a stronger reduction of the particle number examined in Sec. 9.7.4. In Fig. 9.12 mean and rms of the resolved mixture fractions are presented. The number of particles is reduced from 35M (R8) to approximately 9M (R9). The different predictions hardly show differences, which means that the differences in source term evaluation (FC vs. DC) only have minor differences
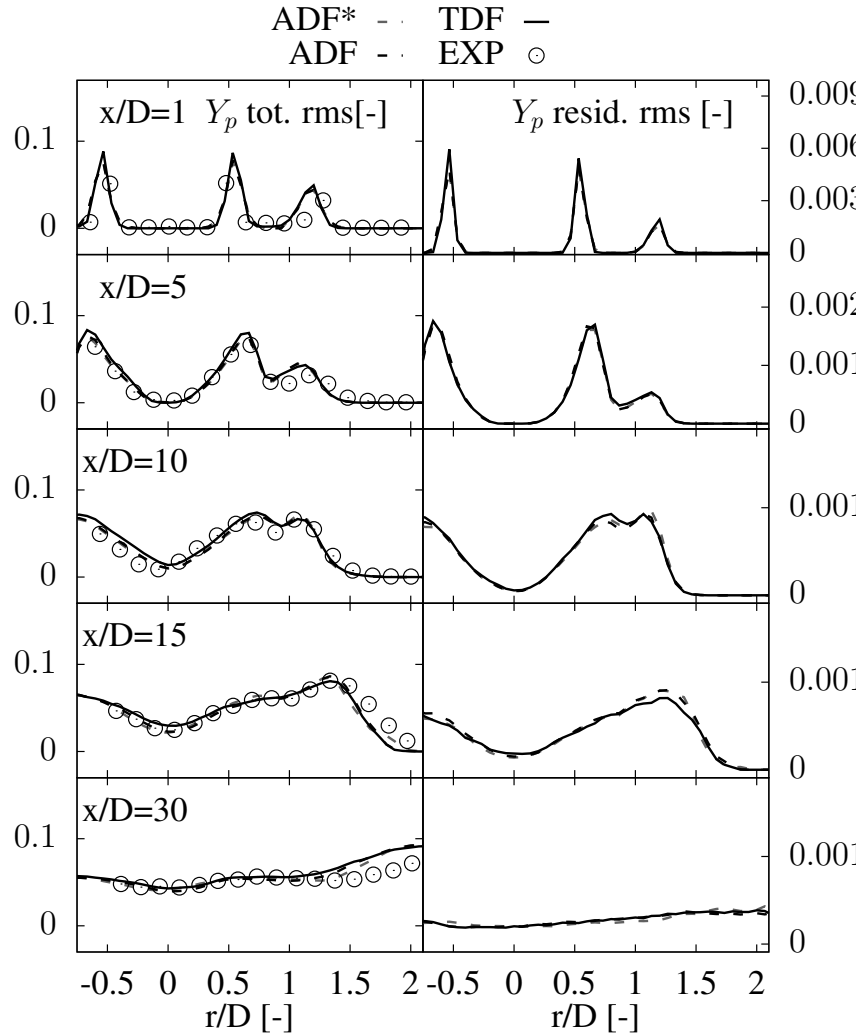
Figure 9.7: Total and subgrid rms of the resolved progress variable for ADF and TDF fields (R2) and ADF* (R1).

on the flow field and hence on the evolution of the mixture fraction. In addition, similar to the HDF-FC examined in previous section (R5), the predictions for HDF-DC are very close to its non-hybrid counterpart (TDF-DC). A more critical quantity to evaluate the performance of the hybrid method is the progress variable, Fig. 9.13. However, there is a good agreement between the non-hybrid and hybrid run. It should be noted that the progress variable prediction seems to be well captured by both FC and DC. However, as will be shown below, the different species from which the progress variable is computed as well as the chemical source term show clear differences. This indicates that the FC is able to predict the progress variable very well because differences in species predictions are compensated for if looking at a 'lumped' quantity such as progress variable. Figure 9.14 presents results for CO_2. Here, clear differences between FC and DC can be observed. It is known that premixed based methods are not able to perfectly predict CO_2 for configurations that involve premixed mixtures above the flammability limit (i.e., that
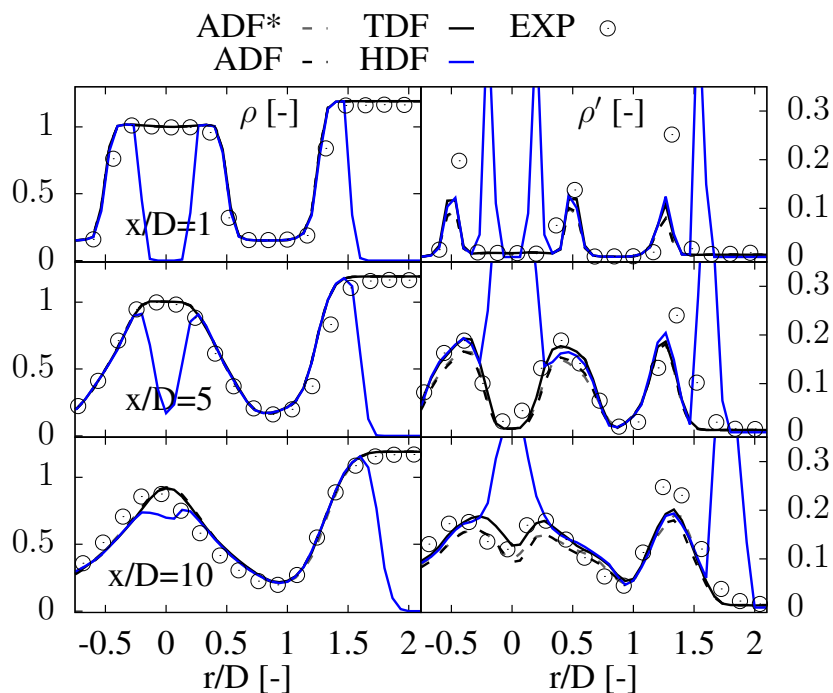
Figure 9.8: Mean and rms of the resolved density for ADF* (R3) ADF and TDF of non-hybrid LES-FDF (R4) and HDF of hybrid LES-FDF (R5). All results with FC.
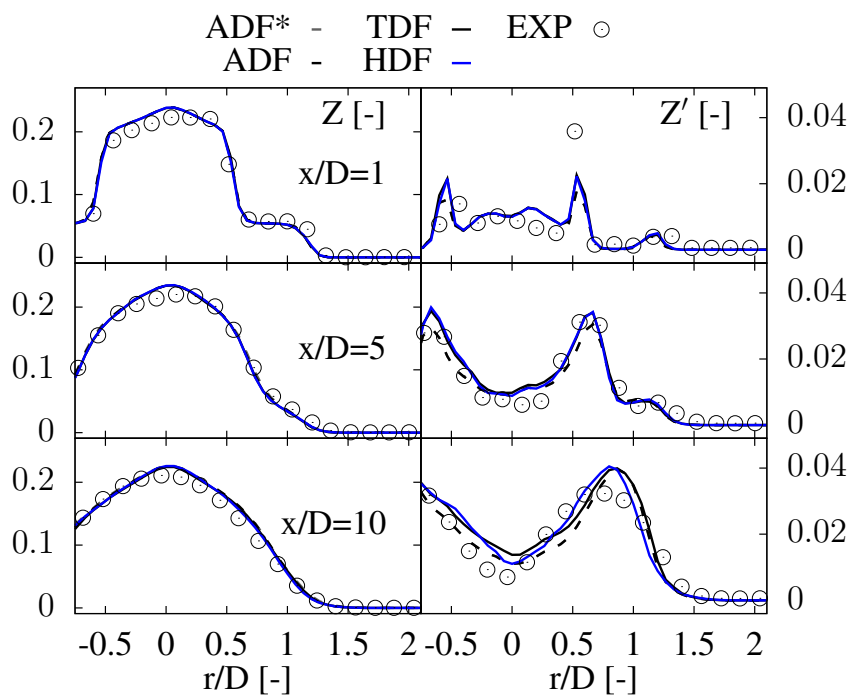
Figure 9.9: Mean and rms of the resolved mixture fraction for ADF* (R3) ADF and TDF of non-hybrid LES-FDF (R4) and HDF of hybrid LES-FDF (R5). All results with FC.
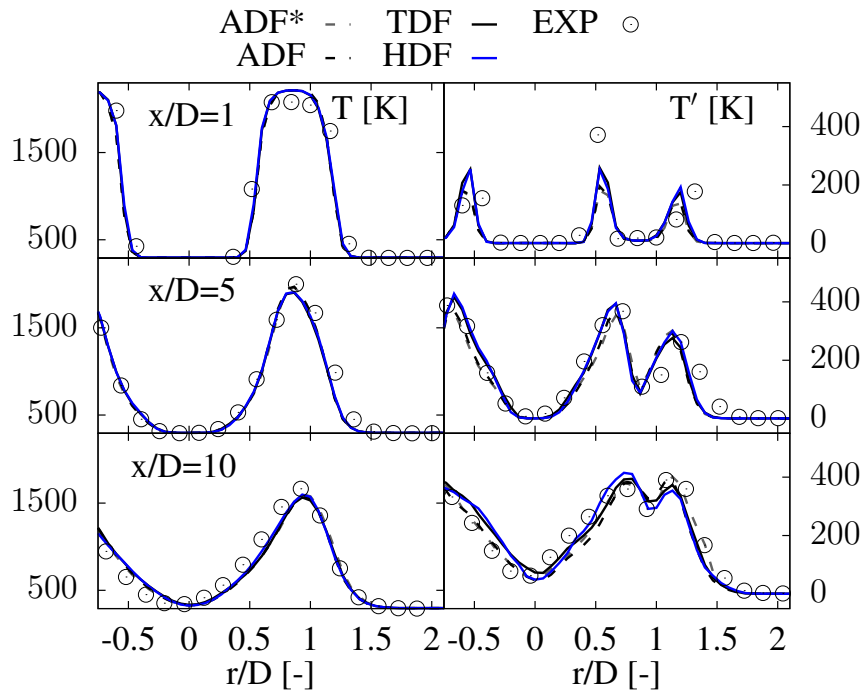
Figure 9.10: Mean and rms of the resolved temperature for ADF* (R3) ADF and TDF of non-hybrid LES-FDF (R4) and HDF of hybrid LES-FDF (R5). All results with FC.
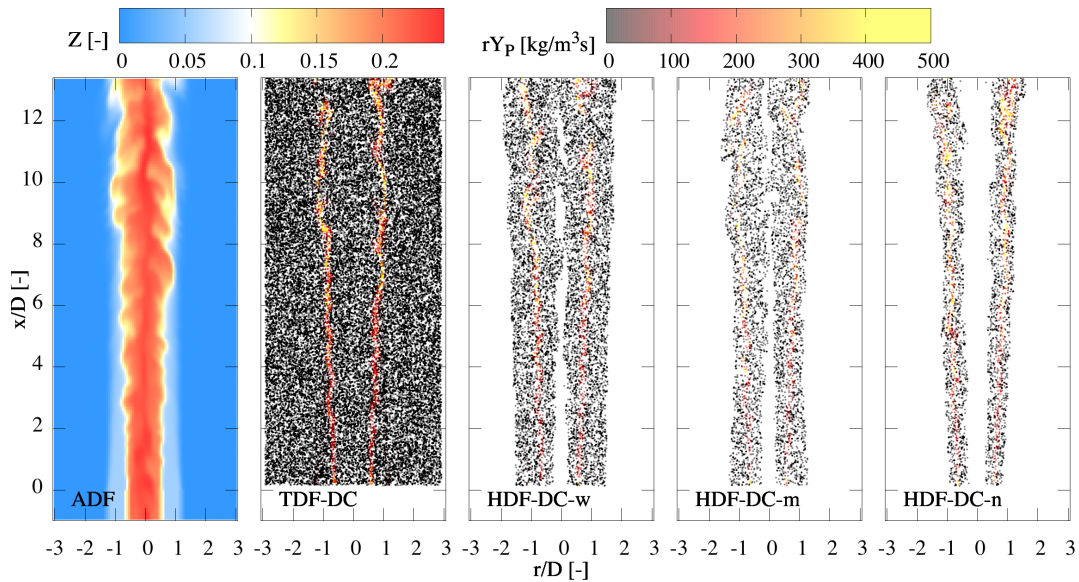
Figure 9.11: Comparison of hybrid method with particles used in different mixture fraction ranges, i.e., wide 0.001-0.18 (HDF-DC-w, R9), medium 0.05-0.18 (HDF-DC-m, R10) and narrow range 0.06-0.1 (HDF-DC-n, R11). Approximately every 10th particle in a layer of 0.5 mm width is shown.
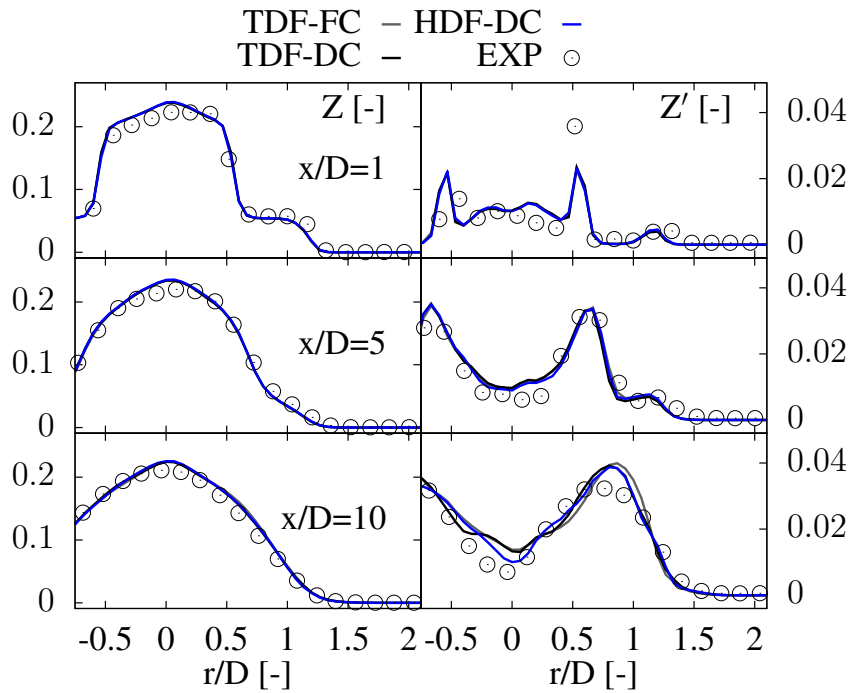
Figure 9.12: Mean and rms of the resolved mixture fraction for TDF-FC (R4), TDF-DC (R8) and HDF-DC (R9).
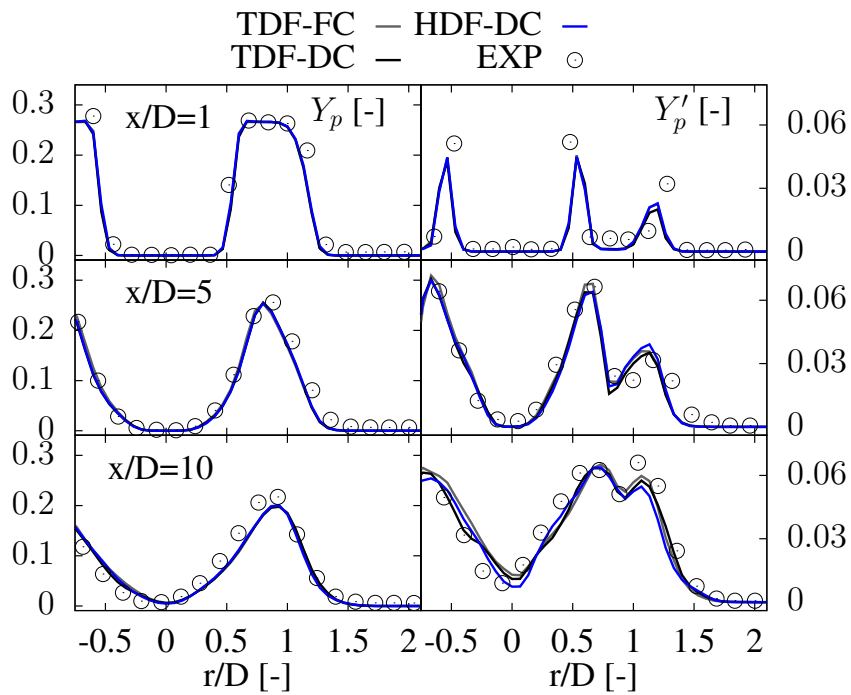
Figure 9.13: Mean and rms of the resolved progress variable for TDF-FC (R4), TDF-DC (R8) and HDF-DC (R9).
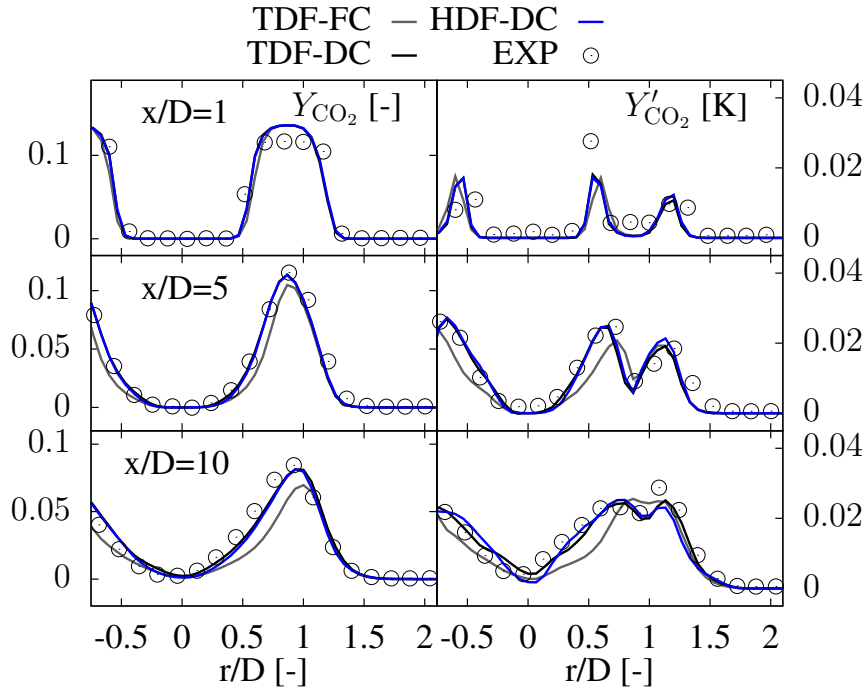
Figure 9.14: Mean and rms of the resolved CO_2 mass fraction for TDF-FC (R4) and TDF-DC (R8) and HDF-DC (R9).

burn in diffusion mode) [46, 240] and as similarly recently observed by Kim & Kim for the Sydney/Sandia flame [102]. Indeed, the results show a clear improvement of the agreement between simulation and experiment if DC instead of FC is used. While FC underpredicts the CO_2 mass fraction clearly in the region where pilot gas mixes with the central stream, TDF-DC shows a very good agreement with the experiment.

The objective of the hybrid method is to reproduce this improvement by only applying TDF particles in regions where DC is actually necessary to improve the results. As can be observed, this is achieved with the present hybrid method. Despite seeding particles based on ADF and FC within the central jet and the pilot at the boundaries of the prescribed TDF region, the particles evolve properly to yield the correct CO_2 mass fractions.

This is further illustrated by Fig. 9.15, which presents conditional mean and rms predictions of the CO_2 mass fraction. The predictions are clearly improved in the region from Z=0.055 to 0.2 and show good agreement with the experiment if DC is applied. Similar as the prediction in physical space, the hybrid method is able to reproduce this improvement. The H_2 mass fraction is a quantity sensitive to the chemistry model applied, as illustrated by Fig. 9.16. Again, DC is able to improve the predictions compared to FC. And again, the hybrid method is able to reproduce these improvements. However, minor differences can be found such as at $x/D = 1$, which might be linked to the influence of the FC based initial conditions of the particles.
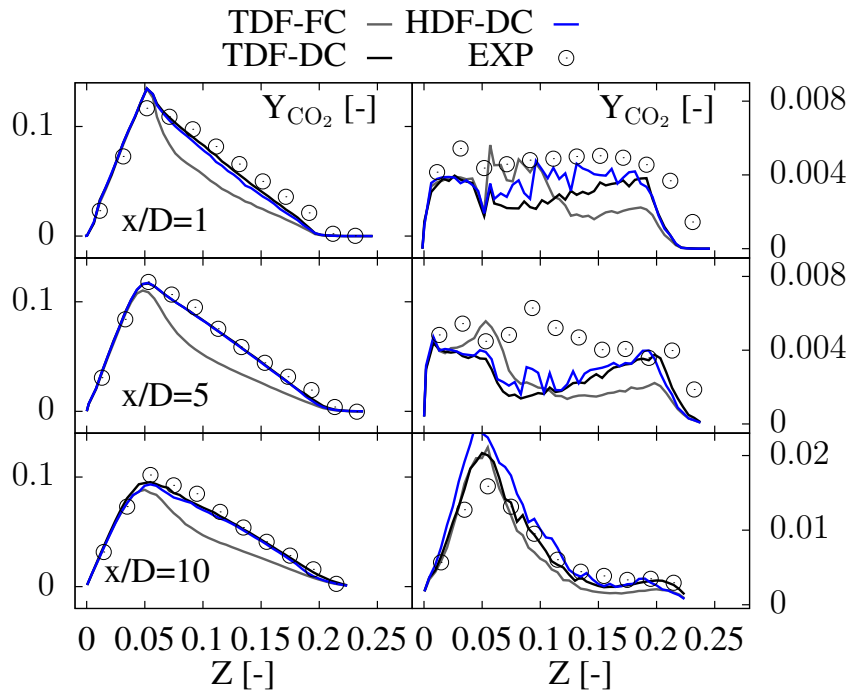
Figure 9.15: Mean and rms of the resolved CO_2 mass fraction conditioned on resolved mixture fraction for TDF-FC (R4), TDF-DC (R8) and HDF-DC (R9).
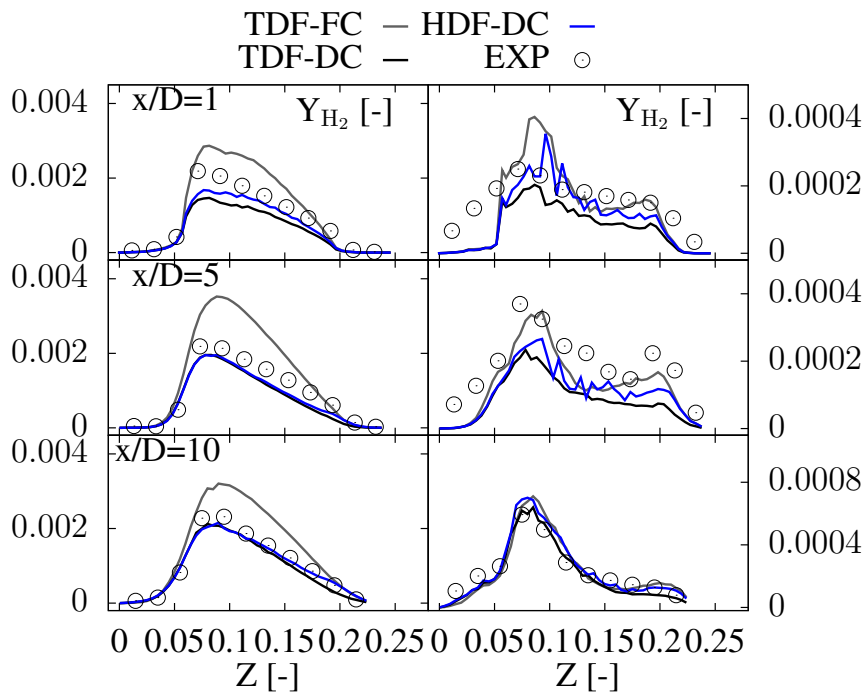
Figure 9.16: Mean and rms of the resolved H_2 mass fraction conditioned on resolved mixture fraction for TDF-FC (R4), TDF-DC (R8) and HDF-DC (R9).

Figure 9.17: Mean and rms of the resolved progress variable for ADF* (R3), TDF (R4), HDF-w (wide range, R5), HDF-m (medium range, R6) and HDF-n (narrow range, R7). All results with FC.

9.7.4   Investigation of Stronger Particle Reduction for the Hybrid Method

In this section, ranges for determining the TDF volume are varied to further investigate the performance of the hybrid method if it is not applied to exactly the range of conditions for which improvement can be expected. The different hybrid runs compared in this section are R5, R6, R7 with FC, as well as R9, R10 and R11, with DC, respectively (cf. Tab. 9.2). Instantaneous particle (TDF) fields for these simulations are shown in Fig. 9.11.

Figure 9.17 shows a comparison of progress variable for runs R5, R6 and R7, where particles are used within mixture fraction ranges of 0.001-0.18, 0.05-0.18 and 0.06-0.1, resulting in approximately 9, 5 and 3.5 M particles, respectively (Tab. 9.2). Runs R5, R6 and R7 are all conducted using FC such that results can be compared without the influence of DC first. It can be observed that the mean progress variable predictions correspond well to each other, showing that the hybrid method provides consistent results even if particles are used within a narrow TDF volume. As expected, the rms predictions by the hybrid method tend to move closer to ADF* if less particles are used. Figure 9.18 presents the same comparison as Fig. 9.17 for the hybrid runs with DC. Larger differences compared to the FC runs can be observed which is due to the effect of the chemistry switch close or within the reactive mixture fraction region. However, results are still close to each other and only minor differences can be observed in regions that

Figure 9.18: Mean and rms of the resolved progress variable for TDF-FC (R4), TDF-DC (R8), HDF-DC-w (wide range, R9), HDF-DC-m (medium range, R10) and HDF-DC-n (narrow range, R11).

are very sensitive to mixing and chemistry. Figure 9.19 shows the CO_2 predictions for the different hybrid runs with DC. The hybrid method with the strongest reduction of particles (HDF-DC-n) cannot be expected to reproduce well CO_2 across the radius since DC is only used within a narrow mixture fraction range. However, it can be observed that the predictions improve compared to FC and are in between the standard DC run (TDF-DC) and the standard FC run (TDF-FC). However, hybrid run HDF-DC-m shows consistent results to HDF-DC-w and TDF-DC, showing that the method works well even if parts of the mixing zone close to the reaction layer are treated by ADF.

9.8 Conclusions

A hybrid large eddy simulation/transported filtered density function (LES-FDF) method is developed that can be used to augment an assumed FDF flamelet simulation at any point by a more sophisticated direct chemistry model with transported FDF. Good consistency between standard LES-FDF and a standalone LES with top-hat assumed FDF is found and an overall good agreement with the experiment could be observed.

A comparison between the flamelet-based standard LES-FDF and flamelet-based hybrid LES-FDF with particles being seeded only at the boundary of a region with mixture fractions between 0.001 and 0.18 illustrates that the hybrid method is capable of reproducing the standard LES-FDF results.

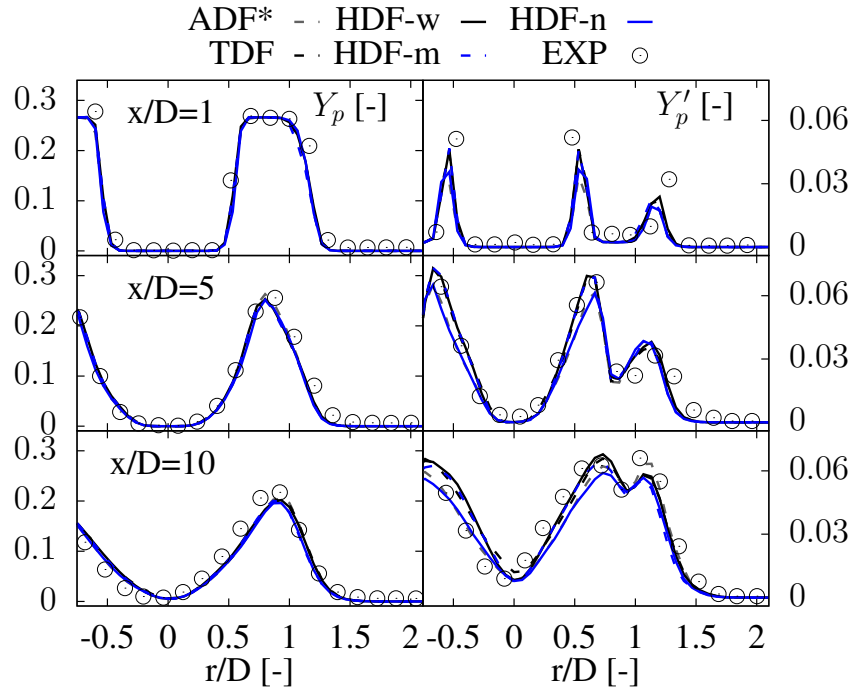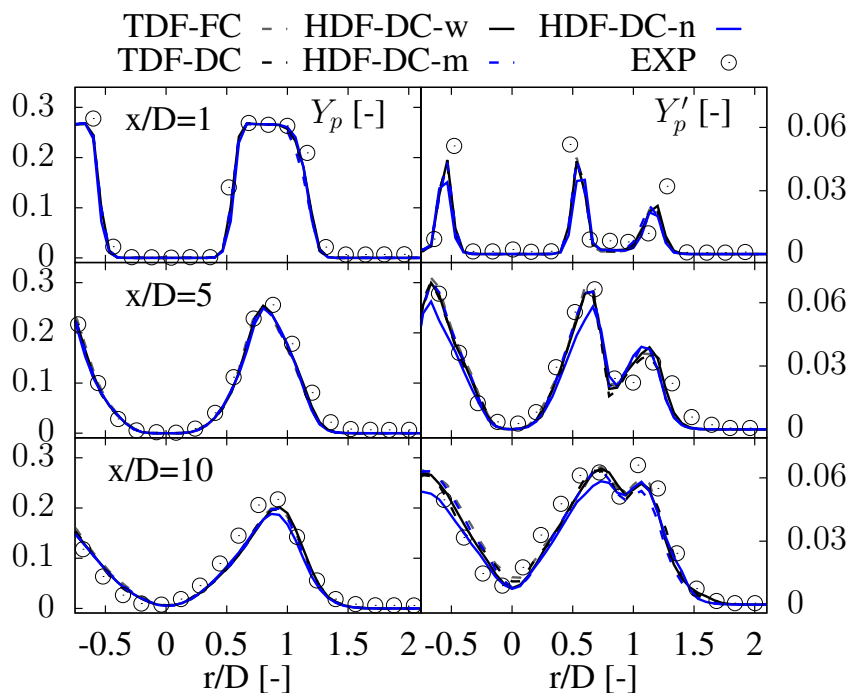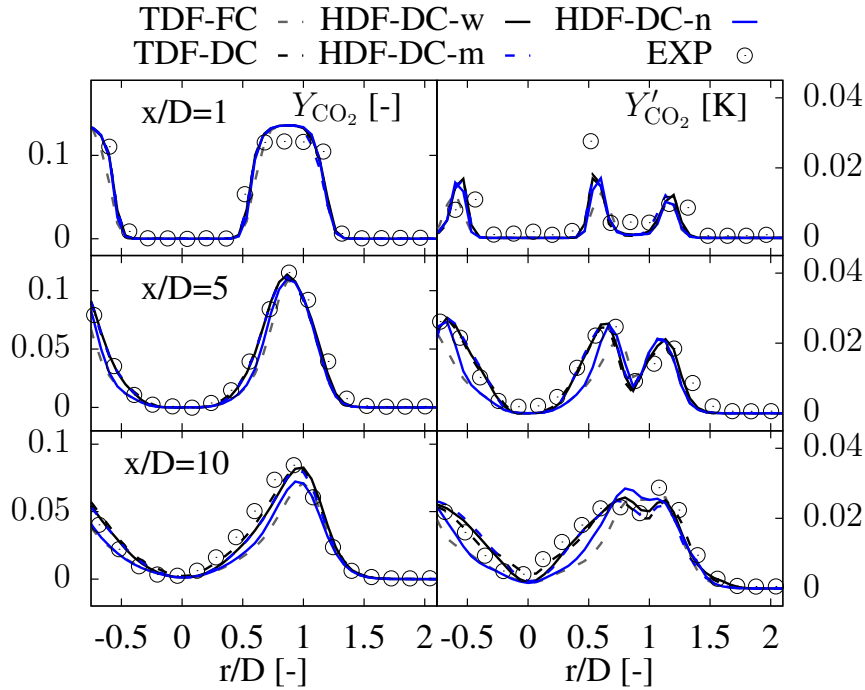Figure 9.19: Mean and rms of the resolved CO_2 mass fraction for TDF-FC (R4), TDF-DC (R8), HDF-DC-w (wide range, R9), HDF-DC-m (medium range, R10) and HDF-DC-n (narrow range, R11).

Comparing the standard LES-FDF with direct chemistry and standard LES-FDF using flamelet chemistry revealed improvements of species predictions such as for CO_2. The hybrid method is validated by demonstrating that it is capable of reproducing this improvement by only seeding particles where necessary.

Finally, the influence of different mixture fraction criteria for particle seeding are examined to further test the method. It is found that the hybrid method with direct chemistry gives consistent results and still minor improvements over the flamelet even if very few particles are used (approx. 1/10 of the number of particles used in the standard LES-FDF).

Future work will be directed towards more general criteria to seed particles and by applying it to different test cases, e.g. partially extinguishing flames where particles could be seeded only close to locations of extinction/re-ignition. Additionally, load balancing will be addressed, e.g. by distributing the state information of direct chemistry particles among processors including those that do not contain particles, which would permit significant cost reductions.

Acknowledgements

Chapter 10

Summary and Outlook

10.1 Summary

This work presented large eddy simulations (LES) and direct numerical simulations (DNS) of multi- and single-phase flows employing Lagrangian particle methods. A multidimensional flamelet model for pulverized coal combustion (PCC) has been implemented to improve the gas phase description in pulverized coal combustion (PCC) LES. LES using this flamelet have been performed on a semi-industrial scale coal furnace and a laboratory scale coal jet flame. The flamelet database was built from non-premixed one-dimensional steady counterflow flames. The variance for subgrid probability density function PDF integration has been obtained by solving an additional transport equation.

The LES of the semi-industrial scale coal furnace could reproduce the experiments well proving the applicability to realistic furnace simulations. However, some deficiencies of the model could be observed, such as in the quarl region where recirculating flue gases are mixed with fresh volatiles. The first study also illustrated that a wide range of scalar dissipation rates is present and that especially very low scalar dissipation rates need to be considered in the flamelet model at downstream locations and in the corner recirculation zones.

The subsequent study on the same furnace extended the flamelet model to also consider scalar dissipation rate. This was achieved by switching from beta to top-hat PDF for integration, reducing the dimensionality of the flamelet table, and replacing the variance dimension with scalar dissipation rate. In addition, this work showed results on a refined grid with a total of 1.7 billion cells, allowing to obtain a detailed physical insight into the furnace flow and combustion.

To obtain a more detailed understanding of the effect of devolatilization, an LES study on the CRIEPI jet flame has been performed. To this end, single and competing rates devolatilization models have been compared to the detailed Chemical Percolation model for Devolatilization (CPD), which has been directly applied to the LES for the first time. This study revealed that applying the CPD model in LES is affordable. However, the results surprisingly showed that the agreement of species predictions compared to the experiment is best with the competing rates model that has not been fitted to the heating rate conditions of the CRIEPI flame (i.e., devolatilization rates are too slow).

This apparent agreement could be linked to compensating effects regarding the methane pilot flame, which, different to experimental observations, always burns stably with the steady flamelet model. However, it could also be observed that the steady flamelet model provides good agreement of species with the experiment if the right amount of volatiles is released to the gas phase.

To better understand coal particle ignition phenomena and to create a database for further modeling, a three-dimensional DNS of a particle-laden turbulent mixing layer has been performed. The analysis revealed that initial heat release occurs under very lean conditions, and that subsequent volatile combustion shows a complex behavior of premixed and non-premixed zones. It could also be observed how the flame partially quenches due to heat losses to fresh particles. A pseudo-flamelet analysis revealed that in some regions steady flamelet models are likely to fail and highlighted the need of more sophisticated approaches, such as based on a progress variable.

In the final study presented in this work, a hybrid framework that combines assumed PDF and transported filtered density function (FDF) methods in the LES is developed. This method is tested on the partially premixed Sydney/Sandia flame with inhomogeneous inlets. The study showed that both a) the standalone LES with a flamelet generated manifold combustion model and an assumed top-hat PDF for mixture fraction and progress variable as well as b) the LES with a transported FDF approach applying the flamelet generated manifold model could reproduce the experiment very well. However, deficiencies in the species predictions could be observed. These deviations from the experimental results could be greatly decreased by applying direct chemistry by means of the DRM19 mechanism in the transported FDF method. Subsequently, the hybrid method was tested such that transported FDF particles were only seeded where they promised an improvement of the prediction. It could be shown that the hybrid method could very well reproduce the baseline results with particles used throughout the domain, while using much fewer particles.

10.2   Outlook

The studies conducted in this work showed the applicability of the flamelet model to PCC. However, the capabilities of PCC LES can be further improved. The subgrid PDF integration approach can be extended to fully consider the variances of all tracking scalars individually, such as done in the LES-FDF study for mixture fraction and progress variable. This requires the solution of variance transport equations for the individual mixture fractions (e.g., volatiles and char off-gases) as well as for the other scalars. In addition, an improved flamelet model additionally relying on a progress variable should be considered. This promises to improve the prediction in inner recirculation regions and of the methane pilot flame in the coal jet flame case.

The PCC DNS case allows for a much more detailed investigation of ignition and combustion behavior, e.g., by chemical explosive mode analysis. The database also offers testing new flamelet models in a realistic environment. Furthermore, a parametric study of different DNS cases should be done to obtain a better understanding of ignition and burning and their sensitivities towards particle loading, turbulence intensity, etc. Finally,

a large DNS case with turbulence levels closer to those of realistic furnaces should be performed.

The hybrid LES-FDF work could be applied to PCC cases in the future. In particular, the semi-industrial coal furnace simulation would greatly benefit from a detailed chemistry description in the quarl region without the need for using computationally expensive particles throughout the whole simulation domain. To become an efficient tool, different more general criteria of where to use transported FDF particles need to be developed. These criteria could be based on quantities quantifying the turbulence chemistry interaction, such as scalar dissipation rate.

Appendix A

Code Development

This chapter gives a brief overview of the main code development done by the author of this thesis necessary to accomplish the work presented in the preceding chapters.

I Pulverized Coal Combustion

- Development of Python code to generate flamelet tables using Cantera (either with three dimensions and pre-integrated with beta-PDF or with four dimensions and pre-integrated with top-hat PDF), development of a Fortran code to generate equilibrium solutions as a preliminary step (based on an equilibrium solver by Pope)

- Implementation of efficient four-dimensional look-up, mixture fraction treatment, variance transport, source term treatment, etc., necessary to use four-dimensional flamelet tables for pulverized coal combustion LES

- Extension of coal combustion models (variable heat capacities, competing rates devolatilization model, blowing correction, particle treatment with immersed boundaries; particle swelling and thermophoresis for testing)

- Implementation of additional particle tracking for particle history post-processing

- Implementation of setups for CRIEPI and IFRF cases, case specific post-processing and case specific modeling (e.g., char combustion)

- Incorporation and testing of Chemical Percolation for Devolatilization (CPD) model (based on a preliminary code version from A. Clements)

- Efficiency improvements of code (e.g., improved interpolation between gas and particle phase, mapping from coarse to fine grid at initialization)

- Extension of code to run coal combustion direct numerical simulation (incorporation of finite rate chemistry and detailed/unity Lewis number transport using Fortran Cantera interface; coupling to CVODE solver, implementation of ODEPIM solver)

- Development of Python code for post-processing of direct numerical simulation

II LES with Transported FDF

- Extension/improvement of LES-FDF code (based on the code developed by the author of this thesis during his Master's project) to run different test cases (Darmstadt and Imperial College non-premixed/premixed opposed jet flames)

- Implementation of distributed chemistry treatment for improved load balancing

- Complete re-implementation of transported FDF part of the code

- Implementation of setup for the Sydney/Sandia case (including usage time-resolved inflow data from Princeton University)

- Extension of re-implemented code (Cantera interface for reaction rates and gas properties, IEM with mean-drift mixing model, coupling through additional specific volume equation)

- Extension of hybrid code (flamelet generated manifold for FDF particles, two-dimensional top-hat PDF treatment for gas phase for consistency with transported FDF, dynamic particle generation and usage while maintaining full coupling)

Bibliography

[1] R. I. Backreedy, L. M. Fletcher, L. Ma, M. Pourkashanian, and A. Williams. "Modelling pulverized coal combustion using a detailed coal combustion model". In: *Combustion Science and Technology* 178.4 (2006), pp. 763–787.

[2] S. Badzioch and P. G. W. Hawksley. "Kinetics of Thermal Decomposition of Pulverized Coal Particles". In: *Industrial & Engineering Chemistry Process Design and Development* 9.4 (1970), pp. 521–530.

[3] Y. Bai, K. Luo, K. Qiu, and J. Fan. "Numerical investigation of two-phase flame structures in a simplified coal jet flame". In: *Fuel* 182 (2016), pp. 944–957.

[4] S. Balusamy, M. M. Kamal, S. M. Lowe, B. Tian, Y. Gao, and S. Hochgreb. "Laser diagnostics of pulverized coal combustion in O2/N2 and O2/CO2 conditions: velocity and scalar field measurements". In: *Experiments in Fluids* 56.5 (2015), p. 108.

[5] R. Barlow and J. Frank. "Effects of turbulence on species mass fractions in methane/air jet flames". In: *Proceedings of the Combustion Institute* 27.1 (1998), pp. 1087–1095.

[6] R. Barlow, S. Meares, G. Magnotti, H. Cutcher, and A. Masri. "Local extinction and near-field structure in piloted turbulent CH4/air jet flames with inhomogeneous inlets". In: *Combustion and Flame* 162.10 (2015), pp. 3516–3540.

[7] G. K. Batchelor. *An introduction to fluid dynamics*. Cambridge University Press, 2010.

[8] M. M. Baum and P. J. Street. "Predicting the Combustion Behaviour of Coal Particles". In: *Combustion Science and Technology* 3.5 (1971), pp. 231–243.

[9] L. G. Becker, H. Kosaka, B. Böhm, S. Doost, R. Knappstein, M. Habermehl, R. Kneer, J. Janicka, and A. Dreizler. "Experimental investigation of flame stabilization inside the quarl of an oxyfuel swirl burner". In: *Fuel* 201 (2017), pp. 124–135.

[10] A. Bermúdez, J. Ferrín, A. Liñán, and L. Saavedra. "Numerical simulation of group combustion of pulverized coal". In: *Combustion and Flame* 158.9 (2011), pp. 1852–1865.

[11] R. Bilger, S. Pope, K. Bray, and J. Driscoll. "Paradigms in turbulent combustion research". In: *Proceedings of the Combustion Institute* 30.1 (2005), pp. 21–42.

[12] M. Bini and W. P. Jones. "Large-eddy simulation of particle-laden turbulent flows". In: *Journal of Fluid Mechanics* 614 (2008), pp. 207–252.

[13] M. Bini and W. P. Jones. "Particle acceleration in turbulent flows: A class of nonlinear stochastic models for intermittency". In: *Physics of Fluids* 19.3 (2007), p. 035104.

[14] F. Birol et al. "World energy outlook 2010". In: *International Energy Agency* 1.3 (2015).

[15] R. Borghi. "On the structure and morphology of turbulent premixed flames". In: *Recent advances in the Aerospace Sciences*. Springer, 1985, pp. 117–138.

[16] R. Borghi and P. Moreau. "Turbulent combustion in a premixed flow". In: *Acta Astronautica* 4.3-4 (1977), pp. 321–341.

[17] N. Branley and W. Jones. "Large Eddy simulation of a turbulent non-premixed flame". In: *Combustion and Flame* 127.1 (2001), pp. 1914–1934.

[18] B. S. Brewster, L. L. Baxter, and L. D. Smoot. "Treatment of coal devolatilization in comprehensive combustion modeling". In: *Energy & Fuels* 2.4 (1988), pp. 362–370.

[19] T. Brosh, D. Patel, D. Wacks, and N. Chakraborty. "Numerical investigation of localised forced ignition of pulverised coal particle-laden mixtures: A Direct Numerical Simulation (DNS) analysis". In: *Fuel* 145 (2015), pp. 50–62.

[20] J. Cai, M. Handa, and M. F. Modest. "Eulerian–Eulerian multi-fluid methods for pulverized coal flames with nongray radiation". In: *Combustion and Flame* 162.4 (2015), pp. 1550–1565.

[21] J. Capecelatro and O. Desjardins. "An Euler–Lagrange strategy for simulating particle-laden flows". In: *Journal of Computational Physics* 238 (2013), pp. 1–31.

[22] F. Cavallo Marincola. "Large Eddy Simulation of Coal Combustion". PhD thesis. Imperial College London, 2013.

[23] J. H. Chen, A. Choudhary, B. de Supinski, M. DeVries, E. R. Hawkes, S. Klasky, W. K. Liao, K. L. Ma, J. Mellor-Crummey, N. Podhorszki, R. Sankaran, S. Shende, and C. S. Yoo. "Terascale direct numerical simulations of turbulent combustion using S3D". In: *Computational Science & Discovery* 2.1 (2009), p. 015001.

[24] J.-Y. Chen. "A Eulerian PDF scheme for LES of nonpremixed turbulent combustion with second-order accurate mixture fraction". In: *Combustion Theory and Modelling* 11.5 (2007), pp. 675–695.

[25] J.-Y. Chen, W. Kollmann, and R. W. Dibble. "Pdf Modeling of Turbulent Non-premixed Methane Jet Flames". In: *Combustion Science and Technology* 64.4-6 (1989), pp. 315–346.

[26] L. Chen and A. F. Ghoniem. "Simulation of Oxy-Coal Combustion in a 100 kWth Test Facility Using RANS and LES: A Validation Study". In: *Energy & Fuels* 26.8 (2012), pp. 4783–4798.

[27] L. Chen, S. Z. Yong, and A. F. Ghoniem. "Oxy-fuel combustion of pulverized coal: Characterization, fundamentals, stabilization and CFD modeling". In: *Progress in Energy and Combustion Science* 38.2 (2012), pp. 156–214.

[28] A. J. Chorin. "Numerical solution of the Navier-Stokes equations". In: *Mathematics of computation* 22.104 (1968), pp. 745–762.

[29] E. H. Chui and G. D. Raithby. "Computation of radiant heat transfer on a nonorthogonal mesh using the finite-volume method". In: *Numerical Heat Transfer, Part B: Fundamentals* 23.3 (1993), pp. 269–288.

[30] A. G. Clements, S. Black, J. Szuhánszki, K. Stechły, A. Pranzitelli, W. Nimmo, and M. Pourkashanian. "LES and RANS of air and oxy-coal combustion in a pilot-scale facility: Predictions of radiative heat transfer". In: *Fuel* 151 (2015). The 10th European Conference on Coal Research and its Applications, pp. 146–155.

[31] R. Clift, J. Grace, and M. Weber. *Bubbles, drops and particles.* New York: Academic Press, 1978.

[32] P. Coelho and N. Peters. "Numerical simulation of a mild combustion burner". In: *Combustion and Flame* 124.3 (2001), pp. 503–518.

[33] S. D. Cohen, A. C. Hindmarsh, P. F. Dubois, et al. "CVODE, a stiff/nonstiff ODE solver in C". In: *Computers in physics* 10.2 (1996), pp. 138–143.

[34] P. J. Colucci, F. A. Jaberi, P. Givi, and S. B. Pope. "Filtered density function for large eddy simulation of turbulent reacting flows". In: *Physics of Fluids* 10.2 (1998), pp. 499–515.

[35] A. W. Cook and J. J. Riley. "A subgrid model for equilibrium chemistry in turbulent flows". In: *Physics of Fluids* 6.8 (1994), pp. 2868–2870.

[36] *CRECK Modeling group.* `http://CRECKmodeling.chem.polimi.it`. 2017.

[37] R. L. Curl. "Dispersed phase mixing: I. Theory and effects in simple reactors". In: *AIChE Journal* 9.2 (1963), pp. 175–181.

[38] S. De and S. H. Kim. "Large eddy simulation of dilute reacting sprays: Droplet evaporation and scalar mixing". In: *Combustion and Flame* 160.10 (2013), pp. 2048–2066.

[39] F. Doisneau, M. Arienti, and J. C. Oefelein. "A semi-Lagrangian transport method for kinetic problems with application to dense-to-dilute polydisperse reacting spray flows". In: *Journal of Computational Physics* 329 (2017), pp. 48–72.

[40] P. Domingo, L. Vervisch, and D. Veynante. "Large-eddy simulation of a lifted methane jet flame in a vitiated coflow". In: *Combustion and Flame* 152.3 (2008), pp. 415–432.

[41] C. Dopazo and E. E. O'Brien. "An approach to the autoignition of a turbulent mixture". In: *Acta Astronautica* 1.1239 (1974), pp. 1239–1266.

[42] C. Dopazo and E. E. O'Brien. "Functional formulation of nonisothermal turbulent reactive flows". In: *Physics of Fluids (1958-1988)* 17.11 (1974), pp. 1968–1975.

[43]   P. Edge, S. Gubba, L. Ma, R. Porter, M. Pourkashanian, and A. Williams. "LES modelling of air and oxy-fuel pulverised coal combustion – impact on flame properties". In: *Proceedings of the Combustion Institute* 33.2 (2011), pp. 2709–2716.

[44]   S. Farazi, M. Sadr, S. Kang, M. Schiemann, N. Vorobiev, V. Scherer, and H. Pitsch. "Resolved simulations of single char particle combustion in a laminar flow field". In: *Fuel* 201 (2017), pp. 15–28.

[45]   J. H. Ferziger and M. Peric. *Computational methods for fluid dynamics*. Springer Science & Business Media, 2012.

[46]   B. Fiorina, O. Gicquel, L. Vervisch, S. Carpentier, and N. Darabiha. "Approximating the chemical structure of partially premixed and diffusion counterflow flames using FPI flamelet tabulation". In: *Combustion and Flame* 140.3 (2005), pp. 147–160.

[47]   W. Fiveland. "Three-dimensional radiative heat-transfer solutions by the discrete-ordinates method". In: *Journal of Thermophysics and Heat Transfer* 2.4 (1988), pp. 309–316.

[48]   T. H. Fletcher, A. R. Kerstein, R. J. Pugmire, and D. M. Grant. "Chemical percolation model for devolatilization. 2. Temperature and heating rate effects on product yields". In: *Energy & Fuels* 4.1 (1990), pp. 54–60.

[49]   T. H. Fletcher, A. R. Kerstein, R. J. Pugmire, M. S. Solum, and D. M. Grant. "Chemical percolation model for devolatilization. 3. Direct use of carbon-13 NMR data to predict effects of coal type". In: *Energy & Fuels* 6.4 (1992), pp. 414–431.

[50]   J. Floyd, A. M. Kempf, A. Kronenburg, and R. H. Ram. "A simple model for the filtered density function for passive scalar combustion LES". In: *Combust. Theory Model.* 13.4 (2009), pp. 559–588.

[51]   R. Fox. "A quadrature-based third-order moment method for dilute gas-particle flows". In: *Journal of Computational Physics* 227.12 (2008), pp. 6313–6350.

[52]   B. M. Franchetti. "Large Eddy Simulation of Air and Oxy-Coal Combustion". PhD thesis. Imperial College London, 2013.

[53]   B. Franchetti, F. C. Marincola, S. Navarro-Martinez, and A. Kempf. "Large Eddy simulation of a pulverised coal jet flame". In: *Proceedings of the Combustion Institute* 34.2 (2013), pp. 2419–2426.

[54]   S. Galindo, F. Salehi, M. Cleary, and A. Masri. "MMC-LES simulations of turbulent piloted flames with varying levels of inlet inhomogeneity". In: *Proceedings of the Combustion Institute* 36.2 (2017), pp. 1759–1766.

[55]   F. Gao and E. E. O'Brien. "A large-eddy simulation scheme for turbulent reacting flows". In: *Physics of Fluids* 5.6 (1993), pp. 1282–1284.

[56]   M. Germano, U. Piomelli, P. Moin, and W. H. Cabot. "A dynamic subgrid-scale eddy viscosity model". In: *Physics of Fluids A: Fluid Dynamics* 3.7 (1991), pp. 1760–1765.

[57] M. Gharebaghi, R. Irons, L. Ma, M. Pourkashanian, and A. Pranzitelli. "Large eddy simulation of oxy-coal combustion in an industrial combustion test facility". In: *International Journal of Greenhouse Gas Control* 5, Supplement 1 (2011), S100–S110.

[58] S. S. Girimaji. "Assumed beta-pdf Model for Turbulent Mixing: Validation and Extension to Multiple Scalar Mixing". In: *Combustion Science and Technology* 78.4-6 (1991), pp. 177–196.

[59] P. Givi. "Model-free simulations of turbulent reactive flows". In: *Progress in Energy and Combustion Science* 15.1 (1989), pp. 1–107.

[60] I. Glassman, R. A. Yetter, and N. G. Glumac. *Combustion*. Academic press, 2014.

[61] E. D. Gonzalez-Juez, A. R. Kerstein, R. Ranjan, and S. Menon. "Advances and challenges in modeling high-speed turbulent combustion in propulsion systems". In: *Progress in Energy and Combustion Science* 60 (2017), pp. 26–67.

[62] D. Goodwin. *Cantera an object-oriented software toolkit for chemical kinetics, thermodynamics, and transport processes*. 2009.

[63] B. Goshayeshi and J. C. Sutherland. "A comparison of various models in predicting ignition delay in single-particle coal combustion". In: *Combustion and Flame* 161.7 (2014), pp. 1900–1910.

[64] D. M. Grant, R. J. Pugmire, T. H. Fletcher, and A. R. Kerstein. "Chemical model of coal devolatilization using percolation lattice statistics". In: *Energy & Fuels* 3.2 (1989), pp. 175–186.

[65] W. Han, V. Raman, and Z. Chen. "LES/PDF modeling of autoignition in a lifted turbulent flame: Analysis of flame sensitivity to differential diffusion and scalar mixing time-scale". In: *Combustion and Flame* 171 (2016), pp. 69–86.

[66] T. Hara, M. Muto, T. Kitano, R. Kurose, and S. Komori. "Direct numerical simulation of a pulverized coal jet flame employing a global volatile matter reaction scheme based on detailed reaction mechanism". In: *Combustion and Flame* 162.12 (2015), pp. 4391–4407.

[67] N. Hashimoto, R. Kurose, and H. Shirai. "Numerical simulation of pulverized coal jet flame employing the TDP model". In: *Fuel* 97 (2012), pp. 277–287.

[68] C. Hasse and N. Peters. "A two mixture fraction flamelet model applied to split injections in a DI Diesel engine". In: *Proceedings of the Combustion Institute* 30.2 (2005), pp. 2755–2762.

[69] C. Hasse and N. Peters. "Modelling of ignition mechanisms and pollutant formation in direct-injection diesel engines with multiple injections". In: *International Journal of Engine Research* 6.3 (2005), pp. 231–246.

[70] C. W. Hasse. *A two-dimensional flamelet model for multiple injections in diesel engines*. Cuvillier Verlag, 2004.

[71]   E. R. Hawkes, R. Sankaran, J. C. Sutherland, and J. H. Chen. "Scalar mixing in direct numerical simulations of temporally evolving plane jet flames with skeletal CO/H2 kinetics". In: *Proceedings of the Combustion Institute* 31.1 (2007), pp. 1633–1640.

[72]   D. Haworth. "Progress in probability density function methods for turbulent reacting flows". In: *Progress in Energy and Combustion Science* 36.2 (2010), pp. 168–259.

[73]   J. Hayashi, N. Hashimoto, N. Nakatsuka, H. Tsuji, H. Watanabe, H. Makino, and F. Akamatsu. "Soot formation characteristics in a lab-scale turbulent pulverized coal flame with simultaneous planar measurements of laser induced incandescence of soot and Mie scattering of pulverized coal". In: *Proceedings of the Combustion Institute* 34.2 (2013), pp. 2435–2443.

[74]   A. C. Hindmarsh, P. N. Brown, K. E. Grant, S. L. Lee, R. Serban, D. E. Shumaker, and C. S. Woodward. "SUNDIALS: Suite of Nonlinear and Differential/Algebraic Equation Solvers". In: *ACM Transactions on Mathematical Software* 31.3 (Sept. 2005), pp. 363–396.

[75]   J. Hirschfelder, R. B. Bird, and C. F. Curtiss. *Molecular theory of gases and liquids.* Wiley, 1964.

[76]   L. Hu, L. Zhou, Y. Luo, and C. Xu. "Measurement and simulation of swirling coal combustion". In: *Particuology* 11.2 (2013), pp. 189–197.

[77]   S.-M. Hwang, R. Kurose, F. Akamatsu, H. Tsuji, H. Makino, and M. Katsuki. "Application of Optical Diagnostics Techniques to a Laboratory-Scale Turbulent Pulverized Coal Flame". In: *Energy & Fuels* 19.2 (2005), pp. 382–392.

[78]   S.-M. Hwang, R. Kurose, F. Akamatsu, H. Tsuji, H. Makino, and M. Katsuki. "Observation of Detailed Structure of Turbulent Pulverized-Coal Flame by Optical Measurement. Part 1. Time-Averaged Measurement of Behavior of Pulverized-Coal Particles and Flame Structure". In: *JSME International Journal Series B Fluids and Thermal Engineering* 49.4 (2006), pp. 1316–1327.

[79]   S.-M. Hwang, R. Kurose, F. Akamatsu, H. Tsuji, H. Makino, and M. Katsuki. "Observation of Detailed Structure of Turbulent Pulverized-Coal Flame by Optical Measurement.Part 2. Instantaneous Two-Dimensional Measurement of Combustion Reaction Zone and Pulverized-Coal Particles". In: *JSME International Journal Series B Fluids and Thermal Engineering* 49.4 (2006), pp. 1328–1335.

[80]   M. Ihme, C. M. Cha, and H. Pitsch. "Prediction of local extinction and re-ignition effects in non-premixed turbulent combustion using a flamelet/progress variable approach". In: *Proceedings of the Combustion Institute* 30.1 (2005), pp. 793–800.

[81]   M. Ihme and Y. C. See. "LES flamelet modeling of a three-stream MILD combustor: Analysis of flame sensitivity to scalar inflow conditions". In: *Proceedings of the Combustion Institute* 33.1 (2011), pp. 1309–1317.

[82]   P. J. Ireland and O. Desjardins. "Improving particle drag predictions in Euler–Lagrange simulations with two-way coupling". In: *Journal of Computational Physics* 338 (2017), pp. 405–430.

[83] F. A. Jaberi, P. J. Colucci, S. James, P. Givi, and S. B. Pope. "Filtered mass density function for large-eddy simulation of turbulent reacting flows". In: *Journal of Fluid Mechanics* 401 (Dec. 1999), pp. 85–121.

[84] J. Janicka, W. Kolbe, and W. Kollmann. "Closure of the Transport Equation for the Probability Density Function of Turbulent Scalar Fields". In: *Journal of Non-Equilibrium Thermodynamics* 4 (1979).

[85] J. Janicka and A. Sadiki. "Large eddy simulation of turbulent combustion systems". In: *Proceedings of the Combustion Institute* 30.1 (2005), pp. 537–547.

[86] C. Jiménez, F. Ducros, B. Cuenot, and B. Bédat. "Subgrid scale variance and dissipation of a scalar field in large eddy simulations". In: *Physics of Fluids* 13.6 (2001), pp. 1748–1754.

[87] R. Johnson, H. Wu, and M. Ihme. "A general probabilistic approach for the quantitative assessment of LES combustion models". In: *Combustion and Flame* 183 (2017), pp. 88–101.

[88] W. Jones, S. Lyra, and S. Navarro-Martinez. "Large Eddy Simulation of a swirl stabilized spray flame". In: *Proceedings of the Combustion Institute* 33.2 (2011), pp. 2153–2160.

[89] T. Kangwanpongpan, F. H. França, R. C. da Silva, P. S. Schneider, and H. J. Krautz. "New correlations for the weighted-sum-of-gray-gases model in oxy-fuel conditions based on HITEMP 2010 database". In: *International Journal of Heat and Mass Transfer* 55.25–26 (2012), pp. 7419–7433.

[90] V. R. Katta and W. M. Roquemore. "Calculation of multidimensional flames using large chemical kinetics". In: *AIAA Journal* 46.7 (2008), pp. 1640–1650.

[91] C. M. Kaul, V. Raman, E. Knudsen, E. S. Richardson, and J. H. Chen. "Large eddy simulation of a lifted ethylene flame using a dynamic nonequilibrium model for subfilter scalar variance and dissipation rate". In: *Proceedings of the Combustion Institute* 34.1 (2013), pp. 1289–1297.

[92] A. Kazakov and M. Frenklach. *http://www.me.berkeley.edu/drm/*. 1994.

[93] R. Kee, F. Rupley, and J. Miller. *Chemkin-II: A Fortran chemical kinetics package for the analysis of gas-phase chemical kinetics*. Tech. rep. SAND89-8009. Sandia National Laboratories, 1989.

[94] K. A. Kemenov, H. Wang, and S. B. Pope. "Modelling effects of subgrid-scale mixture fraction variance in LES of a piloted diffusion flame". In: *Combustion Theory and Modelling* 16.4 (2012), pp. 611–638.

[95] A. M. Kempf. "Large Eddy Simulation of Non-Premixed Turbulent Flames". PhD thesis. TU Darmstadt, 2003.

[96] A. Kempf, R. Lindstedt, and J. Janicka. "Large-eddy simulation of a bluff-body stabilized nonpremixed flame". In: *Combustion and Flame* 144.1 (2006), pp. 170–189.

[97]   A. Kempf, B. Geurts, and J. Oefelein. "Error analysis of large-eddy simulation of the turbulent non-premixed Sydney bluff-body flame". In: *Combustion and Flame* 158.12 (2011), pp. 2408–2419.

[98]   A. Kempf, S. Wysocki, and M. Pettit. "An efficient, parallel low-storage implementation of Klein's turbulence generator for LES and DNS". In: *Computers & Fluids* 60 (2012), pp. 58–60.

[99]   A. M. Kempf, H. Forkel, J.-Y. Chen, A. Sadiki, and J. Janicka. "Large-eddy simulation of a counterflow configuration with and without combustion". In: *Proceedings of the Combustion Institute* 28 (2000), pp. 35–40.

[100]   A. Kempf, M. Klein, and J. Janicka. "Efficient generation of initial-and inflow-conditions for transient turbulent flows in arbitrary geometries". In: *Flow, Turbulence and Combustion* 74.1 (2005), pp. 67–84.

[101]   J. Kim and S. B. Pope. "Effects of combined dimension reduction and tabulation on the simulations of a turbulent premixed flame using a large-eddy simulation/probability density function method". In: *Combustion Theory and Modelling* 18.3 (2014), pp. 388–413.

[102]   N. Kim and Y. Kim. "Multi-environment probability density function approach for turbulent partially-premixed methane/air flame with inhomogeneous inlets". In: *Combustion and Flame* 182 (2017), pp. 190–205.

[103]   M. Klein, A. Sadiki, and J. Janicka. "A digital filter based generation of inflow data for spatially developing direct numerical or large eddy simulations". In: *Journal of Computational Physics* 186.2 (2003), pp. 652–665.

[104]   K. Kleinheinz, T. Kubis, P. Trisjono, M. Bode, and H. Pitsch. "Computational study of flame characteristics of a turbulent piloted jet burner with inhomogeneous inlets". In: *Proceedings of the Combustion Institute* 36.2 (2017), pp. 1747–1757.

[105]   P. E. Kloeden and E. Platen. *Numerical solution of stochastic differential equations.* Vol. 23. Springer Science & Business Media, 1992.

[106]   R. Knappstein, G. Kuenne, T. Meier, A. Sadiki, and J. Janicka. "Evaluation of coal particle volatiles reaction by using detailed kinetics and FGM tabulated chemistry". In: *Fuel* 201 (2017), pp. 39–52.

[107]   K. Knill, T. Maalman, and M. Morgan. *Development of a combustion characterization technique for high volatile bituminous coals - report on the CC 4 trials.* Tech. rep. F 88/a/10. International Flame Research Foundation (IFRF), 1989.

[108]   H. Kobayashi, J. Howard, and A. Sarofim. "Coal devolatilization at high temperatures". In: *Symposium (International) on Combustion* 16.1 (1977), pp. 411–425.

[109]   A. N. Kolmogorov. "Dissipation of energy in locally isotropic turbulence". In: *Dokl. Akad. Nauk SSSR*. Vol. 32. 1. 1941, pp. 19–21.

[110]   A. N. Kolmogorov. "The local structure of turbulence in incompressible viscous fluid for very large Reynolds numbers". In: *Dokl. Akad. Nauk SSSR*. Vol. 30. 4. 1941, pp. 299–303.

[111] J. Köser, L. G. Becker, A.-K. Goßmann, B. Böhm, and A. Dreizler. "Investigation of ignition and volatile combustion of single coal particles within oxygen-enriched atmospheres using high-speed OH-PLIF". In: *Proceedings of the Combustion Institute* 36.2 (2017), pp. 2103–2111.

[112] J. Krüger, N. E. Haugen, D. Mitra, and T. Løvås. "The effect of turbulent clustering on particle reactivity". In: *Proceedings of the Combustion Institute* 36.2 (2017), pp. 2333–2340.

[113] G. Kuenne, A. Avdić, and J. Janicka. "Assessment of subgrid interpolation for the source term evaluation within premixed combustion simulations". In: *Combustion and Flame* 178.Supplement C (2017), pp. 225–256.

[114] R. Kurose and H. Makino. "Large eddy simulation of a solid-fuel jet flame". In: *Combustion and Flame* 135.1–2 (2003), pp. 1–16.

[115] V. R. Kuznetsov. "Influence of turbulence on the formation of high nonequilibrium concentrations of atoms and free radicals in diffusion flames". In: *Fluid Dynamics* 17.6 (1982), pp. 815–820.

[116] J. Lamouroux, M. Ihme, B. Fiorina, and O. Gicquel. "Tabulated chemistry approach for diluted combustion regimes with internal recirculation and heat losses". In: *Combustion and Flame* 161.8 (2014), pp. 2120–2136.

[117] L. Liang, S.-C. Kong, C. Jung, and R. D. Reitz. "Development of a semi-implicit solver for detailed chemistry in internal combustion engine simulations". In: *Journal of Engineering for Gas Turbines and Power* 129.1 (2007), pp. 271–278.

[118] D. K. Lilly. "A proposed modification of the Germano-subgrid-scale closure method". In: *Physics of Fluids* 4.3 (1992), 633–635.

[119] A. N. Lipatnikov. "Stratified turbulent flames: Recent advances in understanding the influence of mixture inhomogeneities on premixed combustion and modeling challenges". In: *Progress in Energy and Combustion Science* 62 (2017), pp. 87–132.

[120] K. Luo, H. Wang, J. Fan, and F. Yi. "Direct Numerical Simulation of Pulverized Coal Combustion in a Hot Vitiated Co-flow". In: *Energy & Fuels* 26.10 (2012), pp. 6128–6136.

[121] L. Ma, B. Naud, and D. Roekaerts. "Transported PDF Modeling of Ethanol Spray in Hot-Diluted Coflow Flame". In: *Flow, Turbulence and Combustion* 96.2 (2016), pp. 469–502.

[122] T. Ma, O. Stein, N. Chakraborty, and A. M. Kempf. "A-posteriori testing of Algebraic Flame Surface Density models for LES". In: *Combustion Theory and Modelling* (2013).

[123] C. K. Madnia and P. Givi. "Direct Numerical Simulation and Large Eddy Simulation of Reacting Homogeneous Turbulence". In: *Large Eddy Simulations of Complex Engineering and Geophysical Flows*. Ed. by B. Galperin and S. A. Orszag. Cambridge, UK: Cambridge University Press, 1993. Chap. 15, 315–346.

[124] G. Maio, M. Cailler, R. Mercier, V. Moureau, and B. Fiorina. "LES modeling of piloted jet flames with inhomogeneous inlets using tabulated chemistry methods". In: *55th AIAA Aerospace Sciences Meeting*. 2017, p. 1471.

[125] A. Majda and J. Sethian. "The Derivation and Numerical Solution of the Equations for Zero Mach Number Combustion". In: *Combustion Science and Technology* 42.3-4 (1985), pp. 185–205.

[126] F. C. Marincola, T. Ma, and A. Kempf. "Large eddy simulations of the Darmstadt turbulent stratified flame series". In: *Proceedings of the Combustion Institute* 34.1 (2013), pp. 1307–1315.

[127] J. McConnell, B. Goshayeshi, and J. C. Sutherland. "An evaluation of the efficacy of various coal combustion models for predicting char burnout". In: *Fuel* 201 (2017), pp. 53–64.

[128] R. McDermott and S. Pope. "A particle formulation for treating differential diffusion in filtered density function methods". In: *Journal of Computational Physics* 226.1 (2007), pp. 947–993.

[129] S. Meares, V. Prasad, G. Magnotti, R. Barlow, and A. Masri. "Stabilization of piloted turbulent flames with inhomogeneous inlets". In: *Proceedings of the Combustion Institute* 35.2 (2015), pp. 1477–1484.

[130] S. Meares and A. R. Masri. "A modified piloted burner for stabilizing turbulent flames of inhomogeneous mixtures". In: *Combustion and Flame* 161.2 (2014), pp. 484–495.

[131] C. Meneveau, T. S. Lund, and W. H. Cabot. "A Lagrangian dynamic subgrid-scale model of turbulence". In: *Journal of Fluid Mechanics* 319 (1996), pp. 353–385.

[132] D. Merrick. "Mathematical models of the thermal decomposition of coal. 3. Density, porosity and contraction behaviour." In: *Fuel* 62 (1983), pp. 547–552.

[133] D. Merrick. "Mathematical models of the thermal decomposition of coal: 2. Specific heats and heats of reaction". In: *Fuel* 62.5 (1983), pp. 540–546.

[134] D. Messig, M. Vascellari, and C. Hasse. "Flame Structure Analysis and Flamelet Progress Variable Modeling of Strained Coal Flames". In: *Combustion Theory and Modelling* 21 (2017), pp. 700–721.

[135] J.-P. Minier. "On Lagrangian stochastic methods for turbulent polydisperse two-phase reactive flows". In: *Progress in Energy and Combustion Science* 50 (2015), pp. 1–62.

[136] P. Moin, K. Squires, W. Cabot, and S. Lee. "A dynamic subgrid-scale model for compressible turbulence and scalar transport". In: *Physics of Fluids A: Fluid Dynamics* 3.11 (1991), pp. 2746–2757.

[137] P. Moin and S. V. Apte. "Large-eddy simulation of realistic gas turbine combustors". In: *AIAA Journal* 44.4 (2006), pp. 698–708.

[138] A. Molina and C. R. Shaddix. "Ignition and devolatilization of pulverized bituminous coal particles during oxygen/carbon dioxide coal combustion". In: *Proceedings of the Combustion Institute* 31.2 (2007), pp. 1905–1912.

[139]   V. Moureau, P. Domingo, and L. Vervisch. "From Large-Eddy Simulation to Direct
         Numerical Simulation of a lean premixed swirl flame: Filtered laminar flame-PDF
         modeling". In: *Combustion and Flame* 158.7 (2011), pp. 1340–1357.

[140]   M. Muto, H. Watanabe, R. Kurose, S. Komori, S. Balusamy, and S. Hochgreb.
         "Large-eddy simulation of pulverized coal jet flame – Effect of oxygen concentra-
         tion on NOx formation". In: *Fuel* 142 (2015), pp. 152–163.

[141]   M. Muto, K. Yuasa, and R. Kurose. "Numerical simulation of ignition in pulverized
         coal combustion with detailed chemical reaction mechanism". In: *Fuel* 190 (2017),
         pp. 136–144.

[142]   S. Nambully, P. Domingo, V. Moureau, and L. Vervisch. "A filtered-laminar-flame
         PDF sub-grid scale closure for LES of premixed turbulent flames. Part I: For-
         malism and application to a bluff-body burner with differential diffusion". In:
         Combustion and Flame 161.7 (2014), pp. 1756–1774.

[143]   B. Naud. "PDF modeling of turbulent sprays and flames using a particle stochastic
         approach". PhD thesis. TU Delft, 2003.

[144]   F. Nicoud and F. Ducros. "Subgrid-Scale Stress Modelling Based on the Square of
         the Velocity Gradient Tensor". In: *Flow, Turbulence and Combustion* 62.3 (1999),
         pp. 183–200.

[145]   F. Nicoud, H. B. Toda, O. Cabrit, S. Bose, and J. Lee. "Using singular values to
         build a subgrid-scale model for large eddy simulations". In: *Physics of Fluids* 23.8
         (2011), p. 085106.

[146]   S. Niksa and A. R. Kerstein. "FLASHCHAIN theory for rapid coal devolatilization
         kinetics. 1. Formulation". In: *Energy & Fuels* 5.5 (1991), pp. 647–665.

[147]   P. Nooren, H. Wouters, T. Peeters, D. Roekaerts, U. Maas, and D. Schmidt.
         "Monte Carlo PDF modelling of a turbulent natural-gas diffusion flame". In: *Com-
         bustion Theory and Modelling* 1.1 (1997), pp. 79–96.

[148]   E. E. O'Brien. "The probability density function (pdf) approach to reacting turbu-
         lent flows". In: *Turbulent Reacting Flows*. Ed. by P. A. Libby and F. A. Williams.
         Vol. 44. Topics in Applied Physics. Springer Berlin Heidelberg, 1980, pp. 185–218.

[149]   J. C. Oefelein, V. Sankaran, and T. G. Drozda. "Large eddy simulation of swirling
         particle-laden flow in a model axisymmetric combustor". In: *Proceedings of the
         Combustion Institute* 31.2 (2007), pp. 2291–2299.

[150]   J. van Oijen, R. Bastiaans, and L. de Goey. "Low-dimensional manifolds in di-
         rect numerical simulations of premixed turbulent flames". In: *Proceedings of the
         Combustion Institute* 31.1 (2007), pp. 1377–1384.

[151]   J. van Oijen and L. de Goey. "Modelling of Premixed Laminar Flames using
         Flamelet-Generated Manifolds". In: *Combustion Science and Technology* 161.1
         (2000), pp. 113–137.

[152]   C. Olbricht, O. Stein, J. Janicka, J. van Oijen, S. Wysocki, and A. Kempf. "LES
         of lifted flames in a gas turbine model combustor using top-hat filtered PFGM
         chemistry". In: *Fuel* 96 (2012), pp. 100–107.

[153] G. Olenik, O. Stein, and A. Kronenburg. "LES of swirl-stabilised pulverised coal combustion in IFRF furnace No. 1". In: *Proceedings of the Combustion Institute* 35.3 (2015), pp. 2819–2828.

[154] H. Olguin and E. Gutheil. "Influence of evaporation on spray flamelet structures". In: *Combustion and Flame* 161.4 (2014), pp. 987–996.

[155] S. Patankar. *Numerical heat transfer and fluid flow.* CRC press, 1980.

[156] J. Pedel, J. N. Thornock, and P. J. Smith. "Ignition of co-axial turbulent diffusion oxy-coal jet flames: Experiments and simulations collaboration". In: *Combustion and Flame* 160.6 (2013), pp. 1112–1128.

[157] J. Pedel, J. N. Thornock, and P. J. Smith. "Large Eddy Simulation of Pulverized Coal Jet Flame Ignition Using the Direct Quadrature Method of Moments". In: *Energy & Fuels* 26.11 (2012), pp. 6686–6694.

[158] C. Pera, J. Réveillon, L. Vervisch, and P. Domingo. "Modeling subgrid scale mixture fraction variance in LES of evaporating spray". In: *Combustion and Flame* 146.4 (2006), pp. 635–648.

[159] B. A. Perry, M. E. Mueller, and A. R. Masri. "A two mixture fraction flamelet model for large eddy simulation of turbulent flames with inhomogeneous inlets". In: *Proceedings of the Combustion Institute* 36.2 (2017), pp. 1767–1775.

[160] A. Peters and R. Weber. "Mathematical Modelling of a 2.4 MW Swirling Pulverized Coal Flame". In: *Combust. Sci. Techn.* 122 (1997), pp. 131–182.

[161] A. A. F. Peters and R. Weber. "Mathematical Modeling of a 2.4 MW Swirling Pulverized Coal Flame". In: *Combustion Science and Technology* 122.1-6 (1997), pp. 131–182.

[162] N. Peters. "Laminar diffusion flamelet models in non-premixed turbulent combustion". In: *Progress in Energy and Combustion Science* 10.3 (1984), pp. 319–339.

[163] N. Peters. "Laminar flamelet concepts in turbulent combustion". In: *Symposium (International) on Combustion* 21.1 (1986), pp. 1231–1250.

[164] N. Peters. "Local Quenching Due to Flame Stretch and Non-Premixed Turbulent Combustion". In: *Combustion Science and Technology* 30.1-6 (1983), pp. 1–17.

[165] N. Peters. "Local quenching of diffusion flamelets and non-premixed turbulent combustion". In: *Western States Section of the Combustion Institute* (1980), , Spring Meeting, Irvine, CA.

[166] N. Peters. *Turbulent combustion.* Cambridge University Press, 2000.

[167] I. Petersen and J. Werther. "Experimental investigation and modeling of gasification of sewage sludge in the circulating fluidized bed". In: *Chemical Engineering and Processing: Process Intensification* 44.7 (2005), pp. 717–736.

[168] M. Pettit, B. Coriton, A. Gomez, and A. Kempf. "Large-Eddy Simulation and experiments on non-premixed highly turbulent opposed jet flows". In: *Proceedings of the Combustion Institute* 33.1 (2011), pp. 1391–1399.

[169]   C. D. Pierce and P. Moin. "Progress-variable approach for large-eddy simulation of non-premixed turbulent combustion". In: *Journal of Fluid Mechanics* 504 (2004), pp. 73–97.

[170]   C. D. Pierce and P. Moin. "A dynamic model for subgrid-scale variance and dissipation rate of a conserved scalar". In: *Physics of Fluids* 10.12 (1998), pp. 3041–3044.

[171]   U. Piomelli. "Large-eddy simulation: achievements and challenges". In: *Progress in Aerospace Sciences* 35.4 (1999), pp. 335–362.

[172]   U. Piomelli and J. Liu. "Large-eddy simulation of rotating channel flows using a localized dynamic model". In: *Physics of Fluids* 7.4 (1995), p. 839.

[173]   H. Pitsch and N. Peters. "A Consistent Flamelet Formulation for Non-Premixed Combustion Considering Differential Diffusion Effects". In: *Combustion and Flame* 114.1–2 (1998), pp. 26–40.

[174]   H. Pitsch. "Large-eddy simulation of turbulent combustion". In: *Annual Review of Fluid Mechanics* 38.1 (2006), pp. 453–482.

[175]   R. H. Pletcher, J. C. Tannehill, and D. Anderson. *Computational fluid mechanics and heat transfer*. CRC Press, 2012.

[176]   T. Poinsot and D. Veynante. *Theoretical and numerical combustion*. RT Edwards, 2005.

[177]   S. B. Pope. "Computations of turbulent combustion: Progress and challenges". In: *Proceedings of the Combustion Institute* 23.1 (1991), pp. 591–612.

[178]   S. B. Pope. "PDF methods for turbulent reactive flows". In: *Progress in Energy and Combustion Science* 19 (1985), pp. 119–192.

[179]   S. B. Pope. "The probability approach to the modelling of turbulent reacting flows". In: *Combustion and Flame* 27 (1976), pp. 299–312.

[180]   S. B. Pope. "Transport equation for the joint probability density function of velocity and scalars in turbulent flow". In: *Physics of Fluids (1958-1988)* 24.4 (1981), pp. 588–596.

[181]   S. B. Pope. *Turbulent Flows*. Cambridge University Press, 2000.

[182]   P. P. Popov and S. B. Pope. "Implicit and explicit schemes for mass consistency preservation in hybrid particle/finite-volume algorithms for turbulent reactive flows". In: *Journal of Computational Physics* 257, Part A (2014), pp. 352–373.

[183]   P. P. Popov, H. Wang, and S. B. Pope. "Specific volume coupling and convergence properties in hybrid particle/finite volume algorithms for turbulent reactive flows". In: *Journal of Computational Physics* 294 (2015), pp. 110–126.

[184]   F. Proch and A. Kempf. "Modeling heat loss effects in the large eddy simulation of a model gas turbine combustor with premixed flamelet generated manifolds". In: *Proceedings of the Combustion Institute* 35.3 (2015), pp. 3337–3345.

[185] F. Proch. "Highly-resolved numerical simulation of turbulent premixed and strat-
       ified combustion under adiabatic and non-adiabatic conditions with tabulated
       chemistry". PhD thesis. Universität Duisburg-Essen, 2016.

[186] F. Proch, P. Domingo, L. Vervisch, and A. M. Kempf. "Flame resolved simulation
       of a turbulent premixed bluff-body burner experiment. Part I: Analysis of the
       reaction zone dynamics with tabulated chemistry". In: *Combustion and Flame*
       180 (2017), pp. 321–339.

[187] F. Proch and A. M. Kempf. "Numerical analysis of the Cambridge stratified flame
       series using artificial thickened flame LES with tabulated premixed flame chem-
       istry". In: *Combustion and Flame* 161.10 (2014), pp. 2627–2646.

[188] M. Queiroz, M. P. Bonin, J. S. Shirolkar, and R. W. Dawson. "Experimentally
       Determined Particle Number Density Statistics in an Industrial-Scale, Pulverized-
       Coal-Fired Boiler". In: *Energy & Fuels* 7 (1993), pp. 842–851.

[189] M. Rabaçal, B. Franchetti, F. C. Marincola, F. Proch, M. Costa, C. Hasse, and
       A. Kempf. "Large Eddy Simulation of coal combustion in a large-scale laboratory
       furnace". In: *Proceedings of the Combustion Institute* 35.3 (2015), pp. 3609–3617.

[190] M. Rabaçal. "Large Eddy Simulation of Coal and Biomass Combustion in Large-
       Scale Laboratory Furnaces". PhD thesis. Universidade de Lisboa, Instituto Supe-
       rior Técnico, 2016.

[191] V. Raman and H. Pitsch. "A consistent LES/filtered-density function formulation
       for the simulation of turbulent flames with detailed chemistry". In: *Proceedings of
       the Combustion Institute* 31.2 (2007), pp. 1711–1719.

[192] V. Raman, H. Pitsch, and R. O. Fox. "Hybrid large-eddy simulation/Lagrangian
       filtered-density-function approach for simulating turbulent combustion". In: *Com-
       bustion and Flame* 143.1 (2005), pp. 56–78.

[193] W. Ranz and W. Marshall. "Evaporation from drops". In: *Chemical Engineering
       Progress* 48.3 (1952), pp. 141–146.

[194] E. Ranzi, A. Frassoldati, S. Granata, and T. Faravelli. "Wide-Range Kinetic Mod-
       eling Study of the Pyrolysis, Partial Oxidation, and Combustion of Heavy n-
       Alkanes". In: *Industrial & Engineering Chemistry Research* 44.14 (2005), pp. 5170–
       5183.

[195] O. Reynolds. "On the dynamical theory of incompressible viscous fluids and the
       determination of the criterion." In: *Proceedings of the Royal Society of London*
       56.336-339 (1894), pp. 40–45.

[196] C. Rhie and W. L. Chow. "Numerical study of the turbulent flow past an airfoil
       with trailing edge separation". In: *AIAA Journal* 21.11 (1983), pp. 1525–1532.

[197] L. F. Richardson. *Weather prediction by numerical process.* Cambridge University
       Press, 1922.

[198] M. Rieth, J.-Y. Chen, S. Menon, and A. Kempf. "A Hybrid Flamelet Finite-
       Rate Chemistry Approach for Efficient LES with a Transported FDF". In: *To be
       submitted to Combustion and Flame* (2017).

[199] M. Rieth, A. Clements, M. Rabaçal, F. Proch, O. T. Stein, and A. M. Kempf. "Flamelet LES modeling of coal combustion with detailed devolatilization by directly coupled CPD". In: *Proceedings of the Combustion Institute* 36.2 (2017), pp. 2181–2189.

[200] M. Rieth, A. Kempf, A. Kronenburg, and O. Stein. "Carrier-phase DNS of pulverized coal particle ignition and volatile burning in a turbulent mixing layer". In: *Fuel* 212 (2018), pp. 364–374.

[201] M. Rieth, F. Proch, A. G. Clements, M. Rabaçal, and A. M. Kempf. "Highly resolved flamelet LES of a semi-industrial scale coal furnace". In: *Proceedings of the Combustion Institute* 36.3 (2017), pp. 3371–3379.

[202] M. Rieth, F. Proch, M. Rabaçal, B. Franchetti, F. C. Marincola, and A. Kempf. "Flamelet LES of a semi-industrial pulverized coal furnace". In: *Combustion and Flame* 173 (2016), pp. 39–56.

[203] M. Rieth, F. Proch, O. Stein, M. Pettit, and A. Kempf. "Comparison of the Sigma and Smagorinsky LES models for grid generated turbulence and a channel flow". In: *Computers & Fluids* 99 (2014), pp. 172–181.

[204] A. Rittler, F. Proch, and A. M. Kempf. "LES of the Sydney piloted spray flame series with the PFGM/ATF approach and different sub-filter models". In: *Combustion and Flame* 162.4 (2015), pp. 1575–1598.

[205] M. Saha, A. Chinnici, B. B. Dally, and P. R. Medwell. "Numerical Study of Pulverized Coal MILD Combustion in a Self-Recuperative Furnace". In: *Energy & Fuels* 29.11 (2015), pp. 7650–7669.

[206] R. F. Sawyer. "Science based policy for addressing energy and environmental problems". In: *Proceedings of the Combustion Institute* 32.1 (2009), pp. 45–56.

[207] T. Sayadi, S. Farazi, S. Kang, and H. Pitsch. "Transient multiple particle simulations of char particle combustion". In: *Fuel* 199 (2017), pp. 289–298.

[208] N. Schaffel, M. Mancini, A. Szlek, and R. Weber. "Mathematical modeling of MILD combustion of pulverized coal". In: *Combustion and Flame* 156.9 (2009), pp. 1771–1784.

[209] L. Schiller and A. Naumann. "Über die grundlegenden Berechnungen bei der Schwerkraftaufbereitung". In: *Zeitschrift des Vereines Deutscher Ingenieure* 77.12 (1933), pp. 318–320.

[210] J. H. Seinfeld and S. N. Pandis. *Atmospheric chemistry and physics: from air pollution to climate change.* John Wiley & Sons, 2016.

[211] M. Sheikhi, T. Drozda, P. Givi, F. Jaberi, and S. Pope. "Large eddy simulation of a turbulent nonpremixed piloted methane jet flame (Sandia Flame D)". In: *Proceedings of the Combustion Institute* 30.1 (2005), pp. 549–556.

[212] G. A. Simons. "The pore tree structure of porous char". In: *Proceedings of the Combustion Institute* 19.1 (1982), pp. 1067–1076.

[213] J. S. Smagorinsky. "General circulation experiments with the primitive equations, 1. The basic experiment". In: *Monthly Weather Review* 91 (1963), pp. 99–164.

[214] G. Smith, D. Golden, M. Frenklach, N. Moriarty, B. Eiteneer, M. Goldenberg, C. Bowman, R. Hanson, S. Song, W. Gardiner, V. Lissianski, and Z. Qin. *http://www.me.berkeley.edu/gri_mech/*. 2000.

[215] I. Smith. "The combustion rates of coal chars: A review". In: *Symposium (International) on Combustion* 19.1 (1982), pp. 1045–1065.

[216] L. D. Smoot and D. T. Pratt. *Pulverized-coal combustion and gasification.* Springer, 1979.

[217] L. D. Smoot and P. J. Smith. *Coal combustion and gasification.* Plenum Press, New York, NY, 1985.

[218] P. R. Solomon, D. G. Hamblen, R. M. Carangelo, M. A. Serio, and G. V. Deshpande. "General model of coal devolatilization". In: *Energy & Fuels* 2.4 (1988), pp. 405–422.

[219] A. Stagni, A. Frassoldati, A. Cuoci, T. Faravelli, and E. Ranzi. "Skeletal mechanism reduction through species-targeted sensitivity analysis". In: *Combustion and Flame* 163 (2016), pp. 382–393.

[220] O. T. Stein. "Large Eddy Simulation of Combustion in Swirling and Opposed Jet Flows". PhD thesis. Imperial College London, 2008.

[221] O. Stein, G. Olenik, A. Kronenburg, F. Cavallo Marincola, B. Franchetti, A. Kempf, M. Ghiani, M. Vascellari, and C. Hasse. "Towards Comprehensive Coal Combustion Modelling for LES". In: *Flow, Turbulence and Combustion* 90.4 (2013), pp. 859–884.

[222] M. Stöllinger, B. Naud, D. Roekaerts, N. Beishuizen, and S. Heinz. "PDF modeling and simulations of pulverized coal combustion – Part 1: Theory and modeling". In: *Combustion and Flame* 160.2 (2013), pp. 384–395.

[223] M. Stöllinger, B. Naud, D. Roekaerts, N. Beishuizen, and S. Heinz. "PDF modeling and simulations of pulverized coal combustion – Part 2: Application". In: *Combustion and Flame* 160.2 (2013), pp. 396–410.

[224] S. Subramaniam. "Lagrangian–Eulerian methods for multiphase flows". In: *Progress in Energy and Combustion Science* 39.2 (2013), pp. 215–245.

[225] Y. Sung, S. Lee, S. Eom, C. Moon, S. Ahn, G. Choi, and D. Kim. "Optical non-intrusive measurements of internal recirculation zone of pulverized coal swirling flames with secondary swirl intensity". In: *Energy* 103 (2016), pp. 61–74.

[226] H. Tennekes and J. L. Lumley. *A First Course in Turbulence.* The MIT press, 1978.

[227] J. Tillou, J.-B. Michel, C. Angelberger, and D. Veynante. "Assessing LES models based on tabulated chemistry for the simulation of Diesel spray combustion". In: *Combustion and Flame* 161.2 (2014), pp. 525–540.

[228] R. R. Tirunagari and S. B. Pope. "An investigation of turbulent premixed counterflow flames using large-eddy simulations and probability density function methods". In: *Combustion and Flame* 166 (2016), pp. 229–242.

[229] R. R. Tirunagari and S. B. Pope. "LES/PDF for premixed combustion in the DNS limit". In: *Combustion Theory and Modelling* 20.5 (2016), pp. 834–865.

[230] D. Toporov, P. Bocian, P. Heil, A. Kellermann, H. Stadler, S. Tschunko, M. Förster, and R. Kneer. "Detailed investigation of a pulverized fuel swirl flame in CO2/O2 atmosphere". In: *Combustion and Flame* 155.4 (2008), pp. 605–618.

[231] J. Truelove. "Discrete-ordinate solutions of the radiation transport equation". In: *Journal of Heat Transfer* 109.4 (1987), pp. 1048–1051.

[232] G. L. Tufano, O. T. Stein, A. Kronenburg, L. Deng, I. Wlokas, A. M. Kempf, M. Vascellari, and C. Hasse. "Direct numerical simulation of coal particle devolatilization and volatile combustion". In: *Proceedings of the 7th European Combustion Meeting* (2015). paper P5-51.

[233] G. L. Tufano, O. T. Stein, A. Kronenburg, A. Frassoldati, T. Faravelli, L. Deng, A. M. Kempf, M. Vascellari, and C. Hasse. "Resolved flow simulation of pulverized coal particle devolatilization and ignition in air- and O_2/CO_2-atmospheres". In: *Fuel* 186 (2016), pp. 285–292.

[234] S. K. Ubhayakar, D. B. Stickler, C. W. V. Rosenberg, and R. E. Gannon. "Rapid devolatilization of pulverized coal in hot combustion gases". In: *Symposium (International) on Combustion* 16.1 (1977), pp. 427–436.

[235] D. Van Krevelen. *Coal: Typology-Physics-Chemistry-Composition.* 1993.

[236] M. Vascellari, R. Arora, M. Pollack, and C. Hasse. "Simulation of entrained flow gasification with advanced coal conversion submodels. Part 1: Pyrolysis". In: *Fuel* 113 (2013), pp. 654–669.

[237] M. Vascellari, G. L. Tufano, O. T. Stein, A. Kronenburg, A. M. Kempf, A. Scholtissek, and C. Hasse. "A flamelet/progress variable approach for modeling coal particle ignition". In: *Fuel* 201 (2017), pp. 29–38.

[238] M. Vascellari, H. Xu, and C. Hasse. "Flamelet modeling of coal particle ignition". In: *Proceedings of the Combustion Institute* 34.2 (2013), pp. 2445–2452.

[239] J. Villermaux and J. C. Devillion. "Représentation de la coalescence et de la re-dispersion des domaines de ségrégation dans un fluide par un modèle d'interaction phénoménologique". In: *Proceedings of the Second International Symposium on Chemical Reaction Engineering* (1972), pp. 1–13.

[240] A. Vreman, B. Albrecht, J. van Oijen, L. de Goey, and R. Bastiaans. "Premixed and nonpremixed generated manifolds in large-eddy simulation of Sandia flame D and F". In: *Combustion and Flame* 153.3 (2008), pp. 394–416.

[241] C. Wall, B. J. Boersma, and P. Moin. "An evaluation of the assumed beta probability density function subgrid-scale model for large eddy simulation of non-premixed, turbulent combustion with heat release". In: *Physics of Fluids* 12.10 (2000), pp. 2522–2529.

[242] H. Wang and S. B. Pope. "Large eddy simulation/probability density function modeling of a turbulent jet flame". In: *Proceedings of the Combustion Institute* 33.1 (2011), pp. 1319–1330.

[243] H. Wang and P. Zhang. "A unified view of pilot stabilized turbulent jet flames for model assessment across different combustion regimes". In: *Proceedings of the Combustion Institute* 36.2 (2017), pp. 1693–1703.

[244] H. Wang, E. R. Hawkes, J. H. Chen, B. Zhou, Z. Li, and M. Aldén. "Direct numerical simulations of a high Karlovitz number laboratory premixed jet flame – an analysis of flame stretch and flame thickening". In: *Journal of Fluid Mechanics* 815 (2017), pp. 511–536.

[245] P. Warzecha and A. Boguslawski. "LES and RANS modeling of pulverized coal combustion in swirl burner for air and oxy-combustion technologies". In: *Energy* 66 (2014), pp. 732–743.

[246] P. Warzecha and A. Boguslawski. "Simulations of pulverized coal oxy-combustion in swirl burner using RANS and LES methods". In: *Fuel Processing Technology* 119 (2014), pp. 130–135.

[247] J. Watanabe, T. Okazaki, K. Yamamoto, K. Kuramashi, and A. Baba. "Large-eddy simulation of pulverized coal combustion using flamelet model". In: *Proceedings of the Combustion Institute* 36.2 (2017), pp. 2155–2163.

[248] J. Watanabe and K. Yamamoto. "Flamelet model for pulverized coal combustion". In: *Proceedings of the Combustion Institute* 35.2 (2015), pp. 2315–2322.

[249] R. Weber, J. Dugue, A. Sayre, A. A. F. Peters, and B. M. Visser. *Measurements and computations of quarl zone flow field and chemistry in a swirling pulverized coal flame.* Tech. rep. F36/y/20. Int. Flame Res. Found. (IFRF), 1992.

[250] R. Weber, J. Dugué, A. Sayre, A. Peters, and B. Visser. *Measurements and computations of quarl zone flow field and chemistry in a swirling pulverized coal flame.* Tech. rep. F36/y/20. Int. Flame Res. Found. (IFRF), 1992.

[251] R. Weber, J. Dugué, A. Sayre, and B. Visser. "Quarl zone flow field and chemistry of swirling pulverized coal flames: Measurements and computation". In: *Symposium (International) on Combustion* 24.1 (1992). Twenty-Fourth Symposium on Combustion, pp. 1373–1380.

[252] X. Wen, H. Jin, O. T. Stein, J. Fan, and K. Luo. "Large Eddy Simulation of piloted pulverized coal combustion using the velocity-scalar joint filtered density function model". In: *Fuel* 158 (2015), pp. 494–502.

[253] X. Wen, K. Luo, H. Jin, and J. Fan. "Large eddy simulation of piloted pulverised coal combustion using extended flamelet/progress variable model". In: *Combustion Theory and Modelling* (), pp. 1–29.

[254] X. Wen, K. Luo, H. Jin, and J. Fan. "Numerical investigation of coal flamelet characteristics in a laminar counterflow with detailed chemistry". In: *Fuel* 195 (2017), pp. 232–242.

[255] X. Wen, K. Luo, Y. Luo, H. I. Kassem, H. Jin, and J. Fan. "Large eddy simulation of a semi-industrial scale coal furnace using non-adiabatic three-stream flamelet/progress variable model". In: *Applied Energy* 183 (2016), pp. 1086–1097.

[256]   A. Williams, R. Backreedy, R. Habib, J. Jones, and M. Pourkashanian. "Modelling coal combustion: the current position". In: *Fuel* 81.5 (2002), pp. 605–618.

[257]   A. Williams, M. Pourkashanian, and J. Jones. "Combustion of pulverised coal and biomass". In: *Progress in Energy and Combustion Science* 27.6 (2001), pp. 587–610.

[258]   F. A. Williams. *Combustion Theory. The Fundamental Theory of Chemically Reacting Flow Systems*. 1985.

[259]   F. A. Williams. "Spray Combustion and Atomization". In: *The Physics of Fluids* 1.6 (1958), pp. 541–545.

[260]   F. Williams. "Recent advances in theoretical descriptions of turbulent diffusion flames". In: *Turbulent mixing in nonreactive and reactive flows*. Springer, 1975, pp. 189–208.

[261]   J. Williamson. "Low-storage Runge-Kutta schemes". In: *Journal of Computational Physics* 35.1 (1980), pp. 48–56.

[262]   H. Wu and M. Ihme. "Compliance of combustion models for turbulent reacting flow simulations". In: *Fuel* 186 (2016), pp. 853–863.

[263]   H. Xu, F. Hunger, M. Vascellari, and C. Hasse. "A consistent flamelet formulation for a reacting char particle considering curvature effects". In: *Combustion and Flame* 160.11 (2013), pp. 2540–2558.

[264]   K. Yamamoto, T. Murota, T. Okazaki, and M. Taniguchi. "Large eddy simulation of a pulverized coal jet flame ignited by a preheated gas flow". In: *Proceedings of the Combustion Institute* 33.2 (2011), pp. 1771–1778.

[265]   H. Yamashita, M. Shimada, and T. Takeno. "A numerical study on flame stability at the transition point of jet diffusion flames". In: *Symposium (International) on Combustion* 26.1 (1996), pp. 27–34.

[266]   S. Yang, R. Ranjan, V. Yang, S. Menon, and W. Sun. "Parallel on-the-fly adaptive kinetics in direct numerical simulation of turbulent premixed flame". In: *Proceedings of the Combustion Institute* 36.2 (2017), pp. 2025–2032.

[267]   S. Yang, V. Yang, W. Sun, S. Nagaraja, W. Sun, Y. Ju, and X. Gou. "Parallel On-the-fly Adaptive Kinetics for Non-equilibrium Plasma Discharges of C2H4/O2/Ar Mixture". In: *54th AIAA Aerospace Sciences Meeting*. San Diego California. 2016, pp. 2016–0195.

[268]   X.-Y. Zhao and D. C. Haworth. "Transported PDF modeling of pulverized coal jet flames". In: *Combustion and Flame* 161.7 (2014), pp. 1866–1882.

[269]   G. Zhou. *Numerical simulations of physical discontinuities in single and multi-fluid flows for arbitrary Mach numbers*. Chalmers University of Technology, 1995.